Friedrich-Alexander-Universität
Faculty of Sciences

Dissertation

2025

Tim Jonathan Unbehaun

Improvements to event reconstruction and analysis of IACT data and their application to joint-instrument analyses of galactic and extragalactic γ-ray sources

Improvements to event reconstruction and analysis of IACT data and their application to joint-instrument analyses of galactic and extragalactic γ-ray sources

Verbesserung von Rekonstruktions- und Analyseverfahren von IACT-Daten und deren Anwendung in Multi-Instrumentenanalysen galaktischer und extragalaktischer γ-Strahlenquellen

Der Naturwissenschaftlichen Fakultät
der Friedrich-Alexander-Universität Erlangen-Nürnberg
zur Erlangung des Doktorgrades Dr. rer. nat.

Vorgelegt von
Tim Jonathan Unbehaun
aus Nürnberg

Als Dissertation genehmigt von der Naturwissenschaftlichen Fakultät
der Friedrich-Alexander-Universität Erlangen-Nürnberg

Tag der mündlichen Prüfung:	19.09.2025
Prüfungskommission:	Prof. Dr. Klaus Mecke Prof. Dr. Stefan Funk Prof. Dr. Claudio Kopper

Abstract

Imaging Atmospheric Cherenkov Telescopes (IACTs) detect light from γ-ray-induced particle showers and have transformed our understanding of the high-energy universe by revealing astrophysical sources capable of extreme particle acceleration. Examples include Galactic sources such as supernova remnants, pulsar wind nebulae, and stellar clusters, as well as extragalactic sources like supermassive black holes accreting matter. However, the particle composition and acceleration mechanisms at most of these sources remain unclear. Unlike charged particles, γ rays and neutrinos travel undeflected by magnetic fields, enabling precise source identification.

Reconstructing the properties of incident particles from shower images is particularly challenging in monoscopic events. This work introduces a variable event selection cut, novel image parameters, and an algorithm that determines the correct image orientation, improving reconstruction accuracy, enhancing sensitivity, and lowering energy thresholds. It also advances the classification of primary particle types, which is essential for separating γ rays from the cosmic-ray background. These methods are applied to real data from the Crab Nebula, with associated systematic uncertainties carefully evaluated on different sets of simulations.

Subsequent data analysis typically employs binned likelihood methods to compare model predictions to the background-subtracted signal estimates. As asymmetries in the background rates pose challenges to the signal estimation, two correction schemes are developed to improve the accuracy of the background estimate for individual observations. Additionally, binning of events based on their reconstructed properties is avoided in the unbinned analysis, which offers advantages for studying sources with rapid time variability, such as pulsars. Possible implementations within the Gammapy framework are explored, evaluated, and applied to pulsar data.

With the advent of multi-messenger astrophysics, this thesis also explores joint analyses across instruments. A likelihood-level combination of simulated γ-ray data from CTAO and neutrino data from KM3NeT demonstrates sensitivity to leptonic vs. hadronic emission scenarios and Gammapy's ability to handle data from stationary neutrino detectors, despite being originally designed for pointed IACTs.

Similarly, a real-data analysis is conducted on the Crab Nebula—a young pulsar wind nebula system and an ideal target for studying non-thermal emission due to its brightness up to PeV energies. This analysis combines events from H.E.S.S. and Fermi-LAT, along with high-level data from radio to X-ray instruments. It constitutes the first fully self-consistent analysis of the Crab Nebula's γ-ray emission, constraining its spectrum and spatial extension across five orders of magnitude in energy. Probing the radial dependence of the magnetic field density reveals a decline with increasing distance from the center.

The combination of Fermi-LAT and H.E.S.S. data is also applied to the radio galaxy Centaurus A, a candidate site for ultra-high-energy particle acceleration. Several emission components and the radial dependence of the magnetic field are constrained with careful consideration of systematic uncertainties. In the core spectrum measured by Fermi-LAT, an unusual hardening is confirmed above 3 GeV, indicating the presence of a second emission component. Furthermore, analysis of the lobe emission using new templates derived from radio data reveals that a scenario involving a radially declining magnetic field is favored by the Fermi-LAT data. The combined analysis with H.E.S.S. data indicates a softening of the spectral index of the second core component toward higher energies, although no spectral cutoff is identified. While the core spectrum results are robust against uncertainties in background templates, the lobe emission is more significantly affected.

Zusammenfassung

Bildgebende atmosphärische Cherenkov-Teleskope (IACTs) detektieren Licht von durch γ-Strahlen ausgelösten Teilchenschauern und haben unser Verständnis des Hochenergie-Universums grundlegend verändert, indem sie astrophysikalische Quellen entdeckten, die zu extremer Teilchenbeschleunigung fähig sind. Beispiele hierfür sind galaktische Quellen wie Supernova-Überreste, Pulsarwindnebel und Sternhaufen, sowie extragalaktische Quellen wie supermassereiche Schwarze Löcher, die Materie aufnehmen. Die Teilchenzusammensetzung und die Beschleunigungsmechanismen an den meisten dieser Quellen sind jedoch weiterhin unklar. Im Gegensatz zu geladenen Teilchen werden γ-Strahlen und Neutrinos nicht durch Magnetfelder abgelenkt, was eine präzise Identifikation ihrer Ursprungsquellen ermöglicht.

Die Eigenschaften einfallender Teilchen anhand von Schauerbildern zu rekonstruieren ist insbesondere bei Mono-Ereignissen eine Herausforderung. Diese Arbeit stellt einen variablen Ereignisselektions-Cut, neue Bildparameter und einen Algorithmus vor, der die korrekte Bildausrichtung bestimmt. Dadurch wird die Rekonstruktionsgenauigkeit verbessert, die Sensitivität erhöht und die Energieschwelle gesenkt. Außerdem wird die Klassifikation der Primärteilchentypen verbessert, was essenziell für die Trennung von γ-Strahlen vom kosmischen Strahlungshintergrund ist. Diese Methoden werden auf reale Daten vom Krebsnebel angewandt, wobei die damit verbundenen systematischen Unsicherheiten mithilfe unterschiedlicher Simulationen sorgfältig untersucht werden.

Die anschließende Datenanalyse nutzt typischerweise binned-Likelihood-Methoden, um Modellvorhersagen mit den nach Abzug des Hintergrunds erhaltenen Signalabschätzungen zu vergleichen. Da Asymmetrien in den Hintergrundraten die Signalschätzung erschweren, werden zwei Korrekturmethoden entwickelt, um die Genauigkeit der Hintergrundabschätzung für einzelne Beobachtungen zu verbessern. Darüber hinaus wird bei der unbinned Analyse auf die Gruppierung von Ereignissen basierend auf ihren rekonstruierten Eigenschaften verzichtet, was Vorteile für die Untersuchung schnell variabler Quellen wie Pulsare bietet. Mögliche Implementierungen innerhalb des Gammapy-Pakets werden untersucht, bewertet und auf Pulsardaten angewandt.

Mit dem Aufkommen der Multi-Messenger-Astrophysik untersucht diese Dissertation auch gemeinsame Analysen verschiedener Instrumente. Eine Kombination von simulierten γ-Strahlungsdaten aus CTAO mit Neutrinodaten von KM3NeT auf der Likelihood-Ebene demonstriert eine Sensitivität gegenüber leptonischen vs. hadronischen Emissionsszenarien sowie die Fähigkeit von Gammapy, Daten stationärer Neutrinodetektoren zu analysieren, obwohl das Softwarepaket ursprünglich für gerichtete IACTs entwickelt wurde.

Ebenso wird eine Analyse mit realen Daten des Krebsnebels durchgeführt—einem jungen Pulsarwindnebel-System und einem idealen Objekt für die Untersuchung nicht-thermischer Emission aufgrund seiner Helligkeit bis hin zu PeV-Energien. Diese Analyse kombiniert Ereignisse von H.E.S.S. und Fermi-LAT sowie prozessierte Daten von Radiowellen- bis hin zu Röntgeninstrumenten. Sie stellt die erste vollständig konsistente Analyse der γ-Strahlen-Emission des Krebsnebels dar und misst dessen Spektrum und räumliche Ausdehnung über fünf Größenordnungen in der Energie. Die Untersuchung der radialen Abhängigkeit der Magnetfelddichte zeigt eine Abnahme mit zunehmender Entfernung vom Zentrum.

Die Kombination von Fermi-LAT- und H.E.S.S.-Daten wird auch auf die Radiogalaxie Centaurus A angewandt, einen potenziellen Ort für die Beschleunigung ultrahochenergetischer Teilchen. Mehrere Emissionskomponenten und die radiale Abhängigkeit des Magnetfeldes werden unter sorgfältiger Berücksichtigung systematischer Unsicherheiten eingegrenzt. Im vom Fermi-LAT gemessenen Spektrum der zentralen Punktquelle wird ein ungewöhnlicher Anstieg in der Steigung oberhalb von 3 GeV bestätigt, was auf eine zweite Emissionskomponente hinweist. Darüber hinaus zeigt die Analyse der Lobes unter Verwendung neuer räumlicher Modelle, die aus Radiodaten abgeleitet wurden, dass ein

radial abnehmendes Magnetfeld von den Fermi-LAT-Daten bevorzugt wird. Die kombinierte Analyse mit H.E.S.S.-Daten weist auf eine abnehmende Steigung der zweiten Kernkomponente bei höheren Energien hin, obwohl kein abruptes Ende identifiziert wird. Während die Ergebnisse für das Spektrum der Punktquelle robust gegenüber Unsicherheiten in den Hintergrundmodellen sind, ist die Lobe-Emission deutlich stärker davon betroffen.

Contents

1 Introduction to high-energy astrophysics **1**
1.1 Particle acceleration mechanisms . . . 3
1.2 Production of γ rays . . . 5
1.3 Sources of γ rays . . . 6
1.3.1 Supernova remnants . . . 7
1.3.2 Pulsars . . . 8
1.3.3 Pulsar wind nebulae . . . 9
1.3.4 Stellar clusters . . . 11
1.3.5 Active galactic nuclei . . . 12
1.4 Detection of γ rays with Fermi-LAT . . . 14
1.5 Ground-based detection of γ rays with IACTs . . . 16
1.5.1 Particle showers in the atmosphere . . . 16
1.5.2 Cherenkov light emission . . . 19
1.5.3 Imaging Atmospheric Cherenkov Telescopes . . . 20
1.6 Source analysis in the context of Gammapy . . . 23
1.6.1 Forward-folding . . . 24
1.6.2 Statistical methods . . . 28
1.7 Galactic and Equatorial coordinates . . . 32

2 Prospects for combined analyses of hadronic emission from γ-ray sources in the Milky Way with CTA and KM3NeT **34**
2.1 Introduction . . . 34
2.2 Methodology . . . 37
2.2.1 Generation of KM3NeT IRFs . . . 38
2.2.2 Comparison of IRFs . . . 39
2.2.3 Input models . . . 41
2.2.4 Generation of pseudo data sets . . . 43
2.2.5 Likelihood analysis . . . 44
2.2.6 Constraining the hadronic contribution . . . 46
2.3 Results . . . 47
2.3.1 Analysis scenarios . . . 47
2.3.2 Analysis results . . . 48
2.3.3 Discussion . . . 48
2.4 Conclusion . . . 51

3 Unbinned Analysis **52**
3.1 Derivation of the unbinned likelihood . . . 52
3.1.1 Computation of the differential predicted counts . . . 53
3.1.2 Computation of the total number of predicted counts . . . 56
3.2 Accuracy evaluation . . . 58
3.3 Performance evaluation . . . 61
3.4 Application to pulsar analyses . . . 63
3.4.1 Pulsar analysis of the Crab Pulsar . . . 63
3.4.2 Pulsar glitches in PSR J1906+0722 . . . 66
3.5 Discussion . . . 69

4 Spectrum and extension of the inverse-Compton emission of the Crab Nebula from a combined Fermi-LAT and H.E.S.S. analysis 71
4.1 Introduction 71
4.2 Data analysis 73
4.2.1 H.E.S.S. data analysis 73
4.2.2 Fermi-LAT data analysis 77
4.3 Combined analysis 80
4.3.1 Preparation of Fermi-LAT data in GAMMAPY 80
4.3.2 Measuring the Crab Nebula's combined energy spectrum and extension 81
4.4 Modelling of the Crab Nebula 84
4.4.1 Physical emission models for the Crab Nebula 84
4.4.2 Fitting of the models 90
4.4.3 Discussion of the models 91
4.5 Systematic uncertainties and energy scale 99
4.6 Conclusion 102

5 Improvements to monoscopic analysis for imaging atmospheric Cherenkov telescopes: Application to H.E.S.S. 104
5.1 Introduction 104
5.2 Implementation 105
5.3 Definition of training variables 106
5.3.1 Hillas parameter-based variables 107
5.3.2 Sector-based variables 108
5.3.3 Continuous variables 109
5.3.4 Pixel Variables 112
5.3.5 NSB sensitivity of the image parameters 113
5.4 Architecture of training algorithms 114
5.4.1 Flip determination algorithm 115
5.4.2 Energy and disp regression algorithm 116
5.4.3 Particle identification algorithm 117
5.5 Size-dependent selection cut 118
5.6 Performance evaluation 119
5.6.1 Event reconstruction 119
5.6.2 Background rejection 122
5.6.3 Sensitivity 124
5.6.4 Application to test dataset 125
5.7 Conclusion 126

6 Asymmetries in the background of H.E.S.S. mono data 128
6.1 Plane background correction 129
6.2 Profile background correction 131
6.3 Application to data 133

7 Fermi-LAT and H.E.S.S. analysis of Centaurus A 136
7.1 Fermipy analysis 137
7.1.1 The core model 138
7.1.2 The lobe models 139
7.2 H.E.S.S. analysis 145
7.3 Combined analysis 147
7.4 Conclusion 150

8 Summary and Discussion **152**
8.1 Improvements to the analyses 152
8.1.1 Low-level analysis 152
8.1.2 High-level analyses 155
8.2 Applications of the improvements 157

9 Conclusion and Outlook **161**

Acronyms **163**

Appendix **167**
A Likelihood scan results for all sources 167
B Comparison with the reflected regions background method 169
C Variable distribution plots 170
D Variables summary 177

Bibliography **179**

Acknowledgments **193**

The heavens declare the glory of God; the skies proclaim the work of his hands.

— King David, Psalm 19:1

1 Introduction to high-energy astrophysics

With his balloon flights in 1912, Viktor Hess discovered the first evidence of a flux of charged particles arriving from the cosmos (Hess, 1912). He demonstrated that the intensity of ionizing radiation does not decrease continuously with altitude, as one would expect for radiation of terrestrial origin. Instead, the intensity increased significantly above altitudes of 3 km, indicating the presence of extraterrestrial sources. Since then, the spectral energy distribution (SED) of these cosmic rays (CRs) has been measured by various experiments over many orders of magnitude. Figure 1.1 shows the steep power-law nature of the spectrum, ranging from one particle per cm^2 per second at GeV energies to less than one particle per km^2 per year above several EeV[1]. Very large detector arrays, such as the Pierre Auger Observatory (Pierre Auger Collaboration, 2015) or the Telescope Array (Tokuno et al., 2008; Abu-Zayyad et al., 2012), with several hundred km^2 surface area, are necessary to collect the few particles at the highest energies.

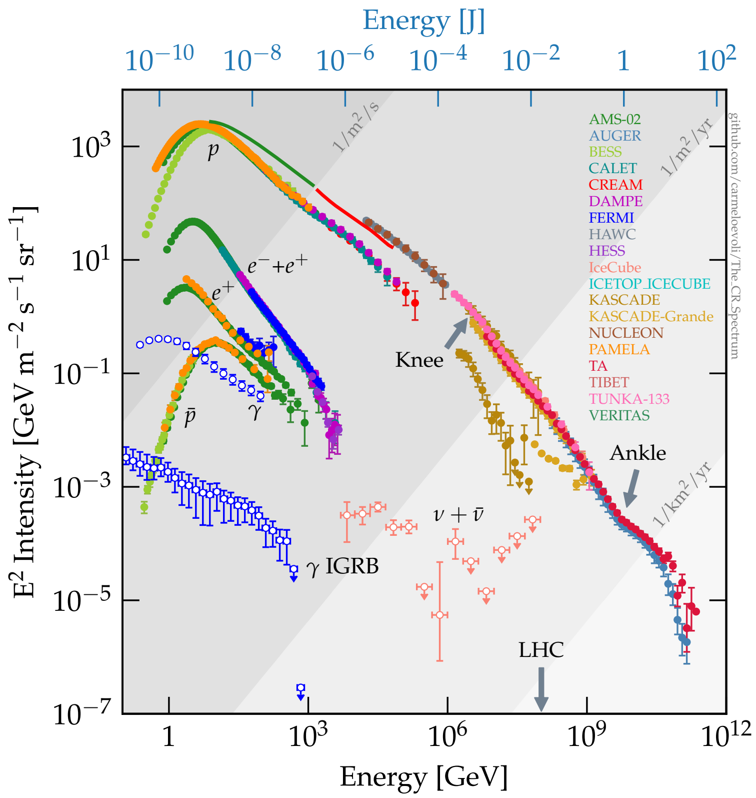

Figure 1.1: Cosmic ray spectrum as measured by the experiments listed in the legend. Individual particle contributions are shown for protons (p) and anti-protons ($\bar{p}$), positrons (e^+) and their combination with electrons (e^-+e^+). Additionally, diffuse Galactic γ-ray fluxes (γ) are shown, along with the isotropic gamma-ray background (γ IGRB) and astrophysical (anti-)neutrino fluxes ($\nu+\bar{\nu}$). The spectral 'Knee' and 'Ankle' are marked at 3 PeV and 7 EeV, respectively, as well as the fixed-target equivalent of the LHC center-of-mass energy at 104 PeV. Taken from Evoli (2025).

As discussed in Tjus and Merten, 2020, the differential CR flux, expressed as the number of particles dN per energy interval dE, is well-described by a series of power laws over a wide range of energies:

$$dN(E) = A \cdot E^{-\Gamma} dE, \tag{1.1}$$

[1] 1 EeV = 10^9 GeV = 10^{18} eV, where 1 eV is an energy unit used for subatomic particles and corresponds to the energy gained per elementary charge e when accelerated by an electric potential of one volt.

where A is the amplitude and Γ is the power-law index, typically ranging between 2.5 and 3.1. Similar power-law indices are generally interpreted as signatures of comparable source classes and acceleration mechanisms shaping the CR spectrum across these energies. Between $\sim 10\,\mathrm{GeV}$ and the spectral 'knee' around $\sim 3\,\mathrm{PeV}$, the index remains close to a value of 2.7. In this region, the observed CRs are mostly attributed to Galactic accelerators, since extragalactic accelerators are too distant to account for the large observed luminosities. Above the knee, the index softens to a value around 3.1, indicating either a maximum energy limit of the prevailing Galactic source population or changes in CR transport properties. At the 'ankle', near $7\,\mathrm{EeV}$, the spectrum hardens again to an index of $x \approx 2.3$, marking the transition to a regime dominated by extragalactic sources. Current estimates suggest that extragalactic accelerators can account for the flux beyond this energy threshold, whereas no known Galactic source class is expected to reach such extreme energies (Tjus and Merten, 2020).

Notably, the energies to which CR particles are accelerated require extreme acceleration environments and exceed the highest energies achievable in particle accelerators at Earth by several orders of magnitude. Particle colliders, such as the Large Hadron Collider (LHC), achieve energies E_{CMS} in the center of mass system (CMS) of up to $14\,\mathrm{TeV}$ in head-on proton collisions (Evans, 2011). Reaching the same CMS energy in a fixed-target experiment requires an energy E_1 for the moving particle of

$$E_1 = \frac{1}{2}\frac{E_{\mathrm{CMS}}^2}{m_p} = 104\,\mathrm{PeV}, \tag{1.2}$$

for the proton mass $m_p = 0.938\,\mathrm{GeV}$. This value for E_1 is also indicated in Fig. 1.1 on the lower energy axis. Considering that the kinematics of particle collisions at the EeV scale differ from those, e.g., at the TeV scale, studying CRs enables tests of fundamental physics at extreme energy limits. By analyzing the spectral features and composition of the CRs and identifying their sources, researchers can gain insights into both the smallest building blocks of matter and the largest, most extreme environments in our universe. However, the identification of individual sources is challenging as charged particles are deflected by ambient magnetic fields in the interstellar medium (ISM) on their way to Earth. Subsequently, their arrival direction no longer points back to their source in the sky, and the CR flux appears isotropic, i.e., uniform in all directions. This isotropy holds at most energies, except at the highest energies, where deflection angles are too small to fully obscure the source directions. Even above $8\,\mathrm{EeV}$, however, the level of the CR anisotropy remains small, with a measured amplitude of only $(6.0 \pm 1.5)\%$ (Pierre Auger Collaboration et al., 2017). Additionally, the regions of excess flux are large and encompass multiple potential sources.

Over the past few decades, significant advancements have been made through the development of theoretical models for potential acceleration regions and particle interactions (e.g. Schlickeiser, 1996; Amato and Casanova, 2021; Kirk et al., 2023; Huang et al., 2023). These models provide predictions that can be compared with observational data using statistical methods. Such comparisons facilitate the rejection of specific parameter spaces or even entire models, as well as their refinement or validation.

Current theories on particle acceleration within astrophysical sources are explored in Section 1.1, followed by an examination of particle interactions within sources that produce neutral particles, particularly photons in the γ-ray regime in Section 1.2. These interactions are of interest because the neutral particles point back to their origins, offering a pathway to identify individual sources of CRs, some of which are presented in Section 1.3. Sections 1.4 and 1.5 introduce space-based and ground-based detection techniques for γ rays, respectively. The statistical methods used to compare observational data with model predictions are described in Section 1.6. Finally, this section concludes with an overview of relevant coordinate systems employed in this work, presented in Section 1.7.

1.1 Particle acceleration mechanisms

The following summary of possible acceleration mechanisms is intended to provide a brief introduction to particle acceleration theory relevant to this work. More context and details may be found, e.g., in Longair (2011) (Chapter 17.3).

A theory of non-thermal particle acceleration needs to account for the power-law nature of the energy spectrum (cf. 1.1), with typical indices Γ in the range of 2 to 3. Furthermore, acceleration mechanisms have to be able to efficiently accelerate particles up to the highest energies observed (10^{21} eV). In 1949, Fermi proposed an acceleration mechanism, in which charged particles are reflected by clouds, acting as "magnetic mirrors", and moving randomly with velocity $\beta = {}^{v}\!/_{c}$ (Fermi, 1949). Lorentz transformations of the particle's momentum in and out of the magnetic cloud frame result in an energy gain for head-on collisions but an energy loss for trailing collisions. Fermi showed that particles would stochastically gain energy according to

$$\left\langle \frac{\Delta E}{E} \right\rangle = \frac{8}{3}\beta^2, \tag{1.3}$$

due to the higher probability of head-on collisions. This leads to an exponential increase in particle energy and a power-law energy spectrum if particles are assumed to stay in the acceleration region for a certain time τ_{esc}. However, the index of the power law does not naturally match the observed values, but rather depends on the rate of energy gain and τ_{esc}, which are expected to vary between different acceleration sites. Furthermore, this process is inefficient, since the energy gain is proportional to $\beta^2 \sim 10^{-8}$, and the number of collisions is expected to be only a few per year (Longair, 2011).

In the 1970s, a theory of diffusive shock acceleration expanded on Fermi's initial idea, where a shock front expands into the interstellar medium (Bell, 1978, among others). Diffusive shock acceleration could describe scenarios such as the aftermath of supernovae explosions or, on larger scales, when stellar winds combine to form a shock front around young stellar clusters. The shock front moves with a supersonic velocity v_1 relative to the medium ahead of the shock (upstream), while the shocked medium (downstream) moves with velocity $v_2 < v_1$. In this scenario, particles crossing the shock front experience a head-on collision every time, gaining energy proportional to ${}^{v_1}\!/_{c}$. Therefore, this acceleration process is also referred to as first-order Fermi acceleration, being proportional to β instead of β^2. Naturally, a power-law spectrum with an index of 2 follows (see Longair (2011), Chapter 17.4 for details). While this mechanism applies to nearly all shocks (except those expanding perpendicular to the magnetic field), it assumes another process that accelerates particles from thermal energies to the required energy level for this mechanism to be efficient. These other possible acceleration mechanisms include one-shot acceleration and magnetic reconnection, but are not further discussed here.

Magnetic fields are responsible for randomizing the particle's direction of motion on each side of the shock front and confining the particles within the shock region. In the downstream medium, the necessary magnetic turbulence can be generated from the kinetic streaming energy of the upstream plasma (Bell, 1978). Upstream of the shock, CRs interact resonantly with weak perturbations, B_1, in the ambient magnetic field, B, amplifying these perturbations and giving rise to so-called Alfvén waves. Named after Hannes Alfvén, these waves are "a kind of combined electromagnetic-hydrodynamic wave" (Alfvén, 1942), supported by interactions between the magnetic field and the plasma's ionized particles. They propagate at the Alfvén velocity, v_A, determined by the ambient magnetic field strength and the mass density of the interstellar medium, ρ:

$$v_A = \frac{B}{\sqrt{\mu_0 \rho}}, \tag{1.4}$$

where μ_0 is the permeability of free space. These waves travel along the magnetic field direction, inducing oscillations in gas ions perpendicular to it. The resonance condition is met when the CR particle performs one gyration around B while traversing the perturbation length λ,

$$\lambda = \frac{2\pi v_{||}}{\Omega} = \frac{2\pi v_{||} E}{qBc}, \tag{1.5}$$

with $\Omega = {}^{qBc}\!/_{E}$ the relativistic gyro frequency, which depends on the particle's charge q and energy E (Wentzel, 1974). Consequently, CRs with different energies resonate with perturbations at different scales, increasing their amplitude and leading to scattering on the self-generated waves. If the streaming velocity of the CRs, $\langle v \rangle$, is larger than v_A, the anisotropy in the wave frame leads to a higher rate of back-scattering. This leads to a net momentum transfer to the waves, effectively reducing $\langle v \rangle$ to approximately v_A (Wentzel, 1974), thereby allowing the shock front to overtake the particles once again (Bell, 1978).

The maximum energy above which the particles are no longer confined in the acceleration region can be estimated from the *Hillas criterion* (Hillas, 1984), equating the size of the source with the Larmor radius r_L of particles with charge Ze in the magnetic field B:

$$E_\mathrm{max} \approx Ze\, c\, B\, r_\mathrm{L}. \tag{1.6}$$

Figure 1.2 shows a comparison of different source candidates against the requirements of size and magnetic field strength. A large variety of astrophysical objects – from active galactic nuclei and their jets, over supernova remnants, to white dwarfs and neutron stars – fulfill this criterion and are candidates to reach the highest energies. However, many more requirements need to be satisfied, such as the presence of charged particles, fast shocks lasting over a long enough time span, and a positive balance between energy gain and loss mechanisms (Longair, 2011).

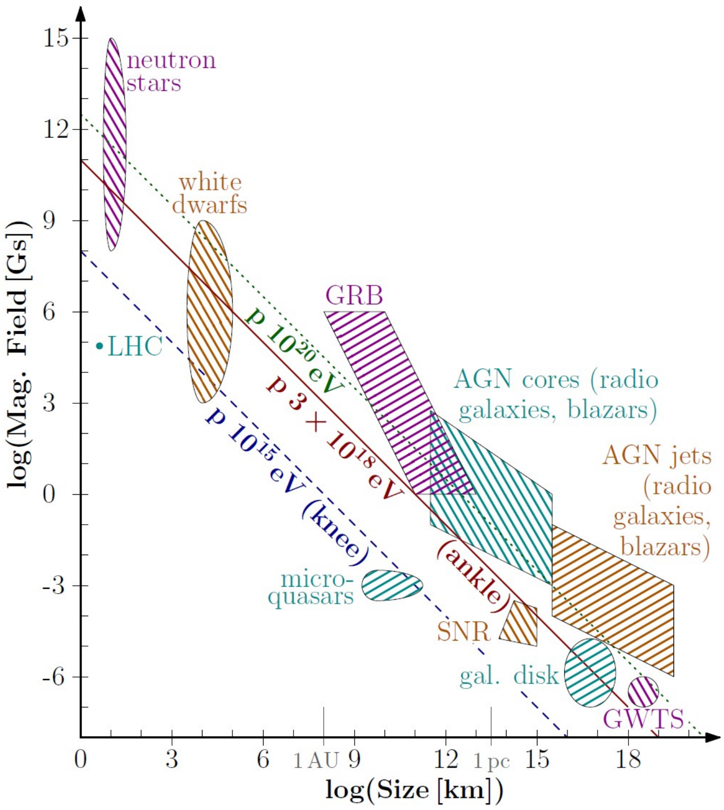

Figure 1.2: Hillas diagram comparing source candidates at various length scales and magnetic field strengths to the Hillas criterion from Eq. 1.6. Sources located below the diagonal lines are not expected to achieve the corresponding proton energies. Taken from Tjus and Merten (2020).

1.2 Production of γ rays

There are different ways in which high-energy CRs interact with the ambient medium or fields, some of which lead to the production of neutral particles that point back to their sources. Depending on the particle type, one generally separates these interactions into leptonic and hadronic processes.

The former lead to the production of γ rays when high-energy electrons (referring to e^- and e^+) emit synchrotron radiation in local magnetic fields or undergo Inverse Compton (IC) scattering. In the IC process, a low-energy photon is upscattered by a high-energy electron. These low-energy photons are called "seed photons" and may have multiple origins, including the cosmic microwave background (CMB), infrared (IR) emission from stars or nearby dust, as well as synchrotron emission from the high-energy electrons themselves. Figure 1.3 (top) shows the resulting γ-ray spectrum produced by an electron population. The synchrotron emission is responsible for the bump at lower energies, while the IC emission almost reaches the highest electron energies. Typical γ-ray sources believed to have a leptonic production mechanism include pulsars and pulsar wind nebulae (Torres, 2017; Mitchell and Gelfand, 2022, and references therein). By measuring their broadband electromagnetic emission and making assumptions about the local magnetic field strength and seed photon field densities, one can infer the spectrum of electrons at the source. A detailed model for the synchrotron and IC emission of the Crab Nebula is presented in Sect. 4.4.1.

In the case of a proton population at the source, the dominant processes are hadronic interactions with local gas or photon fields, leading to a population of secondary pions and heavier mesons. These subsequently decay, where the neutral mesons decay into γ rays, while the charged mesons decay into muon neutrinos and muons. The muons, in turn, decay into electrons and the corresponding neutrinos. The characteristic pion-bump expected from a proton population is shown in the bottom panel of Fig. 1.3. Protons rarely emit synchrotron radiation due to their large mass. This can be seen when considering the energy loss rate of relativistic particles derived in Longair, 2011:

$$-\left(\frac{dE}{dt}\right)_{\mathrm{rad}} \propto q^2\gamma^4, \tag{1.7}$$

with q the particle's charge and $\gamma = E/mc^2$ its Lorentz factor. The energy loss ratio of protons to electrons with the same energy follows as $\left(m_e/m_p\right)^4 \approx 8 \times 10^{-14}$. In the hadronic scenario, synchrotron radiation is dominantly produced by secondary electrons.

Distinguishing between leptonic and hadronic production of the γ rays is possible by either measuring the SED over many orders of magnitude or by the (non-)detection of neutrinos, which are characteristic of the hadronic case. Based on γ-ray data alone, it is often challenging to determine the production scenario with high confidence.

Besides its connection to CRs, γ-ray and neutrino observations are of interest on their own, with many studies focusing on physics beyond the Standard Model. Heavy dark matter particles might decay or annihilate, leading to the production of γ rays and neutrinos in regions with high dark matter concentration. In the past, γ-ray observations have been used to put constraints on some of the proposed dark matter models (Abdalla et al., 2016; Chianese et al., 2021).

Furthermore, the propagation of γ rays could be affected by potential Lorentz invariance violations, such that time signatures of γ-ray bursts or the TeV spectra of γ-ray sources constrain possible violations (Lang et al., 2019). Less exotic models can also be probed by their influence on γ-ray propagation. Interactions with the extragalactic background

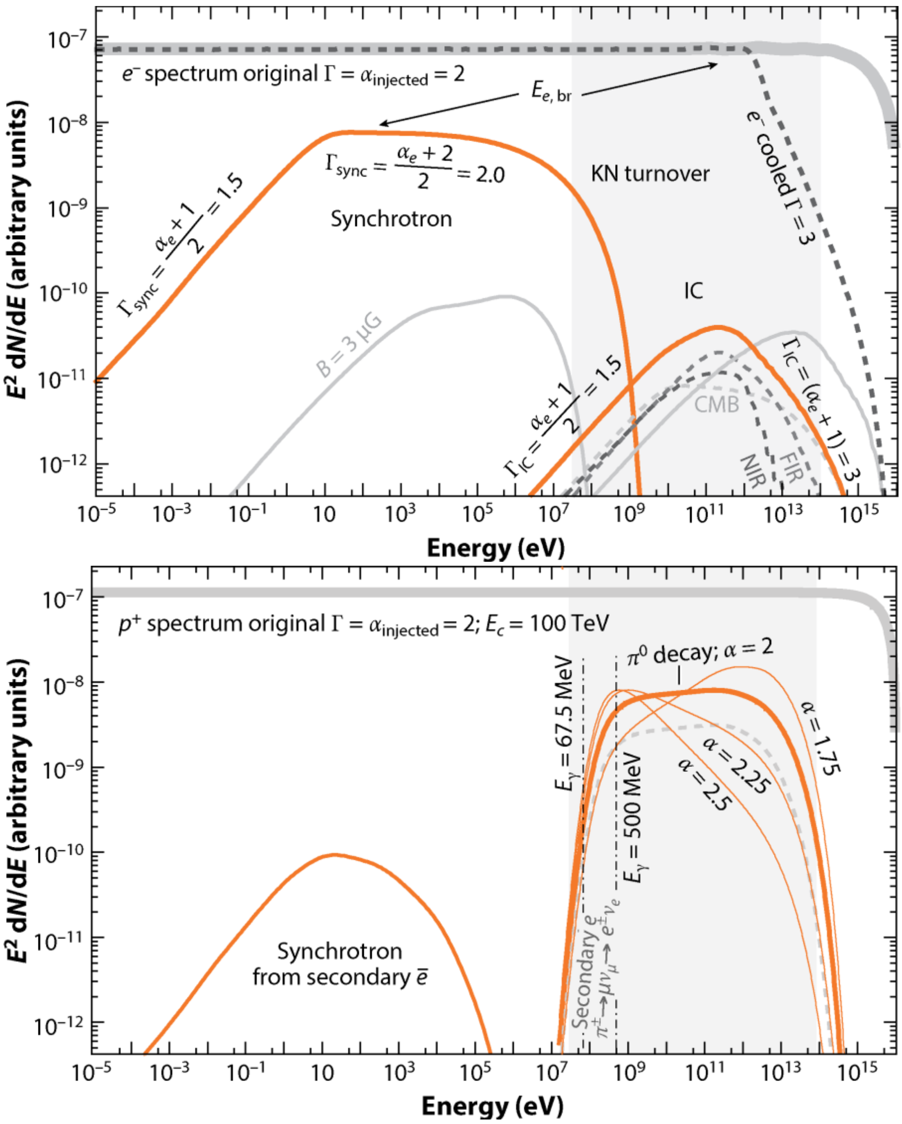

Figure 1.3: *Top:* SED of an electron spectrum (light gray) and the resulting synchrotron and Inverse Compton flux (orange). *Bottom:* SED of a proton spectrum (light gray) and the resulting γ-ray spectrum from Pion Decay (orange) (Funk, 2015).

light (EBL) lead to pair production at very high energies, enabling the probing of the EBL photon densities using the γ-ray spectra of distant sources (Singh et al., 2021). If the produced pairs are deflected by intergalactic magnetic fields and upscatter EBL photons again, the spatial distribution of γ rays from distant point-like sources can be used to probe the strength of these fields (Alonso et al., 2018). These are just some examples of how γ-ray observations can contribute to our current understanding of fundamental physics, with additional examples outlined in Biteau and Meyer (2022).

1.3 Sources of γ rays

This section provides an overview of various astrophysical objects for which high-energy (HE; $100\,\mathrm{MeV} < E < 100\,\mathrm{GeV}$) and very-high-energy (VHE; $100\,\mathrm{GeV} < E < 100\,\mathrm{TeV}$) γ-ray emission has been observed. Rather than a comprehensive catalog of all known source classes, it focuses on those most relevant to this work. More detailed information and additional source classes are described, e.g., in Aharonian, 2004 and Bose et al., 2022. We begin with typical Galactic sources before considering even more extreme objects observable from distant galaxies.

1.3.1 Supernova remnants

As discussed in Section 1.1, the acceleration of charged particles is possible in the presence of astrophysical shock fronts. These are produced, for example, when the outer layers of massive stars are ejected into the interstellar medium (ISM). The remainder of the star usually consists of either a neutron star or a black hole in the center, surrounded by an expanding shell of stellar material — the supernova remnant (SNR).

During the initial phase following the explosion, the ejecta expands freely, with its mass M_{ej} exceeding that of the swept-up material ($M_{\mathrm{sw}} < M_{\mathrm{ej}}$). As the shock propagates outward ($R_s \propto t^m$), an increasing amount of material is accumulated by the shock, and its velocity v_s decreases ($v_s \propto t^{m-1}$). The expansion parameter m equals 1 only during the very early "free" expansion. As the ejecta interacts with the surrounding medium, energy exchange causes the expansion parameter to drop below unity ($m < 1$), with its exact value depending on the density profile of the ambient material (Vink, 2020). Once the mass of the swept-up material surpasses that of the ejecta ($M_{\mathrm{sw}} > M_{\mathrm{ej}}$), the system transitions into the second phase, known as the *Sedov-Taylor* phase. Under the assumption of instantaneous energy transfer to the ambient medium without additional losses, theoretical models predict an expansion parameter of $m = 2/5$ during this phase (Vink, 2020, Chapter 5.4). The transition between the two phases typically occurs within a few decades to a few hundred years after the supernova explosion and is associated with a break in the spectrum of escaping particles, as outlined in Cardillo et al., 2015.

While the highest particle energies are reached at early times, the shock radius and the amount of processed mass are small, resulting in a low flux of escaping particles. Below the maximum energy reached at the beginning of the *Sedov-Taylor* phase, the spectrum follows a power law with index close to 2, increasing in steepness above this energy. According to Cardillo et al., 2015, magnetic field amplification at the shock front can reduce the acceleration time required to reach PeV energies to 10–30 yrs, which is much lower than the conventional estimate of several hundred years. A slightly different calculation is presented in (Bell and Lucek, 2001), where magnetic field amplification near the shock front by a factor of ~ 100 relative to the ISM results in an efficiently acceleration of charged particles to ultra-relativistic energies of even 10^{17} eV. However, recent observations of the two SNRs, Cassiopeia A (age ≈ 350 yrs) and IC 443 (age ~ 3–30 kyr), suggest an upper limit on proton energies of approximately 100 TeV in these systems. While not necessarily representative of all SNRs, this finding raises important questions regarding the maximum energies that SNRs can actually achieve (Banik, 2024).

The question of maximum particle energy is crucial, as it relates to the fraction of Galactic CRs that are accelerated by SNRs and whether these reach energies up to the knee. Estimates suggest that up to 25% of the energy released is converted to CRs for individual SNRs (Sinitsyna and Sinitsyna, 2024), a substantial amount considering a total energy release of approximately 10^{51} erg (Reynolds, 2008). Adopting a SNR rate of $(1.63 \pm 0.46)\,\mathrm{century}^{-1}$ in our galaxy (Rozwadowska et al., 2021) and an average CR conversion efficiency of 10%, the resulting CR luminosity is $5 \times 10^{40}\,\mathrm{erg\,s^{-1}}$, approaching the estimated total CR luminosity of $(6.26 \pm 0.72) \times 10^{40}\,\mathrm{erg\,s^{-1}}$ above 10 GeV (Tjus and Merten, 2020). Since no other Galactic source class offers a comparable energy budget, SNRs are prime candidates for accelerating CRs below the knee (Tjus and Merten, 2020).

Several SNRs have been detected in the γ-ray regime. Due to their large physical extent, their morphology is often resolved by γ-ray instruments, frequently revealing a shell-like structure. This is evident in Fig. 1.4 (*left*) for the young SNR RX J1713.7−3946, observed with H.E.S.S. (Abdalla et al., 2018a). Their emission remains steady over timescales of years

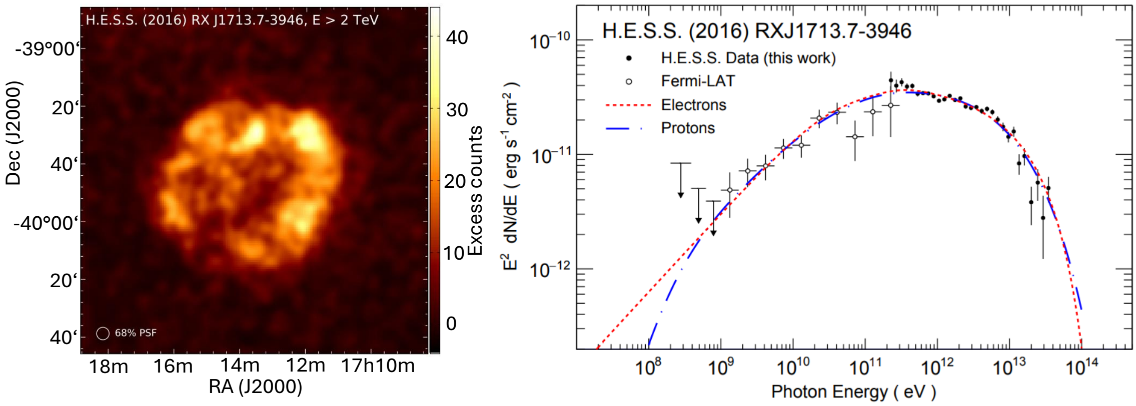

Figure 1.4: Morphology (*left*) and SED (*right*) of RX J1713.7−3946, adapted from Abdalla et al., 2018a.

with no observed variability. The dominant γ-ray emission mechanism, whether leptonic or hadronic, remains under debate, as different sources likely exhibit varying contributions from both processes (Reynolds, 2008; Funk, 2015). As in the case of RX J1713.7−3946 (cf. Fig. 1.4, *right*), the SED can often be described equally well by a leptonic IC or a hadronic pion decay (PD) model. Information about the local gas and photon field densities and the magnetic field strength could break this degeneracy.

For a more comprehensive discussion on SNRs, including their classification, evolution, environments, and particle acceleration mechanisms, see Reynolds, 2008 and Vink, 2020.

1.3.2 Pulsars

In some cases, the supernova explosion leaves behind a neutron star. Due to the conservation of angular momentum, these compact objects ($r \sim 10\,\mathrm{km}$) acquire high rotation frequencies of order $\mathcal{O}(\mathrm{Hz} - \mathrm{kHz})$ during their collapse. Over time, additional angular momentum can be gained through accretion from a companion star. As a result, the shortest orbital periods are observed for older neutron stars in binary systems. The magnetic field strength at the surface of neutron stars is usually extremely large (10^{10}–10^{15} G), and the orientation of the dipole field can be misaligned with the spin axis (Vink, 2020). Radiation from this rotating dipole primarily consists of low-frequency radio waves, leading to a gradual loss of rotational energy. Depending on the system's orientation relative to Earth, the lighthouse effect can result in periodic radio pulses when the magnetic poles sweep across our line of sight. Neutron stars exhibiting this characteristic pulsed emission in the radio or other wavelengths are referred to as pulsars. An illustration of such a system is shown in the left panel of Fig. 1.5.

The rotation period P of the pulsar decreases over time due to the loss of rotational energy $\dot{E}$, the spin-down power. If this energy loss is only caused by the magnetic dipole radiation, the surface magnetic field remains constant, and the birth period $P_0 \ll P$, one can approximate the pulsar's age by its characteristic age τ_c, defined as:

$$\tau_c = \frac{P}{2\dot{P}}, \tag{1.8}$$

where $\dot{P}$ is the current rate of change of the rotation period. A detailed derivation of this expression is provided in Chapter 6.2 of Vink, 2020, which also presents examples of pulsars whose characteristic ages align with their true ages within $\sim 25\%$, as well as cases where the discrepancy reaches an order of magnitude.

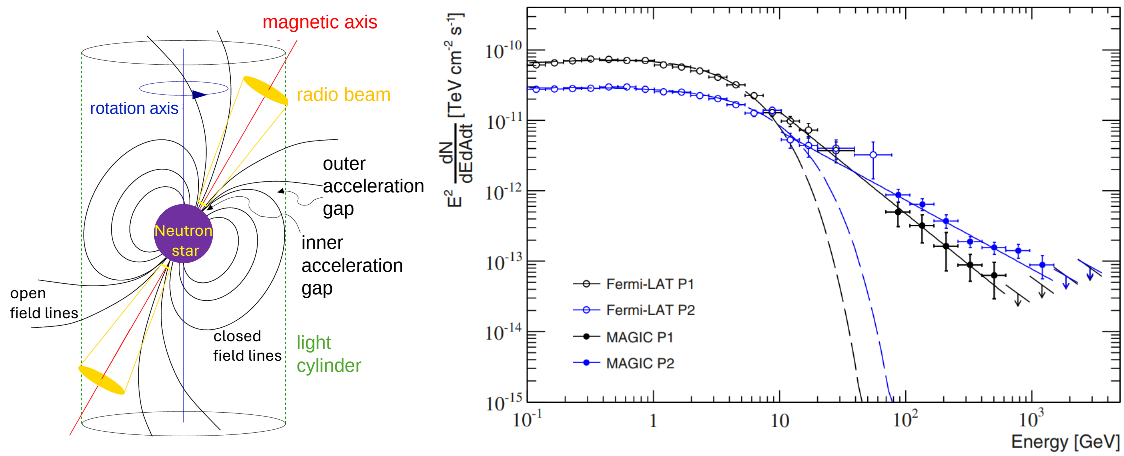

Figure 1.5: *Left*: Schematic diagram of a pulsar magnetosphere (adapted from Mitchell and Gelfand, 2022, see references therein). *Right*: SED of the two pulses, P1 and P2, from the Crab Pulsar, as measured by Fermi-LAT and MAGIC (adapted from Ansoldi et al., 2016).

Charged particles can escape from the neutron star's surface when the strong Lorentz force exceeds the gravitational pull. The co-rotating magnetic field induces extremely strong electric fields, accelerating charged particles to energies of several GeV (Vink, 2020). According to Kotera et al., 2015, young systems – less than 100 years old with $P_0 \sim 1\,\mathrm{ms}$ – may even accelerate particles to energies as high as 10^9 GeV. Poorly constrained quantities, like the temperature evolution of the neutron star's surface, lead to larger uncertainties on this estimate for older systems. While the accelerated particles travel along the magnetic field lines, they emit high-energy synchrotron and curvature[2] radiation, and up-scatter photons through IC scattering. These emissions carry sufficient energy to initiate electron-positron pair production in the strong magnetic field. The resulting cascades of electron-positron productions fill the inner magnetosphere (Vink, 2020). At the boundary of this region – the radius R_{LC} at which the co-rotating frame exceeds the speed of light, known as the light cylinder – magnetic field lines open, releasing ultra-relativistic electrons into the outer region.

Pulsed emission from many of these objects has been observed at γ-ray energies up to a few GeV, with 117 pulsars listed in the second Fermi-LAT pulsar catalog (Abdo et al., 2013). Extreme cases, such as the Crab and Vela pulsars, have been observed at energies exceeding 100 GeV, with the Crab Pulsar reaching up to 1 TeV (cf. Fig. 1.5 (*right*), Ansoldi et al. (2016)) and Vela 20 TeV (HESS Collaboration et al., 2023). This confirms the presence of ultra-relativistic electrons in these systems. However, the precise mechanism and location of the pulsed emission remain uncertain (Buehler and Blandford, 2014).

1.3.3 Pulsar wind nebulae

While pulsars are observed up to $\sim$TeV energies, even higher energies are observed in pulsar wind nebula (PWN) systems. The so-called "pulsar wind" is formed by the particles and Poynting flux[3] escaping the magnetosphere. The magnetization parameter σ is defined as the ratio of electromagnetic energy flux to particle energy flux and evolves with distance from the pulsar. At a certain distance, where the pressure of the pulsar wind equals the pressure of the surrounding material, a termination shock forms. At this location, a significant fraction of the Poynting flux is converted into particle flux, although the exact

[2]Curvature radiation (similar to synchrotron radiation) is emitted when charged particles travel along curved magnetic field lines.

[3]directional energy flux of the electromagnetic field.

mechanism remains uncertain (Mitchell and Gelfand, 2022). Observations indicate that the plasma from the inner regions has sub-relativistic bulk velocities and magnetization $\sigma \ll 1$ (Vink, 2020). Particles are accelerated at the wind termination shock, likely through diffusive shock acceleration or magnetic reconnection. The inferred electron injection spectrum is often characterized by a hard spectral index before a break-energy, transitioning to a softer index of ~ 2.5 at higher energies. While the softer component aligns with expectations from Fermi acceleration at a strong shock, the harder part of the spectrum may suggest acceleration via magnetic reconnection (Mitchell and Gelfand, 2022).

Several PWNs have been detected with a wide range of characteristic pulsar ages. In the early stages ($t \leq 10\,\mathrm{kyr}$), these systems expand into the cold, slow-moving ejecta of the SNR without major disruptions. The most prominent example of a young PWN is the Crab Nebula, originating from a supernova observed by astronomers in 1054 AD (Mayall and Oort, 1942). At later stages, the reverse shock of the SNR can disrupt the well-confined PWN, releasing the accelerated particles into the surrounding region (Giacinti et al., 2020). An example of an older system is Vela X, which appears highly extended ($r \approx 0.8°$), also due to its proximity of 0.29 kpc.

The left panel of Fig. 1.6 shows an X-ray image of the Crab Nebula captured by Chandra[4] (Weisskopf et al., 2000). The central point-like source corresponds to the pulsar, surrounded by a toroidal structure with two jets extending perpendicular to the torus. Spanning only $5'$ (3 pc), the image provides significantly finer spatial resolution than what is achievable in γ-ray observations. An interpretation of the feature is presented

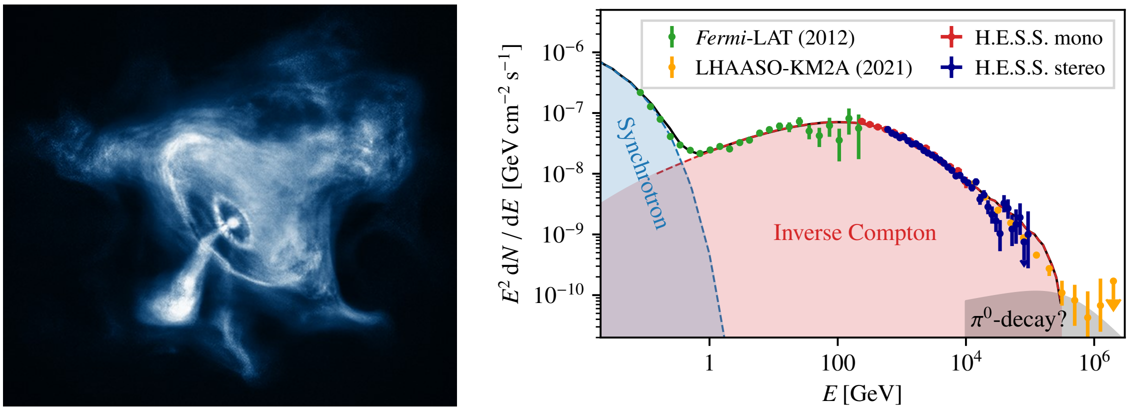

Figure 1.6: *Left:* X-ray image of the Crab Nebula taken by Chandra (Credit: NASA/CXC/SAO). *Right:* SED of the Crab Nebula in the γ-ray regime. Details regarding the data points and model can be found in Chapter 4.

in Bogovalov and Khangoulyan, 2002, where the bright inner ring is associated with the wind termination shock at the equator. At this boundary, the cold, highly magnetized pulsar wind is abruptly decelerated, heated, and converted into electrons and positrons that produce synchrotron radiation. The brighter outer ring may result from a combination of increasing magnetic field strength and rapid electron cooling as particles propagate further outward. The concentration of the emission in the equatorial plane can be explained by the latitudinal dependence of the Poynting flux $P_y \propto \sin^2(\theta)$, characteristic of axisymmetric winds. Their model also predicts a much higher plasma density near the rotational axis, which can be observed as jets given an additional acceleration of particles in the nebula (Bogovalov and Khangoulyan, 2002).

The right panel of Fig. 1.6 shows the SED of the Crab Nebula, as measured by various γ-ray instruments. At lower energies, the high bump in the spectrum is caused by

[4] `https://chandra.harvard.edu/`

synchrotron radiation, strongly supporting a leptonic origin of the γ-ray emission. Toward higher energies, the γ rays are dominantly produced via inverse Compton emission, where the most relevant seed-photon fields include the CMB, IR photons from nearby dust, and low-energy synchrotron photons (see Chapter 4 for details). Moreover, a significant hadronic contribution to the emission at the highest energies around 1 PeV remains a possibility (Liu and Wang, 2021; Nie et al., 2022b; Peng et al., 2022b). Time variability at all resolvable time scales has been observed in the synchrotron emission, however, not in the IC emission. The mechanism and regions responsible for the variability are not unambiguously identified yet (Buehler and Blandford, 2014, and references therein).

Pulsars and PWNs are thus considered potential candidates for CR acceleration in the transition region between knee and ankle. The total energy budget of $\sim 10^{39}\,\mathrm{erg\,s^{-1}}$ is too small for significant contributions down to GeV energies, however, the observed electron and positron flux might be the result of nearby pulsars (Tjus and Merten, 2020).

1.3.4 Stellar clusters

Thus far, we have focused on individual astrophysical objects, but charged particles can also be accelerated to ultra-relativistic velocities in composite systems such as stellar clusters. The most massive known stellar cluster in our galaxy is Westerlund 1, with ~ 200 identified cluster members and a mass estimate of $\sim 10^5\,\mathrm{M_\odot}$ (Clark et al., 2005). Several mechanisms may contribute to particle acceleration within or in the vicinity of the cluster. First, individual objects within the cluster can accelerate particles independently of other cluster members. Given the large population of massive stars, numerous SNRs, pulsars, and PWNs are expected to form as these stars reach the end of their lifetimes. Surprisingly, the only confirmed remnant of a stellar explosion in Westerlund 1 is the X-ray magnetar CXOU J164710.2−455216 (Aharonian et al., 2022b). Nevertheless, unresolved remnants could still contribute to the overall CR flux in the region. Second, different shocks inside the cluster could serve as sites for diffusive shock acceleration. These shocks can form when the stellar winds of the massive stars collide with each other or the shock fronts of SNRs (Bykov et al., 2020). Additionally, a termination shock is expected to form where the collective stellar winds encounter the surrounding ISM just outside the cluster (Morlino et al., 2021).

In the case of Westerlund 1, the situation is complex, with individual γ-ray sources along the line of sight potentially contributing to the emission. These are shown in the left panel of Fig. 1.7, next to the γ-ray emission from the Westerlund 1 region. The analysis in Aharonian et al., 2022b suggests that the total observed emission cannot be fully explained by known individual sources alone, given its large spatial extent and energy

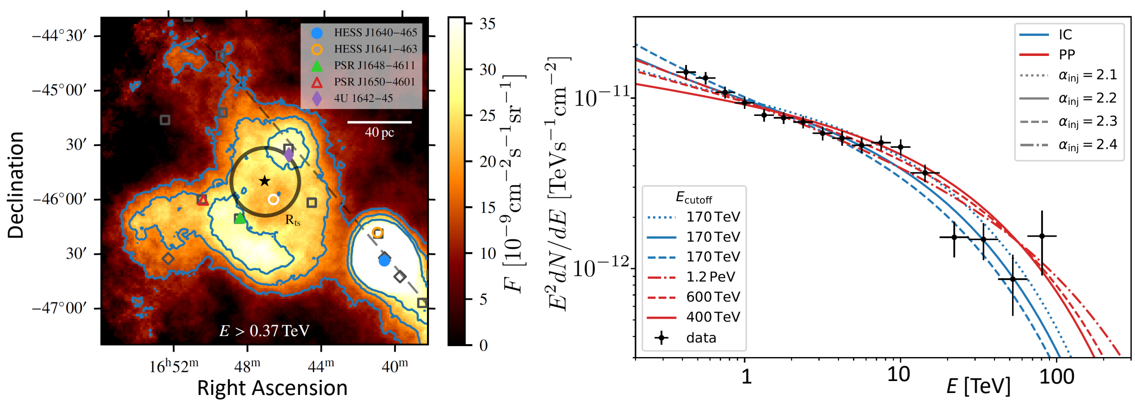

Figure 1.7: Morphology (*left*, Aharonian et al., 2022b) and SED (*right*, Härer et al., 2023) of Westerlund 1 in the VHE γ-ray regime.

requirements. In a leptonic γ-ray production scenario, an energy-dependent morphology and spectral variations would be expected, as energy losses occur when electrons propagate away from their acceleration sites. However, such a trend is not observed. In contrast, a hadronic scenario could account for the complex emission morphology through variations in target gas density. However, a clear correlation between the surface brightness and observed gas densities could not be found. Alternative explanations, such as the presence of "dark" gas or an impulsive CR injection, cannot be excluded. A significant fraction of CRs is likely accelerated by the cluster's termination shock. Considering that the estimated radius of the termination shock ($\sim 32\,\mathrm{pc}$) coincides with the observed peak in the γ-ray excess profile ($\sim 34\,\mathrm{pc}$), this hypothesis seems natural (Aharonian et al., 2022b). It is furthermore supported by considerations about the required energy and magnetic field strength (Aharonian et al., 2022b).

Whether the observed γ-ray emission originates from IC scattering or hadronic proton-proton interactions remains uncertain (Härer et al., 2023; Haubner et al., 2025). The right panel of Fig. 1.7 presents the region's spectrum, with both leptonic and hadronic models fitted under different assumptions. While the leptonic model provides a slightly better fit, the statistical significance of this difference remains inconclusive.

1.3.5 Active galactic nuclei

We have discussed several sources of VHE γ-ray emission within our galaxy and would expect similar sources to exist in other galaxies. However, due to the inverse-square law ($1/d^2$), the flux from such sources at extragalactic distances would often be too weak to be detected. Nevertheless, numerous extragalactic γ-ray sources have been identified, many of which are either rare or absent in the Milky Way. These sources must be intrinsically more luminous than their Galactic counterparts by at least a factor of $(d_2/d_1)^2 = 10^4$, given a maximum Galactic distance of $d_1 = 100\,\mathrm{kly}$ and a minimum extragalactic distance of $d_2 = 10\,\mathrm{Mly}$. Unlike Galactic sources, which are concentrated along the Galactic plane, extragalactic γ-ray sources exhibit a uniform distribution across the sky (cf. Fig. 1.8).

The majority of extragalactic VHE γ-ray sources are active galactic nuclei (AGN), with 90 identified objects[5]. The bright central region of these galaxies often outshines the rest of the galaxy. Current models suggest that AGNs are powered by a supermassive black hole ($10^6 - 10^9\,\mathrm{M}_\odot$) at their center (Bose et al., 2022). As illustrated in Fig. 1.9, gravitationally bound matter orbits the black hole within a thick torus in the outer regions, transitioning into a thin accretion disk toward the center. Due to frictional forces, the gas heats up to temperatures of $5 \times 10^4\,\mathrm{K}$ as it spirals inward (Giustini and Proga, 2019). Line emission from gas clouds can be broadened depending on their speed, leading to the broad line regions at smaller radii and narrow line regions further away from the central mass. Additionally, relativistic jets of material can be launched perpendicular to the accretion disk, producing strong radio emission.

The observed spectral properties and brightness of AGNs vary significantly. According to the AGN unification model (e.g. Antonucci, 1993), all AGNs share the same fundamental physical processes, with observed differences primarily arising from the system's orientation with respect to the Earth and its luminosity. More recent studies suggest that AGNs can furthermore operate in "radiative mode" or in "jet mode". The radiative mode is characterized by efficient particle acceleration and high luminosity, with most energy emitted in the form of electromagnetic radiation. In contrast, the jet-mode AGNs convert most energy to bulk kinetic energy of the two jets and are therefore less luminous (Netzer, 2015, and references therein).

Apart from the exact properties of the central engine, the orientation of the system

[5] According to TeVCat2 `https://tevcat2.tevcat.org/`, checked on the 01.02.2025.

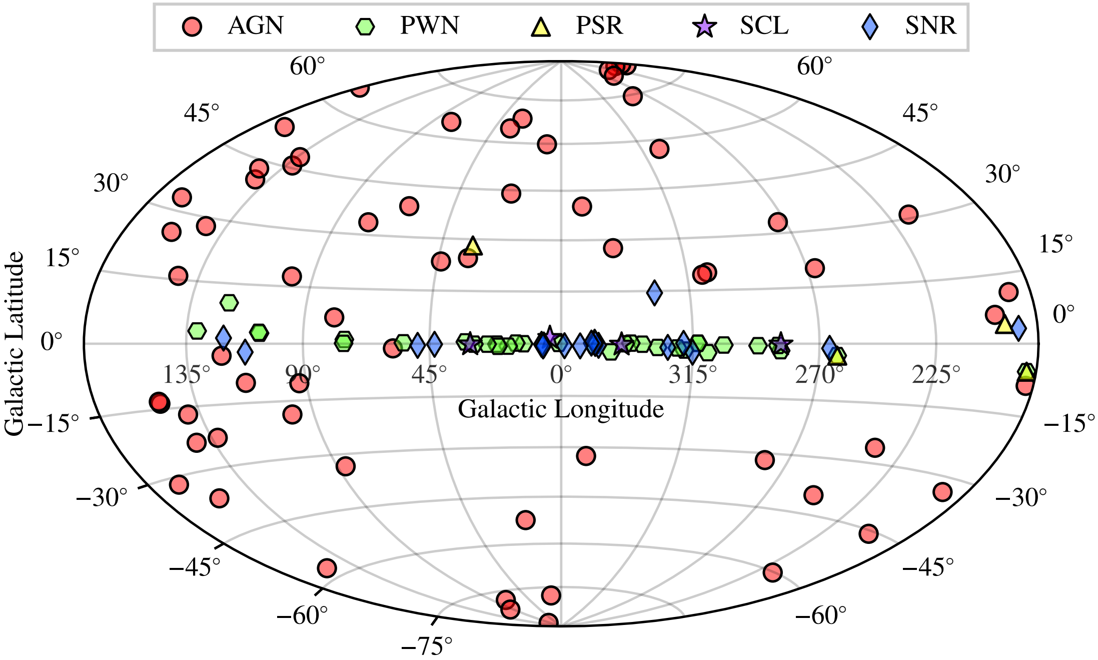

Figure 1.8: Locations of TeV γ-ray sources. The legend labels refer to active galactic nuclei, pulsar wind nebulae, pulsars, stellar clusters, and supernova remnants, in order of their appearance. Data taken from `https://github.com/gammapy/gamma-cat`, an open data collection and source catalog for gamma-ray astronomy.

toward us is still the most important quantity for its classification. The different AGN types and their orientations are illustrated in the left panel of Fig. 1.9. If the relativistic jet is directed toward us, the object is classified as a blazar. Blazars constitute the majority of AGNs detected at VHE energies due to the Doppler-boosted emission from their jets. The intensity $I(\nu)$ emitted in the rest-frame of the source region at a given frequency ν can be transformed to the observer's frame $I'(\nu')$ if the relative velocity $v = \beta c$ and the angle θ between the velocity vector and the line of sight (LoS) are known. Following the calculations in Chapter 22.3 of Longair (2011), the transformation results in shifts for several quantities: the frequency $\nu' = \kappa\nu$, the frequency interval $\Delta\nu' = \kappa\Delta\nu$, the time interval $\Delta t' = \kappa^{-1}\Delta t$, and the solid angle $d\Omega' = \kappa^{-2}d\Omega$. Consequently, the intensity –

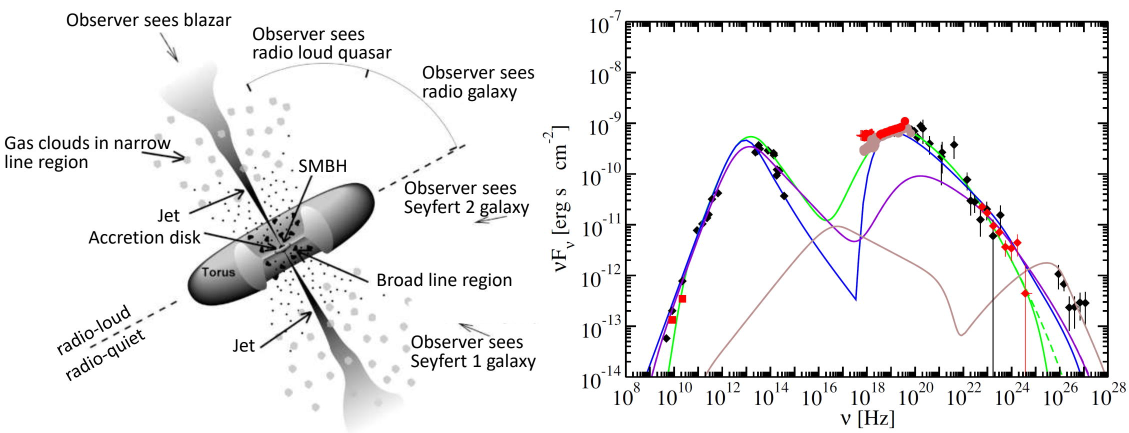

Figure 1.9: Schematic of an AGN observed from different angles (*left*, Credit: Fermi-LAT-collaboration) and the SED (*right*) of Centaurus A, adapted from Abdo et al., 2010.

defined as energy $h\nu N(\nu)$ per frequency interval, per time interval, and per solid angle – transforms as

$$I'(\nu') = I(\nu) \times \kappa^3, \tag{1.9}$$

where

$$\kappa = \frac{1}{\gamma(1-\beta\cos(\theta))}, \tag{1.10}$$

and $\gamma = \sqrt{1-\beta^2}^{\,-1}$ is the Lorentz factor of the emission region.

Blazars exhibit variability across all wavelengths on timescales ranging from minutes to years (Bose et al., 2022). These timescales provide constraints on the maximum size of the emission region, given by $d = c \cdot t = c \cdot \kappa t'$ due to causality. Variations in the source's luminosity should not be observed on timescales smaller than ${}^{d}\!/_{c}$, as this is the time electromagnetic waves need to cross the source or for the cause of the variation to affect the whole region (Longair, 2011).

Emission in AGNs can have a leptonic or hadronic origin (Dermer and Menon, 2009). The low-energy peak in the SED, spanning radio to X-ray frequencies, points toward the presence of ultra-relativistic electrons emitting synchrotron radiation. In this scenario, the second hump at γ-ray energies may result from IC scattering by the same electron population. However, given the insufficient density of seed photons, relativistic motion toward us is required for Doppler boosting. It seems unlikely that the emission of all observed jets can be explained solely by IC emission (Aharonian, 2004). The potential association of some AGNs with neutrino emission suggests a hadronic origin for the γ-ray emission (Aartsen et al., 2018; Abbasi et al., 2022a). Secondary electrons produced in hadronic interactions could account for the observed synchrotron radiation. A mixed scenario is therefore plausible, with the exact contributions still under debate. One of these models is discussed in Aharonian, 2004, where ultra-high-energy (UHE) γ rays (10^3–10^7 TeV) are produced in the vicinity of the black hole via hadronic interactions. The jet can be powered by the resulting beam of γ rays interacting with the CMB, instead of the Poynting flux originating from the black hole. This model circumvents the need for direct particle acceleration within the jet itself and could account for the observed neutrino emission.

As the jet inclination angle increases relative to the LoS, Doppler boosting becomes less significant (cf. Eq. 1.9 and 1.10). These objects, classified as quasars or radio galaxies, exhibit a stronger contribution from accretion disk radiation. Their thermal emission is often characterized by broad emission lines, while their X-ray and γ-ray luminosities are lower. One of the few radio galaxies detected at TeV energies is Centaurus A, with the SED shown in the right panel of Fig. 1.9. The core emission is typically attributed to synchrotron and IC emission. New studies, however, present evidence for an additional, potentially hadronic component dominating the spectrum above 10 GeV (Abdo et al., 2010; H.E.S.S. Collaboration et al., 2018). The slight extension measured at TeV energies that is aligned with the jet direction suggests that the emission originates approximately 2.2 kpc away from the central black hole (Abdalla et al., 2020a). This is particularly intriguing, as Centaurus A lies within the UHE CR hotspot region mentioned earlier in this introduction. It remains a prime candidate for the acceleration of CRs to the highest energies. More details on Centaurus A, its core and lobe emission, as well as recent γ-ray data will be presented in Chapter 7.

1.4 Detection of γ rays with Fermi-LAT

Since the Earth's atmosphere is opaque to electromagnetic radiation with photon energies $\gtrsim$10 eV (Longair, 2011), two basic methods are used to detect γ rays. For energies below $\sim$10 GeV, detectors are placed in orbit above the atmosphere, enabling direct detection of the γ rays (Funk, 2015). At higher energies, ground-based detectors offer an alternative by measuring the secondary particles produced when γ rays interact with the atmosphere.

In this section, the *Fermi Gamma-ray Space Telescope*, which has been in orbit since June 2008 at an altitude of 535 km, is introduced. The *Fermi* satellite hosts two detectors: the Gamma-ray Burst Monitor (GBM) and the Large Area Telescope (LAT). As the name suggests, the GBM is used to monitor the sky for γ-ray bursts, which are very bright outbursts of γ rays lasting from seconds to minutes. Compared to the GBM, which is sensitive to γ rays between 8 keV and 40 MeV, the LAT offers a larger effective area and is most sensitive between 20 MeV and >300 GeV. At higher energies, the LAT's angular resolution improves from $3.5°$ at 100 MeV to less than $0.15°$ above 10 GeV, which is crucial for the analysis of point-like sources or morphology studies. Therefore, this work utilizes only Fermi-LAT data.

The LAT is a pair-conversion telescope, where incoming γ rays interact within the detector to produce e^-/e^+ pairs, as illustrated in the left panel of Fig. 1.10. This occurs in the converter-tracker, which consists of 16 planes of high-Z material interleaved with position-sensitive detectors that record the passage of charged particles. The design of this component must balance the competing requirements for low- and high-energy performance. At energies $\lesssim$100 MeV, the angular resolution is limited by the momentum transfer to atomic nuclei in the converter material. The scattering angle for Coulomb scattering decreases with $^1/_E$, and multiple interactions can occur in each plane of the converter-tracker. It is therefore divided into two sections: an upper part with thin converter plates to minimize multiple scattering, followed by a lower part with thicker plates to enhance the conversion probability for high-energy γ rays. As a consequence of the smaller scattering angles, the angular resolution improves with increasing energy until $\sim$20 GeV, where the intrinsic resolution of the detector becomes the limiting factor, leading to a saturation of the angular resolution (Ackermann et al., 2012b).

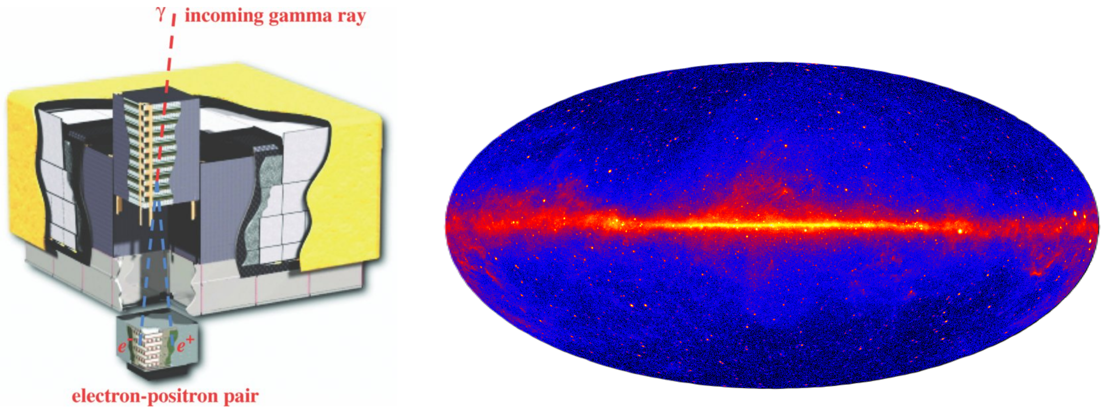

Figure 1.10: *Left:* Schematic of the LAT telescope, taken from Atwood et al. (2009). *Right:* Fermi-LAT 12-year all-sky map for energies above 1 GeV (Credit: NASA/DOE/Fermi LAT Collaboration).

The calorimeter estimates the energy of the γ ray and profiles the particle shower development. Each module of the calorimeter consists of 96 CsI(Tl) crystals that can be read out individually. While the charged particles interact in the calorimeter, they emit scintillation light in the crystals, which is measured by two photodiodes, one at each end. The spatially resolved shower development adds to the reconstruction of the arrival direction of the γ ray and serves as an important background discriminator. Low-energy showers are usually fully contained within the calorimeter, allowing an accurate reconstruction of the primary γ ray's energy based on the total light yield. Using an external γ-ray source, the Fermi-LAT could be calibrated on the ground, achieving an energy resolution of ${}^{\Delta E}\!/_{E} = 7\%$ in the core energy range (Ackermann et al., 2012b). For showers with $E \lesssim 100\,\mathrm{MeV}$, however, energy losses in the converter-tracker degrade the energy resolution. For high-energy showers, which are not fully absorbed, a three-dimensional fit to the recorded part of the shower profile improves the energy estimation, yielding a resolution of $\lesssim 10\%$, even beyond 100 GeV (Ackermann et al., 2012b). By measuring the known geomagnetic cutoff in the low-Earth-orbit CR electron spectrum, the systematic uncertainty on the energy reconstruction can be reduced to $\sim 2\%$ (Ackermann et al., 2012a).

To suppress the overwhelming background from CR events, the detector is enclosed by plastic scintillators that function as a charged-particle veto. These scintillators effectively reject over 99% of background events (Ackermann et al., 2012b). Nevertheless, a small fraction of misclassified CR events still pass the event selection. Together with Earth albedo γ rays and unresolved extragalactic γ-ray sources, these residual backgrounds are modeled using the isotropic diffuse background template. As the name suggests, this background component is assumed to be isotropic, with its energy spectrum derived from residual emission after accounting for all resolved sources in the latest Fermi-LAT source catalog. Regions near the Galactic plane ($|b| < 10°$) and the celestial poles ($|\mathrm{DEC}| > 60°$) are excluded due to contamination from Galactic diffuse emission and γ rays from the Earth's limb, respectively[6]. A separate template accounts for Galactic diffuse emission, which arises from interactions between the diffuse population of Galactic CRs and interstellar gas. For further details on Fermi-LAT, refer to Atwood et al. (2009), and for more information on the Galactic diffuse template, see Sect. 7.1.

Since the start of data taking in August 2008, the Fermi-LAT telescope has monitored the sky with a field of view (FoV) of 2.4 sr, collecting over 1.7×10^9 γ-ray events. During the reconstruction process, each event is assigned a recorded time, reconstructed direction, and energy. These quantities, along with a description of the instrument, are analyzed using the statistical tools presented in Sect. 1.6. The right panel of Fig. 1.10 shows the 12-year all-sky map in Galactic coordinates. Besides the diffuse emission along the Galactic plane, many point-like and extended sources have been detected and classified. The latest Fermi-LAT source catalog, 4FGL-DR4, contains 7194 γ-ray sources (Ballet et al., 2024).

As it is challenging to launch heavy satellites into space, the main limitation of the Fermi-LAT is its detector volume. The steep power-law spectra of most γ-ray sources require larger detectors to gather sufficient statistics at high energies. Additionally, the particle showers caused by events above ~ 1 TeV deposit more and more energy outside the calorimeter, making the energy reconstruction unreliable. For these reasons, the very high end of the γ-ray spectrum is measured with ground-based detectors, which utilize the atmosphere as part of the detection process.

1.5 Ground-based detection of γ rays with IACTs

When very-high-energy γ rays interact with molecules in the upper atmosphere, they produce cascades of secondary particles, referred to as *particle showers* or *air showers*. The Cherenkov light from these secondary, highly relativistic, charged particles can be used to reconstruct the properties of the primary γ ray. This technique was pioneered by the Whipple collaboration, leading to the first detection in 1989 when a significant excess was observed from the Crab Nebula (Weekes et al., 1989).

1.5.1 Particle showers in the atmosphere

We begin by examining the dominant interactions of highly energetic γ rays and CRs in the atmosphere, highlighting how their shower development and particle content differ. For a more in-depth discussion, refer to Chapters 9 and 10 of Longair, 2011.

[6] `https://fermi.gsfc.nasa.gov/ssc/data/access/lat/BackgroundModels.html`

Air showers are classified as either leptonic or hadronic, depending on the primary particle that initiates them, which also influences their particle content and evolution. Leptonic showers are induced by either a γ ray or an electron (in the following, the term electron will refer to both electrons and positrons) and develop through electromagnetic interactions, i.e., the electrons emit γ rays via bremsstrahlung, which in turn undergo pair production. Bremsstrahlung is the process in which a charged particle experiences acceleration in the electromagnetic field of an atomic nucleus and therefore emits radiation. Since the acceleration is stronger for lighter particles, the intensity of the radiation is proportional to the inverse of the particle mass. This makes γ-ray production via bremsstrahlung especially efficient for electrons.

The shower development can be better understood by examining the particle content at different radiation lengths, which are approximately the same for bremsstrahlung and pair production in the ultra-relativistic limit. Figure 1.11 shows a schematic where the mean particle energy is halved after each radiation length R, which is the distance after which an interaction occurs with a 50% probability. If the primary γ ray induces the air shower

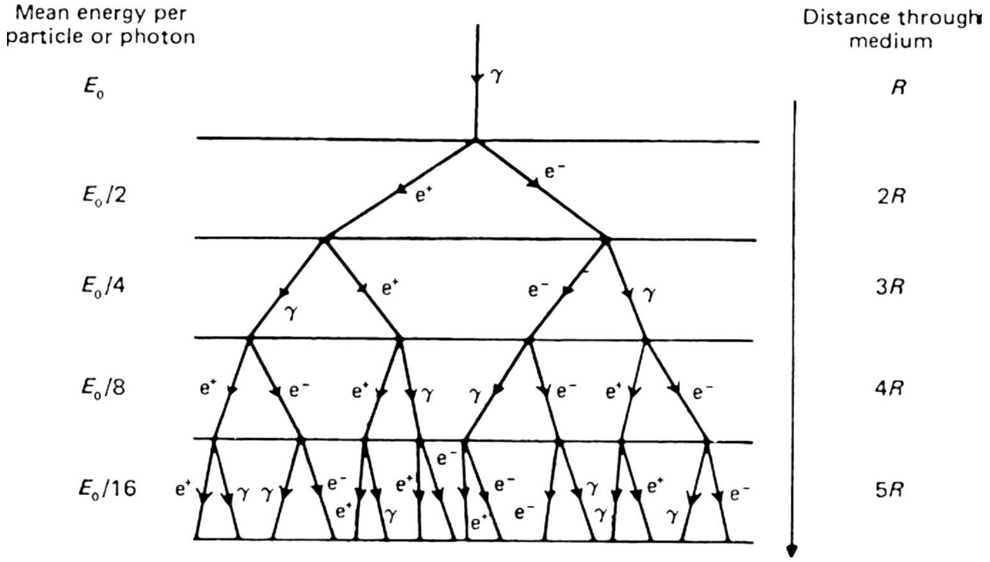

Figure 1.11: Simple schematic of the leptonic shower development. Taken from Longair (2011).

with energy E_0, the expected number of secondary particles after n radiation lengths is 2^n, with an average energy of $E_0/2^n$. This holds until the energy of the secondary particles reaches the critical energy $E_c \sim 85\,\mathrm{MeV}$, below which the electrons lose their energy mostly through ionization rather than bremsstrahlung (Ulrich et al., 2011). Additionally, the cross section for pair production decreases toward lower energies, while the cross sections for Compton scattering and photoelectric absorption increase, preventing further particle production. The shower reaches its maximum after

$$n_c = \log_2\left(\frac{E_0}{E_c}\right) \tag{1.11}$$

radiation lengths, with

$$N_{\mathrm{max}} = \frac{E_0}{E_c} \tag{1.12}$$

particles, of which two-thirds are charged electrons and one-third are photons. Afterward, the air shower quickly fades as ionization losses become dominant.

However, the vast majority of air showers are induced by CRs (mostly protons or heavier nuclei), leading to hadronic air showers, which outnumber the leptonic ones by several orders of magnitude (Malyshev and Mohrmann, 2023). Here, the primary cosmic ray undergoes nucleonic interaction, leading to spallation of the target nucleus and/or itself. In the following nucleonic cascade, mostly pions (the lightest mesons), as well as heavier mesons and antinuclei, are produced. Similar to electrons below their critical energy, protons produced in the nucleonic cascade with energies smaller than 1 GeV are quickly stopped by ionization losses. Figure 1.12 shows that electromagnetic subshowers are produced if the neutral pions decay, after their very short lifetime of 1.78×10^{-16} s, into two γ rays (Longair, 2011). Charged pions, on the other hand, decay almost exclusively

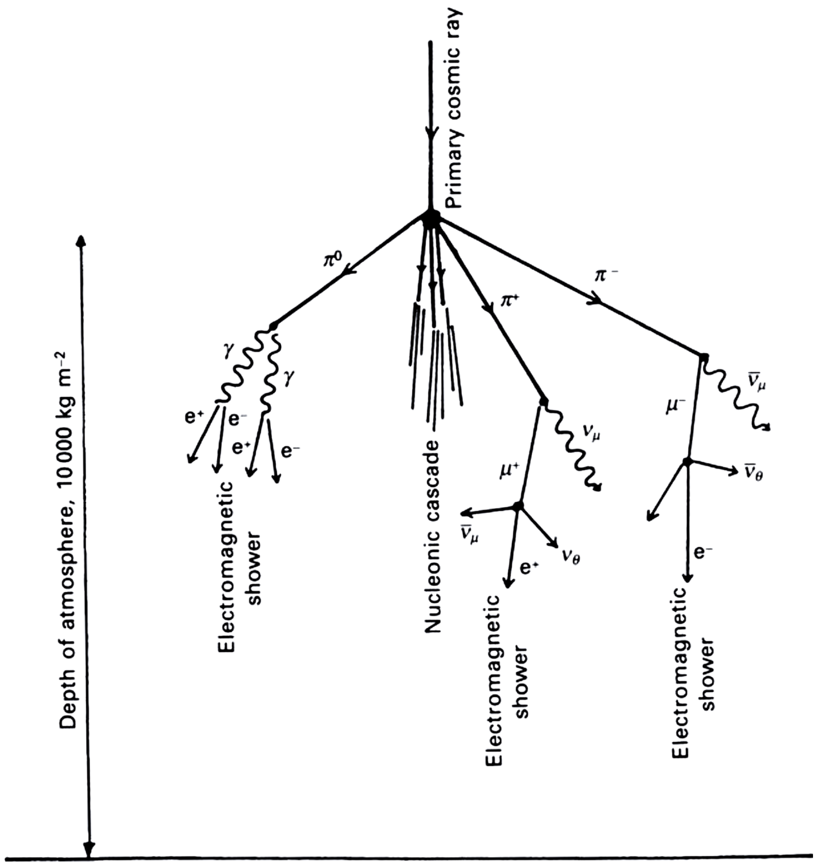

Figure 1.12: Simple schematic of the hadronic shower development. Taken from Longair (2011).

into muons and the corresponding neutrinos due to helicity suppression in the weak decay. Muons with Lorentz factors $\gamma \geq 20$ can reach the ground within their time-dilated lifetime of $\gamma \cdot 2.2\,\mu$s. If the muon decays, another electromagnetic subshower is induced.

Compared to leptonic air showers, hadronic ones appear more irregular as each subshower starts from a secondary particle with different, stochastically distributed energy. They are also more laterally extended, when comparing similar primary energies, as the production of heavier particles with lower Lorentz factors occurs at larger angles between the particles in the Earth's reference frame.

This can be seen from full shower simulations by CORSIKA[7] (v.7.8000, Heck et al., 1998), which are shown in Fig. 1.13 for an electromagnetic shower and a hadronic one. These simulations also show that the showers usually start at ~ 20 km in height, although the point of the first interaction varies statistically from shower to shower. The profiles along the z-axis illustrate how the number of particles N gradually increases for the leptonic shower, while the average energy per particle $\langle E \rangle$ decreases. In contrast, the hadronic shower develops more quickly after the first interaction, where the number of particles

[7]`https://www.iap.kit.edu/corsika/99.php`

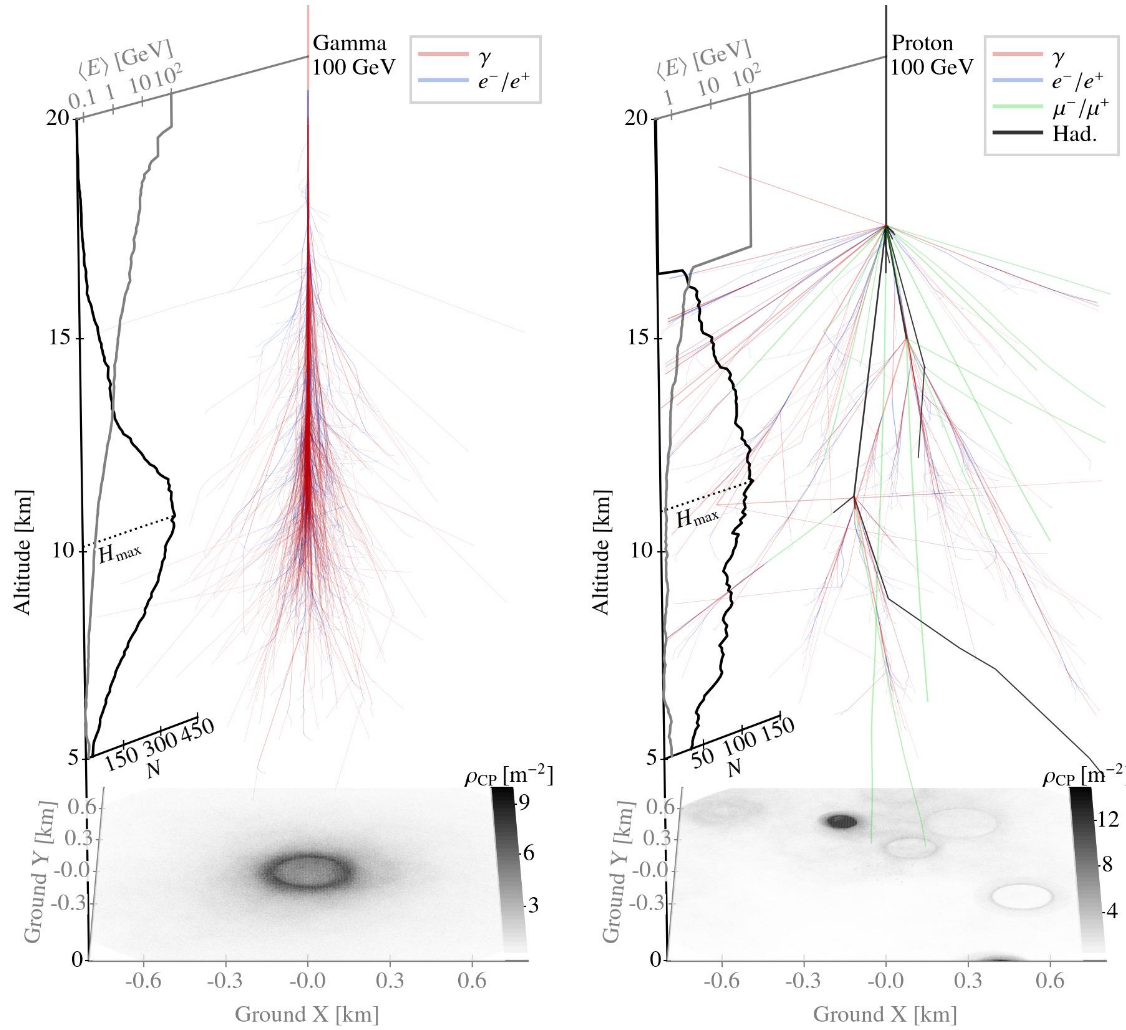

Figure 1.13: Particle tracks for simulated air showers with the Cherenkov photon density ρ_{CP} on the ground. Tracks are clipped at the xy-limits and their widths are proportional to $\log(E)$, with colors indicating the particle type. The profiles along the z-axis show the number of particles N and their average energy $\langle E \rangle$. $H_{\max}$ is the height at which the maximum particle number is reached. The images were created with the help of SHOWERPY (DOI: `10.5281/zenodo.15342222`).

abruptly rises. According to Eq. 1.11, the penetration depth of the shower maximum scales $\propto \ln(E_0)$, reaching altitudes of the shower maximum $H_{\max} \approx 5\,\mathrm{km}$ at $100\,\mathrm{TeV}$ (Aharonian et al., 2008). Except for the highest primary energies, only very few shower particles actually reach altitudes below 2 km, which allows for two main detection techniques of these showers. One technique is based on the direct detection of secondary particles, as employed by water Cherenkov detectors like the High-Altitude Water Cherenkov Observatory (HAWC) (Abeysekara et al., 2023), which are built at altitudes around 5 km above sea level (a.s.l.). The other technique collects the Cherenkov light emitted by the charged shower particles in the atmosphere during dark nights, which is discussed in more detail below.

1.5.2 Cherenkov light emission

Each charged particle in the shower with velocity $v > {}^{c}\!/_{n}$, where c is the speed of light in vacuum and n is the altitude-dependent refractive index of air, leads to coherent dipole emission when the nearby polarized medium relaxes again. Figure 1.14 illustrates how the spherical wavelets emitted from each point along the particle's trajectory overlap and add up constructively under the angle θ if the particle moves faster than the wavelets. From

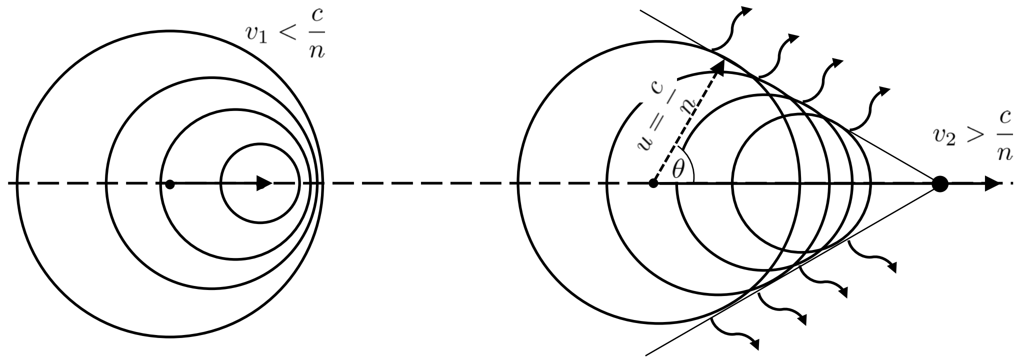

Figure 1.14: *Left:* Illustration of the wavelets when the particle velocity v_1 is smaller than the speed of light in the medium u. *Right:* Construction of the coherent wavefront from Huygens' principle if v_2 is larger than u.

geometrical considerations, it follows that

$$\cos(\theta) = \frac{c}{n \cdot v}, \tag{1.13}$$

with n ranging from 1.0003 at sea level to very close to 1 in the upper atmosphere, resulting in Cherenkov angles around 1.4° at sea level and smaller angles further up. This leads to a circle on the ground with a diameter of $\approx 250\,\mathrm{m}$, containing most of the Cherenkov photons of one air shower, with densities $\rho_{\mathrm{CP}} \sim 10\,\mathrm{photons}\ \mathrm{m}^{-2}$ per 100 GeV of primary energy (cf. Fig. 1.13). As the particles and the photons travel at very similar velocities and angles, most of the Cherenkov photons are expected to reach the ground within a very narrow time window of $\sim 10\,\mathrm{ns}$. This means that one can detect the faint Cherenkov flashes above the background light from the night sky by integrating only the narrow time window around the flash with extremely fast detectors.

1.5.3 Imaging Atmospheric Cherenkov Telescopes

Imaging Atmospheric Cherenkov Telescopes (IACTs) are unique optical telescopes with large mirrors, poor spatial resolution[8] but with extremely high temporal resolution. The mirrors collect the Cherenkov (and background) light and reflect it into the camera. Typical cameras of IACTs consist of multiple photo multiplier tubes (PMTs) or silicon photomultipliers (SiPMs) that serve as photon detectors. The PMTs (or SiPMs) are arranged in a grid on the camera plane and represent the individual camera pixels. Cherenkov photons from the shower hitting the mirror of the telescope are reflected into the corresponding pixels in the camera based on their arrival direction. This means that all photons from one region in the sky, arriving under a common incidence angle relative to the telescope's axis, are collected in the same camera region, irrespective of where they hit the mirror. If the telescope is triggered, the PMT signal is sampled and converted to ADC counts, resulting in a waveform for each pixel. The time-dependent waveform information can be reduced by extracting the peak position (pixel time) and the integral of the waveform in the narrow time window around the peak (pixel amplitude).

Figure 1.15 summarizes the imaging of an air shower by two IACTs. Different densities of charged particles in the shower produce different Cherenkov light densities at each position, leading to different numbers of photons from each direction, which is reflected in the waveform from each pixel. The characteristic air shower images can be visualized by plotting the pixel amplitudes in the camera frame. Pixels with low signal-to-background

[8]Compared to telescopes used for conventional optical astronomy. A higher resolution would increase costs without being essential for the telescopes' primary objective: image reconstruction.

ratio (SBR) are set to zero (image cleaning) to remove noise from night sky background (NSB) light. Despite the poor spatial resolution of the images, one can reconstruct the basic properties of the primary γ ray, i.e., energy, arrival direction, and a "gammaness" score, which separates leptonic showers from hadronic ones.

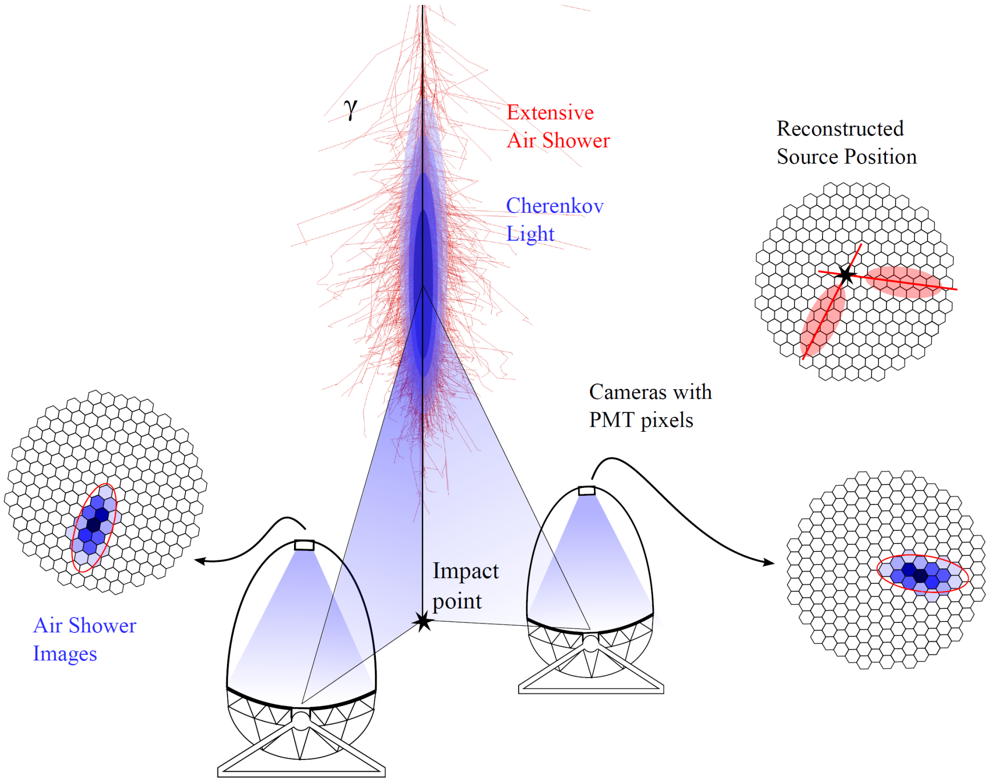

Figure 1.15: Schematic of the stereoscopic reconstruction technique of IACT images, adapted from Fruck, 2015.

Although there are various methods for event reconstruction, we primarily focus on the traditional geometrical analysis (Aharonian et al., 2006), based on the so-called "Hillas parameters" (Hillas, 1985). These parameters characterize the moments of the amplitude distribution, providing information for an intuitive reconstruction of the primary γ-ray properties.

If the shower is seen by more than one telescope, as illustrated in Fig. 1.15, one can estimate the shower direction as the intersection between the major axes of the shower ellipse in the sky frame, while the impact point is the same intersection in the ground frame. The major axis of the shower image is the line through the center of gravity (CoG) which minimizes the root mean square (RMS) of the pixel amplitude distribution perpendicular to it. One typically refers to the RMS along and perpendicular to the shower axis as Hillas-length and Hillas-width, respectively.

Figure 1.16 illustrates these quantities on top of an individual image. The major axis of the ellipse corresponds to the longitudinal shower development. In cases with no other telescope available for image reconstruction[9], the arrival direction of the γ ray can be anywhere along the major axis, especially on both sides of the CoG. In these cases, machine-learning techniques can be used to estimate the value of the "Disp", which is the separation between the CoG and the shower direction. One can also estimate the direction

[9]This is generally not desirable and stereoscopic IACT arrays usually apply a two-telescope multiplicity cut.

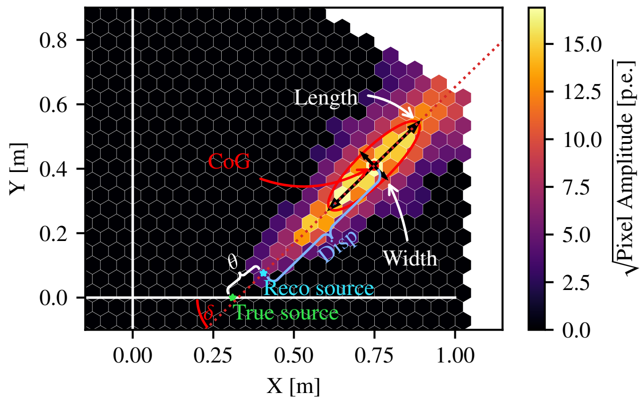

Figure 1.16: Example image of a simulated γ-ray event overlaid with selected image parameters. The colors represent pixel amplitudes using a square root scale to also highlight the edge pixels of the shower with low amplitudes. All image parameters are depicted according to their actual values, except for "Disp", and therefore the position of the reconstructed source and θ, which are shown for illustrative purposes only.

of the shower development based on asymmetries in the image, like its Skewness (details in Chapter 5).

The energy of the primary γ ray is proportional to the number of secondary electrons (cf. Eq. 1.12), which in turn is proportional to the number of emitted Cherenkov photons and consequently proportional to the total "size" of the shower image, i.e., the sum over all shower pixel amplitudes. As the image size is not only a function of the true energy but also of the distance between the emission region and the telescope, one needs to accurately determine the shower trajectory, i.e., its impact point on the ground and direction. The proportionality factor between shower size and energy is determined from Monte Carlo (MC) simulations, where the full shower development, Cherenkov light emission and propagation, as well as the entire telescope, are simulated.

Some of these simulated showers are shown in Fig. 1.17 for γ rays and protons of different energies. While the few events shown are not representative of the entire variety of possible shower images, one can imagine that separating small images in terms of leptonic or hadronic origin is difficult, whereas larger images show the different shower morphology more clearly. Signal selection from background events can be performed using simple cuts on the Hillas parameters, such as the Hillas-width, which tends to be smaller for γ-ray showers. Alternatively, a gammaness score can be obtained by training a machine-learning classifier on the image parameters (Ohm et al., 2009). A cut on the gammaness score can then be chosen to optimize sensitivity, a topic that will be explored in more detail in Chapter 5.

Beyond traditional reconstruction based on image parameters, an alternative approach involves generating templates from MC simulations and fitting them to the observed shower images. This Image Pixel-wise fit for Atmospheric Cherenkov Telescopes (ImPACT) method can further enhance the accuracy of the reconstructed energy and direction (Parsons and Hinton, 2014). More recent advancements investigate the potential of machine-learning techniques, including convolutional neural networks trained directly on reduced or raw pixel data (Miener et al., 2022; Glombitza et al., 2023; Abe, K. et al., 2024).

The selected reconstruction method can be applied to simulated events, which, combined with their known true properties, allows for the derivation of the telescope's instrument response functions (IRFs). The IRFs typically include the effective area (A_{eff}), point spread function (PSF), and energy dispersion (EDisp), characterizing the telescope system's response and reconstruction accuracy relative to the true input. Each component of the

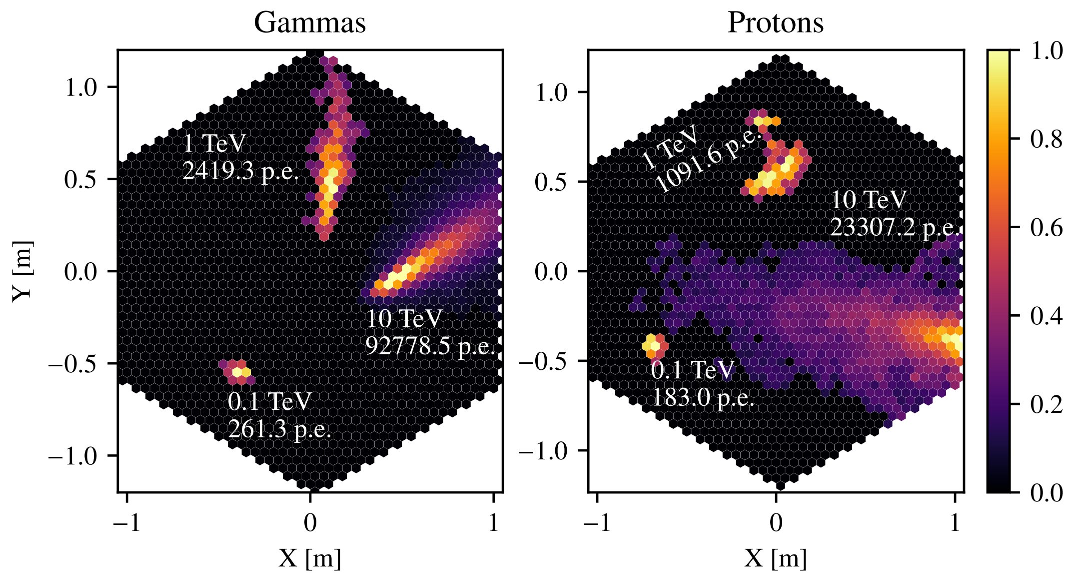

Figure 1.17: Shower images for simulated γ rays (*left*) and simulated protons (*right*). The color bar corresponds to a square root scale, and each image is normalized to the brightest pixel. The total image size is provided below the event's energy.

IRFs will be discussed in detail in Sect. 1.6.1.

There have been multiple generations of IACTs built in the past, improving in light-collecting area, camera resolution, electronics, and analysis techniques. The Whipple telescope collected Cherenkov light using a segmented mirror with 10 m diameter, reflecting the light into a camera with only 37 pixels in the beginning (Kildea et al., 2007). It is regarded as the first successful IACT and remained operational until 2006. Observing the same air shower from multiple directions and employing a stereoscopic reconstruction technique enabled the HEGRA collaboration to further reduce the background and improve the reconstruction (Daum et al., 1997). Current-generation IACTs include the High Energy Stereoscopic System (H.E.S.S.), located on the Southern Hemisphere in Namibia, the Major Atmospheric Gamma Imaging Cherenkov (MAGIC) telescopes, and the Very Energetic Radiation Imaging Telescope Array System (VERITAS). MAGIC and VERITAS are located in the Northern Hemisphere on La Palma and in Arizona, respectively. These instruments are built at altitudes between 1270 m (a.s.l.) for VERITAS (Weekes et al., 2002), which focuses on high energies with four 12 m telescopes, and 2200 m (a.s.l.) for MAGIC (Aleksić et al., 2016), which focuses more on low energies with two 17 m telescopes. Higher altitudes and larger mirrors enable the observation of γ rays with lower energies, as more of the faint Cherenkov light flash can be collected. The large central telescope of the H.E.S.S. array (CT5) has a mirror diameter of 28 m and was equipped with a camera with 1758 pixels in 2019 (Eldik et al., 2016; Bi et al., 2021). Figures 1.16 and 1.17 show images as seen by this camera. Additional details about H.E.S.S. and its phases can be found in Sect. 4.2.1. Currently, the next generation Cherenkov Telescope Array Observatory (CTAO) is under construction and will consist of telescopes of three different sizes, located at one site in the Northern Hemisphere and one in the Southern Hemisphere.

1.6 Source analysis in the context of Gammapy

To extract information about the properties of a γ-ray source (its flux, spectrum, and morphology), one can use the so-called "forward-folding" process along with statistical tools that allow fitting models to the data. One open-source library for γ-ray data analysis is GAMMAPY (Donath et al., 2023), which is being developed for CTAO but is also applicable in analyses of existing IACTs, as well as non-pointing instruments like Fermi-LAT or HAWC. GAMMAPY is implemented in PYTHON and is built on foundational libraries such as ASTROPY (Astropy Collaboration, 2013; Astropy Collaboration, 2018; Astropy Collaboration, 2022), NUMPY (Harris et al., 2020), and SCIPY (Virtanen et al., 2020).

1.6.1 Forward-folding

The core components of any analysis include the reconstructed events, characterized by their energy and position, the IRFs, and a source model. Optionally, one can provide a background model, which is usually constructed from many observations with excluded source regions, or estimate the background from source-free regions within the observation itself (Berge et al., 2007; Mohrmann et al., 2019). Each of these components is represented by its respective class, which are all combined in a dataset.

Currently, GAMMAPY supports only binned analyses in up to four dimensions, where the events are binned along the energy, time, and/or spatial dimensions. This binning is often referred to as "reconstructed geometry", as it applies to the reconstructed quantities of the events. Appropriate bin sizes for this geometry are determined by the resolution of the event reconstruction. Choosing a bin size larger than the instrument's resolution can lead to a loss of sensitivity, while using very fine bins, well below the resolution, primarily increases computational costs.

Additionally, there is the "true geometry", which is identical in the spatial dimensions but may differ in the energy axis and serves as a grid for the numerical integration of the source model. The true energy axis typically extends beyond the reconstructed one by one or two energy resolutions to account for events with true energies outside the analyzed energy range being reconstructed inside it, due to the limited energy resolution. The binning of the true energy axis should be fine enough to ensure that errors from the numerical integration are minimal. This integration is performed using the trapezoidal rule in log-log space, meaning that for a simple power law, the result will be accurate regardless of the bin size. However, any deviations of the A_{eff} or the true spectral model from a power law need to be resolved with appropriate accuracy. Typical bin sizes for the true energy axis range between 8–16 bins per decade.

Once all components are in place, the true model can be forward-folded to compute the predicted number of counts, ν, as follows:

$$\nu(E, r, \xi) = \int dE' \int dr' D(E|E', r') \times P(r|E', r') \times A(E', r') \times \phi'(E', r', \xi), \tag{1.14}$$

where E and r denote the reconstructed energy and position coordinates, while E' and r' are the coordinates of the true geometry, respectively. The parameters of the model are represented by the parameter vector ξ. This equation assumes that the IRFs factorizes into three independent parts and can be interpreted as the true source flux ϕ' being integrated over the true geometry and multiplied by the exposure A before being convolved with the PSF P and finally with the EDisp D. For some instruments, the PSF is provided as a function of reconstructed energy, which means that the EDisp needs to be applied before the PSF.

In the following, the components are described in more detail and illustrated using the example of CTAO South, where the IRFs are publicly available[10].

[10]DOI: `https://doi.org/10.5281/zenodo.5499840`

Source models One advantage of GAMMAPY is the ability to implement custom source models, which can be parametric, phenomenological, or physical in nature. The `SkyModel` class is called on a set of coordinates and returns the true differential source flux in units equivalent to $\mathrm{TeV}^{-1}\ \mathrm{s}^{-1}\ \mathrm{cm}^{-2}\ \mathrm{sr}^{-1}$. Upon integration over the true geometry, the model is evaluated at the energy bin edges and spatial bin centers. As mentioned before, the energy integration follows the trapezoidal rule in log-log space, while the spatial integration assumes constant source flux within the solid angle of the pixel, resulting in the source flux with dimensions of $[L^{-2} \cdot T^{-1}]$.

The exposure is computed by multiplying the A_{eff} by the observation time and is expected as a function of true energy and position in dimensions of $[L^2 \cdot T]$. For example, Fig. 1.18 shows the effective area of CTAO South for different zenith and offset angles. It is derived from MC simulations of point sources at different offsets, where the known simulated area is multiplied by the fraction of events triggering the telescope and passing the selection cuts for different energies. The exposure cube[11] of the analysis would be derived by interpolation based on the observation zenith angle and the offset of each pixel with respect to the camera pointing, i.e., projecting from the instrument frame to the sky. In the case of IACTs, the effective area decreases with further offset from the pointing (except for the highest energies), while larger zenith angles increase the effective area well above the increasing energy threshold. After multiplying the integrated true source flux by

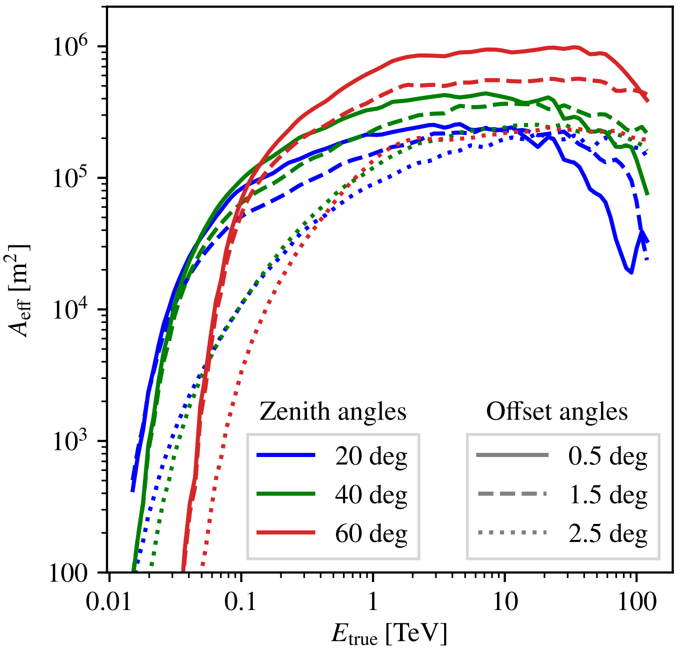

Figure 1.18: Effective areas of CTAO South for a combination of different zenith and offset angles.

the exposure, the number of expected counts in each bin is obtained, though still in true coordinates.

The point spread function In reality, uncertainties in the event reconstruction lead to a smearing of the true source flux's spatial distribution. This effect is modeled by the PSF, which is also constructed from the simulated events, where true and reconstructed event directions are known. As the PSF for IACTs is expected to be roughly symmetric, it is sufficient to bin the events based on the angular separation θ between their true and

[11] The term "cube" refers to 3- (or 4-)dimensional arrays, where two dimensions usually represent the spatial coordinates and the other dimensions may correspond to energy or other quantities. It is used in contrast to the term "map", which refers to 2D arrays.

reconstructed positions. The quantity stored in the PSF is ${}^{dP}\!/_{d\Omega(\theta)}$, the probability density function (PDF) of reconstructing an event in the solid angle $d\Omega$ at the distance θ from the true position. This can be obtained by dividing the number of events contained in each bin by the solid angle of the θ-bin and normalizing such that the integral $\int {}^{dP}\!/_{d\Omega(\theta)} d\Omega = 1$ along the θ axis. Gammapy would then integrate this PDF in each pixel of the true geometry, assuming the central pixel is at $\theta = 0$, and obtain the PSF kernel, which can then be used to convolve the spatial distribution of the expected counts in true coordinates.

Figure 1.19 illustrates the PSF using the example of CTAO South for different zenith angles and energies. Generally, the PSF improves towards lower zenith angles and higher energies, as seen by the more rapidly decreasing PDFs. The right side of the figure shows

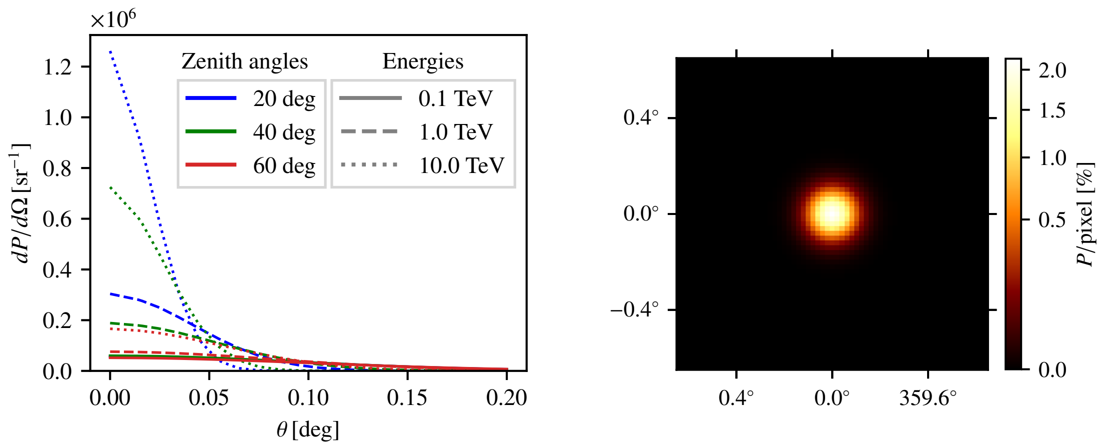

Figure 1.19: Illustration of the CTAO PSF. *Left:* PDF for angular reconstruction at different energies and for different zenith angles at 0.5° offset. *Right:* The PSF kernel for 40° zenith and at 1 TeV on a 0.02° grid.

the PSF kernel, which contains the fraction of counts in each pixel for a source located at the center position. After correcting the spatial distribution of the predicted counts, energy reconstruction uncertainties and biases still need to be accounted for.

The energy dispersion Similar to the PSF, PDFs for the energy migration $\mu = {}^{E_\mathrm{reco}}\!/_{E_\mathrm{true}}$ are constructed, as shown in the left panel of Fig. 1.20. For higher energies, the energy resolution improves slightly due to increased precision in reconstructing the shower's impact distance on the ground, combined with smaller relative fluctuations in the Poissonian Cherenkov photon distribution. At lower energies, close to the threshold, only showers with upward fluctuating light yield will trigger the telescope, introducing a positive bias in energy reconstruction. This is evident from the shift of the 60° zenith curve at 0.1 TeV relative to the curve at 20° zenith angle, where the energy threshold is at even lower energies. Contrary, at the highest energies, saturation effects in the camera generally cause an underestimation of the shower's energy, leading to a negative energy bias.

To obtain the EDisp kernel – a matrix that describes the re-distribution from true energy into reconstructed energy bins – the PDF ${}^{dP}\!/_{d\mu}$ is converted to ${}^{dP}\!/_{dE_\mathrm{reco}}$ for each true energy bin and integrated over the reconstructed energy axis. The result can be seen in the right panel of Fig. 1.20, where good energy reconstruction is indicated by the black diagonal line. Note that the first two true energy bins, which extend beyond the reconstructed energy range, still contribute significantly to the first (two) reconstructed energy bins. By matrix multiplication along the true energy axis, the predicted counts cube of true energies is transformed into the predicted counts cube, which can finally be compared to the data.

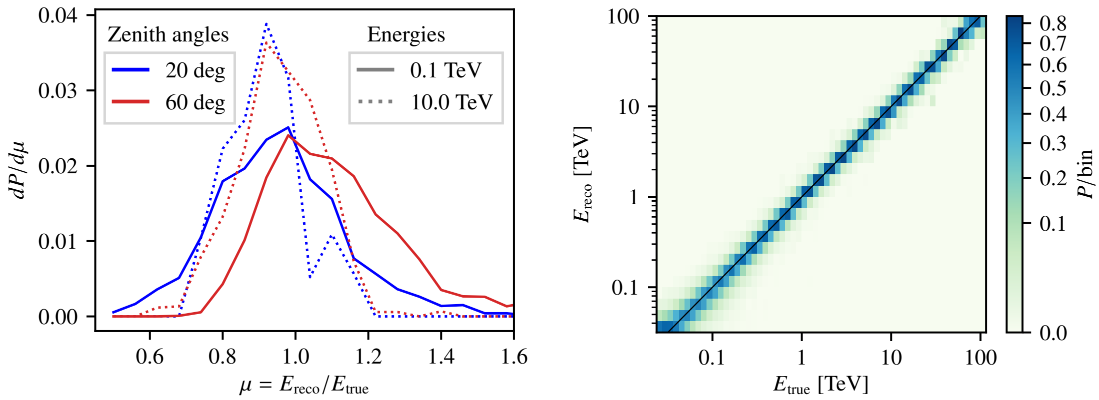

Figure 1.20: Illustration of the CTAO energy dispersion. *Left:* PDF for energy reconstruction at various energies and for different zenith angles at 0.5° offset. *Right:* The EDisp kernel matrix for 40° zenith and 0.5° offset. The colorbar shows the fraction of events from each true energy bin that are reconstructed in the corresponding reco energy bin.

Background estimation However, besides the contribution of true γ-ray events, the measured counts cube also consists of misclassified background events. This contribution can either be estimated from source-free regions in the FoV of the observation itself, or a model of expected background rates can be constructed, either from simulations or from measured data (Mohrmann et al., 2019).

The simulated background rates for CTAO South are shown in Fig. 1.21, where, similar to the effective area, the rates decrease with further offset from the camera center, and larger zenith angles appear to shift the curves to higher energies. This can be understood

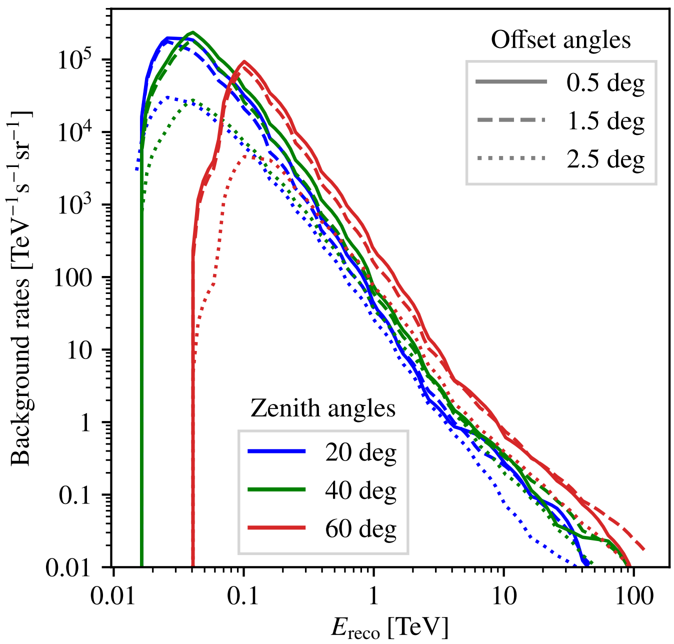

Figure 1.21: Differential background rates for CTAO South, plotted for a combination of different zenith and offset angles.

as the cosmic ray spectrum, from which the background events originate, being multiplied by the effective area and an energy-dependent factor describing the background rejection. Typically, the background model is provided as a function of reconstructed energy, so the number of predicted background counts can be computed by integrating the rates within each bin of the analysis geometry without applying energy dispersion.

The forward-folded predicted counts from the source model are added to those from the background model, and the resulting predictions are compared to the measured counts using statistical inference.

1.6.2 Statistical methods

In counting experiments, the occurrence of independent events – where no event influences the probability that another event will occur – follows the Poisson distribution. The probability of measuring n events while ν are expected is given by

$$\mathcal{P}(n|\nu) = \frac{\nu^n}{n!} \cdot e^{-\nu}. \tag{1.15}$$

Figure 1.22 shows the probability distribution for different numbers of predicted counts, which is asymmetric for small ν but approximates a Gaussian distribution for larger ν. The expected value and variance of a Poisson distribution are both equal to ν, so the standard deviation of the distribution is given by $\sqrt{\nu}$.

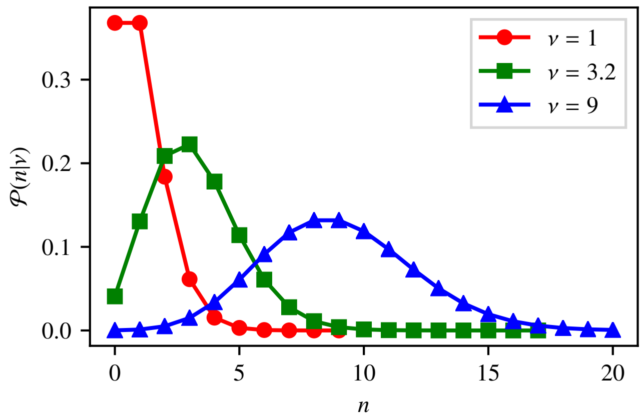

Figure 1.22: The probability mass function of Poisson distributions for various predicted counts ν.

***Cash* statistic** Based on the Poisson distribution, one can construct a likelihood for 3D datasets with a background model following Cash (1979), where the probabilities of observing n_i counts given the prediction ν_i in each bin i are multiplied:

$$\mathcal{L} = \prod_i \mathcal{P}(n_i|\nu_i). \tag{1.16}$$

This is the total probability of observing exactly the measured distribution of counts, given that the source and background models are true, which is generally very small. For computational reasons and for the application of Wilks' theorem (Wilks, 1938), one usually computes the *Cash* statistic C

$$C = -2\ln\mathcal{L} = -2\sum_i \left(\nu_i - n_i \ln \nu_i\right), \tag{1.17}$$

where the term $n_i!$ is dropped as it does not depend on the model parameters and represents a constant offset to the *Cash* statistic. The optimal set of parameters $\hat{\xi}$ can be found by minimizing the C-value, which maximizes the likelihood.

Profile-likelihood scans Uncertainties on individual parameters can be estimated based on the likelihood profile scan, where the parameter of interest x is fixed to values around its optimum $\hat{x}$ while all other parameters are optimized again. According to Wilks' theorem, the difference in the *Cash* statistic

$$\Delta C(x) = C(x, \xi) - C(\hat{\xi}) \tag{1.18}$$

is χ^2 distributed with one degree of freedom. The quantity ΔC is also referred to as the test statistic (TS) or denoted as ΔTS, both of which are used interchangeably in this thesis. In cases where x includes multiple parameters, the theorem still holds, but the degrees of freedom increase to the number of parameters in x. This means that the $n^{\text{th}}\sigma$ uncertainty of the parameter can be found by evaluating the width of the profile where $\Delta C = n^2$. Figure 1.23 illustrates the likelihood landscape for a simple power law (cf. Eq. 1.1) with index and amplitude as free parameters. The correlation between the two parameters causes the major axis of the elliptical confidence contours to be rotated relative to the two parameter axes. It also shows how re-optimization during the profile scan widens the profile in cases of correlation, which in turn increases the uncertainty. Wilks' theorem

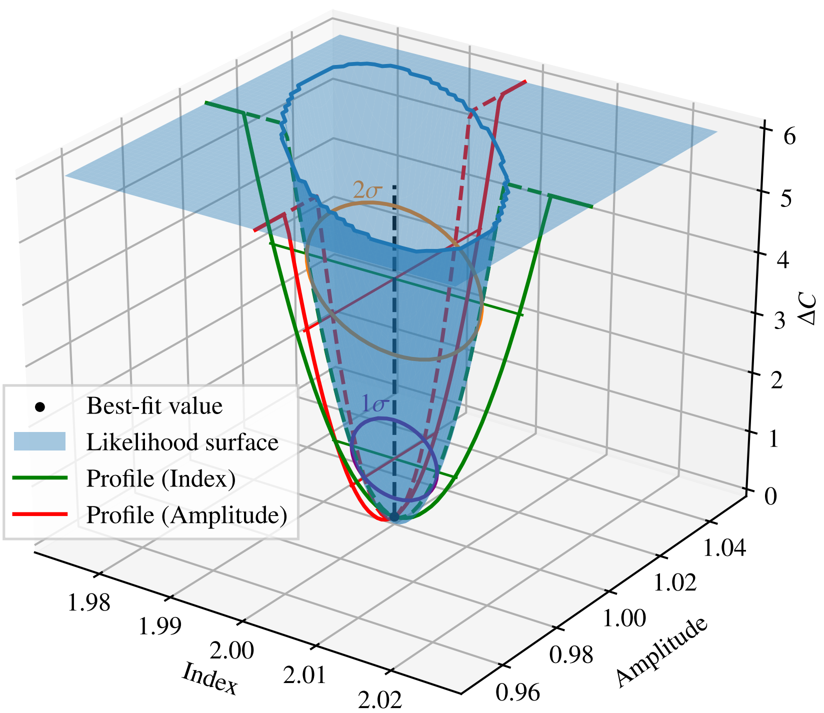

Figure 1.23: Likelihood surface for a power-law model with an index of 2 and an amplitude of 1. The dashed profiles show likelihood scans without reoptimization, where the other parameter is fixed to its optimal value. The solid profiles account for the correlations between parameters and show the ΔC value when the other parameter is reoptimized. The 1σ (purple) and 2σ (orange) confidence contours are drawn at $\Delta C = 1$ and $\Delta C = 4$, respectively. The resulting uncertainties on the index and amplitude are depicted as horizontal lines between the profiles. For illustrational purposes, the surface and the profiles are clipped at $\Delta C = 6$.

also implies that the shape of the likelihood profiles is supposed to be parabolic at the minimum, such that the likelihood ratios follow a Gaussian distribution:

$$\frac{\mathcal{L}(x, \xi)}{\mathcal{L}(\hat{\xi})} = \exp\left(-\frac{1}{2}\Delta C(x)\right). \tag{1.19}$$

Frequentist and Bayesian interpretation of uncertainties Thus far, the statistical interpretation of the uncertainties or confidence intervals needs to follow the frequentist interpretation, i.e., assuming the best-fit value is the true value. One expects the measured values for many repetitions of the experiment to lie within the confidence interval with a frequency of, e.g., 68% for a 1σ interval. One cannot conclude that the true value is within the uncertainty with 68% probability, as this would be the Bayesian interpretation.

For a Bayesian interpretation, one always requires a prior probability distribution $P(x)$, which is then updated based on Bayes' theorem:

$$P(x|\text{data}) = \frac{P(\text{data}|x)P(x)}{P(\text{data})}, \tag{1.20}$$

where $P(\text{data}|x) = \mathcal{L}$ is the probability of measuring the data given the parameter x, which is equal to the likelihood constructed in Eq. 1.16. The probability $P(\text{data})$ of observing the data is also called the marginal probability and normalizes the posterior probability distribution $P(x|\text{data})$. One can then find the so-called credible intervals such that, e.g., 68% of the posterior probability distribution is contained within that interval.

***W*-statistic** An alternative likelihood needs to be constructed for a 1D analysis where the background is estimated from source-free regions within the same observation as described in Berge et al. (2007). This likelihood must account for statistical uncertainties in the background estimation, which are negligible when the background template is constructed from a large number of observations. One effectively performs the 3D analysis all in one pixel, which is the "On Region" illustrated in Fig. 1.24. The counts in the on-region n_{on} consist of signal events μ_{sig} and background events μ_{bkg}, whereas the counts in the off-regions n_{off} are only due to background events. To reduce systematic uncertainties, the

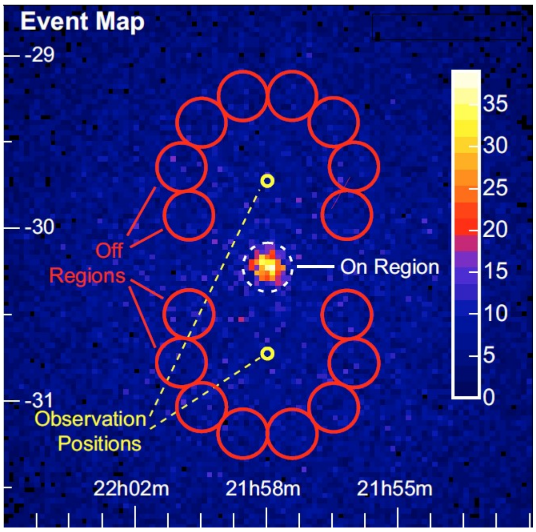

Figure 1.24: Illustration of the background estimation based on reflected regions. Taken from Berge et al. (2007).

off-regions are selected to have the same offset from the telescope's pointing direction and the same size as the on-region. This approach helps to mitigate the impact of variations in camera acceptance, which are mostly radially symmetric and primarily dependent on the offset from the camera center. At the same time, the limited number of off-regions α leads to a non-negligible statistical error on the estimated background counts in the on-region.

This is all combined in the likelihood:

$$\mathcal{L}_{\text{on/off}} = \frac{(\mu_{\text{sig}} + \mu_{\text{bkg}})^{n_{\text{on}}}}{n_{\text{on}}!} \exp\{-(\mu_{\text{sig}} + \mu_{\text{bkg}})\} \times \frac{(\mu_{\text{bkg}} \cdot \alpha)^{n_{\text{off}}}}{n_{\text{off}}!} \exp\{-\mu_{\text{bkg}} \cdot \alpha\}, \tag{1.21}$$

which combines the Poisson probabilities of measuring the on-counts given the prediction of signal and background combined, and simultaneously measuring the off-counts given only the background prediction. Similar to the *Cash* statistic, one can form the W statistic by taking

$$W = -2\ln\mathcal{L}_{\mathrm{on/off}} = 2\big(\mu_{\mathrm{sig}} + (1+\alpha)\mu_{\mathrm{bkg}} - n_{\mathrm{on}}\ln\left(\mu_{\mathrm{sig}} + \mu_{\mathrm{bkg}}\right) - n_{\mathrm{off}}\ln\left(\mu_{\mathrm{bkg}}\cdot\alpha\right)\big), \quad (1.22)$$

where again, the model-independent terms $n_{\mathrm{on/off}}!$ are dropped. This statistic can be summed for different energy bins so that one can also fit spectral models to the data, where μ_{sig} would be the forward-folded model prediction.

Comparison of 1D and 3D analyses To better understand the differences between the 1D and 3D analyses, one can estimate the sensitivities for a 5σ point source detection for 50 h and CTAO South IRFs. For each energy bin, the true model flux required to achieve a ΔC- or ΔW-value of 25 is estimated, where the null-hypothesis (background only) is compared to the signal-hypothesis (background + best-fit source model). Consequently, the overall normalization of the differential sensitivities is influenced by the energy bin size, which is consistently set to 8 bins per decade in this case. So-called Asimov datasets are employed, where the measured counts are set equal to the model prediction, which leads to the average ΔC-value across many realizations of count distributions (Cowan et al., 2011). Before estimating the sensitivity for the 1D dataset, one needs to optimize the size of the on-region based on the maximum integrated sensitivity.

The results are shown in Fig. 1.25, where the sensitivity of the 3D dataset is superior to that of the 1D datasets. This can be understood by considering the differences between the three methods.

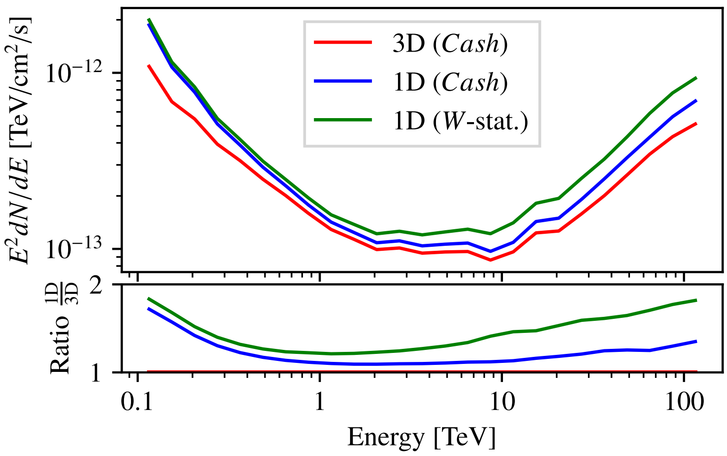

Figure 1.25: Comparison of differential sensitivities (5σ point-source detection) for 50 h CTAO data between 3D and 1D analyses. The 1D sensitivity using *Cash* statistics assumes a perfectly known background, while the 1D sensitivity using W-statistics estimates the background from 8 off-regions and includes the associated statistical uncertainty.

First, the 1D analyses neglect all the signal events outside the on-region while treating all the events inside the on-region the same, irrespective of the distance to the source. In contrast, the 3D analysis multiplies the likelihoods of all pixels, where the pixels close to the source contribute more while still keeping the residual information in the pixels further away. The optimal size of the on-region is mainly determined by the size of the PSF and the background flux, both of which are energy-dependent, while the size of the on-region is not. As a result, the on-region is optimized for the medium energy range, where most of the sensitivity is gained. Consequently, the region is too small at low energies, where the PSF is large, while the opposite is true at high energies.

Another difference is the assumptions about the background. As mentioned before, the *Cash* statistic assumes a background model from which the background contamination can be estimated without statistical uncertainties. This can be a good approximation if the background model is accurate and enough source-free regions are available to fit the background model to the data. It can be thought of as the limit of infinite off-regions, where the W and $Cash$ statistics would converge. In the case of 8 off-regions, Fig. 1.25 shows that the 1D (W-statistic) sensitivity becomes worse with increasing energy compared to the 1D (*Cash*) sensitivity. The reason is that the relative uncertainty of the background increases with lower background counts in the off-regions, which is natural when looking at the background spectrum in Fig. 1.21.

All of this does not take into account any background systematic uncertainties. These uncertainties arise from different sources depending on the method employed. For the reflected regions method, systematic effects are induced by deviations from circular symmetry in the background rates. Such asymmetries may result from factors like the zenith gradient, the geomagnetic field, or hardware-specific features that break the symmetry.

In contrast, the 3D background model does not assume any circular symmetry of the background rates. However, it is derived from observations taken under different conditions and thus represents the background rates for average conditions. Since the spectral and spatial distributions of the background rates depend on the observation conditions, deviations from these averages can introduce systematic discrepancies in the background template. This issue is absent in the reflected regions method, as no other observations are involved.

Generally, the systematic uncertainties in the background rates can mitigate each other when the source is observed in different camera sectors (for the reflected regions method) and under conditions close to the average (for the 3D template). Under these prerequisites, the reflected regions method is expected to introduce minimal systematic uncertainties. However, the current construction of the background model may lead to significant systematics, up to 10%, as indicated in Nakashima (2023).

1.7 Galactic and Equatorial coordinates

There are several coordinate systems frequently used to describe the position of celestial objects on the sky. Here, we will focus on the ones using spherical coordinates, i.e., an azimuth angle between 0° and 360°, and an altitude angle between -90° and 90°.

For Galactic coordinates, the system is aligned with the Galactic plane, with the Sun at its center. The azimuth angle is called Galactic longitude (l) measuring the angular distance eastward along the Galactic equator from the Galactic Center. Accordingly, the Galactic latitude (b) measures the angular distance northward of the Galactic equator. Therefore, the primary direction $(l, b) = (0, 0)$ points towards the Galactic Center, and the Galactic plane is located at $b = 0^\circ$. These coordinates are especially insightful when the position of a source with respect to our galaxy is of interest. Most Galactic sources (except close ones) are located within $b = \pm 5^\circ$, while extragalactic ones are rarely in that range as matter in the Milky Way obscures the view (cf. Fig. 1.8).

An alternative orientation of the coordinate system is used by Equatorial coordinates, where the Earth is in the center. The origin of the altitude coordinate or Declination (DEC $= 0^\circ$) is given by the projection of the Earth's equator onto the sky, forming the celestial equator. This results in a position of the celestial North pole at DEC $= +90^\circ$ and the South pole at DEC $= -90^\circ$. The other coordinate, called Right ascension (RA), measures the angular distance from the March equinox[12] eastward along the celestial equator. Due to the precession and nutation of the Earth's rotation axis, one needs to specify an epoch of this equinox, typically J2000. Despite the primary direction being of little interest, this coordinate system is especially relevant when planning observations. The Earth's latitude, on which the observatory is located, limits the zenith angles under which a source of a certain Declination appears. Northern sources at large Declinations are difficult to observe from observatories located in the Southern Hemisphere like H.E.S.S..

Another important aspect of sky maps is the projection used to project the 3D spherical coordinates onto the plane. There are many possible projections with different compromises between preserving direction, shape, area, and distance. Relevant for this work are the equal-area Hammer-Aitoff and the equidistant plate carrée projections.

The former preserves the area at all locations at the cost of distorting shapes. Therefore, the entire sphere has an elliptical footprint (cf. Fig. 1.26). It is popular for all-sky maps or in scenarios where the relative size of distant regions is relevant.

In contrast, the plate carrée projection maps lines of constant longitude and latitude to straight horizontal and vertical lines, respectively. It preserves the distance to the poles in equatorial direction, while increasingly distorting the area and shape of regions towards the poles. For small FoVs, typical for IACTs, these distortion effects and the difference to the Hammer-Aitoff projection remain small. The advantage of this projection is the simple relation between pixel position and location on the sky and the rectangular footprint of the entire sky.

Figure 1.26 shows the γ-ray sky as seen by Fermi-LAT in Galactic coordinates using the Hammer-Aitoff projection. The positions of sources relevant to this work are indicated as black dots. One can estimate the Declination of the sources based on their distance to the celestial equator and the poles indicated as black lines.

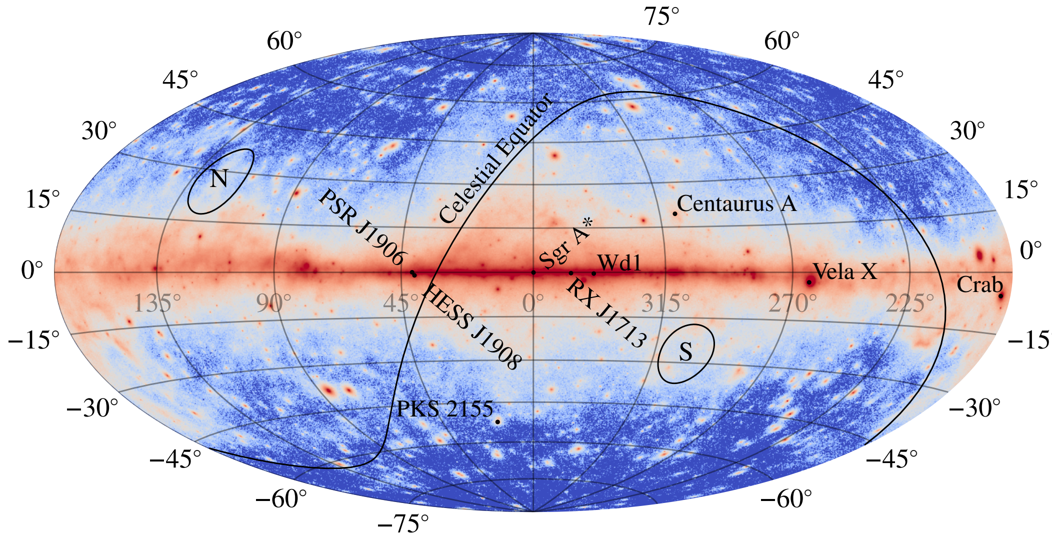

Figure 1.26: Fermi-LAT all-sky map in Galactic coordinates using the Hammer-Aitoff projection (Credit: Fermi-LAT collaboration). The celestial equator (dec=0°) and the 10° regions around the North and South poles are marked, along with relevant source positions for this work.

[12]The March equinox is the point where the Sun's ecliptic intersects the celestial equator in March.

For ever since the world was created, people have seen the earth and sky. Through everything God made, they can clearly see his invisible qualities — his eternal power and divine nature. So they have no excuse for not knowing God.

— Paul, Romans 1:20

2 Prospects for combined analyses of hadronic emission from γ-ray sources in the Milky Way with CTA and KM3NeT

This study originated as a Master's project focused on the technical implementation of a neutrino analysis within the GAMMAPY framework. During the initial phase, it became evident that the primary application would involve the joint analysis of γ-ray and neutrino data from individual galactic sources, with the objective of distinguishing between leptonic and hadronic emission scenarios. Since the completion of the Master's thesis (Unbehaun, 2020), the analysis has undergone further refinement and has been published in The European Physical Journal C (Unbehaun et al., 2024). Substantial portions of that publication are included here, with minimal or no modifications.

2.1 Introduction

We live in the era of multi-messenger astrophysics (Mészáros et al., 2019). Long anticipated, this paradigm advocates that unique insights about astrophysical objects and processes may be gained through the joint consideration of information carried by different messengers: photons, neutrinos, cosmic rays (CRs), and gravitational waves. In the past years, it has truly come to fruition, yielding the first promising results (Abbott et al., 2017; Aartsen et al., 2018).

Astrophysical objects in the Milky Way are not expected to produce gravitational waves detectable by current-generation instruments (but by next-generation detectors, see Gossan et al., 2022). Galactic CRs provide important energetic constraints on their source population, but cannot be used to directly study Galactic objects because they are deflected by magnetic fields. Hence, one needs to resort to photons and neutrinos to employ multi-messenger astrophysics for the study of individual Galactic objects.

Indeed, besides its conceptual attractiveness, the combined study of very-high-energy (VHE; $E > 100\,\mathrm{GeV}$) γ rays and TeV–PeV neutrinos from Galactic sources is well motivated: they are expected to be produced simultaneously in 'hadronic accelerators', where accelerated CR nuclei interact with ambient gas producing pions (and other mesons) that subsequently decay into γ rays and neutrinos (see also Sect. 1.2). In the following, this process is labelled 'PD', for pion decay. The situation is different in 'leptonic accelerators', where Inverse Compton (IC) up-scattering of photons by CR electrons leads to VHE γ-ray emission without neutrino production. This implies that the detection of high-energy neutrinos coming from astrophysical objects is decisive in identifying them as hadronic accelerators (Halzen, 2013). Nevertheless, observations of VHE γ-ray emission from the same objects are indispensable, as they provide a much higher detection sensitivity and allow a measurement of the spectrum and morphology of the emission in greater detail. This, in turn, enables a realistic estimation of the expected flux of neutrinos, and the possibility of detecting it with current (or planned) neutrino telescopes. The latter exercise has been carried out by various authors in the past (see, e.g. Vissani, 2006; Kistler and Beacom, 2006; Villante and Vissani, 2008; Kappes et al., 2007; Gonzalez-Garcia et al., 2014; Halzen et al., 2017; Celli et al., 2017).

In this work, we focus on the Cherenkov Telescope Array (CTA)[13] (Acharya et al., 2018; Hofmann and Zanin, 2023) and the KM3NeT neutrino telescopes (Adrián-Martínez et al., 2016a), as major upcoming facilities for VHE γ-ray and neutrino astronomy, respectively. CTA will be built at La Palma, Spain, and Paranal, Chile, covering the Northern and Southern sky, respectively. Our prime targets of interest being Galactic γ-ray sources, which are more easily observed from the Southern hemisphere, we consider only the site in Chile (CTA-South) for our study. At this site, the installation of $\sim$50 Imaging Atmospheric Cherenkov Telescopes (IACTs) of two different sizes, covering the energy range between 100 GeV and 300 TeV, is foreseen. Compared to current-generation arrays of IACTs, CTA is projected to provide a ten-fold increase in sensitivity.

KM3NeT is a research infrastructure in the Mediterranean, consisting of neutrino telescopes installed in the deep sea at different locations. The 'Oscillation Research with Cosmics in the Abyss' (ORCA) detector, with its dense instrumentation, will focus on the study of neutrino properties measuring atmospheric neutrinos (Aiello et al., 2022b). Here, we only consider the 'Astroparticle Research with Cosmics in the Abyss' (ARCA) detector, which targets the detection of high-energy astrophysical neutrinos with TeV–PeV energies. Hereafter, we will use the term 'KM3NeT' to refer to the ARCA telescope. It is currently under construction off-shore Sicily, Italy, and will ultimately consist of two building blocks comprising 115 vertical detection units each. Each detection unit carries 18 digital optical modules (DOMs) (Adrián-Martínez et al., 2014; Adrián-Martínez et al., 2016b; Aiello et al., 2022a) with a vertical spacing of 36 m and is about 700 m tall. The units are arranged on a grid with about 90 m spacing between them. The DOMs contain light sensors that detect Cherenkov light radiated by secondary particles created in interactions of high-energy neutrinos in or near the detector. Of particular interest for this work are muons created in charged-current interactions of muon neutrinos, as their long propagation distances of up to several km in the water allow a precise reconstruction of the direction of the incoming neutrino. Compared to the largest existing neutrino telescope, the IceCube Neutrino Observatory (Ahlers and Halzen, 2017; Ahlers and Halzen, 2018), KM3NeT utilises water instead of ice as detector medium. This reduces scattering of the Cherenkov light and is expected to lead to an improved angular resolution (Adrián-Martínez et al., 2016a). Its location in the Northern hemisphere implies that neutrinos potentially emitted by many Galactic γ-ray sources would reach KM3NeT through the Earth, which is advantageous for the suppression of atmospheric muon background events (Aiello et al., 2019). Therefore, the combination of CTA-South and KM3NeT data for the study of Galactic objects appears very natural.

The discovery potential for extended Galactic sources by KM3NeT, in relation to the constraining power of CTA, has been investigated in Ambrogi et al., 2018. In this study, we demonstrate how a combined analysis of CTA and KM3NeT data can be used to constrain physical properties of γ-ray sources in our Galaxy, with special attention to the contribution of hadronic emission processes. To this end, using Monte Carlo simulations as input, we have prepared instrument response functions (IRFs) for the KM3NeT detector and stored them in the same 'GADF' data format[14] used for the publicly available CTA IRFs. Then we have employed the Gammapy[15] package (version 0.17; Deil et al., 2017; Deil et al., 2020) to generate pseudo data sets based on the obtained IRFs and to perform a joint 3D likelihood fit on these data sets. Though Gammapy is still under development

[13]CTAO and CTA are used interchangeably in this thesis.
[14]see `https://gamma-astro-data-formats.readthedocs.io` and Deil et al., 2022
[15]`https://gammapy.org`

and application of the 3D likelihood method in IACT data analysis represents a recent approach, both have been validated using a public IACT data set (Mohrmann et al., 2019).

We apply the analysis to a selection of prototypical sources that are promising candidates for the emission of high-energy neutrinos (see Table 2.1). We motivate our choice briefly in the following:

- Vela X is a pulsar wind nebula bright in γ rays (Abramowski et al., 2012b), associated with the well-known Vela pulsar. Pulsars being copious producers of electrons and positrons, the γ-ray emission from Vela X is expected to be largely due to IC emission, and no associated neutrino emission is expected. However, also mixed, lepto-hadronic models have been considered in the past (e.g. Horns et al., 2006; Zhang and Yang, 2009), leaving room for some neutrino emission from this source.

- RX J1713.7−3946 is a shell-type supernova remnant that emits γ rays in excess of 10 TeV (Abdalla et al., 2018a). The emission has been modelled according to leptonic, hadronic, and mixed scenarios (see e.g. Fukui et al., 2021; Cristofari et al., 2021 for recent studies). The observation (but also non-observation) of neutrinos from RX J1713.7−3946 could therefore yield important clues about acceleration processes at play.

- Westerlund 1 is the most massive young stellar cluster in the Milky Way (Clark et al., 2005), and is considered the most likely counterpart of the VHE γ-ray source HESS J1646−458 (Abramowski et al., 2012a; Aharonian et al., 2022b). Massive stellar clusters have recently been hypothesized as PeVatrons (Aharonian et al., 2019), making Westerlund 1 a good candidate for high-energy neutrino emission.

- eHWC J1907+063, also known as HESS J1908+063, is an unidentified γ-ray source (Aharonian et al., 2009a) that was recently detected above energies of 100 TeV by the High-Altitude Water Cherenkov Observatory (HAWC) (Abeysekara et al., 2020) as well as by the Large High Altitude Air Shower Observatory (LHAASO) (Cao et al., 2021b). Like in the case of RX J1713.7−3946, observations with neutrino telescopes could help to constrain the nature of the source.

Our selection of sources is neither a complete list of promising targets for the emission of neutrinos in our Galaxy, nor does it comprise only the most promising ones. Rather, we have aimed for a selection of different types of γ-ray sources that furthermore exhibit favourable locations for the observation with CTA-South and KM3NeT. The source locations are indicated in Fig. 1.26 together with the celestial equator. Figure 2.1 shows the visibility

Table 2.1: Galactic γ-ray sources investigated in this work. The references in order of the table are: Abramowski et al., 2012b, Abdalla et al., 2018a, Abramowski et al., 2012a, Abeysekara et al., 2020.

Designation	Type	Spatial model	r (deg)	Declination (deg)	Distance (kpc)
Vela X	PWN	disk	0.8	−45.19	0.29
RX J1713.7−3946	SNR	disk	0.6	−39.69	1
Westerlund 1	SC	disk	1.1	−45.85	3.9
eHWC J1907+063	UNID	Gaussian	0.67	+06.18	2.37

'Type' refers to the source type; PWN = pulsar wind nebula; SNR = supernova remnant; SC = stellar cluster; UNID = unidentified. 'Spatial model' specifies which type of spatial model is used in the analysis (cf. section 2.2.4). r denotes the radius of the disk in case of a disk model and the width of the Gaussian in case of a Gaussian model.

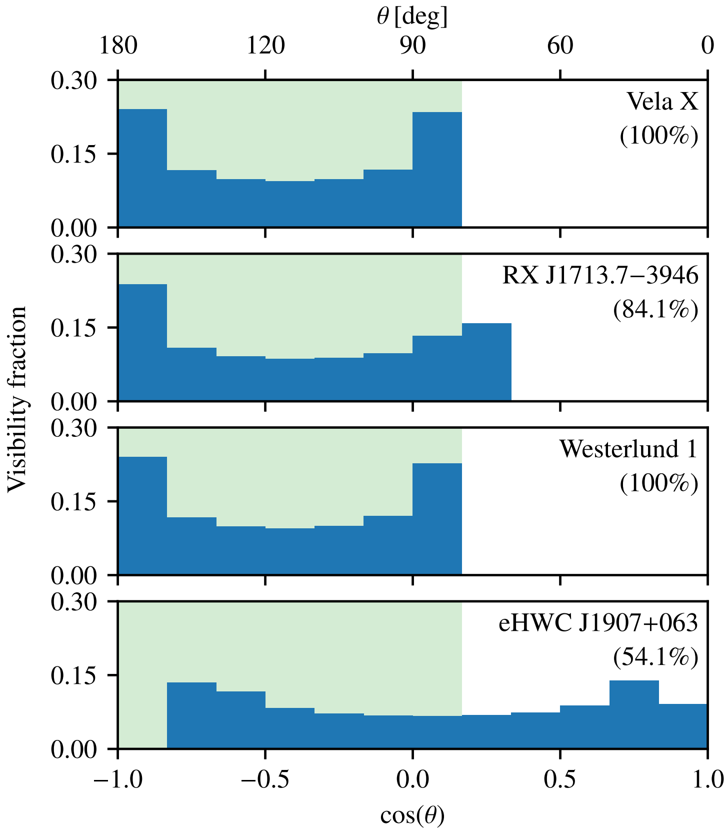

Figure 2.1: Source visibility with KM3NeT. Shown is the fraction of time that each source is visible under a zenith angle θ, over the course of one year. The green-shaded area indicates the zenith angle range used in the analysis and the percentage value in parentheses specifies the fraction that each source is visible within this range.

of all sources for KM3NeT, as a function of the local zenith angle[16]. For CTA, within one year, the sources are observable above an altitude angle of 50° for a maximum time of ∼400 h (Vela X), ∼510 h (RX J1713.7−3946), ∼500 h (Westerlund 1), and ∼380 h (eHWC J1907+063).

Finally, we note that the IRFs we derived and used in this work are not representative of the final sensitivity of CTA and KM3NeT. They are based on preliminary simulations and event selections that will likely be improved in the future. In particular, the IRFs for KM3NeT are based on a point-source analysis as presented in Muller et al., 2021. This does not impact the conclusions drawn in this work, which are focused more on the conceptual benefits of a combined analysis rather than on numerical results.

This work is structured as follows. In Sect. 2.2, we introduce our methodology: the computation of IRFs (Sects. 2.2.1 and 2.2.2), the preparation of input models (Sect. 2.2.3), the generation of pseudo data sets (Sect. 2.2.4), the combined likelihood analysis (Sect. 2.2.5), and the derivation of constraints on hadronic contributions (Sect. 2.2.6). The results of the analysis are then presented and discussed in Sect. 2.3, before we conclude this study in Sect. 2.4.

2.2 Methodology

As detailed in Sect. 1.6, the IRFs for each experiment allow us to compute how a source would appear in the detector, given a physical source model. In our case, the relevant IRFs comprise the effective area, the energy dispersion, and the point spread function, reflecting the sensitivity, energy resolution, and angular resolution of the instrument,

[16]The zenith angle θ refers to the location of the source. For $\theta = 0°$ the source is above the detector and produces vertically down-going neutrinos, while for $\theta = 180°$ the source is located on the opposite side of the Earth and produces vertically up-going neutrinos.

respectively. Additionally, background templates that yield the expected number of mis-classified background events, arising from CR-induced atmospheric air showers, are necessary.

For IACTs, the IRFs are typically stored as a function of the true γ-ray energy and of the true angular offset of the events with respect to the pointing direction of the telescopes ('offset angle'). The IRFs also depend on the angle with respect to zenith of the pointing position of the telescopes. However, because the variation within a specific observation run (of typically 30 min duration and a field of view of $\sim 5^\circ \times 5^\circ$) is small, IRFs for the average zenith angle of the observation run are commonly employed. For CTA we use the publicly available 'Prod 5' IRFs[17] for the southern array at 20° zenith angle and averaged over azimuth angle (CTAO & CTAC, 2021). The IRFs for KM3NeT have been custom-generated for this study, as detailed in the following section.

2.2.1 Generation of KM3NeT IRFs

The KM3NeT IRFs are based on extensive simulations of neutrinos and anti-neutrinos[18] that interact in or near the detector. We focus on charged-current interactions of muon neutrinos only, as they give rise to long-range muons that appear as characteristic, track-like events in the detector. This leads to a good angular resolution ($< 0.3^\circ$ for energies > 10 TeV), which helps in suppressing background events (but see also Sudoh and Beacom, 2023). The neutrino events have been simulated with the gSeaGen software (Aiello et al., 2020) based on the GENIE neutrino generator (Andreopoulos et al., 2010), which allows the simulation of interactions of all neutrino flavours in the media around the detector.

On the level of a single optical module, the decay of ^{40}K as well as bioluminescence are relevant sources of noise. Due to the design of the optical modules, which contain multiple photo-sensors each, these backgrounds can however be suppressed very efficiently by requiring a local coincidence between the photo-sensors (Adrián-Martínez et al., 2016b). On the analysis level, two types of background events are relevant for KM3NeT: neutrinos and muons, both created in CR-induced atmospheric air showers. Both can be further classified as 'conventional' – resulting mostly from the decays of pions and kaons – and 'prompt' – resulting from the decays of heavy hadrons and light vector mesons. The former exhibit a steeper energy spectrum, because their parent particles have a non-negligible chance to re-interact with air molecules, rather than to decay.

To predict the rate of atmospheric neutrino events, we use the 'HKKMS' model (Honda et al., 2007) for conventional neutrinos and the 'ERS' model (Enberg et al., 2008) for prompt neutrinos. Both models are based on outdated parametrisations of the primary CR flux and have been corrected as described in Aartsen et al., 2014 to conform with the 'H3a' parametrisation from Gaisser, 2012. We note that there is also the possibility of a CR composition around the 'knee' feature in the CR spectrum that is heavier than predicted by the H3a model. This scenario is discussed in more detail in Mascaretti et al., 2020, but not investigated further here.

The resulting event rates of conventional and prompt atmospheric neutrinos, integrated over relevant zenith angles, are shown in Fig. 2.2. The background of atmospheric muons has been estimated using dedicated simulations of muons using the MUPAGE package (Becherini et al., 2006; Carminati et al., 2008; Albert et al., 2021). While there is in principle also a potential background due to diffuse astrophysical neutrinos not connected to the studied source itself (Abbasi et al., 2022b), this background can be safely neglected here.

[17] See `https://www.cta-observatory.org/science/ctao-performance`.

[18] Hereafter, we will use the term 'neutrinos' to refer to both neutrinos and anti-neutrinos, unless explicitly stated otherwise.

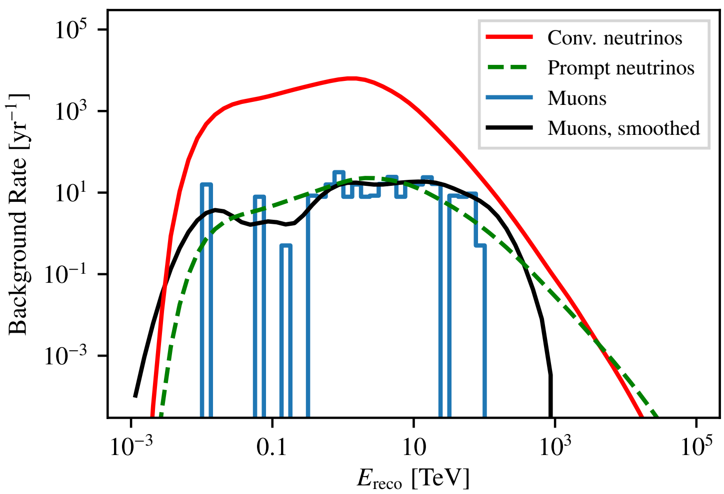

Figure 2.2: Background event rates in KM3NeT as a function of reconstructed energy $E_{\rm reco}$. The atmospheric neutrino rates are integrated over all zenith angles in the analysis region (i.e. $\theta_{\rm reco} > 80°$). The atmospheric muon rate is shown for the zenith angle bin $80° - 90°$ only, since it is completely negligible for larger angles. The black line displays the smoothed curve used in the analysis.

All simulated events are reconstructed using a track reconstruction algorithm and subsequently undergo a selection procedure based on the reconstruction quality and a classification algorithm using boosted decision trees (BDTs), as detailed in Muller et al., 2021. In order to suppress the background of atmospheric muons, which always arrive from above the detector, we restrict the analysis region to reconstructed zenith angles $\theta_{\rm reco} > 80°$. Thus, only very few atmospheric muon events remain in the final sample, almost all concentrated close to the horizon region ($80° < \theta_{\rm reco} < 90°$), see the blue histogram in Fig. 2.2. In order to avoid interpolation problems due to empty bins in the histogram, we fit a spline curve to the histogram and use this curve to predict the expected rate of atmospheric muon events (black line). We note that due to insufficient simulation statistics, the exact shape of the distribution at energies below 1 TeV should not be trusted. Because the muon background is sub-dominant compared to the atmospheric neutrino background by several orders of magnitude at these energies, however, this does not affect our results.

The KM3NeT IRFs mainly depend on neutrino energy and zenith angle. To be able to store the IRFs in the (IACT-centred) GADF data format, we utilise the offset-angle axis defined there to describe the dependence of the KM3NeT IRFs on the zenith angle. The IRFs are then generated by creating histograms of the appropriate event properties (e.g. the angle between the reconstructed and true neutrino direction in case of the PSF) and applying corresponding normalisation factors. For the effective area IRF, we use 48 logarithmic bins in true energy between 100 GeV and 100 PeV and 12 zenith angle bins linear in true $\cos(\theta)$. The energy dispersion and PSF IRFs – featuring one more dimension than the effective area – are created with twice the bin size, in order to ensure sufficient statistics in each bin. In the analysis, a linear interpolation between the individual bins is performed. IRFs for neutrinos and anti-neutrinos are derived separately and subsequently averaged, assuming equipartition of the source flux between the two.

2.2.2 Comparison of IRFs

In this section, we provide a comparison of the IRFs of CTA and KM3NeT. While the KM3NeT IRFs generated by ourselves are defined up to an energy of 100 PeV, the public

CTA IRFs are valid up to an energy of only ~300 TeV. This is because, given its limited duty cycle and need for pointing, CTA is not expected to be able to effectively measure fluxes beyond that energy.

Fig. 2.3 shows a comparison of the effective areas. The effective area of CTA rises sharply at the threshold energy of the instrument (around 0.1 TeV), before the curve gradually flattens as γ rays are detected more and more efficiently. The effective area of KM3NeT for neutrinos is much lower than that of CTA for γ rays because of the low interaction probability of neutrinos. The increase in neutrino effective area with increasing energy reflects a corresponding increase of the interaction cross section and detection efficiency. At the highest energies, the interaction cross section becomes large enough for the Earth to become opaque to neutrinos, leading to a decrease in the effective area for neutrinos that traverse large amounts of matter (green dashed-dotted and red dotted line in Fig. 2.3).

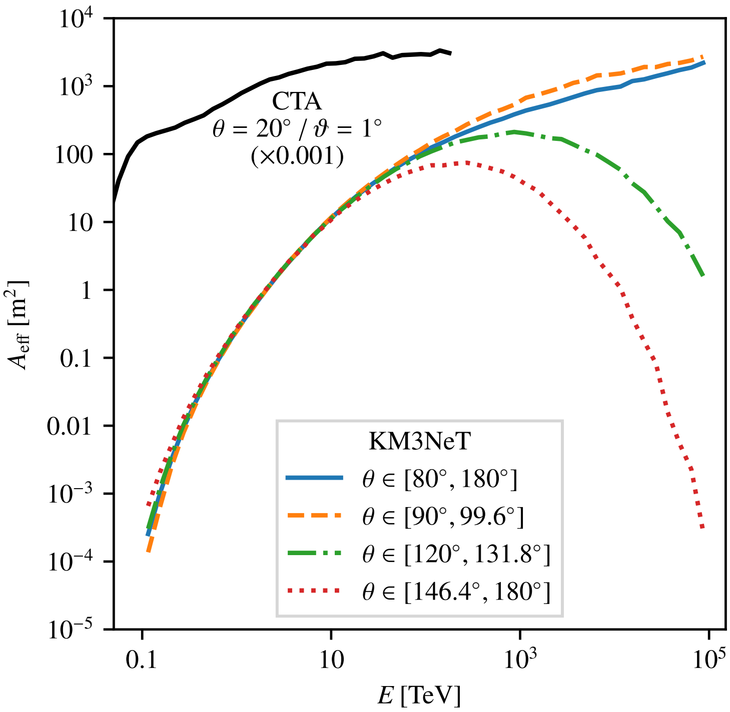

Figure 2.3: Comparison of effective areas. The CTA effective area is shown for a zenith angle of $\theta = 20°$ and an offset angle from the pointing direction of $\vartheta = 1°$. For KM3NeT, average effective areas for the full analysis region as well as for different sub-ranges in zenith angle are shown.

The angular resolutions of the two instruments – here expressed in terms of the 50%, 68%, and 95% quantiles of the respective PSFs – are compared in Fig. 2.4. While the angular resolution of CTA is clearly superior to that of KM3NeT, the selection of track-like events for the KM3NeT analysis still leads to a median resolution of better than 0.3° above ~10 TeV. The PSF strongly affects the sensitivity to point-like or marginally extended sources, as the contribution of background events increases quadratically with the radius of the source after PSF convolution. For a comparison of the KM3NeT PSF with that of the IceCube neutrino telescope, see for example Muller et al., 2021.

Figure 2.5 provides a comparison of the energy resolution of the two instruments, here indicated by the 10%, 50%, and 90% quantiles of the ratio between reconstructed and true energy. In the case of KM3NeT, muons created in muon neutrino interactions may lose energy before entering the detector or carry away energy when leaving it. Because only the energy deposited inside the detector can reliably be estimated, the resulting reconstructed energy is on average lower than the true neutrino energy. This effect becomes more and more prominent as the neutrino energy – and hence the track length of the resulting muon – increases.

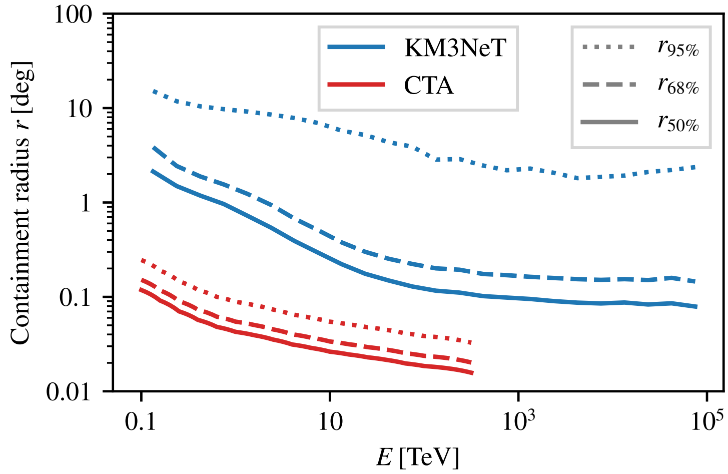

Figure 2.4: Comparison of the directional reconstruction accuracy of CTA and KM3NeT. Shown are the 68% and 95% containment radii of the PSF as a function of the true γ-ray/neutrino energy. Possible differences to previous publications may arise from the finite binning of the PSF applied here.

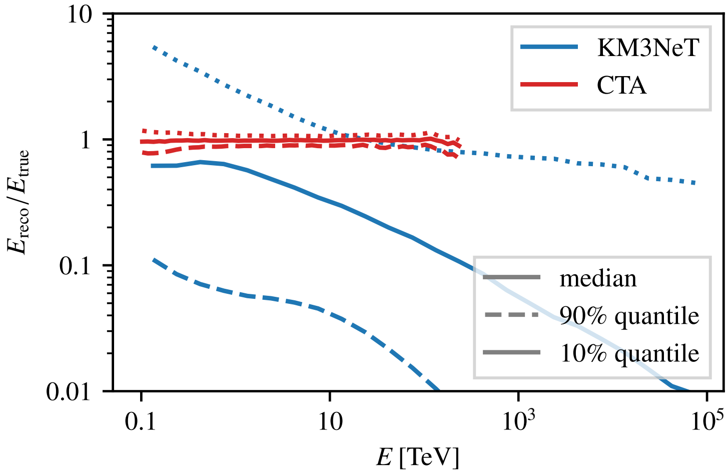

Figure 2.5: Comparison of the energy reconstruction accuracy of CTA and KM3NeT. Shown are the 10%, 50%, and 90% quantiles of the ratio between the reconstructed and true γ-ray/neutrino energy, as a function of the true energy.

2.2.3 Input models

Input models are needed for the likelihood analysis of each analysed source (cf. Table 2.1). During the analysis procedure a spatial model is chosen for each source according to the description found in the literature: either a uniform disk or a two-dimensional Gaussian model. These spatial models are not varied or fitted (i.e. remain fixed) during the entire analysis procedure. This means that the CTA sensitivity to possible differences in the morphology between leptonic and hadronic accelerators is not included in our results. In addition, two different spectral models have been considered for each source in order to study the fraction of hadronic γ-ray emission: an IC model, assuming a purely leptonic emission and a PD model, to describe a purely hadronic emission. Both models have independently been fitted to published γ-ray spectra of the sources (cf. references in Table 2.1). For the IC model, we have used the implementation of the `InverseCompton` model in the NAIMA package (Zabalza, 2015), which provides one-zone, time-independent radiative models. For the PD model, we have implemented a corresponding model based on the parametrisation in Kelner et al., 2006[19]. For both the IC and PD models, we assume a power-law model with an exponential cut-off for the primary electron and proton distributions,

$$\Phi(E) = A \cdot \left(\frac{E}{E_0}\right)^{-\Gamma} \exp\left[-\left(\frac{E}{E_{\mathrm{cut}}}\right)^{\beta}\right], \tag{2.1}$$

where A denotes the amplitude, E_0 the reference energy, Γ the spectral index, E_{cut} the cut-off energy, and β the cut-off strength. For each source and for both the IC and PD models, we have adjusted the amplitude, spectral index, and cut-off energy using a simple χ^2 fit, keeping the reference energy and cut-off strength fixed (at $E_0 = 10\,\mathrm{TeV}$ and $\beta = 1$, respectively).

Input model fits for all sources are shown in Fig. 2.6. The best-fit parameter values are summarised in Table 2.2. In all fits, we have adopted a distance to the source as listed in

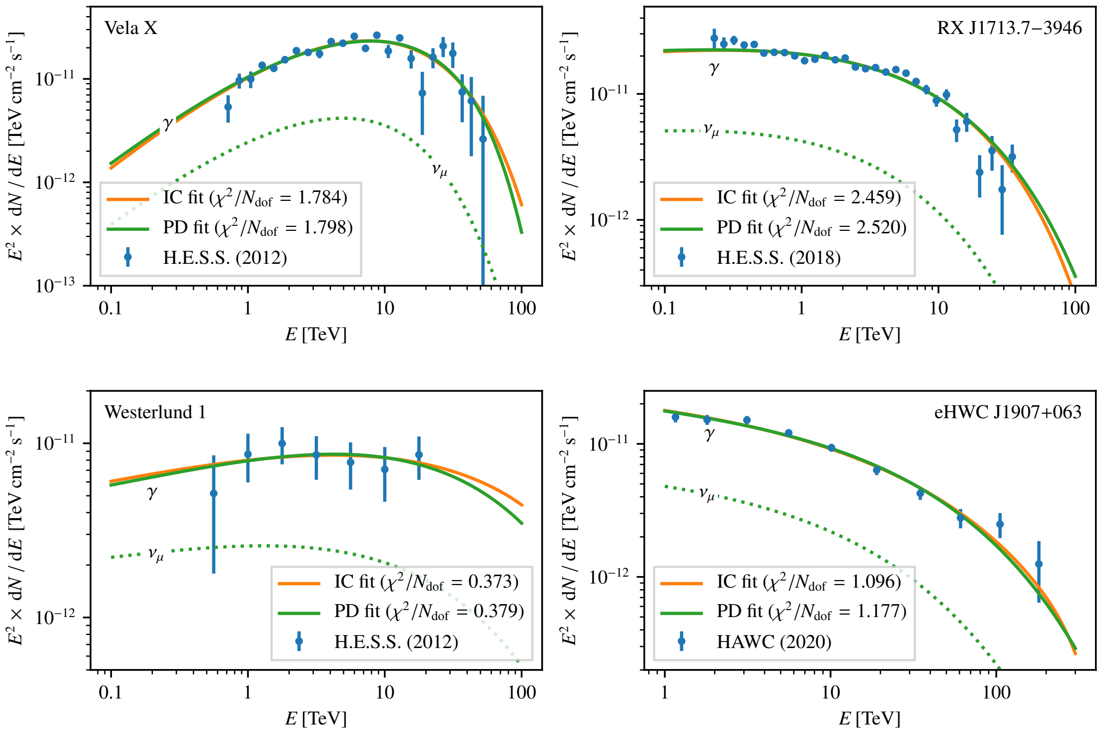

Figure 2.6: Summary of the γ-ray input models used for this study. The muon-neutrino prediction based on the best-fit PD model is shown as dashed line. (a) Fit of hadronic (PD) and leptonic (IC) input models for Vela X. The data points are taken from Abramowski et al., 2012b, and based on 53 h of H.E.S.S. observations.; (b) RX J1713.7−3946, flux points taken from Abdalla et al., 2018a; (c) Westerlund 1, flux points taken from Abramowski et al., 2012a; (d) eHWC J1907+063, flux points taken from Abeysekara et al., 2020. For every source, both a PD and an IC model are fitted to the flux points. The goodness-of-fit of the χ^2 fits is indicated in the legend. The prediction of the muon-neutrino flux based on the best-fit PD model is shown as a dotted line.

Table 2.1. For the PD model, we have assumed an ambient gas density of $1\,\mathrm{cm}^{-3}$. While this density is certainly not a valid assumption for all of the studied sources, this has no

[19]We are aware of more recent parametrisations such as that provided by Kafexhiu et al., 2014, which is also used in the `PionDecay` model implementation in NAIMA. That parametrisation, however, does not provide a prediction for the expected neutrino flux, required for our analysis. The focus of this study lying on the technical feasibility of a joint γ-ray/neutrino analysis, the choice of parametrisation for the hadronic model is not relevant here.

impact on the analysis results presented in Sect. 2.3.2, as the sum of the γ-ray emission predicted by the leptonic and hadronic models is always constrained to match the total observed flux. Different gas densities would thus only imply different normalisations of the primary particle spectra, but have no effect on the derived constraints on the hadronic fraction.

Table 2.2: Best-fit parameter values of input models.

Model	Parameter	Unit	Vela X [a]	RX J1713.7−3946	Westerlund 1	eHWC J1907+063
	A	$10^{35}\,\mathrm{eV}^{-1}$	$(4 \pm 45) \times 10^{-5}$	1.50 ± 0.07	6.2 ± 1.5	6.4 ± 0.5
PD	Γ	–	-4.9 ± 9.9	2.00 ± 0.08	1.92 ± 0.35	2.23 ± 0.09
	E_{cut}	TeV	14 ± 22	110 ± 30	890 ± 2340	540 ± 220
	A	$10^{33}\,\mathrm{eV}^{-1}$	0.0059 ± 0.0008	0.283 ± 0.013	1.17 ± 0.19	1.20 ± 0.10
IC	Γ	–	0.58 ± 0.40	2.74 ± 0.12	2.65 ± 0.49	3.15 ± 0.12
	E_{cut}	TeV	24 ± 6	49 ± 12	960 ± 11200	380 ± 290

See Eq. 2.1 for a definition of the parameter values.
[a] The value of Γ for the PD model for Vela X is extreme. Furthermore, the large uncertainties of all parameters of this model indicate a strong correlation between them. These results reflect that the γ-ray emission of Vela X is likely dominantly of leptonic origin, and the strongly curved spectrum can be fitted with the PD model with difficulty only.

Both models describe the γ-ray flux equally well, illustrating the difficulty to distinguish between the leptonic and hadronic scenarios based on γ-ray data alone. We note that the addition of lower-energy radio or X-ray data would further constrain the fit, but regard this as beyond the scope of this work.

2.2.4 Generation of pseudo data sets

With the IRFs and input models in hand, we generated 100 pseudo data sets for each source and each instrument, both for the PD and IC models. We note that for both instruments, we do not take into account diffuse astrophysical γ-ray or neutrino emission that is unrelated to the source itself. For the CTA data sets we used an analysis setup with 16 energy bins per decade between 0.1 TeV and 154 TeV and spatial bins of $0.02° \times 0.02°$ size. For each pseudo data set, we assumed a total observation time of 200 hours, split equally between four pointing positions with 1° offset with respect to the source position. The predicted number of source and background events are summed for each pixel and Poisson-distributed random counts are drawn based on those values. As an example, in Figs. 2.7 and 2.8, we show projections of one generated pseudo CTA data set based on the PD model for the source Vela X onto the spatial and energy axes, respectively.

A similar procedure has been used to generate the KM3NeT pseudo data sets, for which we assume a total detector operation time of 10 years. For each zenith angle bin (cf. Fig. 2.1), we generate an observation set evaluating the associated IRFs, according to the corresponding fraction of the total observation time. This results in 6 or 7 observation sets for each source, depending on the visibility. The exposure and expected background for every data set are computed in equatorial coordinates by integrating over time the respective IRFs (defined in terms of the local zenith angle). Data are binned using spatial pixels of $0.1° \times 0.1°$ size and 4 bins per decade in energy, between 100 GeV and 1 PeV. The IRFs are evaluated using a finer binning in energy, with 16 bins per decade between 100 GeV and 10 PeV. Several tests have been performed with finer zenith, energy, and spatial binning, yielding consistent results and no significant change in sensitivity. An example of a KM3NeT pseudo data set is visualised in Figs. 2.9 and 2.10, respectively.

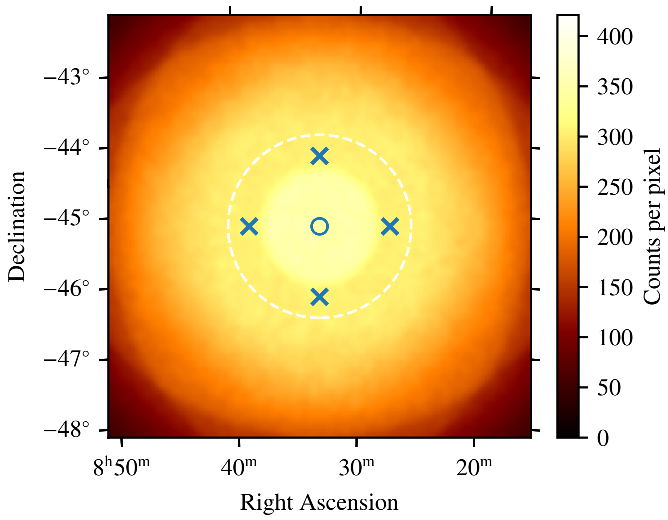

Figure 2.7: Counts map of a pseudo CTA data set based on the PD model for Vela X with 200 hours of observation time. The counts are Poisson-randomised based on the model prediction for Vela X (modelled as a disk with radius 0.8°) and the residual hadronic background, summed over all energies and smoothed with a 0.05° Gaussian. The blue circle and '×' markers denote the source and pointing positions, respectively. The white dashed circle shows the source region for which the counts spectra shown in Fig. 2.8 have been extracted.

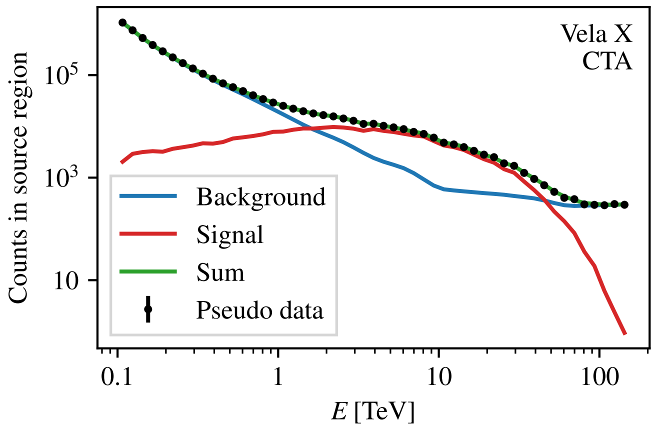

Figure 2.8: Counts spectra for the Vela X CTA PD data set, extracted for a region encompassing the source (cf. Fig. 2.7). The coloured lines denote the number of predicted counts within the source region for an observation time of 200 hours. The black data points visualise one random Poisson realisation, drawn from the model predictions.

2.2.5 Likelihood analysis

The analysis is performed using the binned likelihood formalism implemented in the GAMMAPY package[20] (see Sect. 1.6). Leptonic and hadronic models are fitted to the generated pseudo data sets[21] by minimising the 'Cash statistic' (Cash, 1979) of Eq. 1.17.

Several data sets can be simultaneously fitted by multiplying their respective likelihood values. Because the data sets are analysed with the same IRFs that were also used to create them, systematic uncertainties related to the generation of the IRFs are not taken into account here.

[20]We note that analyses carried out with the analysis tools normally employed by the KM3NeT Collaboration are typically performed using an unbinned likelihood formalism, which can enhance the sensitivity. An unbinned analysis is however not yet implemented in GAMMAPY.

[21]The IC model, predicting γ rays but no neutrinos, is of course fitted to the CTA data sets only.

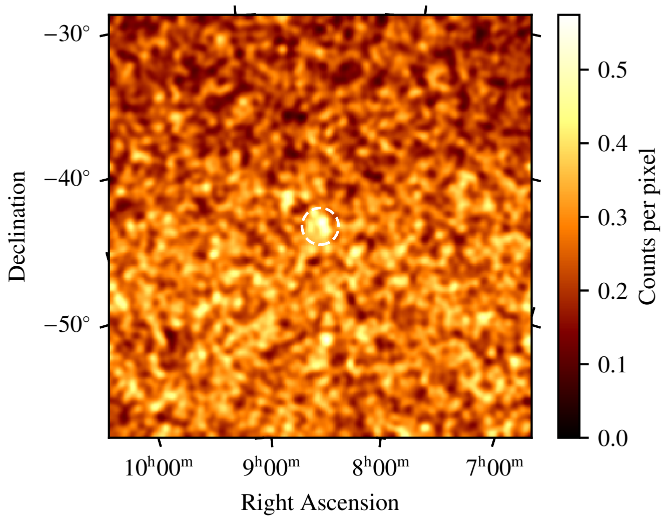

Figure 2.9: Counts map of a pseudo KM3NeT data set based on the PD model for Vela X with 10 years of observation time. The counts are Poisson-randomised based on the model prediction for Vela X, summed over all energies and smoothed with a 0.25° Gaussian. The white dashed circle shows the source region for which the counts spectra shown in Fig. 2.10 have been extracted (same region as in Fig. 2.7).

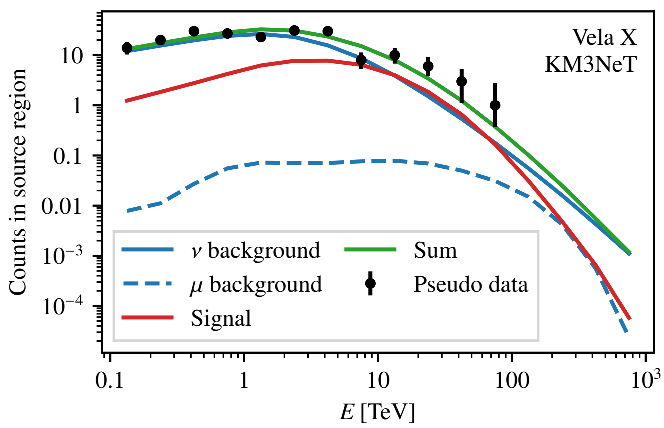

Figure 2.10: Counts spectra for the Vela X KM3NeT PD data set, extracted for a region encompassing the source (cf. Fig. 2.9). The coloured lines denote the number of predicted counts within the source region for an observation time of 10 years. The black data points visualise one random Poisson realisation, drawn from the model predictions.

As described in Sect. 1.6.2, confidence intervals for specific model parameters can be obtained by means of a profile likelihood scan. In the scan, the parameter of interest x is consecutively fixed to values x_{scan} around the optimum value $\hat{x}$, while the other model parameters are optimised in each step. A confidence interval can then be derived from the difference in 'test statistic' (TS),

$$\Delta\text{TS}(x_{\text{scan}}) = -2\ln\left(\frac{\mathcal{L}(x_{\text{scan}}, \xi)}{\mathcal{L}(\hat{\xi})}\right) , \tag{2.2}$$

where $\hat{\xi}$ are the parameter values for which $\mathcal{L}$ is maximal. As a result of the re-optimisation of the other parameters ξ the test statistic is effectively only a function of the parameter of interest.

2.2.6 Constraining the hadronic contribution

In this work, we derive credible intervals for the contribution of hadronic emission processes (i.e. the PD model) to the total γ-ray emission of the investigated sources. To this end, we simultaneously fit a PD model and an IC model to each of the pseudo data sets (i.e. the total γ-ray emission is given by the sum of the two models), which were generated with either the PD model or the IC model as input. The free parameters ξ of this composite model are the parameters ξ_{p} describing the proton population and the parameters ξ_{e} for the electron distribution (cf. Eq. 2.1). Our parameter of interest is then the 'hadronic fraction'

$$f(\xi) = \frac{I_{\mathrm{had}}(\xi_{\mathrm{p}})}{I_{\mathrm{had}}(\xi_{\mathrm{p}}) + I_{\mathrm{lep}}(\xi_{\mathrm{e}})}\,, \tag{2.3}$$

where I_{had} and I_{lep} denote the integrated γ-ray flux between 100 GeV and 100 TeV for the best-fit hadronic (PD) and leptonic (IC) model, respectively. Since the hadronic fraction is not a direct parameter of the model and we cannot simply fix it to certain values, we add a penalty term P to the Cash statistic,

$$\mathcal{C}_{\mathrm{tot}} = \mathcal{C}(\xi) + P(\xi, f_{\mathrm{scan}})\,, \tag{2.4}$$

where

$$P(\xi, f_{\mathrm{scan}}) = A_p \cdot (f(\xi) - f_{\mathrm{scan}})^2/\Delta f^2 \tag{2.5}$$

and f_{scan} is the value of f that we want to probe. This penalty term allows us to fully re-optimise the model (i.e. all its direct parameters ξ) while maintaining a hadronic fraction close to $f_{\mathrm{scan}} \pm \Delta f$. It is thus mostly a technical tool that enables us to carry out profile likelihood scans for f. We scan 21 values equally spaced between 0 and 1.[22] Values of $A_p = 0.1$ and $\Delta f = 0.01$ were empirically found to lead to a strong-enough constraint – that is, to ensure that the allowed variation in f is small compared to the spacing of the scan values – while yielding stable results. In the following, we denote with $\hat{\hat{\xi}}_{\mathrm{scan}}$ the best-fit parameter values for a given f_{scan}, and with $\hat{\xi}$ the parameter values corresponding to the overall best fit (i.e. without a penalty term that constrains f).

In the limit of sufficient statistics and for parameter values far enough from parameter boundaries, Wilk's theorem (Wilks, 1938) states that ΔTS follows a χ^2 distribution and can therefore directly be used to deduce confidence intervals (Workman et al., 2022). However, as the parameter f is bounded between 0 and 1, we cannot invoke Wilk's theorem here. An alternative method would be to derive the expected distribution of ΔTS by generating and fitting a large number ($\gg$100) of pseudo data sets. Unfortunately, the profile likelihood scan with full re-optimisation of all model parameters is rather computing-intensive, implying that this approach is also not feasible here. We therefore adopt a Bayesian approach, in which we infer a posterior probability density function (PDF) $\Phi(f)$ from the likelihood ratio $\mathcal{L}(\hat{\hat{\xi}}_{\mathrm{scan}})/\mathcal{L}(\hat{\xi})$. By definition (cf. Eq. 2.2),

$$\frac{\mathcal{L}(\hat{\hat{\xi}}_{\mathrm{scan}})}{\mathcal{L}(\hat{\xi})} = \frac{\mathcal{L}(f_{\mathrm{scan}}, \xi)}{\mathcal{L}(\hat{\xi})} = \exp\left(-\frac{1}{2}\Delta\mathrm{TS}(f_{\mathrm{scan}})\right)\,, \tag{2.6}$$

which we use to derive the PDF as

$$\Phi(f) = c \cdot \exp\left(-\frac{1}{2}\Delta\mathrm{TS}(f)\right)\,, \tag{2.7}$$

[22] We note that the contribution of the penalty term is not included in the further evaluation of the likelihood. Furthermore, in order to take into account the small possible variations of f around f_{scan}, the exact hadronic fractions resulting from the optimised model are used in the subsequent analysis.

where $f \equiv f(\hat{\xi}_{\mathrm{scan}})$ and c is a normalisation constant that can be determined by requiring $\int_0^1 \Phi(f)\,\mathrm{d}f = 1$. To obtain a smooth curve, we fit the ΔTS values obtained from the profile likelihood scan with a cubic spline function. A central Bayesian credible interval for f can then be derived by integrating the PDF around the best-fit value up to a certain probability (e.g. 68% or 90%) – this is also known as the construction of a highest posterior density interval (Berger, 1980). We assume a flat prior distribution for f in this procedure. In Fig. 2.11, we show an example of the PDF $\Phi(f)$ constructed from the likelihood scan (defined in Eq. 2.7) for an individual pseudo experiment in the hadronic scenario of Vela X. The pseudo experiment is hand-picked to show one of the few cases where the upper limit f_{max}^{90} does not coincide with 1.0. We construct the limits such that all likelihood values included in the shaded interval are larger than those outside. For this reason, the intersections of the limits with the PDF are at the same height y^{90}, which results in the smallest 90% credible interval possible.

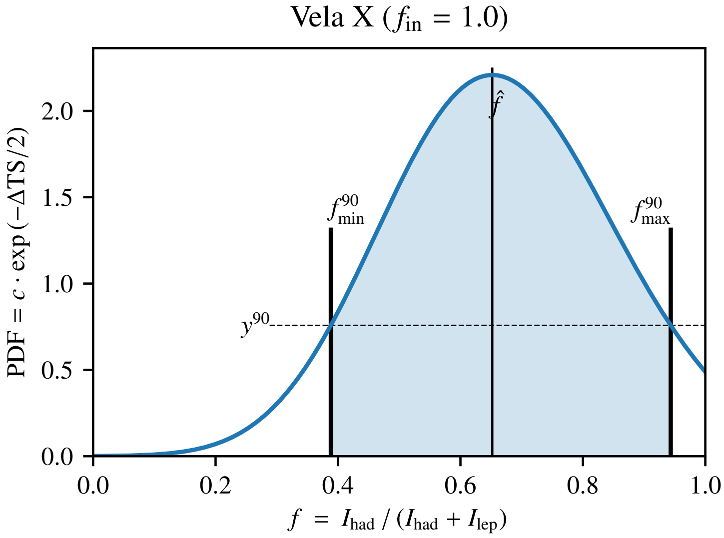

Figure 2.11: PDF for the hadronic fraction f for a single pseudo experiment, constructed from the corresponding likelihood scan. The vertical line at the peak of the PDF marks the best-fit value $\hat{f}$, while the lines at f_{min}^{90} and f_{max}^{90} show the lower and upper bound of the 90% credible interval, respectively. The shaded area between the bounds contains 90% of the total area between 0 and 1. The horizontal dashed line at y^{90} shows that the intersections of the PDF with the bounds occur at the same height.

2.3 Results

In this section, we will introduce the different analysis scenarios we have considered (Sect. 2.3.1), present the results (Sect. 2.3.2) and discuss their implications (Sect. 2.3.3).

2.3.1 Analysis scenarios

For every source, input model (leptonic or hadronic), and pseudo data set, we begin by fitting the PD and IC model to only the CTA data sets. Here we obtain the optimal parameters ξ_{p} and ξ_{e} for each model, which serve as starting parameters for the following, more complicated, composite model. In total we perform the analysis in three different scenarios, each with the goal of recovering the hadronic fraction and its uncertainty (cf. Sect. 2.2.6). The first scenario is a "CTA only" analysis, in which we analyse only the γ-ray data provided by CTA and ignore the KM3NeT neutrino data. This scenario is intended to illustrate to which degree CTA alone can differentiate between the two models, based on the γ-ray energy spectrum. As mentioned before, we perform a profile likelihood scan of the hadronic fraction by re-optimising the composite model (the sum of PD and IC model) at different ratios of hadronic to leptonic γ-ray flux prediction. Second, we perform a "KM3NeT only" analysis, where we include only the neutrino data provided by KM3NeT. However, as the primary CR energy spectrum can presently not be measured well with neutrinos alone, we constrain the parameters of the PD model to be consistent with those derived in the fit of the pure PD model to the CTA data sets, using the same concept of penalty terms as for the hadronic fraction f (cf. the previous section). Specifically, for each free parameter p of the PD model, we add a term $(p - \hat{p})^2/\Delta\hat{p}^2$, where $\hat{p}$ and $\Delta\hat{p}$ are the best-fit parameter value and its uncertainty, respectively. Thus, the second scenario shows how well the leptonic and hadronic scenario can be distinguished with KM3NeT data if the primary CR energy spectrum is known to a certain degree. As the IC model is irrelevant for the neutrino flux, the hadronic fraction now corresponds to the ratio of γ-ray flux expected from the fitted proton distribution to the total γ-ray flux measured with CTA. Finally, in a third scenario we combine the γ-ray and neutrino data and perform a joint analysis of the CTA and KM3NeT data sets. As the primary CR energy spectra are now directly constrained by the CTA data, the prior terms added for the second scenario are removed again. This scenario demonstrates the benefits of the combined analysis. We note that, if the best-fit models obtained in the three scenarios are similar, a combination of the profile likelihood scans performed in the first two scenarios will lead to the same constraints on the hadronic fraction as the combined analysis in the third scenario. While this is often the case for the relatively simple models employed here, the situation can be different for more complex models, for which the combined analysis may be able to break degeneracies between model parameters.

2.3.2 Analysis results

As an example, we show in Fig. 2.12 average profile likelihood scans of the hadronic fraction f for Vela X, where the hadronic PD model has been used as input when generating the pseudo data sets. Corresponding plots for the other sources and for a purely leptonic (IC) input model can be found in Appendix A. By definition, $\Delta\mathrm{TS} = 0$ at the minimum of the curves, which (as expected) occurs at the value of f that corresponds to the input model (i.e. $f_{\mathrm{in}} = 0$ for a purely leptonic input model and $f_{\mathrm{in}} = 1$ for a purely hadronic input model). Moving away from the minimum, larger values of $\Delta\mathrm{TS}$ imply a stronger rejection of the corresponding hadronic fraction f.

In Fig. 2.13, we display the 68% and 90% quantile intervals of the distribution of best-fit values of the hadronic fraction f for all 100 pseudo data sets. Furthermore, as described in Sect. 2.2.6, we obtain credible intervals for f from the profile likelihood scans. The average expected 68% credible intervals are indicated by the black bars. We note that, for individual pseudo data sets, it is possible that the 68% credible interval does not contain the true input value of f. Hence, this is also the case for the averaged interval: this is an artefact caused by the fact that the input values lie at the boundaries of the allowed values for f.

2.3.3 Discussion

It is evident that in essentially all cases, the "CTA only" and "KM3NeT only" scenarios yield results that correspond exactly to the contributions of the two instruments in the combined analysis. That is, in Fig. 2.12, and the rest of the scans shown in Appendix A, the red and blue crosses fall on top of the red and blue dashed lines, respectively. This means that consistent source models are fitted in all three scenarios and implies that, in principle, a sensitivity identical to that of the combined analysis can be achieved by

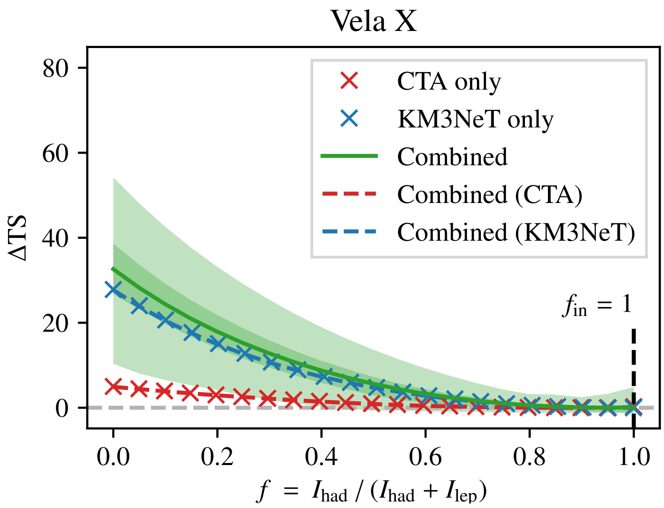

Figure 2.12: Profile likelihood scan results for Vela X and a hadronic input model ($f_{\text{in}} = 1$). The displayed curves show the average of the curves obtained for the 100 generated pseudo data sets. The red and blue '×' markers correspond to the analysis scenarios "CTA only" and "KM3NeT only", respectively. The green line shows the result for the combined analysis, together with 68% and 95% quantile intervals to indicate the statistical spread. The dashed red and blue lines show the respective contributions of the CTA and KM3NeT data sets to the combined result.

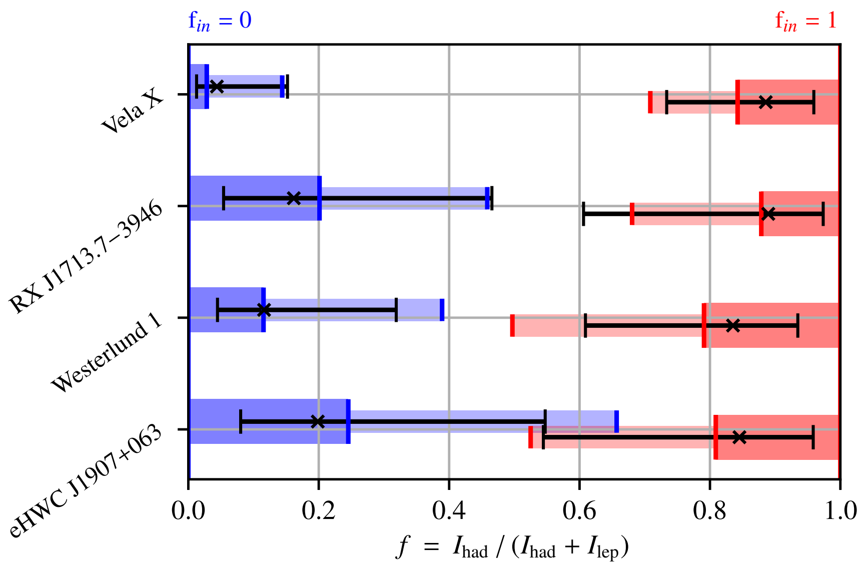

Figure 2.13: Summary of results for all sources and input models. The blue and red horizontal bars show the 68% and 90% quantile intervals of the distribution of best-fit values for the leptonic ($f_{\text{in}} = 0$) and hadronic ($f_{\text{in}} = 1$) input models, respectively. The black bars indicate the average position and sizes of the 68% credible intervals derived for each input model.

combining the results of the profile likelihood scans of the single-instrument analyses. We note, however, that this only holds because we use the same source models in all analysis scenarios, and because we incorporate the CTA constraints on the primary CR spectrum in the "KM3NeT only" analysis. In practice, ensuring this consistency between two separate analyses may not always be possible – in particular when more sophisticated source models are considered, which could, for example, feature different spatial models for the leptonic and hadronic cases. The combined analysis, on the other hand, naturally ensures that the γ-ray and neutrino data are described with the same physical models. Furthermore, a combined analysis enables a consistent incorporation of systematic uncertainties: for example, it would be possible to add to the analysis a nuisance parameter that modifies the relative energy scale between the two instruments – something that would be much more difficult to take into account when combining the results of two single-instrument analyses.

Investigating the profile likelihood scans for the different sources, we note that the curves obtained from the KM3NeT data sets are usually very similar for the leptonic and hadronic input model, except being flipped horizontally, and often yield stronger constraints on the hadronic fraction f compared to the CTA curves. This is not unexpected, as the predicted neutrino fluxes differ fundamentally between the leptonic model (no neutrinos) and the hadronic model (neutrino flux approximately equal to γ-ray flux), whereas the predicted γ-ray fluxes can look very similar (cf. Fig. 2.6). This is especially true here, as we use the same spatial models for the leptonic and hadronic scenario, implying that for CTA any separation power between the models originates from differences in the predicted γ-ray spectra. For more realistic models that also differ in their morphology, the CTA data will lead to better constraints than achieved here – the presented curves should therefore not be regarded as a generally valid estimate of the CTA sensitivity to differentiate between leptonic and hadronic models. The KM3NeT results, on the other hand, are more representative of the true expected sensitivity of the instrument. Here, the achieved constraints on f mostly depend on the hardness of the fitted input spectra, that is, the predicted γ-ray flux at the highest energies ($> 10\,\mathrm{TeV}$). The large statistical spread in the achieved constraints (indicated by the green bands in Fig. 2.12 and by the blue and red bars in Fig. 2.13) is caused by the small number of neutrinos that is expected to be detectable with KM3NeT, even for the most promising sources.

In the following, we briefly discuss the results obtained for the individual studied sources. A more general assessment of the sensitivity of KM3NeT to the sources studied in this work, except for Westerlund 1, can be found in Aiello et al., 2019.

Vela X — For Vela X we found the strongest discrimination potential for all sources investigated in this study. This is largely due to its full visibility for KM3NeT and its large γ-ray flux in the 10–100 TeV range. The large ΔTS values obtained with the CTA data sets for the leptonic input model are a result of the strongly curved measured γ-ray spectrum, which is easier to reproduce with an IC model. While it appears clear that a purely hadronic origin of the γ-ray emission is already excluded by studies in the γ-ray domain (e.g. Abramowski et al., 2012b; Tibaldo et al., 2018), our results indicate that, in the case of a purely leptonic origin, a combined analysis of γ-ray and neutrino data may help in ruling out a potential small contribution to the γ-ray flux from hadronic processes. Specifically, the obtained average 68% credible interval constrains the hadronic fraction f to below 15%.

RX J1713.7−3946 — Compared to Vela X, the spectrum of RX J1713.7−3946 exhibits less curvature, which reflects in the flat ΔTS curves obtained with CTA for this source. As the expected neutrino flux is slightly lower than for Vela X, the resulting constraints on the hadronic fraction f are weaker and the statistical spread is larger. Nevertheless, as the physical processes responsible for the γ-ray emission from RX J1713.7−3946 are not yet totally clear, the addition of neutrino data from KM3NeT may yield important new constraints.

Westerlund 1 — Compared to the other sources studied in this work, the stellar cluster Westerlund 1 has a relatively hard energy spectrum without a strong cut-off, which leads – in a hadronic scenario – to an expected flux of neutrinos that is detectable with KM3NeT. Therefore, despite Westerlund 1 being a significantly extended source (which implies a larger background contamination), a combined analysis can, on average, distinguish between the leptonic and hadronic models investigated here. However, as the statistical spread is very large, the limits obtained from the different pseudo data sets differ strongly.

eHWC J1907+063 — In contrast to the other sources, eHWC J1907+063 is modelled using a Gaussian spatial model and has the largest 68% flux containment radius. Because it is furthermore visible for only 54% of the time for KM3NeT, the constraints obtained for this source are the weakest in this study. This is reflected in the overlapping 90% quantile intervals of the fitted hadronic fractions f for the leptonic and hadronic input models (see Fig. 2.13). For the case of a hadronic input model, the CTA data sets yield some separation power as the IC model, being intrinsically curved, cannot reproduce well the measured spectrum which shows only a small curvature. Nevertheless, we conclude that even with 200 h of CTA data and 10 yr of KM3NeT data, a differentiation between a leptonic and a hadronic scenario is challenging.

2.4 Conclusion

In this work, we explore the prospects of a combined analysis of γ-ray and neutrino measurements with the upcoming CTA and KM3NeT facilities. To this end, we demonstrate the capability of the open-source γ-ray analysis package GAMMAPY to also analyse data from neutrino telescopes such as KM3NeT, even though these observe the sky in a conceptually different way compared to γ-ray telescope arrays such as CTA.[23] For the combined analysis, we use publicly available IRFs for CTA and generate custom IRFs for KM3NeT. We fit measured γ-ray spectra of four prototypical Galactic γ-ray sources to obtain both a leptonic model and a hadronic model. Using either of these models as well as the IRFs as input, we calculate the expected γ-ray and neutrino flux and generate pseudo data sets for both CTA and KM3NeT for all sources. Using a binned likelihood analysis approach, we derive from these pseudo data sets average expected constraints on the contribution of hadronic emission processes to the total emission.

We find that our combined analysis approach enables a consistent modelling of the γ-ray and neutrino observations. Due to simplifying assumptions (e.g. fixed spatial models), the sensitivity to constrain the physical mechanism responsible for the γ-ray emission is often dominated by the KM3NeT data; we note that this will not generally be the case when employing more sophisticated models. For sources that emit a sufficiently large flux of γ rays at high energies ($> 10\,\mathrm{TeV}$), our results indicate that a combined analysis of 200 h of CTA and 10 yr of KM3NeT data will be able to differentiate between a leptonic and a hadronic emission scenario.

This work constitutes the first demonstration of a general framework for jointly analysing event-level data from γ-ray and neutrino telescopes in a likelihood formalism. Here, we have applied it to simulated data from the CTA and KM3NeT observatories, for a selection of Galactic γ-ray sources, with the aim of deriving expected constraints on the contribution of hadronic emission processes. This approach may be complemented with others, for example the analysis of multi-wavelength data (e.g. in the radio or X-ray domain). On the other hand, the combination of γ-ray and neutrino data can be applied to many more questions. For example, there is increasing evidence that active galactic nuclei – a prominent extragalactic γ-ray source class – are also neutrino sources, see for example Aartsen et al., 2018; Abbasi et al., 2022a. In this regard, it is worth noting that the data recorded with both the CTA and KM3NeT observatories will be made publicly available – opening a bright future for multi-messenger analyses.

We release along with this paper a software repository that provides the necessary code, in the form of JUPYTER notebooks, to reproduce the presented results and figures (Unbehaun et al., 2023), following URL: `https://zenodo.org/record/8298464`.

[23]We note that, since the initiation of this work, several improvements to both the GAMMAPY package and the 'GADF' data format specifications have further eased the analysis of data from wide-field instruments, which besides neutrino telescopes also include γ-ray observatories that employ particle sampling detectors, like the HAWC experiment (Abeysekara et al., 2017; Albert et al., 2022).

The first to speak in court sounds right – until the cross-examination begins.

— King Solomon, Proverbs 18:17

3 Unbinned Analysis

As discussed in Sect. 1.6.2, given an observation, the likelihood value resulting from a particular model can be computed by comparing the measured counts to the model predictions using the Poisson distribution. However, this approach requires the data to be binned, inherently leading to a loss of information. The extent of this information loss depends on the bin size relative to the instrument's resolution and the actual variation of the model within each bin.

If the model exhibits a strong energy dependence, the observed energy dependence in the data will be constrained by the instrument's energy resolution. Even under the optimistic scenario of an energy resolution of $\Delta E/E \approx 5\%$ for CTAO[24], this would necessitate 48 bins per energy decade, resulting in a total of 144 energy bins over the range 0.1–100 TeV. For most source spectra, 12 energy bins per decade are usually sufficient to maintain sensitivity, which is manageable in a binned analysis.

The situation becomes more challenging when considering spatial resolution. The CTAO will achieve an angular resolution of approximately $0.02°$ at the highest energies. For a field of view (FoV) of $5°\times5°$, this corresponds to $250 \times 250 = 62,500$ spatial bins. In the increasingly popular 3D analyses (two spatial dimensions plus one energy dimension), the total number of bins is further multiplied by the number of energy bins. For scenarios with large event numbers, comparable to the total number of bins, a binned analysis is computationally favorable because the required integrations and convolutions can be performed on regular data grids. However, the situation changes in cases of low event numbers, where high resolution is needed — for example, at high energies or when including the time dimension. Given that the time resolution of instruments is typically below 1 μs, the required time resolution of the analysis depends on the variability timescale of the source. This can range from milliseconds for pulsars, to seconds or minutes for gamma-ray bursts, and up to days or years for AGNs. In particular, pulsar analyses often require an unbinned treatment of the time dimension, as the number of time bins required for such high resolution is impractical.

Currently, Gammapy (versions 1.3 and below) does not support unbinned analyses. In the following sections, the formulation of the unbinned likelihood will be derived and strategies discussed for efficient implementation within the Gammapy framework.

3.1 Derivation of the unbinned likelihood

The formulation of the unbinned likelihood can be derived from two different perspectives. First, we can start from the expression for the binned likelihood (cf. Eq. 1.16) and consider the limit of infinitesimally small bins, where the number of counts in each bin can only be 1 or 0:

$$\mathcal{L} = \lim_{N\to\infty} \prod_{i=1}^{N} \frac{\nu_i^{n_i}(\xi)}{n_i!} \cdot e^{-\nu_i(\xi)} = \begin{cases} \prod_{i=1}^{N} e^{-\nu_i(\xi)} & \text{, if } n_i = 0, \\ \prod_{i=1}^{N} \nu_i(\xi) \cdot e^{-\nu_i(\xi)} & \text{, if } n_i = 1, \end{cases} \tag{3.1}$$

[24] `https://www.cta-observatory.org/science/ctao-performance/`

where ν_i and n_i represent the predicted and measured counts in each bin i, respectively, and ξ denotes the set of model parameters. By taking the logarithm of this expression, we obtain two sums: one over $-\nu_i(\xi)$ for all bins, since the term $e^{-\nu_i(\xi)}$ appears in both cases, and another over $\ln(\nu_i(\xi))$, which only applies to bins containing one event. In the limit of infinitesimally small bins, the first sum simplifies to the integral of all predicted counts, N_{pred}. The second sum is no longer over all bins but rather over all events, summing the differential predicted counts at the coordinates of the events, ν_c. Therefore, the log-likelihood expression becomes:

$$\ln(\mathcal{L}) = \sum_{c=1}^{N_{\text{tot}}} \ln(\nu_c(\xi)) - N_{\text{pred}}, \tag{3.2}$$

with N_{tot} the total number of measured events.

An alternative way to reach the same expression is to start with the general form of the likelihood and multiply it by a Poisson term that accounts for the probability of measuring N_{tot} events when N_{pred} events are predicted:

$$\mathcal{L} = \frac{N_{\text{pred}}(\xi)^{N_{\text{tot}}}}{N_{\text{tot}}!} \cdot e^{-N_{\text{pred}}(\xi)} \cdot \prod_{i=1} f(x_i, \xi)\, dx_i, \tag{3.3}$$

where $f(x_i, \xi)$ is a normalized PDF that gives the probability that the observable x_i falls within the interval $[x_i, x_i + dx_i]$. For a counting experiment, this corresponds to the number of predicted counts in that interval divided by the total number of predicted counts. Using the same notation as above, we can write:

$$\mathcal{L} = \frac{N_{\text{pred}}(\xi)^{N_{\text{tot}}}}{N_{\text{tot}}!} \cdot e^{-N_{\text{pred}}(\xi)} \cdot \prod_{c=1}^{N_{\text{tot}}} \frac{\nu_c(\xi)}{N_{\text{pred}}}. \tag{3.4}$$

The term $N_{\text{pred}}(\xi)^{N_{\text{tot}}}$ from the Poisson probability cancels with the normalization term in the PDF when it is factored out of the product. We can also disregard the constant normalization term $N_{\text{tot}}!$, as it only results in a constant offset in the log-likelihood, which is typically omitted in Poisson likelihoods. Taking the logarithm of the remaining terms, we arrive at the same expression as in Eq. 3.2.

To maximize the log-likelihood, the model must maximize the predicted counts at each coordinate where events are observed, while minimizing the total number of predicted counts. For the computation of the unbinned statistic $C = -2 \cdot \ln(\mathcal{L})$, we must access the model's predictions at the coordinates of the events, which correspond to specific subsets of the reconstructed energy, position, and time. Additionally, the total number of predicted counts, integrated over the entire region of interest (RoI), is required. Both of these quantities could be extracted from the binned predicted counts cube; ν_c by interpolating at the events' coordinates and N_{pred} by summing over all bins. This illustrates that in cases with fine bins, where the predicted counts cube varies only slightly between neighboring bins, interpolation has a negligible effect, providing no sensitivity gain. However, this approach would never offer any computational advantage, as the binned analysis has to be computed prior to the unbinned likelihood. In the following sections, I will outline possible methods for performing these computations independently from the binned analysis and discuss their advantages and disadvantages.

3.1.1 Computation of the differential predicted counts

When the FoV model consists of multiple components j (such as background and source models), all components must be summed for each event's coordinate before taking the logarithm:

$$\nu_c = \sum_j \nu_c^j \tag{3.5}$$

In the context of GAMMAPY, there are different types of `SkyModels`, each requiring individual handling.

For example, the `TemplateNPredModel` and `FoVBackgroundModel` contain the number of predicted counts in a geometry defined by reconstructed coordinates. For binned likelihood analyses, this geometry must match the binning of the observed events to allow for a direct bin-to-bin comparison. In unbinned analyses, the geometry can, in principle, be chosen arbitrarily, but it should be fine enough that a linear interpolation between bins yields accurate results. To obtain differential predicted counts for these models, one has to perform a linear interpolation of the template at the event's coordinates and divide the result by the bin volume (solid angle Ω times the energy interval ΔE). GAMMAPY already provides functionality for this, which can be directly applied here. Compared to the binned analysis, an additional interpolation step is required, which may reduce performance. However, since the interpolated values can be cached, this step only needs to be executed once – unless model parameters change. This applies to all parameters except the normalization, which can be directly adjusted in the cached values without reinterpolation. In general, template models are primarily employed to represent background contributions with known spectral properties, making free parameters beyond a normalization uncommon. As a result, the computational cost of interpolation remains minimal in typical use cases. On the other hand, when linear interpolation provides greater accuracy than nearest-neighbor interpolation, the resulting improvement in precision can be considered an advantage of this method.

A more common model type is one where the model returns the flux prediction $\phi'(E', r')$ in true coordinates based on an analytical or numerical formula (cf. Sect. 1.6.1). To compare this to the measured events, one must forward-fold the true flux prediction and compute the corresponding prediction in reconstructed coordinates, as observed by the telescope. GAMMAPY already provides this functionality for binned analyses through the `MapEvaluator`, where the model is first integrated over a true geometry, multiplied by the exposure cube, convolved with the PSF kernel, and then matrix-multiplied with the EDisp matrix along the energy dimension. The result is a cube of predicted counts, which could be treated like the `TemplateNPredModel` and interpolated at the event's coordinates.

As mentioned before, despite the simplicity of this implementation, there are several disadvantages. First, there can be no computational advantage compared to the binned analysis, since most steps from the binned analysis are required, including computing the predicted counts for each pixel, followed by interpolation. Second, the result still depends on the reconstructed geometry used for interpolation. While this is also the case for binned analyses, it can, in principle, be circumvented by performing numerical integration for each event individually. Furthermore, some information, and thus sensitivity, may be lost due to the binning step, even with subsequent interpolation. For these reasons, computing the differential predicted counts at each event coordinate individually seems preferable here.

The calculation of $\nu_c \equiv \nu(E_i, r_i) \equiv dN_{\mathrm{pred}}/d\Omega/dE$ for event i is given as

$$\nu(E_i, r_i) = \int dE' \int dr' D(E_i|E', r') \times P(r_i|E', r') \times A(E', r') \times \phi'(E', r'), \tag{3.6}$$

where quantities with a prime denote true quantities, as opposed to reconstructed quantities (without the prime). Here, $D(E_i|E', r')$ represents the probability (the EDisp term) that an event from the direction r' and energy E' is reconstructed at the measured energy E_i.

Similarly, $P(r_i|E', r')$ models the angular resolution of the telescope, representing the probability that an event from direction r' and energy E' is reconstructed at the sky position r_i. $A(E', r')$ is the exposure, computed as effective area multiplied by the observation time. Since none of the factors in the integral needs to be analytic, the integral is computed numerically. In PYTHON, a for-loop over events is inefficient, so `numpy` arrays are used, with an underlying fixed geometry tailored to the model. The integration over dr' can be restricted to the region where the PSF term contributes non-zero values. This allows the integration geometry to focus on the model's vicinity, limited to the PSF's 99.9% containment radius, typically defined by the resolution at low energies. At higher energies, where the PSF is usually narrower, the outer regions of the integration grid will not contribute. However, finer binning is required to accurately resolve the spatial model. To enhance the precision of PSF factors, the integration grid is oversampled, similar to the approach used in computing the binned PSF kernel.

An irregular geometry, tailored even better to the changing containment radius, is currently not supported by GAMMAPY and would require loops over events and energy bins. Therefore, one is limited to a regular three-dimensional integration geometry with k energy bins, and l and b longitude and latitude bins, respectively.

The EDisp and PSF terms are evaluated on that geometry for each event, resulting in a four-dimensional IRF-cube ($i \times k \times l \times b$), which is later used for integration. This is a computationally intensive step, but since these terms are independent of the model and its parameters, it needs to be executed only once and can be cached for future use. Similarly, the exposure needs to be evaluated on the integration grid only once. The computation of the differential predicted counts is then the product of the individual cubes, summed over the energy, longitude, and latitude axes:

$$\nu(E_i, r_i) = \sum_k \Delta E'_k \sum_{l,b} \Delta r'_{l,b} D(E_i|E'_k, r'_{l,b}) \times P(r_i|E'_k, r'_{l,b}) \times A(E'_k, r'_{l,b}) \times \phi'(E'_k, r'_{l,b}) \quad (3.7)$$

In Fig. 3.1, this procedure is illustrated by plotting the IRF-cubes of individual events ($C_{\text{irf},i} = D(E_i|E'_k, r'_{l,b}) \times P(r_i|E'_k, r'_{l,b})$) on the same map alongside the true source model. Each event's contribution is centered at its reconstructed position, with the size reflecting

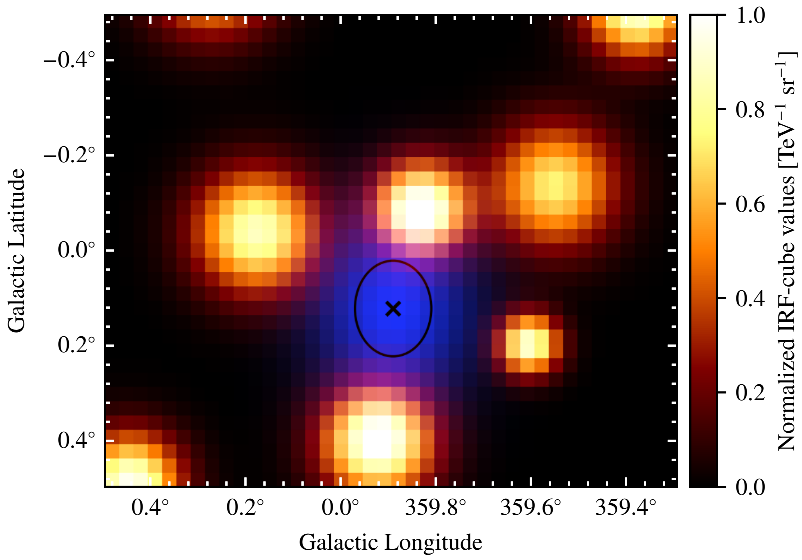

Figure 3.1: Illustration of the energy-integrated IRF-cube values for individual events at different locations and energies. An eccentric Gaussian source model ($\sigma = 0.1°$) is shown in blue colors, overlapping with the IRF-cubes, and thus contributing to their differential predicted counts.

its positional uncertainty. As the maps include contributions from all energy bins, smaller "circles" correspond to higher-energy events, where the PSF is narrower in the contributing true energy bins. The degree of overlap between each event's response and the true model prediction (shown in blue in Fig. 3.1) is proportional to the differential predicted counts for that event (cf. Eq. 3.7). The energy profile for three representative events is illustrated by the red lines in Fig. 3.2.

The main issue with this method is that the cached cubes can become very large as the number of events increases, potentially leading to memory overflow. An alternative could be to use a tighter, or even adaptive, integration grid with NUMBA[25]-accelerated loops through the events and bins. A more memory-efficient approach would be to compute the values on-the-fly for each event, which would also require NUMBA-accelerated loops and improved interpolation functionality. If the cube-based calculations are retained, one could read and write parts of the cube that correspond to subsets of events to and from disk, processing them in smaller chunks.

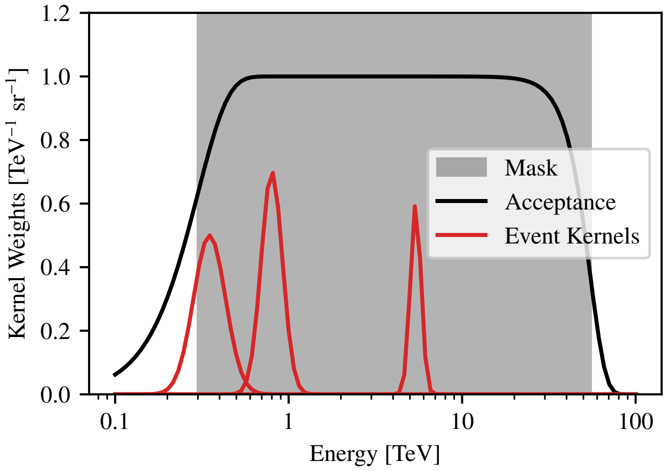

Figure 3.2: Illustration of the IRF and acceptance cubes along the true energy axis. The acceptance cube is averaged over the spatial dimensions, while the event kernels are summed. The values of the acceptance cube are unitless. An exemplary analysis mask is shown as shaded region, where only reconstructed event energies between 0.3 TeV and 55 TeV are included in the analysis.

3.1.2 Computation of the total number of predicted counts

We are still missing the term in Eq. 3.2 representing the total number of predicted counts. In the approach of the binned analysis with interpolation, one could sum the counts over all pixels of the predicted counts cube. This is particularly useful in the common scenario where the user defines a mask to exclude parts of the RoI and the energy range in which the data cannot be trusted. In this approach, the mask can be directly applied to the cube. However, as previously discussed, using a predicted counts cube for the calculations removes any computational advantage. It also introduces dependencies on the choice of reconstructed geometry and can result in potential sensitivity loss.

Therefore, instead of a predicted counts cube, a so-called "acceptance" cube is computed and cached, which can then be multiplied by the model integrated on the true integration geometry. This acceptance cube $Acc(E', r')$ contains the fraction of true predicted counts (i.e., without applying EDisp or PSF, but with exposure considered) that are reconstructed inside the mask, which is defined in reconstructed coordinates. After multiplication with

[25]NUMBA translates PYTHON functions to optimized machine code at runtime (`https://numba.pydata.org/`, Lam et al., 2015).

the true predicted counts, summing over all pixels provides N_{pred}, the total number of predicted counts within the mask. Originally, the computation of N_{pred} would involve integrating $\phi(E,r) \cdot M(E,r)$ over the entire RoI. However, if the entire term is considered, one realizes that the order of the true and reconstructed integrals can be exchanged and the terms rearranged:

$$
\begin{aligned}
&N_{\text{pred}} = \\
&\int dE \int dr \left[\int dE' \int dr' D(E|E',r') \times P(r|E',r') \times A(E',r') \times \phi'(E',r') \right] \cdot M(E,r) = \\
&\int dE' \int dr' \underbrace{\left[\int dE \int dr D(E|E',r') \times P(r|E',r') \times M(E,r) \right]}_{Acc(E',r')} \cdot A(E',r') \times \phi'(E',r') =
\end{aligned}
\tag{3.8}
$$

The calculation of the acceptance cube can be interpreted as the forward-folding of the mask, where the roles of true and reconstructed coordinates are inverted.

This procedure is again illustrated in Figs. 3.2 and 3.3. Figure 3.2 presents the energy profile of the acceptance cube, defined in true energy, alongside the analysis mask, which is defined in reconstructed energy. Well within the analysis energy range, the acceptance cube equals one, meaning these true energy bins fully contribute to the total model counts. Near the mask edges, the acceptance profile decreases, as not all events predicted with these energies are reconstructed within the analysis range. The accuracy of the acceptance profile's alignment with the analysis mask is determined by the energy resolution.

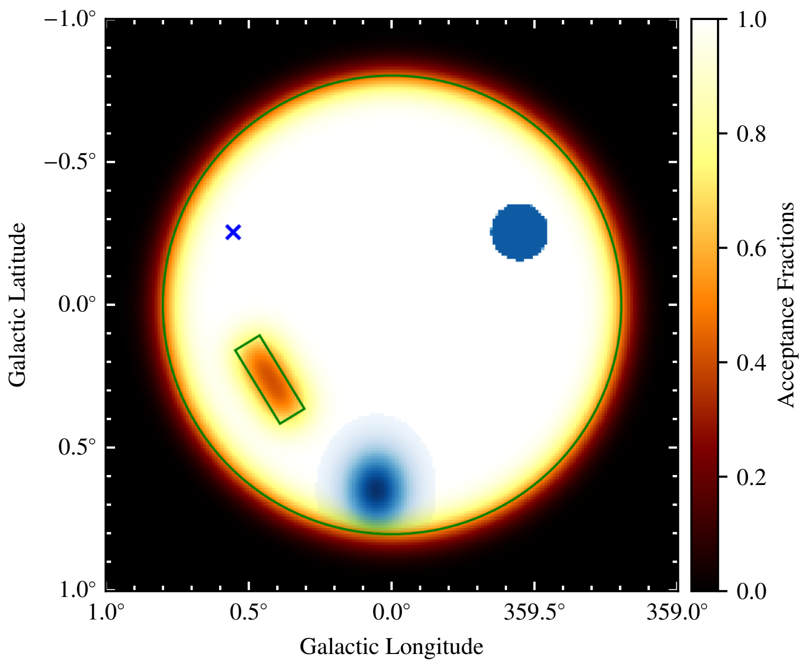

Figure 3.3: Illustration of the acceptance map. Regions outside the green circle and inside the green rectangle are excluded from the analysis. The blue patches represent exemplary sources for which the contribution inside the analysis region needs to be computed.

Additionally, Fig. 3.3 shows the spatial projection of the acceptance cube, with a rectangular analysis mask inside a circular one. This represents a common scenario where the circular mask defines a maximum event offset beyond which the IRFs and background model become unreliable. The rectangular mask may exclude a known source with complex morphology or spectrum from the analysis. Three exemplary sources are highlighted in blue: a point-like source, a disk, and an asymmetric Gaussian source. For each part of these sources, the total number of predicted counts contributing to the analysis can be calculated based on acceptance fractions. The precision with which the acceptance map traces the mask boundaries depends on the telescope's angular resolution at the corresponding energy.

3.2 Accuracy evaluation

We now compare the predicted counts for a test source between unbinned and binned datasets. This comparison employs the CTAO South IRFs at a zenith angle of 20°. The binned dataset uses an energy binning of eight bins per decade and a spatial binning with 0.01° bin size, which is below the spatial resolution of the instrument. In the following, the differential predicted counts for a point source with a power-law spectrum $\propto E^{-2}$ are compared between the binned and unbinned datasets across various energies and offsets from the source.

Figure 3.4 illustrates the radial profile of the predicted counts. In the binned case, predictions remain constant within each bin, resulting in the red step function. For comparison with the unbinned profile, a linear interpolation between bin centers is applied. The ratio panel highlights systematic differences, particularly at larger offsets where absolute values decrease significantly. The true PSF profile is provided as a reference and is in good agreement with the unbinned profile.

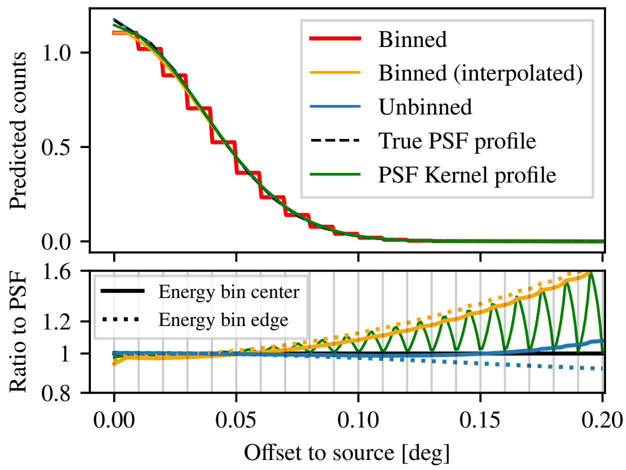

Figure 3.4: Comparison of the differential predicted counts at 1 TeV, computed for a binned dataset with 0.01° spatial binsize and using the unbinned method. The profiles are compared to the prediction of the true PSF and to the profile of the PSF kernel used for the binned convolution. The lower panel shows the ratios to the true PSF profile: solid lines represent events at the energy bin center (lines from the upper panel), and dotted lines additionally represent events at an energy bin edge. Vertical lines indicate the bin edges of the true PSF.

This difference stems from the PSF kernel profile used to convolve the spatial distribution of the point source in the binned case. The kernel is derived by evaluating the PSF at the kernel map's bin centers, which are up-sampled by a factor of two (for this bin size and angular resolution). These four evaluation points per pixel, however, do not constitute a full integration of the PSF profile within each pixel. At larger offsets, where the PSF profile declines steeply over few bins, linear interpolation introduces oscillations at the bin-width frequency. While the relative difference from the true PSF profile increases in these regions, absolute values remain small, suggesting minimal impact from these oscillations.

Additional effects emerge when the point source lies at the edge of two pixels. First, the true source flux is distributed between neighboring pixels such that a continuous shift in the source position results in a continuous shift in the predicted counts. This approach introduces an additional extension to the source model that is reflected in the slightly smoother profile in Fig. 3.5. Second, the oscillations of the profile are now transferred to the interpolated predicted counts profile, as the interpolation points moved from pixel centers to edges. In summary, the unbinned radial profile aligns well with the true PSF profile. Minor deviations, particularly at large offsets, result from interpolation effects, opposite for events reconstructed at energy bin centers or edges.

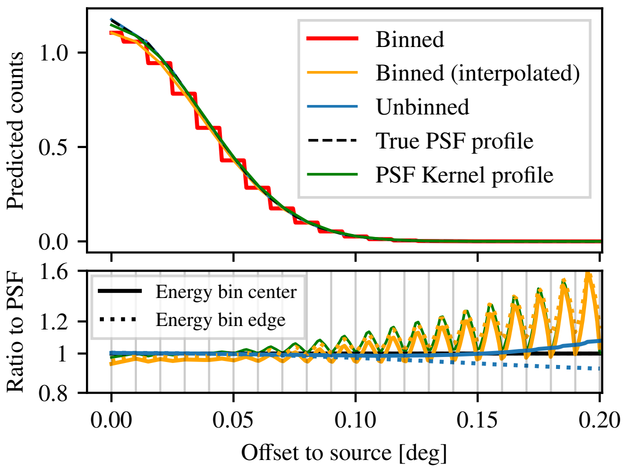

Figure 3.5: The same comparison as shown in Fig. 3.4, but for a source position shifted by half a bin size, located at a bin edge.

The next comparison focuses on the energy profile of the predicted counts at different offsets to the source. Figure 3.6 compares the energy profiles for binned and unbinned datasets and the linearly interpolated binned counts. As the true profile in reconstructed energy is unknown, there is no reference line for this comparison. A $\sim$10% deviation is

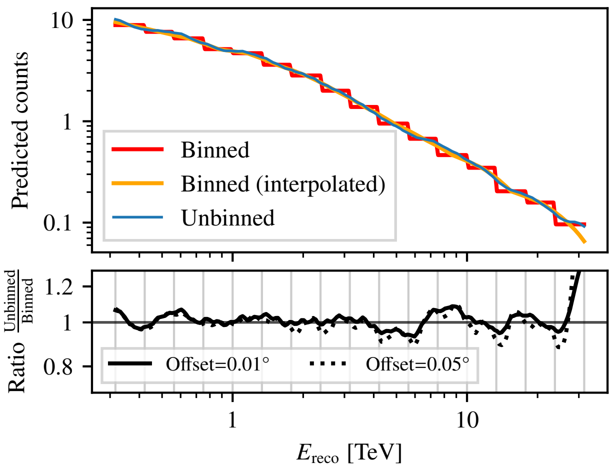

Figure 3.6: Comparison of the differential predicted counts at different energies with a fixed offset of 0.01°. The lower panel shows the ratios of the unbinned calculation to the binned one, interpolated at the corresponding energies and offsets. Additionally, the dotted lines show the ratio at a larger offset of 0.05°.

evident between the methods, without alignment to the IRF's energy binning. These deviations remain consistent in shape across different offsets but slightly increase in amplitude at higher offsets and energies. Understanding the origin of these deviations is challenging. Apart from energy dispersion, the spectrum at fixed offset is affected by the energy-dependent PSF, introducing curvature in the predicted counts spectrum, whereas the true source spectrum follows a simple power law.

One challenge in the unbinned approach is oversampling in the energy dimension when computing the response for each event. This is necessary because the EDisp factors depend strongly on the distance between reconstructed and true energy. As a result, the EDisp factors are significantly lower for events reconstructed between the true energy bin centers compared to those aligned directly with these centers. If the energy response is computed solely at the true geometry's bin centers, fluctuations arise due to the alignment between reconstructed and true energy centers. To obtain an accurate response, contributions from all true energies in each energy bin should be included. However, this integration within each energy bin is not weighted by the spectrum, leading to potential inaccuracies. A similar effect is also expected for the binned EDisp kernel that is obtained by integrating $dP/d\mu$ within each reconstructed energy bin, also neglecting the energy spectrum. For a sufficiently fine energy binning, this effect is expected to be small and cannot account for the differences in the spectrum.

Overall, the predicted counts from the unbinned dataset generally agree within 10% with those from the binned dataset, except at large offsets well above the angular resolution, where effects on analysis are minimal. A cross-check analysis using the binned method as a well-tested standard is recommended if feasible.

Another aspect is the numerical precision of the final statistic, $\mathcal{C} = -2\ln(\mathcal{L})$. This precision becomes particularly significant in fitting algorithms, such as MINUIT, which rely on gradients in the likelihood landscape to find the optimum. An illustrative example is the computation of the estimated distance to minimum (EDM), a measure used to assess the convergence of the fit. The EDM is calculated as:

$$\mathrm{EDM} = G^T \cdot V \cdot G, \tag{3.9}$$

where G is the gradient vector, G^T its transpose, and V the covariance matrix (the inverse of the Hessian matrix). Since the EDM is proportional to the square of the gradients, its precision is determined by the square root of the gradient's precision. Given that the resolution of NUMPY's `float64` is 10^{-15}, the resolution of the EDM is approximately $\sqrt{10^{-15}} \approx 3.2 \times 10^{-8}$. To avoid limitations in the optimization process caused by the "machine accuracy limit", the magnitude of $|\mathcal{C}|$ should remain below 3.2×10^5, ensuring the EDM has a precision of about 10^{-2}.

The value of $\mathcal{C}$ can be shifted by adopting different units for the differential predicted counts ν_c, which have dimensions of $[E^{-1}\Omega^{-1}]$. As long as all source and background models share the same units, scaling ν_c by a factor u affects $\mathcal{C}$ additively through the logarithm. From Eq. 3.2, the scaled statistic $\mathcal{C}_u$ is given by:

$$\mathcal{C}_u = \mathcal{C} + N\ln(u), \tag{3.10}$$

where N represents the total number of events in the dataset, and u is the unit scaling factor. Figure 3.7 illustrates how different units influence the magnitude of $\mathcal{C}$ across various dataset sizes, presented on a log-log scale. It is important to note that $\mathcal{C}$ is quantitatively also influenced by the source models, their total and differential predicted counts. If the differential predicted counts are computed in units that yield values significantly larger or smaller than unity, the resulting statistic will similarly deviate from unity by orders of magnitude. However, appropriate unit scaling can always reduce the magnitude of $\mathcal{C}$

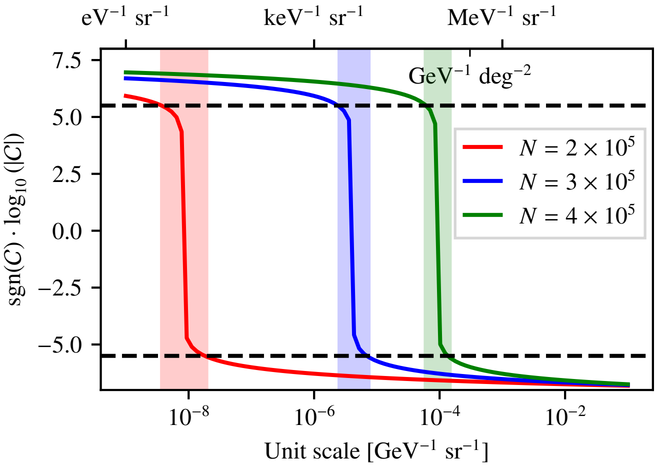

Figure 3.7: Magnitude of the statistic value $\mathcal{C}$ of an exemplary dataset with different numbers of events N. The dashed horizontal lines indicate the accuracy limit described in the main text, and the shaded regions show suitable values for the unit scale.

below the recommended threshold of 3.2×10^5, as indicated by the shaded regions in the plot. The optimal unit scaling depends heavily on the number of events in the dataset and cannot be precisely estimated prior to model evaluation and optimization. Nonetheless, after an initial rough optimization, the appropriate scaling can be determined.

3.3 Performance evaluation

This section compares sensitivity and computational performance between the binned and unbinned analyses. As before, both datasets are derived from IRFs for CTAO South at a zenith angle of 20°.

For the first comparison of point-source sensitivity, random events are sampled based on the prediction of the binned dataset for a toy point source and background, using Gammapy's `MapDatasetEventSampler`. Employing an Asimov dataset (see Sect. 1.6.2) with a known true source spectrum is not possible here, since individual events are required for the unbinned dataset. The source and background models are optimized for the sampled events in both datasets individually. The source significance $\sqrt{\mathrm{TS}} = \sqrt{\mathcal{C}_0 - \mathcal{C}_1}$ is computed based on the difference in $\mathcal{C} = -2\ln(\mathcal{L})$ with and without the source model (cf. Sect. 1.6.2). The likelihood is calculated using Eq. 1.17 for the binned dataset and Eq. 3.2 for the unbinned dataset. In both datasets, the energy binning is fixed at eight bins per decade, while the binned dataset's spatial bin size is progressively reduced from 0.2° to 0.01°, with pixel areas ranging from $4 \times 10^{-2}\,\mathrm{deg}^2$ to $10^{-4}\,\mathrm{deg}^2$. For each bin size, the source significance is calculated and compared with the unbinned dataset in Fig. 3.8. As expected, the two significance values converge at finer binning scales. At a bin size of 0.02°, about three times smaller than CTAO's angular resolution at 1 TeV, the unbinned dataset's sensitivity is reached. This bin size is considered standard for most binned analyses and not difficult to realize for most RoI sizes, making the sensitivity argument for unbinned analyses less compelling. Achieving adequate binning in the energy dimension is also straightforward, even for complex spectral models with breaks, cutoffs, or other features.

Another advantage of unbinned analyses is computational efficiency in low event-count scenarios. To quantify this, the time required for a single likelihood computation is measured. Since data analysis often involves repeated likelihood calculations for different model parameters, the time for one likelihood computation is representative of the analysis

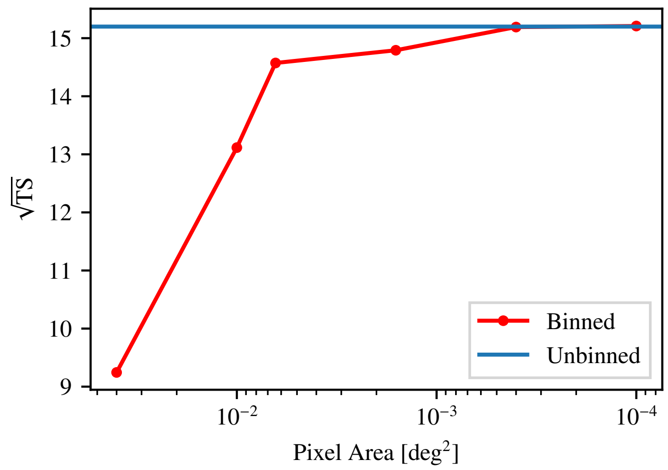

Figure 3.8: Detection significance of a point source above background as a function of the pixel area.

speed. Comparing total model-fitting times directly is challenging due to varying fit iterations and model caching efficiencies. Here, observations with different durations are simulated, based on event numbers predicted by the background and one point-source model. For each simulation, the speed of the likelihood computation is measured for a binned and unbinned dataset. The source model's predicted counts are recalculated, while the background model prediction is cached, approximating real analyses where the background model is usually cached and scaled to different normalizations. Most computation time is spent evaluating varying parameter combinations in the source models.

Figure 3.9 presents the timing results, with CPU time on the y-axis as a function of observation time for three cases. The first case represents a binned dataset with 20 energy and 200×200 spatial bins, sufficient to cover 3-4 orders of magnitude in energy and a $4^{\circ} \times 4^{\circ}$

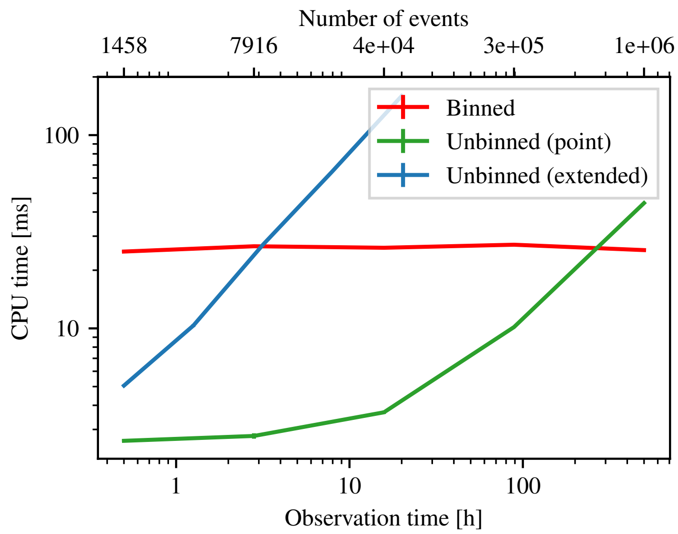

Figure 3.9: CPU time for a single likelihood calculation as a function of observation time. The two lines for the unbinned analysis represent the scenarios of a fixed point source (green), where the spatial integration is not required, and an extended source (blue), where the spatial integration is comparable to the binned dataset. The numbers of events on the upper x-axis are given for the unbinned analysis (see main text for details).

RoI with 0.02° spatial binsize. As anticipated, computation time remains mostly unaffected by observation time or event counts. A second case (blue line in Fig. 3.9) corresponds to the unbinned dataset with spatial model integration, necessary for extended models or those with free position. Observation time itself is not significant, only the event count impacts timing. Thus, the upper x-axis shows the number of events for which the unbinned evaluator computes signal response (signal and background events within 0.58° from the source). This radius is determined by the worst angular resolution within the energy range of interest, ensuring all relevant events are included. For this configuration, the CPU time of the binned analysis is reached with approximately 8×10^3 events, representing only 1% of the 8×10^5 bins in the binned analysis. This highlights the inefficiency of unbinned analyses requiring spatial integration per event compared to binned analyses using one regular grid.

Finally, spatial integration is unnecessary for fixed-position point sources, shown as the green line in Fig. 3.9. In this scenario, the computational advantage persists until event counts approach the number of bins.

3.4 Application to pulsar analyses

One potential application of the unbinned analysis is pulsar studies using γ-ray data. These observations typically span several tens of hours in the case of IACTs and even years in the case of instruments like the Fermi-LAT. The required time resolution for such analyses is often on the order of milliseconds to resolve individual pulses in the emission. Consequently, binned analyses are unsuitable for pulsar studies in the time domain, which are frequently conducted for γ-ray data. Recent examples of pulsar analyses include those presented in the second Fermi-LAT catalog of γ-ray pulsars (Abdo et al., 2013). Additionally, detailed studies of the Crab Pulsar have been performed by MAGIC (Aliu et al., 2008; Aleksić et al., 2011; Ansoldi et al., 2016) and VERITAS (VERITAS collaboration et al., 2011), as well as the detection of the Vela pulsar by H.E.S.S. (HESS Collaboration et al., 2023).

Pulsed emission in the γ-ray regime provides critical constraints to models of pulsar magnetospheres and regions of γ-ray production (Amato and Olmi, 2021b, and references therein). However, the analysis of pulsar data remains challenging to carry out directly within Gammapy. Instead, specialized tools such as Tempo2 (Hobbs et al., 2006) and Pint (Luo et al., 2021) are commonly employed. Since pulsars are point-like sources with well-determined positions, all advantages for point sources with fixed positions directly apply here. Especially, handling large event numbers, up to 10^6, is feasible, as the following example demonstrates. For researchers already familiar with Gammapy, incorporating pulsar analyses into their workflow could simplify data handling and allow for seamless integration of observations from multiple instruments. Another major advantage of unbinned analyses is the possibility of joint optimization of all relevant model components. This includes not only the spectral source model but also the background models, which can be refined simultaneously to enhance the overall fit and scientific interpretation.

3.4.1 Pulsar analysis of the Crab Pulsar

Pulsed emission from rapidly rotating neutron stars (pulsars) follows a regular time profile, repeating itself with a period $T = 1/f_0$ in the pulsar's reference frame. The exceptional time resolution of IACTs, on the order of nanoseconds, enables the precise recording of an event's time of arrival (TOA) at the observatory. However, the relative motion and varying distance between the emitter and the observatory introduce shifts in the observed frequency and delays in the TOAs. To determine the phase of an individual event in the pulsar reference frame, one must account for these effects, which are typically dominated by the Earth's motion. Additional effects, such as the Shapiro delay – relativistic time dilation caused by massive objects like the Sun or planets – usually contribute less significantly. PINT provides the capability to compute the TOAs in barycentric time for a given observatory and source coordinates. It accounts for all relevant motions and delays relative to the solar system's barycenter. Using a timing model that includes a reference time, base frequency, and higher-order derivatives, one can assign a phase $\Phi(t)$ to each event:

$$\Phi(t) = \Phi_0 + f_0 \cdot (t - t_0) + \frac{1}{2!}\dot{f}_0 \cdot (t - t_0)^2 + \frac{1}{3!}\ddot{f}_0 \cdot (t - t_0)^3 + \ldots, \tag{3.11}$$

with Φ_0 a constant phase offset, t_0 the reference time, f_0 the base frequency, and $\dot{f}_0$, $\ddot{f}_0$ its first and second derivatives, respectively. Higher-order terms can also be included as needed.

In the case of the Crab Pulsar, the timing model is well-determined up to the 10th order from radio observations, where individual pulses can be detected. In γ-ray observations, however, the situation differs: while individual events are detected with accurate timing, their energy and arrival directions are reconstructed only within the instrument's resolution. These events also include background from hadronic background events passing the event selection, as well as non-pulsed γ rays from the bright Crab Nebula. For instance, events from the Crab Pulsar are detected by the Fermi-LAT approximately once every few hours.

The pulsed nature of the emission is often visualized using phase-folded histograms, where the abundance of events in certain bins corresponds to the phases of pulsed emission (cf. Fig. 4.4 in Sect. 4.2.2). Pulsed emission from the Crab region is detectable not only in the energy range covered by Fermi-LAT but also at higher energies observable with IACTs. The phase histogram of events around the Crab Pulsar observed by MAGIC is presented in Fig. 2 of Ansoldi et al. (2016). Within one phase interval $[0, 1]$, they observe two distinct pulses, labeled P1 and P2, differing slightly in brightness and spectral index. In their study, they use 320 hours of observations, of which 221 hours were conducted in stereo mode (using two telescopes). As the Crab Pulsar is located in the Northern Hemisphere (cf. Fig. 1.26), MAGIC observes it at low zenith angles, reducing the energy threshold to approximately 70 GeV. They also employ specialized event selection criteria, accounting for γ rays from the Crab Nebula as additional background.

In this study, approximately 30 hours of H.E.S.S. data are analyzed, observed with only the large central telescope CT5. Despite the large zenith angles of these observations ($>44°$), improvements in the analysis of these events (described in detail in Chapter 5) allow for an energy threshold of $\sim$100 GeV. The phase histogram of these events is shown in Fig. 3.10, where only events within a radius of $0.1°$ from the pulsar position are included. Due to the short exposure time and high background contamination, no significant deviations from a uniform distribution are observed, as expected for such limited data. Nevertheless, this small dataset can be used to validate the capability of the unbinned analysis to perform pulsar studies within GAMMAPY.

The prerequisites for this analysis are the observed counts and IRFs in the standard FITS format, as well as the phase information derived using the PINT package along with the timing model from Abdo et al. (2013)[26]. Since the properties of the timing model are known with high precision, the timing model in the GAMMAPY analysis does not have any free parameters. The contribution of each event to the model is scaled by the value of the assumed pulse profile at its phase (cf. Fig. 3.10). Given the limited statistics and energy range of this analysis (100–700 GeV), the spectral shapes of the models are fixed. Only the normalizations of the background, the Crab Nebula, and the P2 model of the Crab Pulsar are fitted to the data.

A profile likelihood scan is conducted for different amplitudes of the P2 model, and the

[26]Available online: `https://fermi.gsfc.nasa.gov/ssc/data/access/lat/ephems/`

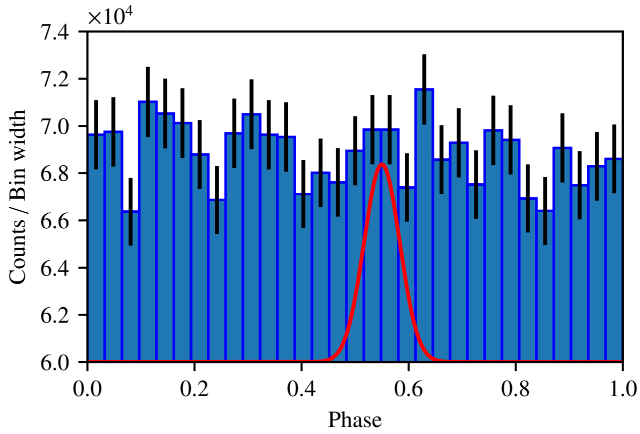

Figure 3.10: Phase histogram of events from a circle with $r = 0.1°$ around the Crab Pulsar position, with energies between 100–700 GeV. The vertical black error bars indicate the statistical uncertainty of each entry, calculated as the square root of the event number divided by the bin width. The red Gaussian profile shows the puls profile used in this work in arbitrary units.

resulting test statistic is shown in Fig. 3.11. The TS is defined with respect to the null hypothesis of zero contribution from the P2 model. For amplitudes near those found by MAGIC, the TS value is slightly negative, as expected when adding an additional degree of freedom to the fit. As the amplitude increases, the P2 model predicts significant pulsations in the data, which are not observed, causing the TS to rise rapidly. A 5σ upper limit on the amplitude can be derived from the amplitude where the TS value reaches 25.

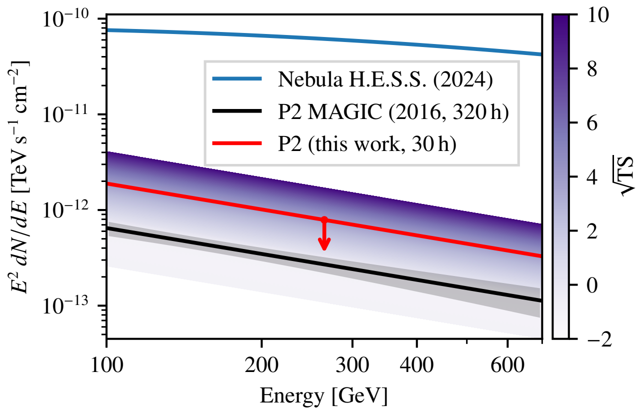

Figure 3.11: SED of the Crab Nebula (Aharonian et al., 2024, see also Chapter 4), the puls P2 as measured by MAGIC, with the uncertainty depicted as a shaded region (Ansoldi et al., 2016), and a 5σ upper limit derived in this work. The purple color map corresponds to the exclusion significance of the corresponding pulsar fluxes.

This result demonstrates that the unbinned analysis enables spectral pulsar studies without dividing the data into on-phase and off-phase intervals, a standard practice in γ-ray pulsar analyses. Instead, a temporal component can be added to each model, and events can be “weighted” according to the model’s predictions. In principle, this weighting of events is also applicable to binned analyses when phase information is fixed. Similarly, pulsar studies often use weights based on the spectral and spatial distribution of events to refine the timing solution.

The primary advantage of unbinned analyses extends beyond convenience. They offer the potential to simultaneously fit both the timing and spectral properties of pulsed emission. An example of such a case is discussed in the following section, where the pulsar is not detected in radio observations, and no precise timing solution is available.

3.4.2 Pulsar glitches in PSR J1906+0722

Despite pulsars being known for their precise and regular spin behavior, there are rare instances where the frequency and its derivatives suddenly change. These events, referred to as pulsar "glitches", have been identified in over 200 pulsars to date (Zhou et al., 2022). The first pulsar glitch was discovered in 1969, when the spin frequency of the Vela pulsar abruptly increased. This finding sparked significant interest in the scientific community, as the frequency evolution of pulsars is closely linked to processes and interactions in the neutron star and its surroundings. Since then, automated searches have identified over 700 glitches, primarily from radio observations. However, some pulsars are detectable only in the γ-ray regime and not in radio, prompting blind searches in Fermi-LAT data (Pletsch and Clark, 2014).

Glitches exhibit diverse characteristics in their spin evolution, which has led to a range of explanations for these sudden changes in frequency. Current models of pulsar glitches include processes in the magnetosphere and the interior of the neutron star, such as accretion, magnetospheric instabilities, crustquakes, corequakes, and catastrophic unpinning of vortex lines. Further classification and detailed explanations of pulsar glitches can be found in Zhou et al. (2022) and references therein.

This section follows the study of Clark et al. (2015) and investigates the glitch properties of the pulsar PSR J1906+0722 using Fermi-LAT data. The pulsar was detected in a blind survey of unidentified Fermi-LAT sources, while dedicated radio observations failed to identify a signal. To ensure consistency with their study, only Fermi-LAT data from 2008 August 4 to 2014 October 1 are used, within the energy range 0.2–100 GeV, and employing the `P8R3_SOURCE_V3` IRFs. The TOAs with barycentric corrections are computed using the PINT package and its `get_satellite_observatory()` method. Event phases $\Phi = \Phi_b + \Phi_g$ are determined based on the glitch model, comprising a base phase Φ_b (cf. Eq. 3.11) and an additional glitch phase Φ_g for events occurring after the glitch epoch t_g. The base phase for all events is calculated as:

$$\Phi_b(t) = \Phi_0 + f_0 \cdot (t - t_0) + \frac{1}{2!}\dot{f}_0 \cdot (t - t_0)^2 + \frac{1}{3!}\ddot{f}_0 \cdot (t - t_0)^3, \tag{3.12}$$

where Φ_0 is a constant phase offset, t_0 is the reference time, f_0 is the base frequency, and $\dot{f}_0$ and $\ddot{f}_0$ are its first and second derivatives, respectively. The glitch phase Φ_g is zero for events before the glitch epoch t_g, and for events after t_g, it is given by:

$$\Phi_g(t) = \Delta\Phi + \Delta f_p \cdot (t - t_g) + \frac{1}{2!}\Delta\dot{f}_p \cdot (t - t_g)^2 + \tau \cdot \Delta f_d \left[1 - \exp\left(\frac{-(t - t_g)}{\tau}\right)\right], \tag{3.13}$$

with $\Delta\Phi$ the phase jump, Δf_p the permanent frequency change with respect to the pre-glitch value, $\Delta\dot{f}_p$ the permanent change in the frequency derivative. The exponential term models the decay in additional spin frequency Δf_d with decay constant τ.

For the data preparation, FERMIPY is used to optimize the RoI models, which are selected from the 4FGL catalog in a $16° \times 16°$ region centered on the pulsar's position. Events are selected from a smaller $12° \times 12°$ region, with a spatial bin size of $0.05°$ and eight bins per decade in energy. Diffuse emission from the Galactic plane and isotropic emission constitute the background templates, where energy dispersion is not applied to the isotropic component. After an initial optimization of the models, those with a TS value below 4 are removed, and the remaining models are refitted to the data. Subsequently, the events, exposure cube, EDisp, and PSF are exported as FITS files for the GAMMAPY analysis. To enhance computational efficiency and reduce memory usage, a template is created for the 4FGL sources by summing their predicted counts. This template, together with the Galactic diffuse and isotropic templates, serve as background models for the analysis, from which the differential predicted counts can be interpolated.

The pulsar model consists of a point-spatial model, an exponential-cutoff power-law spectral model (cf. Eq. 2.1), and the glitch temporal model, which assigns phases to the events and interpolates the puls profile on them. Since the true pulse profile of PSR J1906+0722 is not known, it must be constructed from the data. To achieve this, a weighted phase histogram is computed, including all events. Here, the weights are proportional to the ratio of predicted signal to background flux at each event's coordinate. Events closer to the pulsar are assigned higher weights and contribute more compared to events far away from the pulsar. The same is true for events in spectral regions with a high signal-to-background ratio. For this initial histogram, the parameters of the temporal model are adopted from Clark et al. (2015).

The phase profile estimation is carried out iteratively, starting with a simple Gaussian pulse fitted to the histogram. This profile is then used to refine the pulsar model and background normalizations. Figure 3.12 shows the profiles of the three iterations, together with the weighted phase histogram after the final iteration. After the second iteration, a double-bump feature becomes evident, necessitating the use of two Gaussian components. As the weighted histogram shows negligible changes after the third iteration, the linear combination of these two Gaussians, labeled as "Iteration 3" in Fig. 3.12, is adopted as the pulse profile for subsequent analysis.

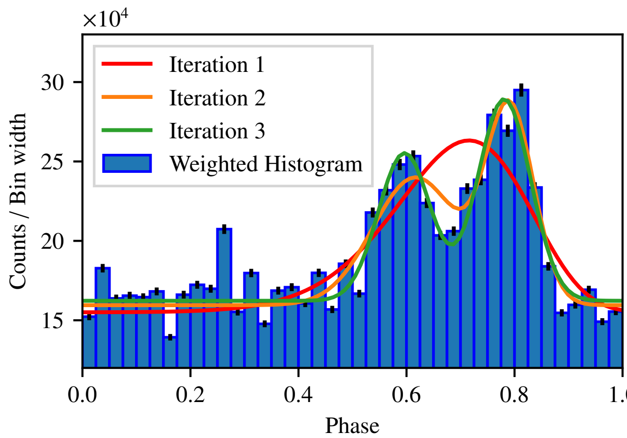

Figure 3.12: Phase histogram of weighted events with energies between 0.35–100 GeV. The vertical black error bars indicate the statistical uncertainty of each entry. The colored lines show the puls profile used for each iteration.

With all models in place, the best-fit parameters from the unbinned analysis are compared with those reported by Clark et al. (2015) in Table 3.1. Not all parameters agree within statistical uncertainties. For some parameters, the relative uncertainties are very small, particularly those computed in this work using the covariance matrix[27]. Notably, the uncertainty in the glitch epoch is three orders of magnitude smaller than the value reported by Clark et al. (2015), an unrealistically small estimate considering that only ≈4.6 weighted photons are observed from the pulsar during one day. The strong and complex parameter correlations within the glitch model likely account for the observed challenges in determining an accurate covariance matrix. A very slight shift in the glitch epoch on the order of half a period can result in a substantial shift in the phases following the glitch,

[27]The covariance matrix is the inverse of the Hessian matrix and the standard method for error estimation in Gammapy.

Table 3.1: Best-fit parameter values of the unbinned glitch analysis compared to the values found by Clark et al. (2015).

Parameter	Clark et al. 2015	This work
f [Hz]	$8.9666688432(1)$	$8.9666688442(1)$
$\dot{f}$ [Hz s^{-1}]	$-2.884709(2) \times 10^{-12}$	$-2.884736(1) \times 10^{-12}$
$\ddot{f}$ [Hz s^{-2}]	$3.18(1) \times 10^{-23}$	$3.123(3) \times 10^{-23}$
Glitch epoch [MJD]	55067^{+2}_{-9}	55066.913 ± 0.001
Δf [Hz]	$4.033(1) \times 10^{-5}$	$4.031641(2) \times 10^{-5}$
$\Delta\dot{f}$ [Hz s^{-1}]	$-2.56(3) \times 10^{-14}$	$-2.54508(4) \times 10^{-14}$
Δf_d [Hz]	$3.64(9) \times 10^{-7}$	$3.636(1) \times 10^{-7}$
τ [days]	$221(12)$	$225.66(13)$
F_{100} [photons cm^{-2} s^{-1}]	$1.1(3) \times 10^{-7}$	$8.9(4) \times 10^{-8}$
index Γ	1.9 ± 0.1	1.91 ± 0.03
E_{cutoff} [GeV]	5.5 ± 1.2	7.5 ± 0.4

See Eq. 3.12 and 3.13 for a definition of the parameter values.
The 1σ uncertainties in the final digits are given in parentheses or stated explicitly.

drastically impacting the likelihood. Conversely, a minor shift in the glitch epoch on the order of one period has minimal effect on the phases and the likelihood. Consequently, the likelihood landscape exhibits strong oscillations along the glitch epoch dimension, posing significant challenges to fitting algorithms.

In the work of Clark et al. (2015), an efficient nested sampling algorithm was employed to maximize the likelihood and derive posterior distributions. In this study, two complementary algorithms supported by Gammapy are used to minimize the TS value and perform a profile likelihood scan of the glitch epoch. This approach addresses the challenges posed by the complex likelihood landscape, which often hinders convergence during fitting. The default algorithm in Gammapy is `migrad` from the Minuit library. This algorithm relies on gradients of the likelihood landscape, which may be unreliable in this scenario. As an alternative, the "Nelder-Mead" method implemented in Scipy is also explored. This algorithm does not depend on gradients, making it more robust in situations where gradients are poorly defined. Neither algorithm consistently outperforms the other across the entire likelihood scan. Therefore, a combined approach is employed, leveraging both algorithms iteratively. The optimization begins with a limited set of parameters, progressively adding parameters in subsequent iterations. For each iteration, the starting values are informed by the optimal parameters obtained from the preceding iteration using either algorithm.

The resulting likelihood scan is presented in Fig. 3.13, where the individual points show the lowest TS value achieved for each value of the glitch epoch. A small degree of

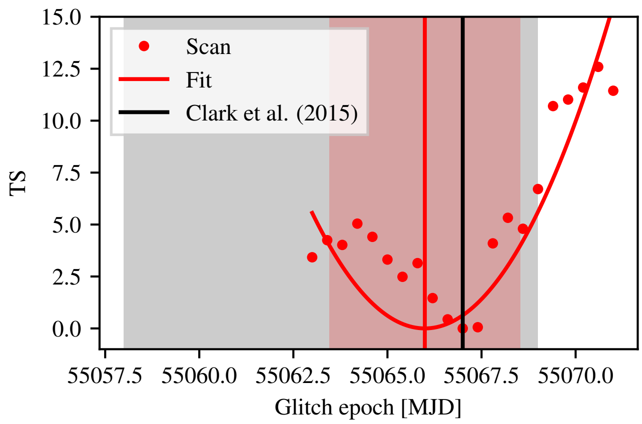

Figure 3.13: Likelihood profile scan for the glitch epoch. The red dots show the TS values for each epoch to which the parabola is fitted. The vertical lines represent the glitch epochs derived from the parabola (red) and the one from Clark et al. (2015) (black), along with 2σ uncertainties shown as shaded regions.

scatter remains between these points, and the profile is not perfectly parabolic at the minimum. While the scatter suggests potential issues with parameter optimization, the asymmetry in the profile is supported by the asymmetric uncertainties reported in Clark et al. (2015). A parabola is fitted to the points to illustrate the expected likelihood profile and estimate symmetric uncertainties. While this approach provides a useful approximation, the uncertainty derived in this manner is influenced by noise in the scan and the assumption of a parabolic shape. Nevertheless, the 2σ uncertainty on the glitch epoch derived here appears comparable to the values reported by Clark et al. (2015). Specifically, the uncertainty is on the order of days but exhibits greater symmetry compared to the asymmetric uncertainties of $^{+2}_{-9}$ days derived from the posterior distribution in their likelihood sampling.

3.5 Discussion

In this chapter, I presented a possible implementation of an unbinned analysis within the existing framework of Gammapy. Core functionalities, such as the interpolation and projection of the IRFs to the sky, model evaluation, regular geometries, and others, can be adapted directly from the binned analysis. However, certain required quantities, including the differential predicted counts at event coordinates and the total number of predicted counts within an analysis region, must be computed without relying on a binned grid. A key challenge in this implementation is preserving the versatility, flexibility, and customizability that make Gammapy popular. The unbinned analysis should support custom source models implemented by users and accommodate complex exclusion regions in the analysis. Additionally, high precision and computational efficiency are critical requirements for practical application. Achieving higher precision necessitates fine numerical integration grids, which are computationally expensive. The approach described here uses integration grids tailored to each model, coupled with caching of values that are independent of the model parameters. While this increases the initialization time for datasets, it significantly reduces the time required for fitting and generating higher-level data products. This method, however, imposes memory limitations, setting a hard cap on the number of events that can be analyzed simultaneously. The exact limit depends on the number and type of models used in the analysis. Point-source and template models are memory-efficient, whereas large extended models with fine structures are memory-intensive. If morphological parameters are not of interest, it is recommended to replace extended models with template models. Another potential solution involves writing large arrays to disk and processing them in smaller chunks, enabling the analysis at the cost of increased computation time. However, this approach is not yet implemented.

The unbinned statistic represents the limit of the binned *Cash* statistic with infinitely fine bins. However, a loss of sensitivity in binned analyses occurs only when the bin sizes approach or exceed the instrument's resolution. For typical analyses with current instruments, adequate binning is almost always achievable, resulting in negligible sensitivity gains from using an unbinned analysis. Furthermore, while the unbinned approach offers computational speed advantages for small event numbers, the time required for binned analyses – typically on the order of minutes – is already feasible. Longer analyses are often limited by the model evaluation time, which is necessary for both binned and unbinned analyses, rather than the forward folding. Hence, no significant computational advantage is expected for these use cases.

Unbinned analysis may prove beneficial in specific scenarios. For example:

- **High-energy events:** These analyses often involve low event numbers but high instrument resolution.
- **Large regions:** Spatial resolutions finer than 0.01° in regions larger than $100\,\mathrm{deg}^2$ may benefit from unbinned methods.

- **Temporal analyses:** Scenarios requiring fine temporal resolution, such as pulsed emission studies, can surpass the limitations of binned analyses. Pulsar analyses, in particular, demand timescales of milliseconds over observation spans of hours to years.

So far, the spectral properties of pulsars are traditionally derived by dividing events into on-phase and off-phase datasets based on fixed phase information from timing models. These models are either obtained from other observatories or can be optimized using the event times with an unbinned likelihood approach. Signal-to-background ratios can be improved by applying spatial cuts around the source or weighting events based on their distance to the source and fixed spectral assumptions. In the previous sections, I presented two pulsar analyses, demonstrating the potential to combine the spectral and temporal analysis. While the optimization of the spectral parameters was found to work reliably, challenges remain in optimizing temporal parameters, especially for glitching pulsars, using the current algorithms supported by Gammapy.

Currently, both binned and unbinned analyses utilize averaged IRFs, the standard practice in IACT analyses. This approach treats all events equally, regardless of their reconstruction quality. The Fermi-LAT collaboration also provides so-called "event types", that separate the events into four distinct classes based on either angular or energy reconstruction quality. In cases where the quality of the events strongly differs, one can gain sensitivity by separating the events. The superior sensitivity of high-quality events is not averaged with this from poorly reconstructed events, but rather the two complement each other in a joint analysis. In principle, maximum sensitivity can be achieved by using dedicated IRFs for individual events, corresponding to infinite event types. Such an approach is already used by neutrino telescopes like IceCube, which handle low event numbers and prioritize sensitivity. In the future, a similar strategy could be implemented in the unbinned analysis as presented here. The IRF-cube used to compute the differential predicted counts could be adapted or computed per event using dedicated response functions, while the total predicted counts would still rely on averaged IRFs. Except for the dataset initialization phase, this approach would not increase computational costs, which is crucial for likelihood calculations. Implementing such a strategy in Gammapy could open new possibilities for unbinned analyses, enhancing their applicability and precision in diverse astrophysical scenarios.

For the law was given by Moses, but grace and truth came by Jesus Christ.

— John the Baptist, John 1:17

4 Spectrum and extension of the inverse-Compton emission of the Crab Nebula from a combined Fermi-LAT and H.E.S.S. analysis

This study originated as a Master's project focused on the validation of a joint Fermi-LAT and H.E.S.S. analysis of the Crab Nebula within the Gammapy framework. After the successful combination of the data reported in Unbehaun (2020), the individual analyses have undergone further refinement, and phenomenological models have been tested against the data. These models were implemented in Gammapy, predicting the spectral and morphological components based on assumed electron, seed photon field, and B-field distributions. The results have been published in Astronomy & Astrophysics (Aharonian et al., 2024) and are reported here with minimal or no modifications.

4.1 Introduction

The Crab Nebula, associated with the pulsar PSR B0531+21, represents the archetype of a pulsar wind nebula and has been extensively studied across all wavelengths of the electromagnetic spectrum (e.g. Hester, 2008; Buehler and Blandford, 2014; Amato and Olmi, 2021a). In the high-energy (HE; $100\,\mathrm{MeV} < E < 100\,\mathrm{GeV}$) and very-high-energy (VHE; $E > 100\,\mathrm{GeV}$) wavebands, it stands out as one of the brightest objects in the sky. In fact, the Crab Nebula was the first γ-ray source to be unambiguously detected at very high energies from 1986–1988 with the Whipple telescope (Weekes et al., 1989). The radiation emitted by the nebula is mostly steady, although temporal variations have been observed in some wavebands (e.g. Wilson-Hodge et al., 2011; Abdo et al., 2011). In the VHE band, no flux variability has been observed so far, and the Crab Nebula has been used as a standard candle for detector calibration in this regime since its first detection (cf. Vacanti et al., 1991; Pühlhofer et al., 2003; Aharonian et al., 2006; Albert et al., 2008; Meyer et al., 2010; Abeysekara et al., 2017; Aharonian et al., 2021; Abe et al., 2023).

We show in Fig. 4.1 the spectral energy distribution (SED) of the Crab Nebula, as measured by a large number of instruments. The distribution exhibits two broad peaks; both are generally accepted to be caused by a population of high-energy electrons[28] that fills the nebula. The first peak is due to synchrotron emission that the electrons emit within the magnetic field of the nebula. The emission at energies close to the second peak is generated by high-energy electrons via the inverse Compton (IC) process. The general formation and structure of the nebula was already discussed by Rees and Gunn (1974), and a number of theoretical models describing the emission from high-energy electrons in the Crab Nebula have been put forward since then (e.g. Kennel and Coroniti, 1984b; de Jager and Harding, 1992; Atoyan and Aharonian, 1996; Hillas et al., 1998; Aharonian et al., 2004; Meyer et al., 2010), including time-dependent models applicable to young pulsar wind nebulae (e.g. Torres et al. 2014; van Rensburg et al. 2018; for a review see also Amato and Olmi 2021a and references therein). Although usually considered sub-dominant over most of the energy range, γ-ray emission due to accelerated cosmic-ray nuclei has

[28]Throughout this paper, the term 'electrons' refers to both electrons and positrons.

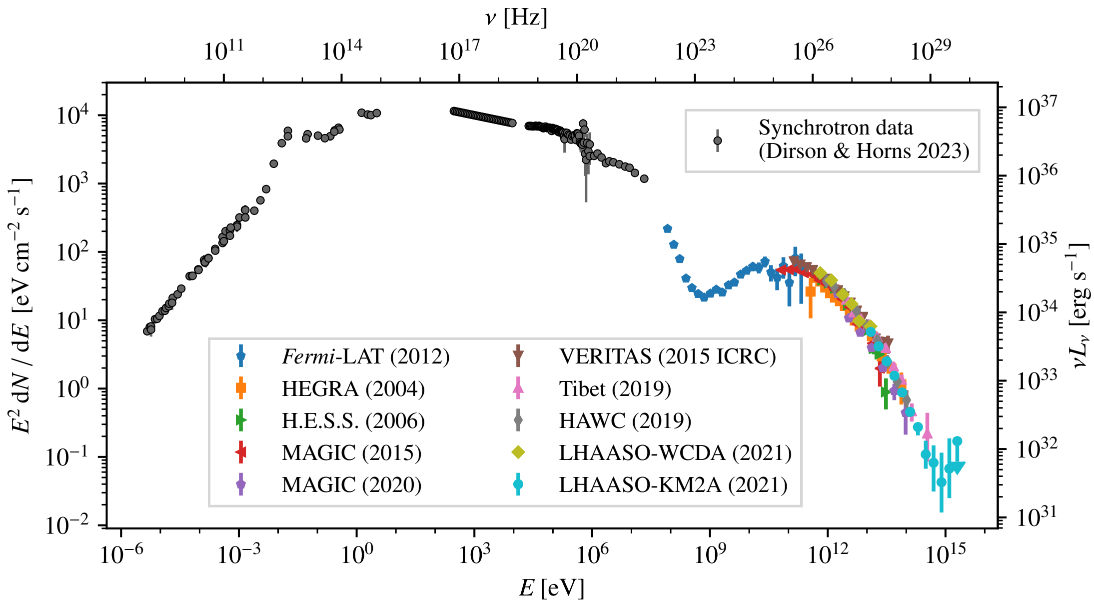

Figure 4.1: SED of the Crab Nebula. The synchrotron data points up to hard X-rays have been taken from Dirson and Horns (2023) and references therein. The HE and VHE data are from Buehler et al. (2012), Aharonian et al. (2004), Aharonian et al. (2006), Aleksić et al. (2015), Acciari et al. (2020), Meagher (2015), Amenomori et al. (2019), Abeysekara et al. (2019), and Cao et al. (2021a), in the order as listed in the legend. A distance of 2 kpc has been assumed to convert to luminosity (see right-hand side axis).

also been considered (e.g. Atoyan and Aharonian, 1996; Arons, 1998; Bednarek, 2003). Recently, following the detection of PeV-energy photons from the Crab Nebula by the LHAASO detector (Cao et al., 2021a), this possibility has received some renewed interest (Peng et al., 2022a; Nie et al., 2022a).

In recent years, it has furthermore become possible to spatially resolve the IC component of the Crab Nebula both in the HE and VHE bands, with extensions (68% containment radii) of $1.8' \pm 0.18'_{\mathrm{stat}} \pm 0.42'_{\mathrm{sys}}$ measured with the *Fermi* Large Area Telescope (LAT; Ackermann et al., 2018) and $1.31' \pm 0.07'_{\mathrm{stat}} \pm 0.17'_{\mathrm{sys}}$ measured with the High Energy Stereoscopic System (H.E.S.S.; Abdalla et al., 2020b), respectively. These measurements provide new, crucial constraints for the theoretical modelling of the IC emission from the Crab Nebula. Generally, because higher-energy electrons cool more efficiently, the extension of the nebula is expected to decrease with increasing electron energy (Kennel and Coroniti, 1984b; de Jager and Harding, 1992; Atoyan and Aharonian, 1996; Hillas et al., 1998; Aharonian et al., 2004). For example, in the X-ray domain – where the emission is due to synchrotron radiation of the highest-energy electrons in the system – the nebula exhibits a torus-like morphology that is only about $0.63' \times 0.3'$ in size (Weisskopf et al., 2000). In contrast, in the ultraviolet, the characteristic extension is approximately $1.6'$ (Abdalla et al., 2020b, where we have converted from a containment fraction of 39% to 68% assuming a Gaussian morphology). However, besides the spatial distribution of the electrons, the apparent size of the nebula also depends on the extension of the nebula's magnetic field (for synchrotron radiation) and its distribution of seed photons (for the IC component). At radio wavelengths the extension is indeed only $\sim 1.9'$, which is smaller than expected solely from the distribution of electrons (Yeung and Horns, 2019). Recently, Dirson and Horns (2023) performed a combined spatial and spectral fit of the multi-wavelength (MWL) data of the Crab Nebula, using a model that features radially dependent electron, seed photon, and magnetic field densities, finding that they can describe the entire data set well.

In this work, we provide, for the first time, a simultaneous measurement of the energy spectrum and spatial extension of the entire IC component of the Crab Nebula. To this end, we combined data from Fermi-LAT and H.E.S.S. at the level of detected γ-ray events in a joint likelihood fit, using the open-source software package Gammapy (Donath et al., 2023). In addition, we fitted phenomenological models based on those developed by Kennel and Coroniti (1984b), Meyer et al. (2010), and Dirson and Horns (2023) to the Fermi-LAT, H.E.S.S., and available synchrotron MWL data. We emphasise that in contrast to previous works, our analysis does not rely on fitting models to derived data products such as flux points, which depend on the assumed underlying spectral or spatial models used in their derivation.

The remainder of the paper is structured as follows. In Sect. 4.2, we first present separate analyses of the H.E.S.S. and Fermi-LAT data. The joint analysis detailed in Sect. 4.3 then provides a measurement of the energy spectrum and extension of the Crab Nebula across the energy range covered by both instruments. In Sect. 4.4, we describe the fit of several phenomenological models to our combined data set. The impact of systematic uncertainties is discussed in Sect. 4.5. Finally, we conclude in Sect. 4.6.

4.2 Data analysis

In parallel with combining the Fermi-LAT and H.E.S.S. data we performed separate analyses using the standard analysis tools of the respective instruments. These results are used to cross-check the joint analysis, which we carried out with the Gammapy package (v0.18.2; Donath et al., 2023; Deil et al., 2020).

The analysis is performed as a three-dimensional (longitude, latitude, and energy), binned likelihood fit, as described in Sect. 1.6. Because the synchrotron emission of the Crab Nebula measured in the X-ray regime is steady to within $\pm 5\%$ over the period considered here (Jourdain and Roques, 2020), we do not expect variations of the flux level or spatial appearance of the IC emission. We therefore do not take into account the time of data taking in our analysis, but perform a time-independent modelling.

4.2.1 H.E.S.S. data analysis

H.E.S.S. is an array of five imaging atmospheric Cherenkov telescopes (IACTs) located in Namibia at an altitude of 1800 m (Aharonian et al., 2006). It is sensitive to γ rays in the energy range from several tens of GeV to $\sim$100 TeV, where the exact achievable energy threshold depends on the observing conditions (in particular the zenith angle). The initial array, denoted H.E.S.S. Phase-I, was completed in 2003 and comprises four telescopes (CT1-4) with 108 m^2 mirror area each, arranged in a square grid. We refer to data taken with this configuration as 'stereo' data. In 2012, a fifth, larger telescope (CT5) with 614 m^2 mirror area was added in the centre of the array, marking the beginning of H.E.S.S. Phase-II. The larger mirror area of CT5 can in favourable conditions lead to energy thresholds significantly below 100 GeV (e.g. Abdalla et al., 2017; Abdalla et al., 2018b). When analysed separately, data taken with the CT5 telescope is referred to as 'mono' data (Murach et al., 2015). In 2019, the camera of CT5 was replaced by a 'FlashCam' prototype camera (Bi et al., 2021; Pühlhofer et al., 2021) that has been designed for the upcoming Cherenkov Telescope Array (CTA; Acharya et al., 2018). H.E.S.S. data taking is conducted in observation runs that typically last 28 min.

IACTs are built to measure the Cherenkov light emitted in γ-ray induced particle showers in the atmosphere. Based on the recorded shower images, we reconstructed the direction and energy of the primary γ ray using the ImPACT reconstruction algorithm (Parsons and Hinton, 2014). The dominant background consists of air showers initiated by charged cosmic rays, which we suppress by means of a multi-variate analysis (Ohm et al., 2009). In contrast to traditional methods that estimate the residual background from 'OFF' regions in the same observation run, we used here a three-dimensional background model constructed from archival H.E.S.S. observations (this is a prerequisite for carrying out the three-dimensional likelihood analysis described at the beginning of this section; Mohrmann et al., 2019). The IRFs are obtained from extensive Monte-Carlo simulations, carried out with the SIM_TELARRAY package (Bernlöhr, 2008). A correction for telescope efficiency, measured for each observation run using muons from atmospheric air showers, is applied as described in Mitchell (2016). Results have been cross-checked with independent calibration and reconstruction methods (Naurois and Rolland, 2009).

We used 114 observation runs (corresponding to an observation time of ≈50 hours) of H.E.S.S. stereo (CT1-4) data taken between Nov. 2004 and Mar. 2015. Only observations with good data quality, excellent atmospheric conditions, zenith angles below 55°, and a maximum angle between the pointing position and the Crab Nebula of 1° have been included. Compared to the standard analysis configuration, we required a minimum of three telescopes for the reconstruction of each event, which leads to fewer detected events mostly at low energies but improves the angular resolution by ∼20%, to 0.06° (68% PSF containment radius) at 1 TeV. At the same energy, the achieved energy resolution is 16% (standard deviation). A comparison of the IRFs used for this work to the standard ones can be found in Fig. 4.2. Because the Crab Nebula culminates at a relatively large zenith angle of ∼45° at the H.E.S.S. site, the energy threshold of the stereo data set is comparatively high (≈560 GeV).

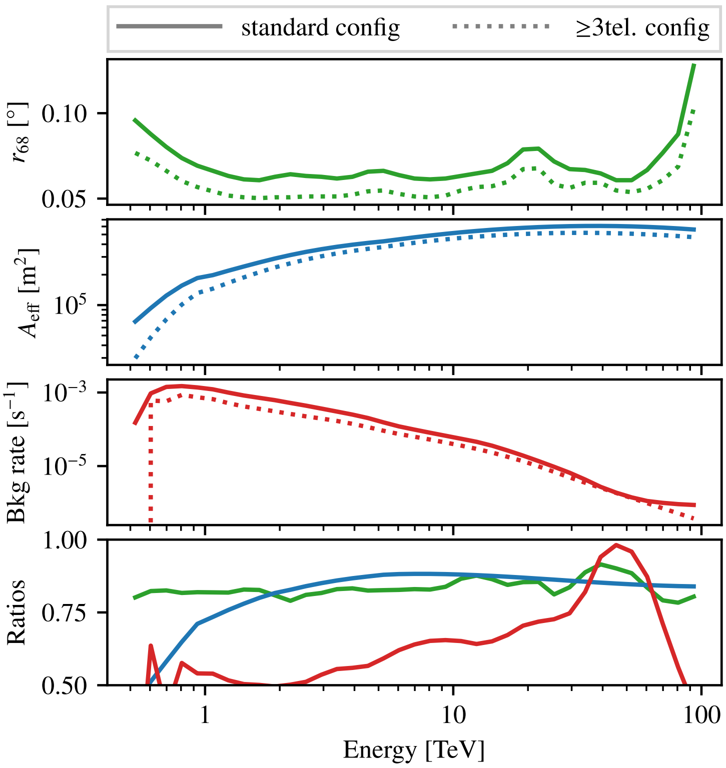

Figure 4.2: Comparison of the H.E.S.S. stereo IRFs between the standard configuration (solid) and the configuration requiring a minimum of 3 telescopes (dotted). The panels show (from top to bottom): the angular resolution, effective area, background rates in a circle around the Crab Nebula with $r = 0.2°$, and the ratios between the 3tel and the standard configuration.

Additionally, we used 65 observation runs (≈30 hours) of mono data taken with the CT5 telescope with its new camera, between Nov. 2019 and Oct. 2021. This data set has a lower energy threshold (≈240 GeV) compared to the stereo one, which increases the overlap with the energy range covered by the *Fermi* LAT (see next section). Because the reconstruction of events uses information from only one telescope in this case, the performance in terms of angular resolution (0.13°) and energy resolution (29%) is worse compared to the stereo data set. A summary of the H.E.S.S. data sets can be found in

Table 4.1.

Table 4.1: Overview of H.E.S.S. data.

Data set	Year	Runs	Observation time (h)
stereo	2004	18	7.82
	2005	6	2.81
	2007	5	2.34
	2008	4	1.43
	2009	10	4.69
	2013	58	25.19
	2014	7	3.01
	2015	6	2.80
mono	2019	18	8.41
	2020	42	19.44
	2021	5	2.09

The separation into years is done only for illustrative purposes here; the data are not separated by year when they enter the analysis.

The region of interest (RoI) for the H.E.S.S. data analysis is defined as a region of $5^\circ \times 5^\circ$ around the position of the Crab Nebula, in Galactic coordinates. Because the extension of the Crab Nebula is at the limit of detectability for H.E.S.S., we chose a relatively fine spatial bin size of 0.01°, to achieve an accurate description of the PSF and to not smear the signal artificially. Furthermore, we binned the data in energy using 16 bins per decade. For better performance, we only considered events with a maximum offset of 1.5° from the pointing position in each observation run.

In a first step, we fitted the normalisation and spectral tilt[29] of the background model template to each observation individually, where we excluded a circular region with radius 0.3° around the Crab Nebula. For the stereo data, we then binned the observations by zenith angle into three bins with edges $[45, 47.5, 52.5, 55]^\circ$, so that the observations in each bin have nearly identical energy thresholds. The mono observations exhibit a smaller variation in zenith, so that this procedure is not necessary. For each bin, as well as for the mono data, we combined the respective observations to a stacked data set. In the stacking process, the counts, exposure, and predicted background are summed while the energy dispersion and point spread function are averaged. The stacking makes the analysis computationally less expensive at the cost of using slightly less accurate IRFs. The binning of observations in zenith angle prevents the averaging of IRFs across observation runs with too dissimilar observing conditions. We additionally smoothed the runs-averaged PSF with a $30''$ one-dimensional Gaussian kernel, which represents the scale of pointing uncertainty of the telescopes (Braun, 2007), where we assume that the pointing error varies from run to run. After this procedure, we are left with three stereo data sets (for low, medium, and high zenith angles) as well as one mono data set.

Subsequently, we modelled the γ-ray emission of the Crab Nebula, that is, we performed a three-dimensional likelihood analysis as introduced in Sect. 1.6 to simultaneously fit the spatial morphology and the energy spectrum. We used a symmetric, two-dimensional Gaussian as spatial model for the intrinsic source distribution, which is then folded with the PSF. At this stage, we did not yet consider a possible energy dependence of the spatial model. All extension measurements reported in this work denote the 68% containment radius of the emission, which for a two-dimensional Gaussian with width σ is given by $r_{68} = \sqrt{-2 \cdot \ln(1 - 0.68)}\,\sigma \approx 1.5 \cdot \sigma$. From the stereo data set, we obtain a fitted extension

[29] The spectral tilt parameter δ modifies the predicted background rate R at energy E as $R' = R \cdot (E/1\,\mathrm{TeV})^{-\delta}$.

(averaged over energy) of $1.62' \pm 0.05'_{\mathrm{stat}}\,{}^{+0.21'}_{-0.24\mathrm{sys}}$. The systematic uncertainty is derived by repeating the analysis with a PSF that has been broadened (narrowed) by 5% with respect to the default one, independent of energy. The variation of 5% in width has been established as a realistic value in a study – with the same analysis configuration as employed here – of the bright blazar PKS 2155−304 (see e.g. Abramowski et al., 2010), which appears as a point-like source for the H.E.S.S. array. It amply covers the 30″-smoothing applied to the PSF earlier. Finally, we note that given the larger systematic uncertainty and considerably larger PSF of the mono data, we cannot constrain the extension with this data set.

The obtained value is larger than the one found in Abdalla et al. (2020b), $r_{68} = 1.30' \pm 0.07'_{\mathrm{stat}} \pm 0.17'_{\mathrm{sys}}$, although we note that the deviation is far from significant when taking into account the systematic uncertainties. We attribute the difference partly to the fact that at the lower energy threshold achieved here (560 GeV instead of 700 GeV), the extension is indeed expected to be slightly larger. Nevertheless, we note that this comparison of results indicates that the systematic uncertainty may be slightly underestimated. The measured extension is compatible with the upper limits provided by the HEGRA telescopes (Aharonian et al., 2000; Aharonian et al., 2004).

For the spectral model, we used a log-parabola function,

$$\frac{dN}{dE} = N_0 \left(\frac{E}{E_0}\right)^{-\alpha-\beta\ln(E/E_0)}, \tag{4.1}$$

with normalisation N_0, reference energy E_0, spectral index α, and curvature parameter β. From a joint fit to all H.E.S.S. data sets, we obtain $N_0 = (4.06 \pm 0.03) \times 10^{-11}\,\mathrm{TeV}^{-1}\,\mathrm{cm}^{-2}\,\mathrm{s}^{-1}$ at $E_0 = 1\,\mathrm{TeV}$ (fixed), $\alpha = 2.530 \pm 0.006$, and $\beta = 0.086 \pm 0.005$; this result is shown as a black line in Fig. 4.3. For both the mono and stereo data, we

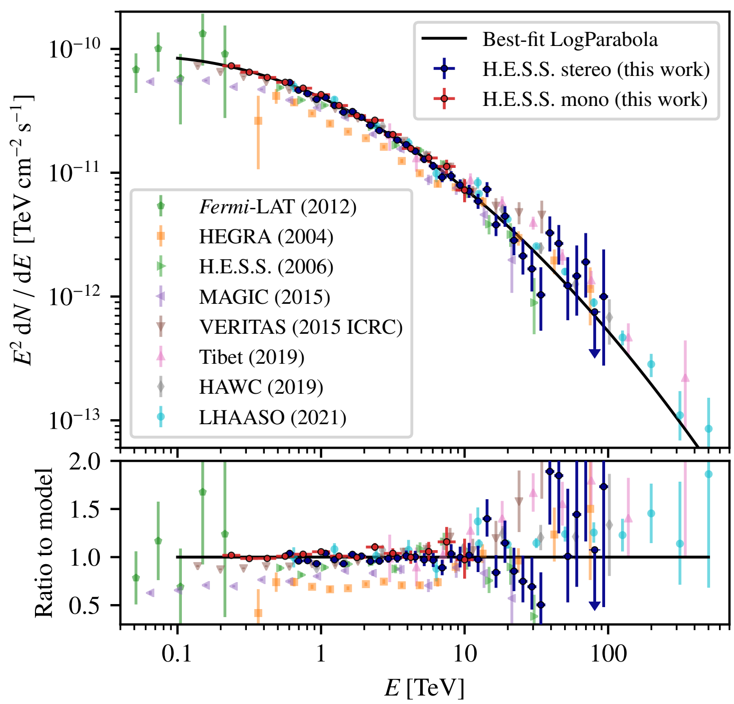

Figure 4.3: H.E.S.S. flux points of the mono (CT5) analysis (red) and stereo (CT1-4) analysis (blue) in comparison to results from other instruments. The error bars show the 68% statistical uncertainty. Points less significant than 2σ are shown as 95% confidence level upper limits. The black line displays the result of fitting a log-parabola model to the H.E.S.S. data of this work. References (in the order of the legend): Aharonian et al. (2004), Aharonian et al. (2006), Aleksić et al. (2015), Meagher (2015), Amenomori et al. (2019), Abeysekara et al. (2019), and Cao et al. (2021a).

subsequently derived separate sets of flux points by first performing the fit separately for each data set, and then re-adjusting the normalisation parameter in narrow energy ranges (where we have ensured that the best-fit models for the two sets are compatible with each other). Taking into account the relatively poor energy resolution of the mono data, we reduced the number of flux points (from 16 to 8 per decade in energy) for this data set in order to avoid correlations between the points. Both the stereo and mono flux points are also displayed in Fig. 4.3. The figure illustrates that the mono data set allows us to extend the measurement to lower energies, whereas the stereo data set extends up to almost $\sim$100 TeV. A comparison with results from other instruments shows that our derived flux is largely compatible, with the noticeable deviations most likely explained by a systematic shift in the energy scale of the instruments. The spectral results have been confirmed in several one-dimensional analyses based on the more traditional reflected-background method (Fomin et al., 1994; Berge et al., 2007). One example of such a comparison is shown in Appendix B. Finally, we note that in contrast to the Fermi-LAT analysis (see next section), the γ-ray emission from the Crab Pulsar itself, despite extending into the TeV energy range (Ansoldi et al., 2016), can safely be neglected for our study. Adopting the measured spectrum of the pulsed emission from Ansoldi et al. (2016), even the contamination for the lowest-energy flux point derived with the H.E.S.S. mono data set is below 0.5%.

4.2.2 Fermi-LAT data analysis

The *Fermi* LAT is a pair conversion telescope designed to measure γ rays with energies from 20 MeV to above 300 GeV (Atwood et al., 2009). We first performed a pulsar phase-resolved reference analysis of the Crab Nebula using the standard FERMITOOLS version 1.2.23[30] and FERMIPY, version 0.19.0+14[31] (Wood et al., 2017). This analysis serves as a comparison for the GAMMAPY analysis.

To this end, we selected γ rays that were observed between 4 August 2008 and 4 January 2020 in the energy range between 100 MeV and 3 TeV and within a $10^\circ \times 10^\circ$ RoI centred on the nominal Crab Nebula position provided in the fourth Fermi-LAT γ-ray source catalogue (4FGL; Abdollahi et al., 2020). As we are interested in emission of the nebula and not the pulsar, we proceeded to determine the off-pulse phase interval. To do so, we used an ephemeris prepared following the methods described in Ajello et al. (2022) and generated a histogram of the pulsar phases ϕ of all photons that have arrived within a 1° radius around the Crab Nebula, see Fig. 4.4. The off-pulse phase interval is determined with the 'quiescent background' (QB) algorithm introduced by Meyer et al. (2019). The resulting interval is $0.51 \leqslant \phi \leqslant 0.89$, as indicated by the red-shaded region in Fig. 4.4.

In the 4FGL, the total emission from the Crab Nebula is modelled with two superimposed source models for the high-energy tail of the synchrotron emission and the emission due to IC scattering, respectively. For the combination with H.E.S.S. data, we are mostly interested in the IC part of the spectrum. As the synchrotron and IC components are of similar intensity around 1 GeV, we proceeded in an iterative fashion: we first optimised an RoI model over the entire energy range. We then fixed the synchrotron component to the best-fit model and performed a second analysis of the nebula above 1 GeV, which is dominated by IC radiation. For this second analysis, we also used a finer spatial binning (see below) in order to be able to determine the extension of the IC nebula.

For the initial RoI model, we selected photons within the off-pulse interval and we further excluded events that have arrived at a zenith angle above 90° in order to mitigate contamination of γ rays originating from Earth's limb. We also excised periods of bright γ-ray bursts and solar flares that have been detected with a test statistic (TS) > 100.[32] We used the `Pass 8` IRFs (Atwood et al., 2013) and selected γ rays passing the `P8R3 SOURCE` event selection. We chose a spatial binning of $0.04^\circ\,\mathrm{pixel}^{-1}$ and eight energy bins per decade.

[30] `http://fermi.gsfc.nasa.gov/ssc/data/analysis/software`

[31] `http://fermipy.readthedocs.io`

[32] The TS is defined as $\mathrm{TS} = -2\ln(\mathcal{L}_1/\mathcal{L}_0)$, i.e. the log-likelihood ratio between the maximised likelihoods $\mathcal{L}_1$ and $\mathcal{L}_0$ for the hypotheses with and without an additional source, respectively (Mattox et al., 1996).

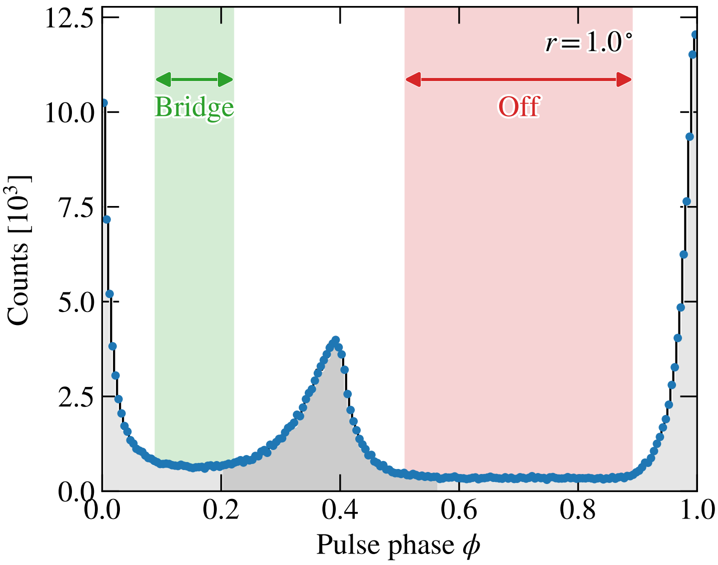

Figure 4.4: Distribution of pulsar phases of γ-ray candidate events detected with Fermi-LAT around the Crab Nebula. The distribution includes events with a reconstructed arrival direction that is within 1° of the Crab Nebula's position. The shaded regions indicate the intervals for the Bridge emission ($0.09 \leqslant \phi \leqslant 0.22$, not relevant here) and Off region ($0.51 \leqslant \phi \leqslant 0.89$) derived with the QB algorithm. The grey shaded areas indicate regions found by the HOP algorithm, which identifies 'watersheds' between local maxima (Meyer et al., 2019). There are shown here for illustration only.

We initialised the RoI model with all point-like and extended γ-ray sources within 20° of the RoI centre as listed in the 4FGL (except the Crab Pulsar), from which we also took the initial spectral source parameters. Additionally, the standard templates for isotropic and Galactic diffuse emission are used.[33] In the Fermi-LAT energy range, the synchrotron component is expected to exhibit only a very small spatial extension that is not resolvable with Fermi-LAT, and therefore modelled as a point-like source. For the IC component, we used the 4FGL default source morphology, which is given by a radial Gaussian with a width of $\sigma = 0.0198°$ ($r_{68} = 1.79'$). As for the spectrum, the synchrotron part is modelled with a simple power law,

$$\frac{dN}{dE} = N_0 \left(\frac{E}{E_0}\right)^{-\Gamma}, \tag{4.2}$$

with normalisation N_0, reference energy E_0, and spectral index Γ, whereas the IC component is described with a log-parabola as defined in Eq. 4.1. After an initial optimisation, we freed the spectral normalisation and spectral shape parameters of sources within 10° from the RoI centre as well as all spectral parameters of the isotropic and diffuse emission templates. We froze all spectral parameters for sources with TS < 5. After successful convergence of the fit, we generated a TS map to search for additional point sources. For each pixel in the RoI, we added a putative point source with a power-law spectrum with index $\Gamma = 2$ and calculated its TS. No additional sources with $\sqrt{\mathrm{TS}} \geqslant 5$ were found. The best-fit spectrum of the synchrotron component is shown in Fig. 4.5 and the parameters are provided in Table 4.2.

The best-fit RoI model was then used to perform an analysis above 1 GeV. In terms of data selection, we followed the official Fermi-LAT recommendations and relaxed the zenith angle cut from 90° to 100°. We shrank the RoI to $6° \times 6°$ and following Ackermann et al.

[33]We used the file gll_iem_v07.fits or the Galactic diffuse emission and the file iso_P8R2_SOURCE_V6_v07.txt for the isotropic diffuse component; see: `http://fermi.gsfc.nasa.gov/ssc/data/access/lat/BackgroundModels.html`

Table 4.2: Best-fit parameters of synchrotron and IC emission models of the Crab Nebula derived from Fermi-LAT data.

	N_0 (10^{-7} MeV^{-1} cm^{-2} s^{-1})	E_0 (MeV)	Γ or α	β
Synchrotron	2.47 ± 0.06	50.6	3.638 ± 0.024	–
IC (full energy range)	$(4.75 \pm 0.10) \times 10^{-6}$	10^4	1.762 ± 0.012	0.053 ± 0.006
IC ($E \geqslant 1$ GeV)	$(4.93 \pm 0.11) \times 10^{-6}$	10^4	1.768 ± 0.013	0.054 ± 0.008
IC ($E \geqslant 1$ GeV, $\gamma\pi$)	$(4.88 \pm 0.11) \times 10^{-6}$	10^4	1.763 ± 0.013	0.056 ± 0.008

$\gamma\pi$ = GAMMAPY

(2018), we chose a finer spatial binning of $0.025°$ pixel^{-1} that we apply in the calculation of the livetime and exposure cubes. Furthermore, we made use of PSF event types (Atwood et al., 2009). The data are split into four sets according to the quality of the reconstruction of the γ-ray arrival directions. Each set is analysed with its own specific IRFs and the four sets are combined by multiplying their respective likelihood values. Accordingly, the isotropic background templates for these event types have been used. We also limited the maximum energy of the analysis to the edge of the energy bin that contains the highest energy photon, that is, 1.78 TeV. The spectral parameters of the synchrotron component have been fixed. The resulting spectrum is presented in Fig. 4.5 and the best-fit spectral parameters are listed in Table 4.2. They agree well with the spectral parameters of the fit over the whole energy range.

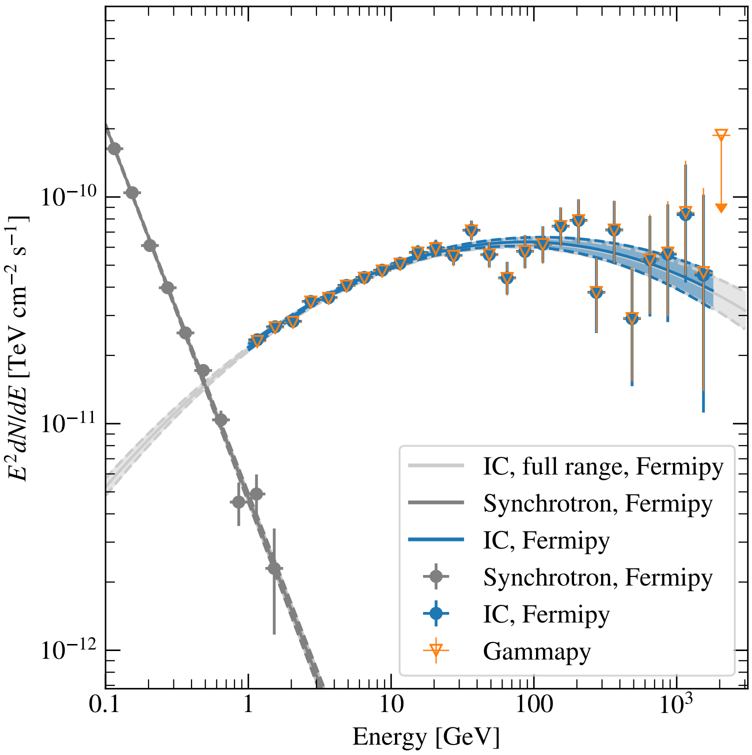

Figure 4.5: Fermi-LAT spectra of synchrotron and IC emission. The IC emission is derived with both FERMIPY and GAMMAPY and the spectra agree remarkably well. Details on the GAMMAPY analysis of Fermi-LAT data are given in Sec. 4.3.1. The error bars on the flux points show the 68% statistical uncertainties.

Finally, we obtained the extension of the nebula using a two-dimensional Gaussian model as before. In this procedure, the nebula's sky coordinates are additional free parameters, as are the spectral normalisation parameters of the diffuse background sources. The spectral parameters of the nebula itself are frozen to their best-fit values. We obtain a 68 % containment radius of $r_{68} = 2.22' \pm 0.18'_{\mathrm{stat}}\ {}^{+0.54\prime}_{-0.48\mathrm{sys}}$, where the systematic uncertainties are derived by using a bracketing method for the PSF (Ackermann et al., 2018). We find a TS value for the extension of $TS_{ext} = 47.6$ with the nominal PSF, which reduces to $TS_{ext} = 16.3$ if the larger bracketing PSF is used instead. These results are compatible with the extension found by Ackermann et al. (2018), $r_{68} = 1.80' \pm 0.18'_{stat} \pm 0.42'_{sys}$, within the uncertainties.

4.3 Combined analysis

In contrast to previous analyses, in which final data products such as flux points or extension measurements from different instruments have been analysed together, here we combine the Fermi-LAT and H.E.S.S. data at the event level. The advantage of this approach is that we are able to exploit more information and ensure consistency of spectral and morphological models between the different instruments. In the combined analysis we simultaneously fitted one three-dimensional source model (spectrum and morphology) to the (binned) event data of Fermi-LAT and H.E.S.S.. The analysis is carried out with Gammapy, where we used the data sets which we generated and cross-checked for the individual analyses and summed their respective Cash statistic values in the combined analysis. The total $\mathcal{C}$ value is then minimised, which corresponds to a joint fit of the model to the Fermi-LAT and H.E.S.S. data sets.

4.3.1 Preparation of Fermi-LAT data in Gammapy

During the Fermipy analysis the events are binned into a counts cube, and the IRFs (exposure, energy dispersion, and PSF) are calculated. We used the data products generated during the Fermi-LAT analysis to set up the combined analysis within Gammapy, where we generated four separate Fermi-LAT data sets, corresponding to the four PSF classes. While the analyses with Fermipy and Gammapy are in principle very similar, there are some differences which require adaptations in the data production steps. These are described in the following.

First, Gammapy only calculates model fluxes of sources within the RoI, whereas the standard Fermi-LAT analysis tools allow the inclusion of source models outside the RoI, which may contribute to the observed counts in the RoI especially at low energies, where the Fermi-LAT PSF is very broad. Consequently, the RoI size of the Fermi-LAT data sets has been increased to $10° \times 10°$, such that the 4FGL sources outside the inner ($6° \times 6°$) analysis region are also evaluated by Gammapy. Additionally, to correctly take into account the energy dispersion at the boundaries of the analysed 'reconstructed' energy range with Gammapy, we need to be able to evaluate the IRFs at 'true' γ-ray energies that extend beyond this range. As it is not possible to separately define the ranges to be considered for reconstructed and true energy in Fermipy, we increased the energy range by two bins at the low-energy end and by one bin at the high-energy end. The added spatial and energy bins were then again masked in the Gammapy analysis, so that exactly the same regions and energy bins as in the Fermipy analysis contribute to the likelihood calculation.

To verify that our analysis setup in Gammapy is correct, we repeated the analysis of the Fermi-LAT data previously carried out with Fermipy (cf. Sect. 4.2.2), using exactly the same model components. In the fit, the model parameters of the Crab Nebula's IC emission as well as normalisation of the isotropic diffuse and Galactic diffuse backgrounds and spectral index of the Galactic diffuse model are left free, while all parameters of the other source models in the RoI are fixed to the best-fit values from the Fermipy analysis. With this procedure, we obtain an excellent agreement between the Fermipy and the Gammapy analysis. For the spectrum, this is illustrated in Fig. 4.5 and summarised in Table 4.2. For the extension, the Gammapy fit yields $r_{68} = (2.10 \pm 0.18_{stat})'$, which is consistent with the Fermipy result given at the end of Sect. 4.2.2.

4.3.2 Measuring the Crab Nebula's combined energy spectrum and extension

Through the combined fit, we can now consistently measure the extension of the Crab Nebula across the combined energy range of Fermi-LAT and H.E.S.S.. To this end, we fitted our models jointly to the Fermi-LAT and H.E.S.S. data sets as defined in the previous sections. As in the separate analyses, we used a two-dimensional Gaussian as the spatial model. Because the log-parabola model does not yield a satisfactory description of the IC component across the entire energy range covered by our combined fit, we used a smoothly broken power-law model for the spectral component:

$$\frac{dN}{dE} = N_0 \left(\frac{E}{E_0}\right)^{-\Gamma_1} \left[1 + \left(\frac{E}{E_{\text{break}}}\right)^{\frac{\Gamma_2 - \Gamma_1}{\beta}}\right]^{-\beta}, \tag{4.3}$$

with E_0 fixed at 1 TeV. A fit over the whole energy range yields the following parameters: $N_0 = (3.35 \pm 0.22) \times 10^{-10}\,\text{TeV}^{-1}\text{s}^{-1}\text{cm}^{-2}$, $\Gamma_1 = 1.61 \pm 0.02$, $\Gamma_2 = 2.95 \pm 0.02$, $E_{\text{break}} = 0.33 \pm 0.02\,\text{TeV}$, and $\beta = 1.73 \pm 0.07$. This model is preferred over the log-parabola model by a difference of 94 in the Akaike information criterion, $\text{AIC} = \mathcal{C} + 2N_{\text{par}}$ (Akaike, 1974), where the number of free model parameters is $N_{\text{par}} = 3$ for the log-parabola model and $N_{\text{par}} = 5$ for the smoothly broken power-law model. Both models are shown in Fig. 4.6, together with the Fermi-LAT and H.E.S.S. flux points derived in this work. A comparison of the models with the LHAASO flux points, also shown in the plot, indicates that an extension of the analysis beyond 100 TeV would require the addition of another break to the spectral model.

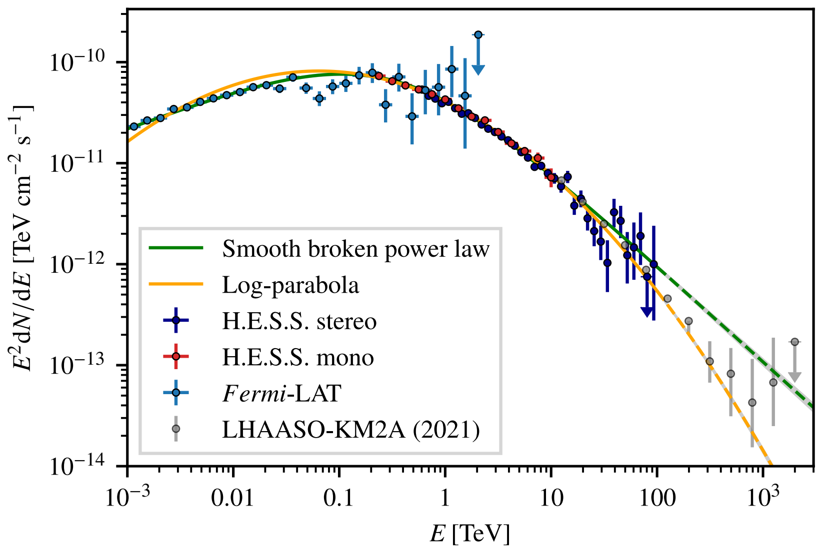

Figure 4.6: Comparison of log-parabola and smoothly broken power law spectral models. Both are fitted to the Fermi-LAT and H.E.S.S. data sets, while the LHAASO flux points are not included in the fit and only shown for comparison.

The best-fit position over the whole IC energy range is $(184.5499 \pm 0.0004_{\text{stat}})°$ Galactic longitude and $(-5.7825 \pm 0.0004_{\text{stat}})°$ Galactic latitude. This position is shifted to the north with respect to that of the Crab Pulsar by $\approx 28''$. In what follows, the only parameter of interest is the extension parameter of the Gaussian spatial model. However, in order to take into account possible correlations with other parameters, the following parameters are also left free: amplitude and position of the Crab Nebula source model, as well as the normalisation parameters of the Fermi-LAT isotropic and Galactic diffuse background models and the H.E.S.S. background models. The rest of the spectral parameters as well as the rest of the Fermi-LAT RoI model remain fixed. To obtain an energy-dependent measurement of the extension, we optimised the free parameters separately in different energy intervals, where we used a binning of two bins per decade in the observed energy range between 1 GeV and 100 TeV. As an important cross-check, we also compared the best-fit position of the Crab Nebula spatial model between all energy bands, finding that they are all compatible with each other within the uncertainties. Furthermore, the fitted extensions remain unchanged if the centre of the spatial model is fixed to a common position for all energy bands.

As the PSF of the H.E.S.S. mono data set is not understood well enough, we did not include this set in the measurement of the extension. Potentially large systematic effects may otherwise dominate the extension measurement between 240 GeV and 560 GeV (where the stereo data set has its threshold), due to the large number of events detected at these energies.

In Fig. 4.7 we show the measured extension as a function of the γ-ray energy. Below the threshold of the H.E.S.S. stereo data set, 560 GeV, only the Fermi-LAT data contribute. To obtain a more significant extension, we have merged the first and last two bins in this range. Above 560 GeV, the H.E.S.S. data immediately dominate the fit due to the much larger effective area and better angular resolution. The highest significance for an extension is reached in the energy bin ranging from 1–3 TeV; this range also dominates the

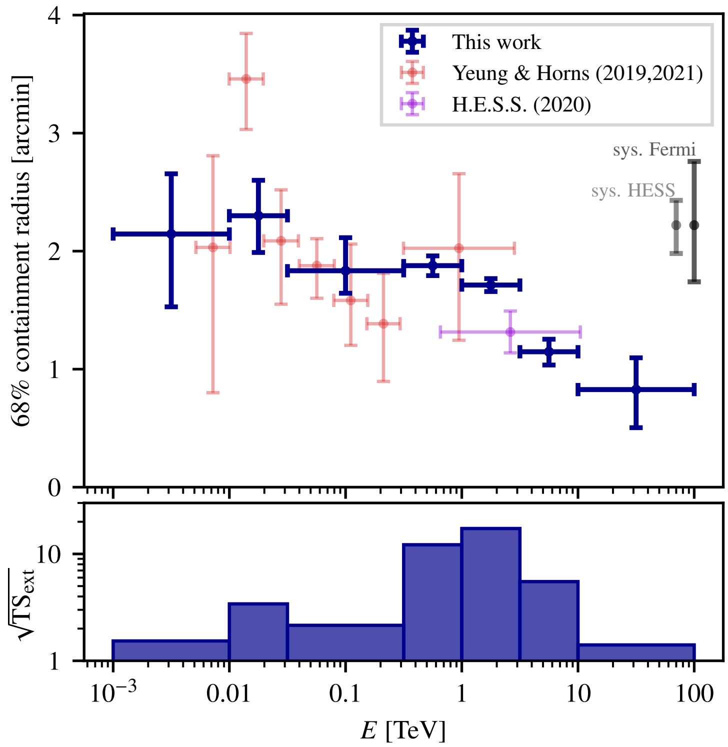

Figure 4.7: 68% containment radius of the γ-ray emission from the Crab Nebula measured with the combined Fermi-LAT and H.E.S.S. data analysis. The error bars denote the 1σ statistical uncertainties and do not include systematic effects. For comparison, the red points show the extension measured with Fermi-LAT by Yeung and Horns (2019) and Yeung and Horns (2021), whereas the purple point displays the extension previously measured with H.E.S.S. (Abdalla et al., 2020b). In grey we show the systematic uncertainty of the H.E.S.S. and Fermi-LAT measurements, respectively (cf. Sect. 4.2.1 & Sect. 4.2.2). The bottom panel shows the square root of the TS value of the measured extension, which gives an indication of the (statistical) significance of the extension with respect to the null hypothesis of a point-like source.

energy-integrated extension measurement with H.E.S.S. presented in Sect. 4.2.1.

The extensions measured in the ranges dominated by the Fermi-LAT and H.E.S.S. data, respectively, connect smoothly and are furthermore consistent with published results. Overall, we find strong evidence for an extension that decreases with energy. As we subsequently see in Sect. 4.4, this result is in very good agreement with theoretical expectations.

The decreasing extension is also illustrated in Fig. 4.8, where we show a measurement of the Crab Nebula in the optical regime and at X-ray energies, and compare this to our extension measurements with Fermi-LAT and H.E.S.S.. As noted earlier, the fit of the

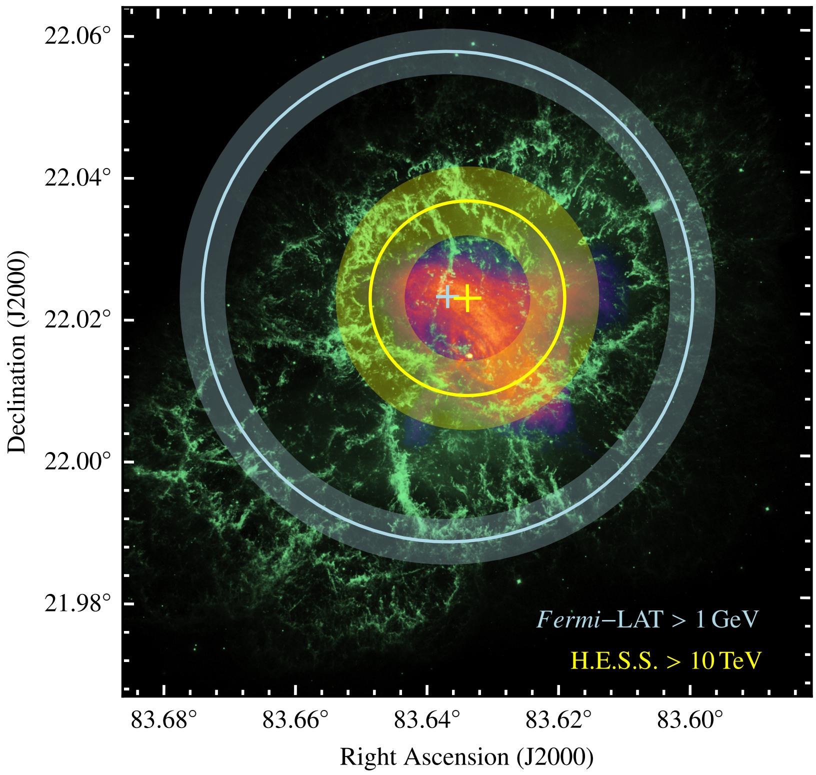

Figure 4.8: Optical image of the Crab Nebula in green (credit: NASA, ESA/Hubble), overlaid with an X-ray image in red, taken with *Chandra* (0.3–10 keV; credit: NASA/CXC/SAO, `https://chandra.harvard.edu/photo/openFITS/crab.html`). The circles show the 68% containment radii of the γ-ray emission measured with Fermi-LAT (>1 GeV; blue) and H.E.S.S. (>10 TeV; yellow), where the bands illustrate the statistical uncertainties. The crosses indicate the fitted position and its uncertainty for the respective data sets.

Fermi-LAT data above 1 GeV yields an extension of $r_{68} = (2.10 \pm 0.18_{\mathrm{stat}})'$. The extension measured with H.E.S.S. above 10 TeV, on the other hand, is $r_{68} = (0.82 \pm 0.29_{\mathrm{stat}})'$. In most models, as will be further detailed in the subsequent section, the optical radiation is produced by electrons that are also responsible for the IC emission in the Fermi-LAT energy range. In agreement with this, the position and extension of the emission measured with Fermi-LAT is roughly consistent with the outline of the nebula seen in the optical image. As the electrons radiating the X-ray synchrotron photons also produce the highest-energy IC emission, a similar agreement between the X-ray image and the H.E.S.S. measurement above 10 TeV is expected. However, while the centroid of the γ-ray emission coincides well with a region of bright X-ray emission, we observe that the 68% containment radius measured with H.E.S.S. almost entirely encloses the X-ray emission, which is an unexpected result. While the argument here is rather qualitative, this point will be addressed again in a more quantitative way in the discussion of the modelling results in Sect. 4.4.3. There, we confirm that the models investigated in this work fail to explain the difference between the extension in X-rays and at the highest-energy γ rays. While the difference could also be due to underestimated systematic effects (which will be discussed in Sect. 4.5), it hints at an incompleteness of the models.

4.4 Modelling of the Crab Nebula

In this section we introduce the phenomenological models that we investigate in this work. We present the results of fitting them to the Fermi-LAT, H.E.S.S., and MWL data and discuss the implications. In total, we tested three time-independent leptonic models that differ in the modelling of the high-energy electrons and the radial dependence of the magnetic field. All models are radially symmetric self-synchrotron Compton (SSC) models, in which the low-energy photons are produced by synchrotron emission and the high-energy photons by IC scattering, where the synchrotron photons themselves serve as one of the targets.

4.4.1 Physical emission models for the Crab Nebula

We model the broadband electromagnetic emission of the Crab Nebula through a radially symmetric steady-state model of the electron distribution, inspired by the constant B-field model introduced by Meyer et al. (2010), which has been extended to a spatially variable B-field model in Dirson and Horns (2023). An alternative description is the radially symmetric magneto-hydrodynamic (MHD) flow solution obtained by Kennel and Coroniti (1984a). For comparison with the data, we need to calculate the predicted emission as a function of energy and angular separation between the line of sight and the nebular centre (this is equal to the two-dimensional sky position in the radially symmetric case). The basic ingredients to do so are the radial profile of the magnetic field, $B(r)$, and the electron distribution, $n_{\mathrm{el}}(\gamma, r) \equiv dN_{\mathrm{el}}/d\gamma dV$, that is, the number of electrons per unit volume and Lorentz factor γ as a function of the distance to the nebula centre. For the description of the radial dependence of the magnetic field, we follow (1) Meyer et al. (2010) for a model where the magnetic field is constant throughout the nebula (constant B-field model); (2) Dirson and Horns (2023), where the magnetic field decreases (with adjustable rate) with increasing distance from the centre of the nebula (variable B-field model); and (3) Kennel and Coroniti (1984a) for a MHD flow model (K&C model). In the following, we refer to the former two models as static models in contrast to the K&C model, which is a result of the MHD flow equations.

Given $B(r)$ and n_{el}, we calculate the spectral volume emissivity $j_\nu^{\mathrm{sync}}(\nu, r) \equiv dE/dtdVd\nu d\Omega$ for the synchrotron emission of a (pitch-angle averaged) chaotic magnetic field through (Blumenthal and Gould, 1970; Aharonian et al., 2010)

$$j_\nu^{\mathrm{sync}}(\nu, r) = \frac{1}{4\pi} \frac{\sqrt{3} e^3 B(r)}{m_e c^2} \int_1^\infty d\gamma n_{\mathrm{el}}(\gamma, r) \; G\left(\frac{\nu}{\nu_c}\right) , \tag{4.4}$$

where $\nu_c = 3eB\gamma^2/4\pi m_e c$ is the critical frequency and $G(x)$ is given by

$$\begin{aligned} G(x) \quad = \quad & \frac{x}{20} \Big[\left(8 + 3x^2\right) \left(K_{1/3}(x/2)\right)^2 + \\ & x K_{2/3}(x/2) \left(2K_{1/3}(x/2) - 3x K_{2/3}(x/2)\right) \Big] , \end{aligned} \tag{4.5}$$

with K_ξ the modified Bessel function of kind ξ. Throughout this paper, we use units of $\mathrm{erg\,s^{-1} Hz^{-1}\,cm^{-3}\,sr^{-1}}$ for j_ν.

For the dust emission, we follow Dirson and Horns (2023), who model the emission as a mixture of two dust populations at different temperatures T_i and total masses M_i, $i = 1, 2$. The two populations are contained in a shell with inner and outer radii $r_{\text{dust, in}}$ and $r_{\text{dust, out}}$, respectively, with respect to the pulsar position (which is equal to the centre of the nebula in our model). The density of dust within the shell is assumed to be constant. Assuming the two populations predominantly consist of amorphous carbon dust grains, the emissivity is given by

$$j_\nu^{\text{dust}}(\nu, r) = \frac{3\kappa_{\text{abs}}\left[\Theta(r - r_{\text{dust, in}}) - \Theta(r - r_{\text{dust, out}})\right]}{4\pi(r^3_{\text{dust, out}} - r^3_{\text{dust, in}})} \sum_{i=1,2} M_i B_\nu(T_i)\,, \tag{4.6}$$

where $\Theta(r)$ is the Heavyside step function, and $B_\nu(T)$ is the intensity of the black body emission at temperature T. The wavelength-dependent absorption coefficient is given by

$$\kappa_{\text{abs}} = 2.15 \times 10^{-4}\,\text{cm}^2\text{g}^{-1} \left(\frac{\lambda}{\mu\text{m}}\right)^{-1.3}\,. \tag{4.7}$$

Both the synchrotron and dust emission together with the CMB act as seed photon fields for IC scattering of the electrons for all models. The seed photon density, n^t_{seed}, $t = $ (sync, dust), as a function of photon energy $\epsilon = h\nu$ is calculated through the integral (Atoyan and Aharonian, 1996)

$$n^t_{\text{seed}}(\epsilon, r) = \frac{r_0}{2hc}\frac{4\pi}{\epsilon} \int\limits_{r_s/r_0}^{1} dy \frac{y}{x} \ln \frac{x+y}{|x-y|} j^t_\nu(\nu, r_0 y)\,, \tag{4.8}$$

in units of photons $\text{eV}^{-1}\,\text{cm}^{-3}$ and where $x = r/r_0$ and $y = r'/r_0$, with r_0 the radius of the nebula and $r_s = 0.13\,\text{pc}$ (Weisskopf et al., 2012) the shock radius until which no emission is assumed.[34] The seed photon density for CMB photons is simply $n^{\text{CMB}}_{\text{seed}} = (4\pi/(hc))B_\nu(T_{\text{CMB}})/(h\nu)$. We do not consider any additional photon fields such as optical line emission from the filaments (e.g. Meyer et al., 2010) or interstellar radiation fields, as these fields will give a subdominant contribution compared to the optical synchrotron and infrared dust emission, respectively.

The IC emissivity for up-scattered photons at frequency ν is then calculated using the integral over the IC kernel f_{IC}, which includes Klein-Nishina effects, and the seed photon density (Blumenthal and Gould, 1970),

$$\begin{aligned} j_\nu^{\text{IC}}(\nu, r) \;&=\; \frac{3\sigma_{\text{T}} hc}{4}\frac{h\nu}{4\pi} \int\limits_1^\infty d\gamma \frac{n_{\text{el}}(\gamma, r)}{\gamma^2} \\ &\times \int\limits_0^\infty d\epsilon f_{\text{IC}}(\nu, \epsilon, \gamma) \sum_t \frac{n^t_{\text{seed}}(\epsilon, r)}{\epsilon}\,, \end{aligned} \tag{4.9}$$

with the usual expression for the full IC kernel,

$$f_{\text{IC}}(\nu, \epsilon, \gamma) = 2q \ln q + (1 + 2q)(1 - q) + \frac{1}{2}\frac{(\Gamma_\epsilon q)^2}{1 + \Gamma_\epsilon q}(1 - q)\,, \tag{4.10}$$

[34] One should note that the actual size of the nebula is unknown as the outer shock is not observed (e.g. Hester, 2008). The size of the observed synchrotron nebula is a free parameter in our fit (see below) and r_0 acts as an arbitrary upper integration bound that should be large enough to accommodate the different nebula sizes probed in the fit. Here, we set it to 3.6 pc, which is twice the value assumed by Atoyan and Aharonian (1996) for the visible nebula size.

where $\Gamma_\epsilon = 4\epsilon\gamma/(mc^2)$ and $q = h\nu/(\Gamma_\epsilon(\gamma mc^2 - h\nu))$. The Thompson limit corresponds to $\Gamma_\epsilon \ll 1$ and IC scattering only occurs for $1/(4\gamma^2) \leqslant q \leqslant 1$.

The integrals are evaluated numerically and the code, fully written in PYTHON, is available online[35]. The IC emissivity of the synchrotron emission involves four integrals for each frequency ν and radius r, see Eqs. (4.4), (4.8), and (4.9). In order to speed up the calculations, we make heavy use of numerical routines of NUMPY, SCIPY, and NUMBA (Harris et al., 2020; Virtanen et al., 2020; Lam et al., 2015) and use multi-dimensional spline interpolations for j_ν^{sync} and $n_{\mathrm{seed}}^{\mathrm{sync}}$.

The specific luminosity for component $t =$ (sync, dust, IC) is found from the integration over radius,

$$\mathcal{L}_\nu^t = \oint d\Omega \int dV j_\nu^t(\nu, r) = (4\pi)^2 \int_{r_s}^{r_0} dr r^2 j_\nu^t(\nu, r)\,, \tag{4.11}$$

where the two factors of 4π come from the volume and solid angle integrations, respectively. For the analysis of H.E.S.S. and Fermi-LAT data, we are also interested in the spatial profile of the emission for which we have to calculate the specific intensity I_ν as a function of the angular distance θ from the centre of the nebula. The intensity is given as an integral over the line of sight (LoS) s ($s = 0$ is the position on the LoS which is closest to the centre of the nebula) through the nebula in which j_ν^t is non-zero,

$$I_\nu^t(\theta) = 2 \int_{s_{\min}}^{s_{\max}} ds j_\nu^t(\nu, r(s))\,. \tag{4.12}$$

This is illustrated in Fig. 4.9. The distance $r(s)$ from each point on the LoS to the centre of the Crab Nebula calculates as

$$r(s) = \sqrt{r_{\min}^2 + s^2}\,. \tag{4.13}$$

In this expression, $r_{\min} = d \sin\theta$ is the smallest distance from the LoS to the centre of the Crab Nebula, which depends on the observing angle θ and the distance d from the earth to the nebula. Consequently, the emissivity along the LoS is symmetric with respect to the $s = 0$ point which results in the factor two in front of the integral if we choose

$$s_{\min} = \begin{cases} \sqrt{r_s^2 - r_{\min}^2} & r_{\min} \leq r_s \\ 0 & \text{otherwise} \end{cases}\,. \tag{4.14}$$

The different cases correspond to a scenario where the LoS intersects with the shock radius and the integration starts at the point of the intersection, and another scenario where θ is large enough so that the LoS misses the shock radius. The upper integration bound $s_{\max}$ is set to the intersection with r_0 where the emissivities are negligible small.

The flux emitted from a point on the outer sphere of the nebula into a solid angle Ω is

$$F_\nu^t(\theta_0, \theta_1) = \int I_\nu \cos\theta d\Omega = 2\pi \int_{\theta_0}^{\theta_1} I_\nu \cos\theta \sin\theta d\theta\,. \tag{4.15}$$

The extension of our emission model is defined as the angle θ_{68} which contains 68 % of the flux, that is,

$$0.68 = \frac{F_\nu^t(0, \theta_{68})}{F_\nu^t(0, \theta_{\max})}\,, \tag{4.16}$$

[35] `https://github.com/me-manu/crabmeyerpy`

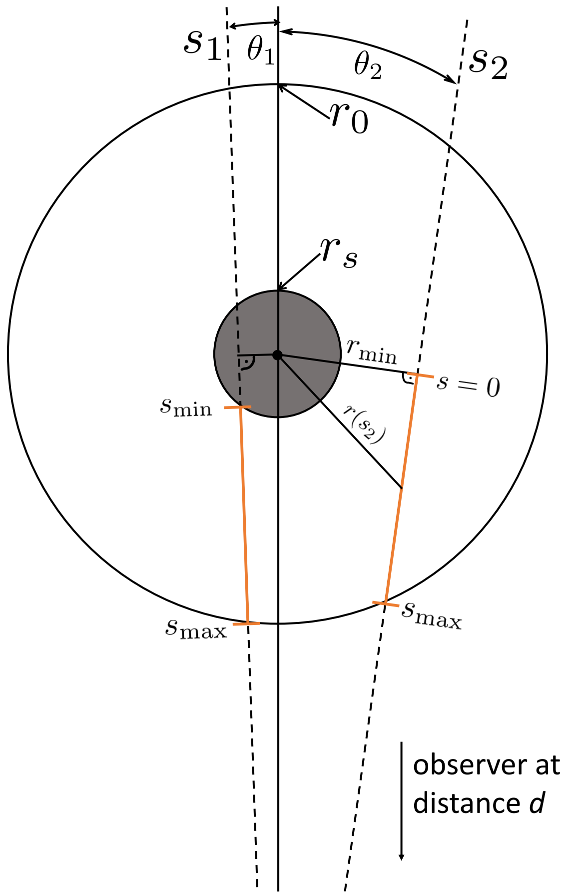

Figure 4.9: Illustration of the LoS integration. The pulsar in the centre is surrounded by a region with no emission, up to the shock radius r_s (dark shaded region). We assume non-zero emission until the maximum radius of the nebula at r_0. Here we illustrate two exemplary lines of sight s_1 and s_2 at angular offsets θ_1 and θ_2 with respect to the centre (dashed lines). s_1 represents a line which intersects the shock whereas s_2 does not. We integrate the emissivity j_ν along the parts of the lines that are marked in solid orange. Because of the radial symmetry of our model, these parts contain exactly half of the emission expected from the full LoS.

where the maximum angle $\theta_{\max}$ is defined through $\tan\theta_{\max} = r_0/d$.

For a full description of the emission model, what remains to be defined are the electron spectrum $n_{\mathrm{el}}(\gamma, r)$ and the magnetic field profile $B(r)$. The tested models are described in the following subsections.

Variable B-field model This is a phenomenological model developed in Meyer et al. (2010) and Dirson and Horns (2023), who expanded the previous works of de Jager and Harding (1992) and Hillas et al. (1998) to describe the Crab Nebula's SED and extension. Two distinct electron populations are assumed: relic 'radio' electrons at lower energies and freshly injected 'wind' electrons at higher energies. The wind electrons are constantly injected by the pulsar wind and accelerated at the wind's termination shock, whereas the origin of the radio electrons is still unclear (Atoyan and Aharonian, 1996). One possibility could be an injection during the early phases of the pulsar spin down (Atoyan, 1999). The shock is commonly associated with a bright X-ray ring feature located at a distance of $r_s = (13.3 \pm 0.2)''$ from the pulsar (Weisskopf et al., 2012), which corresponds to $r_s \approx (0.129 \pm 0.002)\,\mathrm{pc}$ for a distance of $d = 2\,\mathrm{kpc}$ between Earth and the pulsar, which we take as the centre of the nebula in our radially symmetric models. As the name suggests, the radio electrons are responsible for the synchrotron emission from radio frequencies to sub-millimetre / optical wavelengths whereas the wind electrons produce synchrotron emission at higher frequencies. Both wind and radio electron densities are assumed to be zero for radii smaller than the shock radius. The total electron spectrum is given by the sum of the two populations,

$$n_{\mathrm{el}}(\gamma, r) = n_{\mathrm{radio}}(\gamma, r) + n_{\mathrm{wind}}(\gamma, r)\,, \tag{4.17}$$

which are both a function of energy and distance from the nebula centre. The spectrum of the radio electrons is a simple power law with index s_r between gamma factors $\gamma_{r,\min}$ and $\gamma_{r,\max}$ with a super-exponential cutoff,

$$\begin{aligned} n_{\text{radio}}(\gamma, r) &= \frac{n_{r,0}}{\rho_r^3}\gamma^{-s_r}\exp\left[-\left(\frac{\gamma}{\gamma_{r,\max}}\right)^{\beta_{\min}}\right] \\ &\times \Theta(\gamma - \gamma_{r,\min})\exp\left(-\frac{r^2}{2\rho_r^2}\right) \\ &\times \Theta(r - r_s)\,, \end{aligned} \tag{4.18}$$

where $\Theta(x)$ is the Heavyside step function. The spatial dependence of the radio electrons is given by a Gaussian function of constant width ρ_r. Since the synchrotron cooling times are larger than the age of the nebula, the energy-independent spatial distribution of radio electrons is a valid approximation. The wind electrons, on the other hand, are modelled with a double broken power law with super-exponential cut-offs at low and high energies. As the radio electrons, the spatial extension of the wind electrons is assumed to follow a Gaussian whose width, however, also depends on energy. Putting everything together, one finds

$$\begin{aligned} n_{\text{wind}}(\gamma, r) &= \frac{n_{w,0}}{\rho_w(\gamma)^3}\exp\left[-\left(\frac{\gamma_{w,\min}}{\gamma}\right)^{\beta_{\min}}\right]\exp\left[-\left(\frac{\gamma}{\gamma_{w,\max}}\right)^{\beta_{\max}}\right] \\ &\times \left[\left(\frac{\gamma}{\gamma_{w,1}}\right)^{-s_{w,1}}\left(\frac{\gamma_{w,1}}{\gamma_{w,2}}\right)^{-s_{w,2}}(1-\Theta(\gamma-\gamma_{w,1}))\right. \\ &+ \left(\frac{\gamma}{\gamma_{w,2}}\right)^{-s_{w,2}}\mathcal{B}(\gamma,\gamma_{w,1},\gamma_{w,2}) \\ &+ \left.\left(\frac{\gamma}{\gamma_{w,2}}\right)^{-s_{w,3}}\Theta(\gamma-\gamma_{w,2})\right] \\ &\times \exp\left(-\frac{r^2}{2\rho_w(\gamma)^2}\right) \\ &\times \Theta(r-r_s)\,, \end{aligned} \tag{4.19}$$

where $\mathcal{B}(x,a,b)$ is the boxcar function, $\mathcal{B}(x,a,b) = \Theta(x-a) - \Theta(x-b)$. The energy dependence of the spatial extension is modelled through a simple power law

$$\rho_w(\gamma) = \rho_{w,0}\left[\left(\frac{\gamma}{9\cdot 10^5}\right)^2\right]^{-\alpha_w}\,. \tag{4.20}$$

For the free parameters $\gamma_{\text{r,max}}$, $\gamma_{\text{w,min}}$, and $\gamma_{\text{w,max}}$ we do not use abrupt cutoffs as those would lead to discontinuities on the numerical integration grid. Instead we use super-exponential cutoffs which are not motivated physically but help the smoothness of the likelihood landscape. For simplicity, the super-exponential indices are fixed to $\beta_{\min} = 2.8$ (this is the best-fit value obtained by Meyer et al., 2010) and $\beta_{\max} = 2$. Figure 4.10 shows the electron distribution for different energies and radii.

For the magnetic field profile, we follow Dirson and Horns (2023) and choose

$$B(r) = B_0\left(\frac{r}{r_s}\right)^{-\alpha}\,, \tag{4.21}$$

with $\alpha \geqslant 0$. The case of $\alpha = 0$ corresponds to the constant B-field model studied, for example, in Meyer et al. (2010). The profiles are also shown in Fig. 4.12.

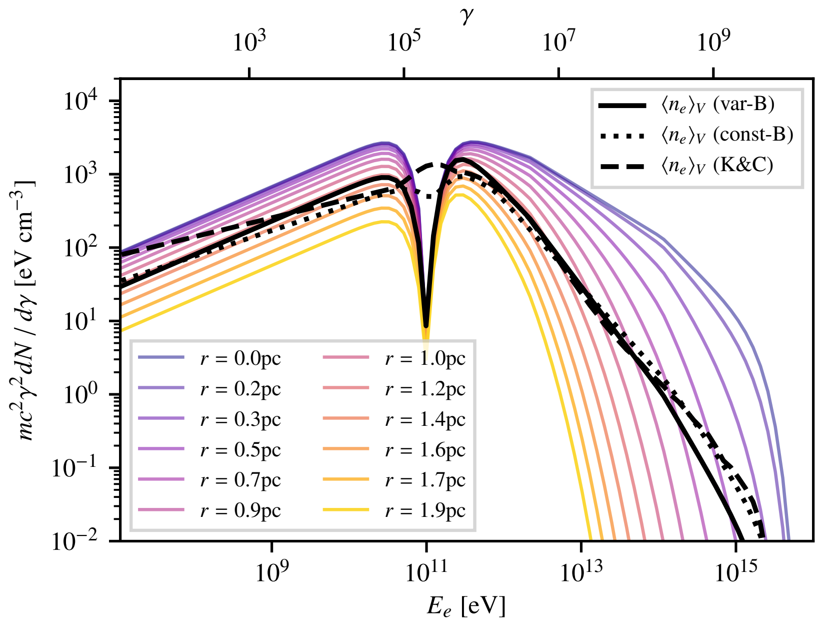

Figure 4.10: Electron densities of models, with parameters as given in Tab. 4.4. The solid, dotted and dashed black lines show the volume-averaged density for the variable B-field, the constant B-field and the K&C model, respectively. The coloured lines show the electron density for the variable B-field model at different radii. The radio electrons (at energies below the 'dip') are modelled with an energy-independent extension, therefore the density drops with radius independent of energy. On the other hand, the density of the freshly injected wind electrons decreases more rapidly for higher energies.

MHD flow model This model follows the solution to the steady-state MHD equations under the assumption of spherical symmetry and describes the flow of the electron plasma from the shock to the nebula's boundary. The MHD flow and the magnetic field are determined by the magnetisation σ at the shock, which is given by the ratio of the electromagnetic and particle energy flux,

$$\sigma = \frac{B_s^2}{4\pi n u_s \gamma m_e c^2}\,, \tag{4.22}$$

where B_s is the magnetic field, n the particle density, and $u_s = \sqrt{\gamma^2 - 1}$ the relativistic four speed (all quantities are at the shock radius).

The (injected) electron spectrum is another free parameter in the model. As in the previous model, we use two distinct electron populations, with the radio electrons modelled in the same way as Eq. 4.18 in the previous paragraph. On the other hand, the spatial and spectral distribution for the wind electrons are the result of solving the MHD equations for some electron population injected at the termination shock. While Kennel and Coroniti (1984a) considered a power law type injection, this was generalised by Atoyan and Aharonian (1996) to a more complex shape, which we also assume here with an additional break in the spectrum:

$$\begin{aligned}
n_s(\gamma) &= n_{0,w} \exp\left[-\left(\frac{\gamma_{w,\min}}{\gamma}\right)^{\beta_{\min}}\right] \exp\left[-\left(\frac{\gamma}{\gamma_{w,\max}}\right)^{\beta_{\max}}\right] \\
&\times \left[\left(1+\frac{\gamma}{\gamma_{w,\min}}\right)^{s_{w,1}} (1-\Theta(\gamma-\gamma_{w,2})) \right. \\
&+ \left. \frac{(1+\gamma/\gamma_{w,\min})^{s_{w,3}}}{(1+\gamma_{w,2}/\gamma_{w,\min})^{s_{w,3}-s_{w,1}}} \Theta(\gamma-\gamma_{w,2}))\right] . \qquad (4.23)
\end{aligned}$$

Similar to the wind electron spectrum for the static models, $\beta_{\min}$ and $\beta_{\max}$ are fixed to 2.8 and 2.0, respectively. From the MHD flow solution, the energy of electrons at some distance $z = r/r_s$ from the shock can be related to the electron Lorentz factor at injection, γ',

$$\gamma(z) = \frac{\gamma'}{(vz^2)^{1/3} + \gamma'/\gamma_{\max}} , \qquad (4.24)$$

where $v(z) = u(z)/u_s$ is the four-velocity of the electrons (see Eqs. (A7a) - (A7d) in Kennel and Coroniti, 1984b) which depends on the magnetisation σ, and $\gamma_{\max}$ is the maximum γ factor at distance z, see, for example, Eq. (6) in Atoyan and Aharonian (1996) (which also depends on vz^2). The wind electron spectrum is then found to be

$$n_{\mathrm{wind}}(\gamma, z) = (vz^2)^{-4/3} \left(\frac{\gamma'}{\gamma(z)}\right)^2 n_s(\gamma') . \qquad (4.25)$$

For small values of the magnetisation, the magnetic field in the MHD solution at the shock is given by

$$B_s = \sqrt{\frac{L_{\mathrm{spin-down}}}{cr_s^2} \frac{\sigma}{1+\sigma}} , \qquad (4.26)$$

where $L_{\mathrm{spin-down}}$ is the spin-down luminosity of the pulsar. Downstream of the shock, the magnetic field in the nebula evolves as

$$B(z) = B_s \frac{3(1-4\sigma)z}{vz^2} . \qquad (4.27)$$

4.4.2 Fitting of the models

All three models give a prediction of the γ-ray intensity as a function of energy and angular separation from the Crab Pulsar, which we forward-folded with the IRFs and fitted to the Fermi-LAT and H.E.S.S. binned event data sets as introduced in the previous sections. As the centroid of the γ-ray emission is slightly offset from the pulsar position (cf. Sect. 4.3.2), we shifted the model prediction spatially such that its centre coincides with the centroid of the γ-ray emission in order to ensure a proper convergence of the fit. This does not affect the predicted spectrum in a noticeable way. In the combined fit, all model components except the Crab Nebula SSC model (i.e. the background models for H.E.S.S. and the Galactic and isotropic diffuse emission models as well as the remaining sources in the RoI for Fermi-LAT) are frozen to pre-fitted values. Additionally, we fixed some of the model parameters to values employed by Dirson and Horns (2023), specifically all parameters relating to the dust model and the shock radius. The fixed parameters are marked as such in Table 4.4.

As the synchrotron photon field is a seed field for the IC up-scattering, we also need to ensure consistency with the observed synchrotron extensions which are measured with higher precision compared to the IC extensions. Therefore, we also included archival flux and extension measurements from radio frequencies to X-ray energies, taken from Dirson and Horns (2023)[36], to constrain the synchrotron flux predicted by our models (see also Fig. 4.1). This is done by computing a χ^2-value between the predicted and observed synchrotron flux and extensions and adding this value as a penalty term to the total $\mathcal{C}$-value of the fit of the IC spectrum,

$$\mathcal{C}_{\text{tot}} = -2 \ln \mathcal{L}_{\text{tot}} = \mathcal{C}_{\text{IC}} + \chi^2_{\text{SYN,flux}} + \chi^2_{\text{SYN,ext}} \,, \tag{4.28}$$

where $\mathcal{C}_{\text{IC}} = -2 \ln \mathcal{L}_{\text{IC}}$ is the Cash statistic of the model fitted to the Fermi-LAT and H.E.S.S. data. Lacking a detailed understanding of the systematic uncertainties associated with each of the synchrotron flux measurements, we added in quadrature to the uncertainty specified for each data point a relative systematic uncertainty of 7% (Meyer et al., 2010, see also Sect. 4.5).

Compared to the analysis in Dirson and Horns (2023), we used data from only two instruments to constrain the IC emission. However, both the Fermi-LAT and H.E.S.S. data sets analysed here are much larger compared to those utilised by Dirson and Horns (2023). Furthermore, we are able to include the extension of the IC nebula self-consistently in the fit because we use the three-dimensional information of the Fermi-LAT and H.E.S.S. event data (i.e. a mis-match in extension would lead to strong residuals in the fit). In order to achieve the largest possible overlap of the energy ranges covered by the Fermi-LAT and H.E.S.S. data, we included the H.E.S.S. mono data set in the combined analysis. This is acceptable despite the systematic uncertainties associated with the PSF of the mono data set because this data set contributes to the fit mostly in a relatively narrow energy range ($\sim$240–560 GeV), and we do not attempt to measure the extension as a function of energy here (in contrast to the analysis presented in Sect. 4.3.2).

Figure 4.11 shows the best-fit spatial models and residuals in five different energy bands for the variable B-field model. The residual maps show the deviations between the total (i.e. background + source) model prediction and the observed number of events in terms of $\sqrt{\text{TS}}$, where $\text{TS} \equiv -2 \ln(\mathcal{L}/\mathcal{L}_{\text{max}})$ and $\mathcal{L}_{\text{max}}$ is the likelihood corresponding to a model that perfectly predicts the observed number of events in each pixel. While not perfectly compatible with purely statistical fluctuations, the residual maps indicate that we achieve a satisfactory description of the extension of the nebula in the part of the IC spectrum probed with Fermi-LAT. However, in the part probed with H.E.S.S., especially in the 1–10 TeV range, we observe stronger residuals. The extension of the Crab Nebula is strongly constrained by the synchrotron measurements and appears too small when compared with the H.E.S.S. data, leading to negative residuals at the position of the Crab Nebula that are surrounded by an unaccounted-for excess. For the other two models this trend is similar, with even slightly larger residuals. This indicates that our models cannot simultaneously describe both the synchrotron and IC extensions together with the broadband SED (however, see Sects. 4.4.3 and 4.5 for a discussion of systematic uncertainties).

4.4.3 Discussion of the models

We now turn to the discussion of the physical models and how well they fit our data. For each of the models, we give a quantitative overview of the fit results in Table 4.3, that is, we provide the Cash statistic minimised by the fit as well as the number of fitted parameters and the number of synchrotron data points. An overview of all best-fit model parameters is provided in Table 4.4. The complexity of the models prevents a detailed assessment of the uncertainties on the model parameters. We therefore note that the best-fit values should

[36]The data points are available at `https://github.com/dieterhorns/crab_pheno`, where we have omitted points that also do not appear in Figs. 1 and 7 of Dirson and Horns (2023).

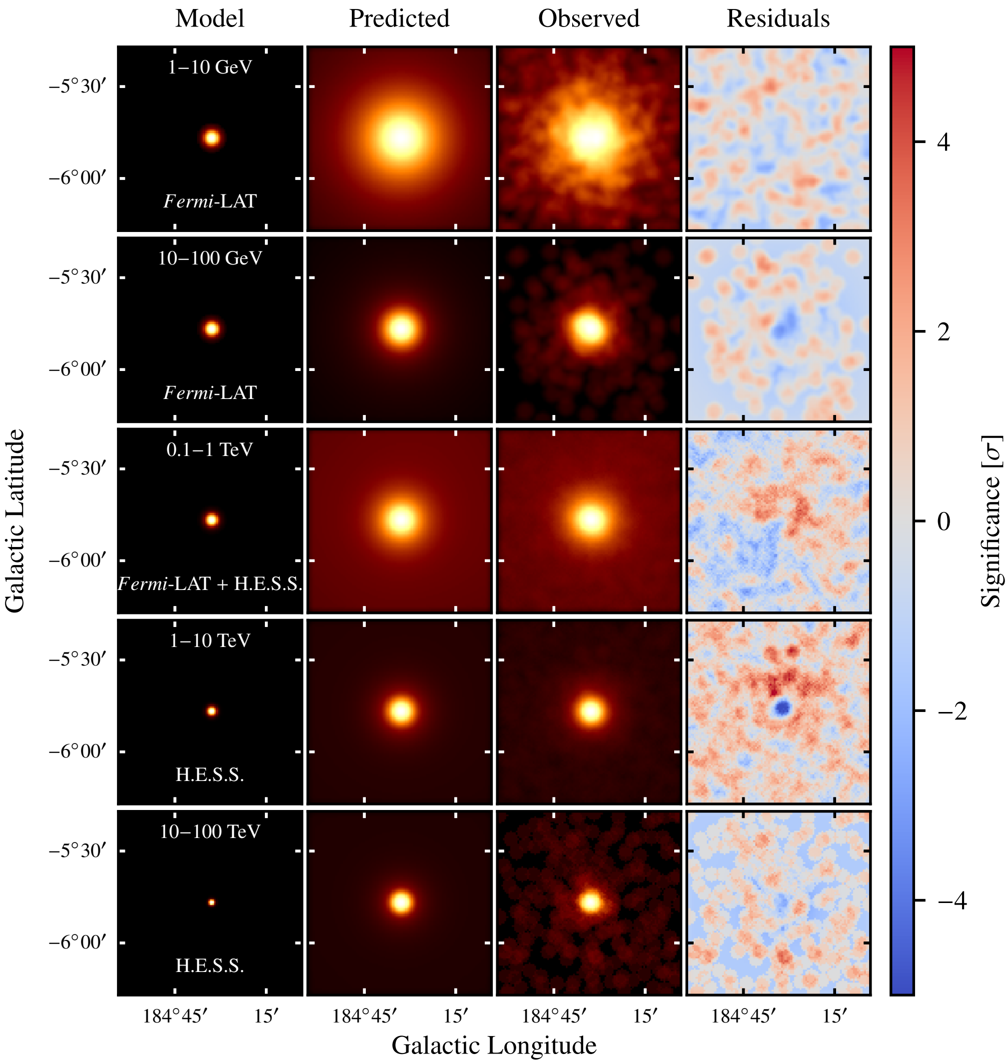

Figure 4.11: Overview showing the best-fit variable B-field model and the observed data in the IC regime, in five different energy bands. Each panel displays a $1^\circ \times 1^\circ$ cutout around the position of the Crab Nebula. The first column gives the best-fit model prior to folding with the IRFs. The second column illustrates the predicted number of events based on source and background models (folded with the IRFs), smoothed with a top-hat kernel of $2.4'$ radius. The third column shows the observed number of events with the same smoothing. Finally, the fourth column displays residual significance maps (see main text for details).

Table 4.3: Overview of $\mathcal{C}$ and χ^2 values obtained in the fits of our physical models.

Model	$\Delta\mathcal{C}_{\mathrm{tot}}$	$\Delta\mathcal{C}_{\mathrm{IC}}$	$\chi^2_{\mathrm{SYN,flux}}$ (#)	$\chi^2_{\mathrm{SYN,ext}}$ (#)	N_{par}	ΔAIC
variable B-field model	0	0	152.7 (194)	60.3 (14)	16	0
constant B-field model	374.0	264.1	246.0 (194)	76.9 (14)	15	372.0
Kennel & Coroniti	292.6	143.0	285.5 (194)	77.1 (14)	12	284.6

The $\Delta\mathcal{C}_{\mathrm{tot}}$, $\Delta\mathcal{C}_{\mathrm{IC}}$ (cf. Eq. 4.28), and ΔAIC values are given with respect to the variable B-field model model. The χ^2-values are given together with the number of flux and extension points included in the fit. N_{par} denotes the number of free parameters of the model. See main text for a definition of the different quantities.

not be regarded as measurements of the corresponding physical quantities, but simply as the set of values that yields the best agreement with the data.

Table 4.4: Best-fit parameter values of the physical models. Parameters that are not free in the fit are indicated by '(fixed)' after their value.

Parameter	variable B-field	constant B-field	Kennel & Coroniti
$\ln(n_{r,0})$	117.170	117.69	118.766
$\ln(\gamma_{r,\text{min}})$	3.09 (fixed)	3.09 (fixed)	3.09 (fixed)
$\ln(\gamma_{r,\text{max}})$	11.599	12.35	12.625
s_r	-1.5439	-1.649	-1.7419
ρ_r [″]	88.3	80.40	88.64
$\ln(n_{w,0})$	76.822	76.8315	-27.625
$\ln(\gamma_{w,\text{min}})$	12.841	12.69	12.8366
$\ln(\gamma_{w,1})$	15.26	14.24	—
$\ln(\gamma_{w,2})$	19.197	19.35379	17.96
$\ln(\gamma_{w,\text{max}})$	22.115	22.371	22.251
β_{min}	2.8 (fixed)	2.8 (fixed)	2.8 (fixed)
β_{max}	2 (fixed)	2 (fixed)	2 (fixed)
$s_{w,1}$	-3.117	-2.75	—
$s_{w,2}$	-3.3928	-3.1764	-2.8695
$s_{w,3}$	-3.782	-3.5118	-2.316
$\rho_{w,0}$ [″]	98.14	78.94	—
α_w	0.12544	0.11973	—
B_0 [µG]	256.4	126.39	—
r_s [″]	13.4 (fixed)	13.4 (fixed)	13.4 (fixed)
α	-0.4691	—	—
σ	—	—	0.021396
$\ln(L_{\text{spin-down}}[\text{erg/s}])$	—	—	88.716
$r_{\text{dust,in}}$ [pc]	0.55 (fixed)	0.55 (fixed)	0.55 (fixed)
$r_{\text{dust,out}}$ [pc]	1.53 (fixed)	1.53 (fixed)	1.53 (fixed)
$\log_{10}(M_1/M_\odot)$	-4.4 (fixed)	-4.4 (fixed)	-4.4 (fixed)
$\log_{10}(M_2/M_\odot)$	-1.2 (fixed)	-1.2 (fixed)	-1.2 (fixed)
T_1 [K]	149 (fixed)	149 (fixed)	149 (fixed)
T_2 [K]	39 (fixed)	39 (fixed)	39 (fixed)

For an explanation of the parameters, see Sect. 4.4.1.

Of the three models tested in this work, we find that the variable B-field model provides the best fit to the data. A comparison between the constant B-field model and the variable B-field model shows that the former is strongly disfavoured with respect to the latter, both in the synchrotron and the IC part of the fit. Since the models are nested (i.e. the variable B-field model can be reduced to the constant B-field model for a particular choice of parameter values), we can perform a likelihood ratio test and invoke Wilks' theorem (Wilks, 1938) to infer that the variable B-field model is preferred by $\sqrt{\Delta\mathcal{C}_\text{tot}} \approx 19.3$ standard deviations. On the other hand, a comparison of the K&C model and the variable B-field model by means of a likelihood ratio test is not possible, since these models are not nested. Instead, for a statistical comparison of the K&C model and the variable B-field model, we use again the Akaike information criterion, now defined as $\text{AIC} = \mathcal{C}_\text{tot} + 2N_\text{par}$. We conclude that the variable B-field model is also strongly favoured over the K&C model, with a difference in AIC of 284.6.

As a caveat to these comparisons, we note that the dust model has been optimised for the variable B-field model only, as a result of adapting the dust parameters from Dirson and Horns (2023). While the other models would potentially benefit from an additional optimisation of the dust parameters, we expect this effect to be minor and to have no impact on the conclusions drawn in this study. In the following, we discuss the models in terms of their predictions for the magnetic field, the broadband SED, and the nebula extension.

Magnetic field As already stated in Dirson and Horns (2023), the VHE data provide the strongest constraint on the shape of the magnetic field. For the variable B-field model, in which the B-field is parameterised as $B(r) = B_0(r/r_s)^{-\alpha}$, we find best-fit values of $\alpha = 0.47$ and $B_0 = 256\,\mu\mathrm{G}$. The steepness of the radial profile of the magnetic field is thus compatible with the value of $\alpha = 0.51 \pm 0.03$ found by Dirson and Horns (2023), who have used other VHE data sets in their fit.

With the K&C model we find a magnetisation of $\sigma = 0.0214$, which is about four to seven times larger compared to previous estimates (Kennel and Coroniti, 1984a; Meyer et al., 2010). Such high values of σ would lead to a high flow speed of $\gtrsim 5000\,\mathrm{km\,s^{-1}}$ at the interface between the nebula and the supernova remnant and a predicted shock radius of $r_s \approx \sqrt{\sigma} r_0 \approx 0.3\,\mathrm{pc}$, where $r_0 \approx 2\,\mathrm{pc}$ is the size of the nebula (Kennel and Coroniti, 1984a). This is at odds with observed expansion and flow speeds of the order of $\sim$2000 $\mathrm{km\,s^{-1}}$ and the shock radius at $r_s = 0.13\,\mathrm{pc}$. A value of σ compatible with these measurements is ruled out by our analysis with high significance, as it would lead to a much larger value of $\mathcal{C}_{\mathrm{tot}}$ and thus be disfavoured by the AIC (cf. Sect. 4.4.3).

Figure 4.12 shows that the B-field profiles of the K&C model and the variable B-field model agree quite well in the outer regions of the nebula ($r > 5r_s$). At the shock radius, the variable B-field model predicts more than twice the magnetic field strength compared to the K&C model. We can also compute a magnetisation for the variable B-field model by comparing the energy in the B-field against the energy in particles as a function of distance to the centre. We find a value of $\sigma \approx 0.1$ at the shock radius and ≈ 0.03 averaged across the whole nebula.

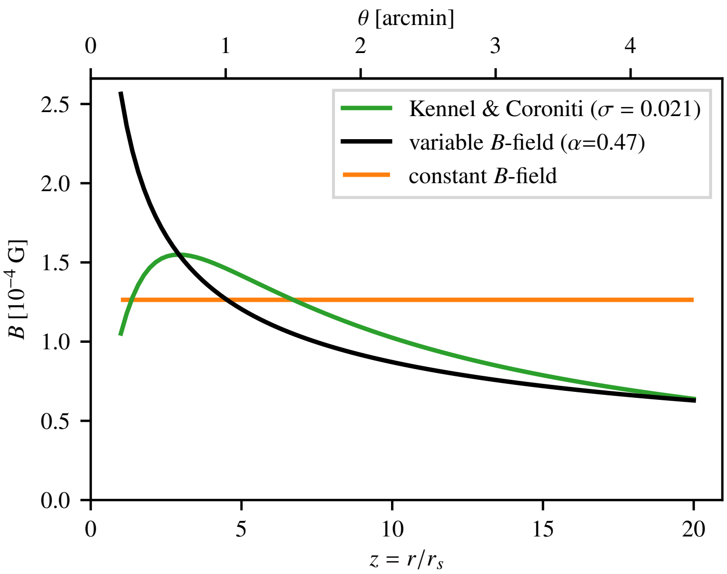

Figure 4.12: Magnetic field strength as predicted by the different models, as function of the distance to the nebula centre in units of the shock radius r_s. For the variable B-field model $B \propto r^{-\alpha}$, with α given in the legend. For the K&C model the magnetisation σ is specified in the legend.

As discussed before, the constant B-field model performs significantly worse, implying that a B field that decreases with distance from the centre is clearly preferred. This confirms the findings of Dirson and Horns (2023), who have reached a similar conclusion.

Broadband SED We compare the synchrotron flux prediction of the models in Fig. 4.13. Even though the parametrisation of the radio electrons is identical for all models, minor differences can be seen in the radio part of the SED (<3 THz). Compared to the variable B-field model, both the K&C model and the constant B-field model prefer a different transition between radio and wind electrons, that is, a larger cutoff energy for the radio electrons. This leads to a slight mis-match in the SED, but is required to fit the spatial extension in the IR and optical regime (see below). Since the parametrisation of the transition is not physically motivated, we will draw no further conclusions from the differences between the models in that regime.

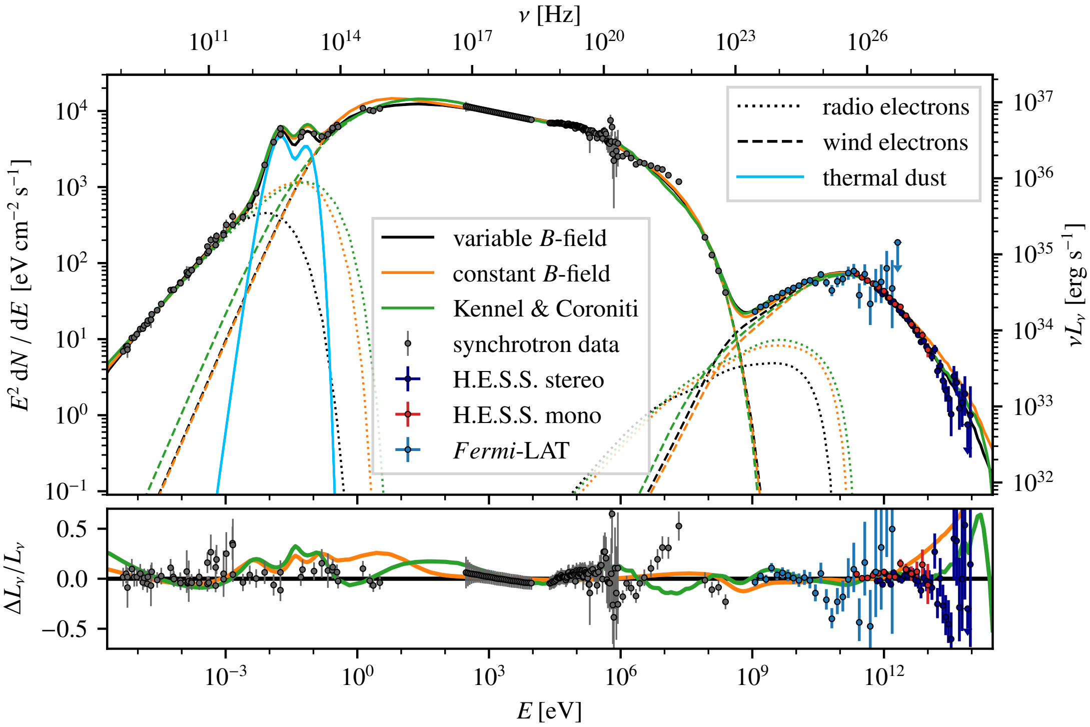

Figure 4.13: SED of the Crab Nebula, together with the predictions of the three models. The dotted lines show the emission produced by the radio electrons, while dashed lines are for the wind electrons (where synchrotron emission from all electrons is always included as IC seed photon field). The total emission is shown by the solid lines. The light blue line denotes infrared dust emission (identical for all models). The synchrotron data points are the same as in Fig. 4.1, with a 7% systematic uncertainty added in quadrature. The IC data are from this work (cf. Fig. 4.3 & 4.5). The bottom panel shows the ratio of the data points as well as the constant B-field and K&C model with respect to the variable B-field model.

The X-ray to γ-ray part of the synchrotron spectrum is not described well by any of the models. Specifically, the data between 10^{20}–10^{22} Hz suggest a slightly harder spectrum followed by a stronger cutoff, which is not matched by the models. Possible reasons for this could be the parametrisation of the super-exponential cutoff at $\gamma_{\mathrm{w,max}}$, or constraints resulting from the measured extension in this part of the spectrum, but also in the high-energy part of the IC spectrum. Comparing the models among each other, we observe a very good agreement between the static models, while the K&C model behaves slightly differently. This is most likely due to the differences in the parametrisation of the wind electron distribution. The first break in the spectrum, just beyond $\gamma_{\mathrm{w,min}}$, helps the static models with the transition between the UV and X-ray flux measurements. The K&C model, on the other hand, has only one break in the wind spectrum as the attempt of adding a second break resulted in no significant improvement. Instead, the wind electrons in the

K&C model follow the form $(\gamma_{\mathrm{w,min}} + \gamma)^s$ (compared to γ^s for the static models), which has a similar effect. It should be noted that the K&C model requires a harder electron index after the break to achieve agreement with the hard X-ray spectrum. Specifically, the spectral index of the electron spectrum hardens from 2.87 to 2.32, which is difficult to explain in the framework of the MHD flow model.

A zoom-in of the IC part of the SED is shown in Fig. 4.14.[37] We stress again that the models have not been fitted to the Fermi-LAT and H.E.S.S. flux points shown in this figure (and Fig. 4.13), but to the binned event data of these instruments directly; the flux points are shown for comparison only here. As indicated by the error bars of the flux points, the data provide the strongest constraints at energies of a few GeV, and at around 1 TeV. As a result, the model predictions are very similar up to an energy of a few TeV. The main differences appear at energies above 10 TeV, where in particular the constant B-field model over-predicts the measured flux. The electrons responsible for this flux are also producing the highest-energy synchrotron flux, where we find an excellent agreement between the static models. However, the variable B-field model predicts the same synchrotron flux with a softer electron spectrum and lower high-energy cutoff (cf. Fig. 4.10), because of the higher B-field strength near the shock radius. This leads to a stronger reduction of the IC flux with respect to the synchrotron flux. When extrapolating the IC flux above 100 TeV, the variable B-field model agrees with the LHAASO data (Cao et al., 2021a) up to ~1 PeV, even though these data are not included in the fit.

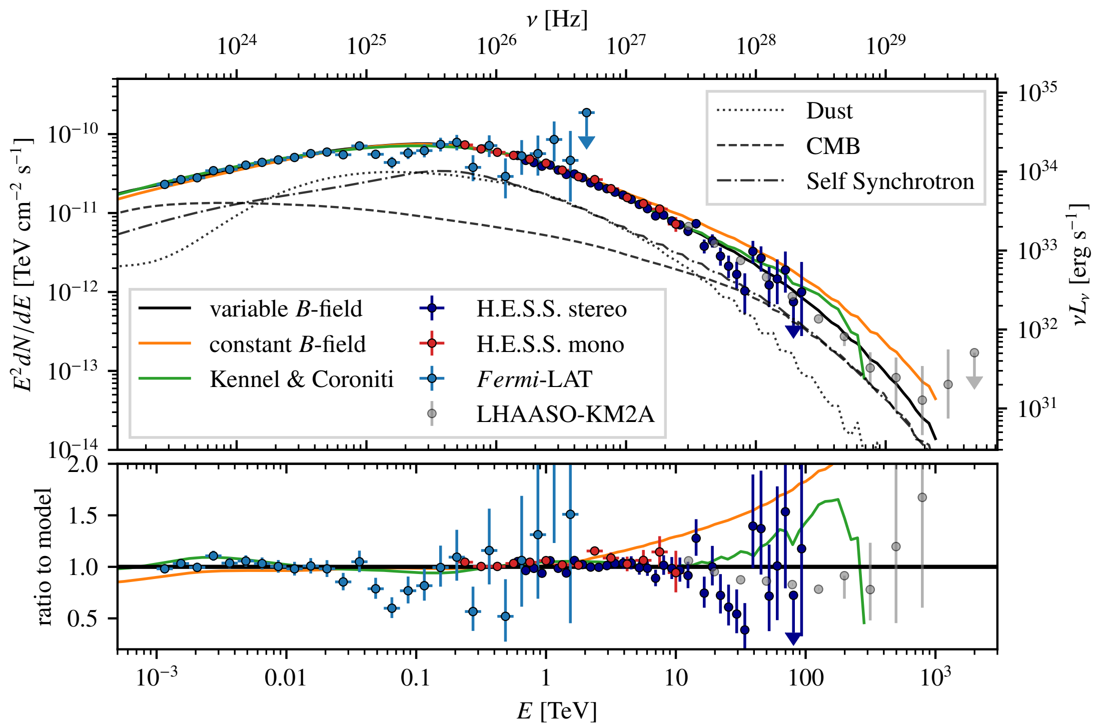

Figure 4.14: IC flux predictions of the three models, together with the Fermi-LAT and H.E.S.S. flux points derived in this work. The LHAASO flux points, taken from Cao et al. (2021a), are only shown for comparison. The dashed, dotted and dash-dotted lines show the individual contributions of seed photon fields for the variable B-field model. The bottom panel shows the ratio of the data points as well as the constant B-field and K&C model with respect to the variable B-field model.

The seed photon field contributions are shown in Fig. 4.14 for the variable B-field model, but are very similar for the other models. It can be seen that the SSC component

[37]We note that the unsteady behaviour of the K&C model at the highest energies is due to numerical instabilities and therefore not physical.

follows the spectral shape across all energies. The dust component is similar in strength to the SSC component between ∼10 GeV and ∼10 TeV, while being suppressed at lower and higher energies. The CMB component, on the other hand, behaves in exactly the opposite way. This rather complex behaviour emerges as the seed photon fields do not only differ in their spectrum, but also their morphology. While the CMB is constant at all radii, the SSC component approximately follows a Gaussian profile and the dust component is modelled as a shell around the nebula. As an example, at several tens of TeV the extension of the electron population becomes smaller than the inner radius of the dust shell, leading to a reduced contribution to the IC emission from dust photons at these energies. Another way of illustrating the spatial distribution of the emission in close vicinity to the centre is displayed in Fig. 4.15, where we show the energy-integrated intensity profiles (emissivity integrated along the line of sight) for the thermal dust, synchrotron, and IC emission, as predicted by our best-fit models. It is evident that, compared to the constant B-field model, the two models with a variable B-field predict a narrower profile for the synchrotron emission. Despite this, the variable B-field model exhibits the flattest IC profile of all models. In other words, the rapidly decreasing B-field allows for a more extended electron distribution while maintaining a narrow synchrotron profile. This leads to a larger predicted extension in the IC regime, which matches the observations best.

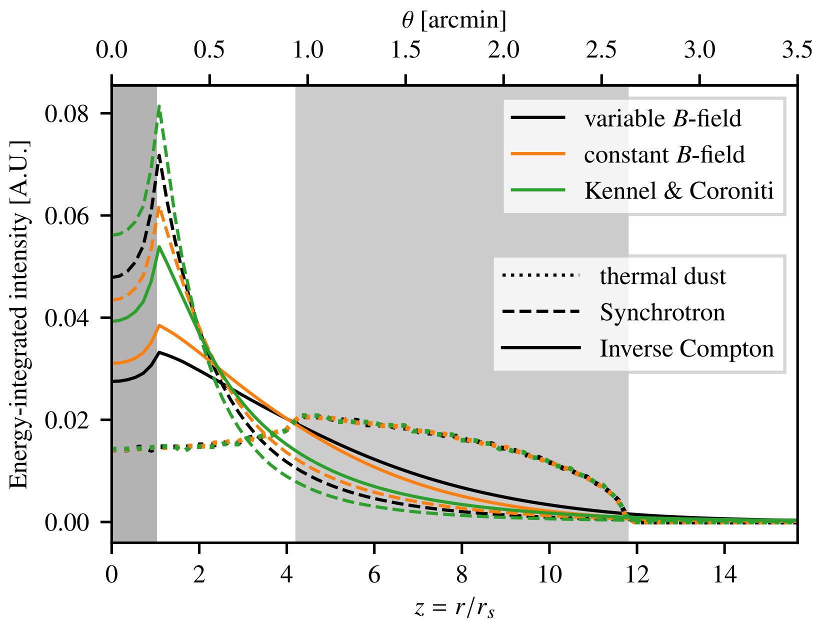

Figure 4.15: Energy-integrated intensity predicted by the three models, as a function of distance from the centre of the Crab Nebula. The solid, dashed, and dotted line correspond to IC, synchrotron, and dust emission, respectively; the colours refer to the three different tested models. The intensity has been integrated above 1 meV for the synchrotron emission and above 1 GeV for the IC emission. The dark grey band up to $z = 1$ indicates the region up to the shock radius, in which no emission is predicted by the models. The light grey band shows the dust shell, in which all the dust emission happens. The profiles show non-zero emission inside the shock region and dust emission outside the dust shell because the emissivity is integrated along the line of sight.

Nebula extension In Fig. 4.16, we show the extension of the nebula predicted by the models from the radio to the γ-ray domain, and compare this to the corresponding measurements. The extensions of the respective electron distributions are shown in Fig. 4.17. At energies for which the radio electrons dominate ($\lesssim$10 meV for the synchrotron and $\lesssim$10 MeV for the IC part), the morphology of the model is independent of energy. When

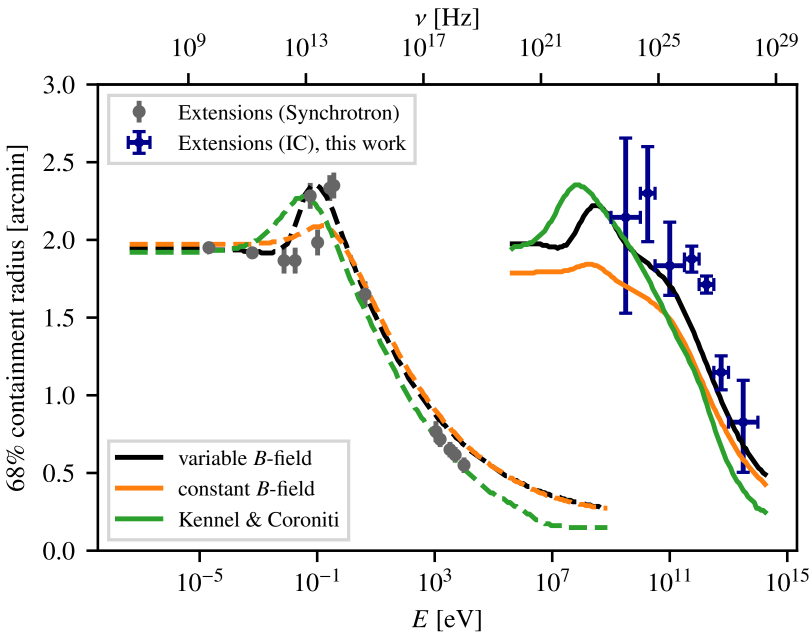

Figure 4.16: Comparison of the 68% flux containment predicted by the models as function of energy (dashed for the synchrotron part and solid for the IC part). The grey synchrotron extension points are taken from Dirson and Horns (2023) and references therein. The error bars of the data points in the IC domain denote statistical uncertainties only.

the more extended low-energy wind electrons start to dominate, the maximal extension is reached in the optical (around 100 MeV for the IC part). That the low-energy wind electrons exhibit a larger extension than the radio electrons can be physically motivated by energy-dependent diffusion, see for example Tang and Chevalier (2012).

First, we note that our measurement of a decreasing extension with increasing energy in the IC regime is generally well in line with the model predictions, and thus not a surprising result. Ultimately, this is a consequence of the already observed decrease of the size of the nebula in the synchrotron domain. Comparing the models in detail, we find that only the K&C model fully predicts the strong decrease in extension towards the X-ray energies, whereas the static models seem to be influenced more by the larger extensions measured at γ-ray energies. Accordingly, the K&C model under-predicts the extension across most of the IC regime, while the variable B-field model – albeit still predicting a too-small extension – provides a better match to the data here. We furthermore find strong correlations between the spectral and spatial parameters, as a narrower spatial distribution also decreases the total number of electrons and thus the γ-ray flux at the corresponding energies. It does not seem possible for any of the models – for the given parameters of the electron spectrum and the seed photon fields – to predict the measured IC extensions together with the broadband SED. We see two possible reasons for that.

First, the discrepancies could be due to simplifying assumptions made by the models. For instance, all models assume spherical symmetry, which is clearly an oversimplification. Additionally, three-dimensional and non-ideal MHD calculations suggest deviations from the predictions of the K&C model (Porth et al., 2014; Bucciantini et al., 2017; Tanaka et al., 2018; Lyutikov et al., 2019; Luo et al., 2020). In particular, non-ideal MHD models which predict turbulent magnetic fields to be present can resolve a number of problems of the K&C model (Luo et al., 2020). This would necessarily alter the magnetic field structure in the nebula and thereby the relation between synchrotron and IC photons. This could potentially lead to a better agreement with the data. However, a spatially resolved

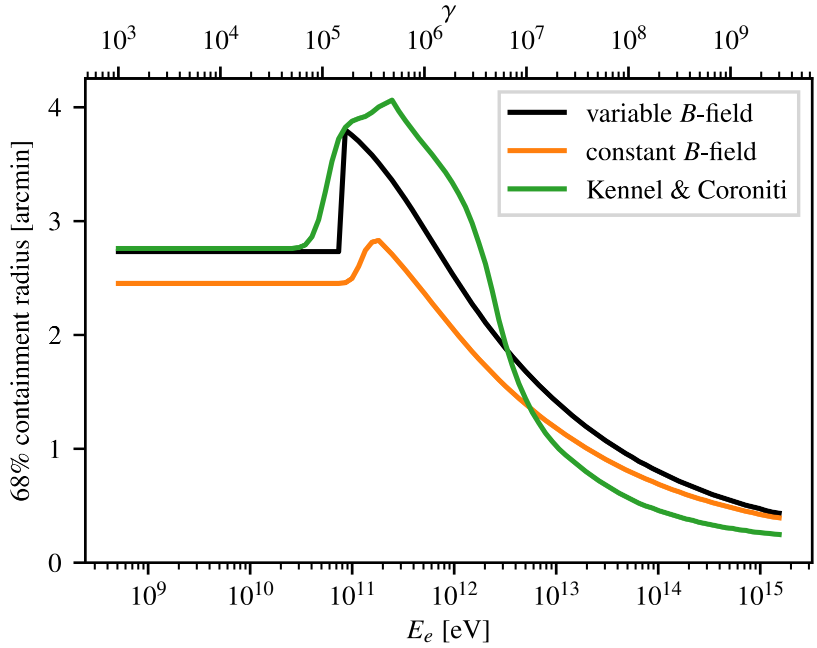

Figure 4.17: Comparison of the 68% containment radii of the electron energy densities of the three models. The radio electrons dominate the low-energy part of the spectrum where the extension is not energy-dependent. The extension of the wind electrons changes with energy, following, in case of the static models, a simple power law. The spectral transition of the two distributions is shown in Fig. 4.10.

calculation of such models is so far not available and the current non-ideal MHD models cannot reproduce the full SED in all its details. Another option would be the presence of an additional electron population that extends beyond the synchrotron nebula, for example electrons that have already escaped the nebula or electrons moving inwards from the so-far unobserved outer shock. The IC scattering of such a population with the CMB could potentially lead to a larger IC extension.

The second possibility is systematic uncertainties, for example a mis-modelling of the H.E.S.S. PSF beyond the estimated systematic uncertainty, which could cause the extension measured in the IC regime to appear larger than it actually is. Systematic uncertainties could also include an unaccounted factor between true and reconstructed energies of the IC photons. However, the required magnitude of such systematic effects appears to be unrealistically high to bring the measurements in agreement with the model predictions. We elaborate on this in the next section.

4.5 Systematic uncertainties and energy scale

Several systematic uncertainties could impact our analysis. For example, the absolute energy scales of Fermi-LAT and H.E.S.S. could differ, as the energy reconstruction of the two instruments is calibrated in different ways. Specifically, for Fermi-LAT a beam test in combination with a measurement of the geo-magnetic cutoff was used to infer the absolute energy scale with an accuracy of $^{+2}_{-5}\%$ (Ackermann et al., 2012a). Reaching this level of accuracy is not possible with H.E.S.S., where the atmosphere effectively is part of the detector and variations in atmospheric conditions can lead to a change in the number of Cherenkov photons reaching the telescopes. While in our selection of observation runs we have excluded observations carried out under sub-optimal conditions, distributions of the 'Cherenkov Transparency Coefficient' (Hahn et al., 2014) for the selected observations indicate that variations of about 10% remain. A difference in energy scale between the instruments could thus lead to a systematic shift between the spectrum of the Crab Nebula measured with Fermi-LAT and H.E.S.S. (cf. also Nigro et al., 2019).

One method of incorporating a scale factor η between the energy scales is to evaluate the H.E.S.S. source model at a modified energy $\eta \cdot E$, while the evaluation of the Fermi-LAT source model is unchanged (Meyer et al., 2010). Leaving η as an additional free 'nuisance' parameter during the fit determines the difference in energy scale between the two instruments. This method, however, depends on the assumed spectral model, and a model that fits the data poorly can falsely indicate a scale factor significantly different from unity if this improves the agreement with the data. For example, adopting a log-parabola spectrum leads to a factor $\eta = 0.79 \pm 0.03$ simply because the model is not suitable for the whole energy range. Other models with the possibility of a sharper break in the spectrum result in values $\eta > 1$. For the variable B-field model, we find $\eta = 1.038$, with only a very minor improvement of the fit ($\Delta\mathcal{C}_{\mathrm{tot}} \approx 2$, implying that η is consistent with a value of 1). As we cannot be certain about the correctness of our models, we therefore chose the approach of fixing $\eta = 1$ in our final analysis. This is further supported by looking at the integrated flux in the overlapping energy range between the Fermi-LAT data and the H.E.S.S. mono data set (i.e. 0.24–1.80 TeV). In this energy range, we do not see an indication for the energy shift as the integrated fluxes agree within statistical uncertainties. Specifically, summing the flux points in this range we find a Fermi-LAT flux of $(1.9 \pm 0.3) \times 10^{-10}\,\mathrm{cm}^{-2}\,\mathrm{s}^{-1}$, which is consistent with the H.E.S.S. mono flux of $(2.09 \pm 0.02) \times 10^{-10}\,\mathrm{cm}^{-2}\,\mathrm{s}^{-1}$ (statistical uncertainties only).

Nonetheless, we have aimed to estimate the systematic uncertainty associated with our flux measurements. To do so, we assessed the quality of the fit of the variable B-field model by means of a χ^2 test, and determined the magnitude of a potential systematic error that would lead to an acceptable fit quality. For the spectral measurements in the γ-ray regime, we added a constant percentage of the flux in quadrature to the statistical uncertainty. To calculate the χ^2 values for the γ-ray data sets, we used the asymmetric errors of each flux point, meaning that we used the positive error if a point falls below the model prediction and vice versa. In the synchrotron range, the systematic error is also added as a percentage of the measured flux in quadrature to the statistical errors (as in the fitting process, see Sect. 4.4). For the synchrotron extension measurements, the assumed systematic error is a constant angle. Finally, in the IC regime, we used the systematic errors of the extensions previously cited in the single-instrument analyses. That is, at energies for which the Fermi-LAT data dominate we added an error of ${}^{+0.54}_{-0.48}{}'$ (cf. Sect. 4.2.2) and at energies for which the H.E.S.S. data dominate we added an error of ${}^{+0.21}_{-0.24}{}'$ (cf. Sect. 4.2.1). Again, all of the systematic uncertainties have been added in quadrature to the statistical ones.

Table 4.5 summarises the χ^2 values for the variable B-field model with and without the added systematic uncertainties, together with the estimated number of degrees of freedom (N_{dof}). For the case of a single data set to which a model has been fitted, N_{dof} is equal to the number of data points minus the number of model parameters (when neglecting correlations between the parameters). We note that in the present case, with the models being fitted to multiple data sets at once, it is not straightforward to properly state the exact N_{dof} for each of the individual sets. The reason for this is that the models have not been adjusted to any of the individual sets alone, but to their combination. The high degree of correlation between some of the model parameters presents an additional complication. In Table 4.5, we therefore provide as a very conservative estimate of N_{dof} the number of points in the data set minus one (taking into account one overall scale factor that remains even if all model parameters are perfectly correlated). We find that without added systematic uncertainties, the χ^2 values are all well above N_{dof}, indicating

Table 4.5: Fit quality with and without including systematic uncertainties.

Data set	w/o systematics χ^2 (sys. error)	N_{dof}	w/ systematics χ^2 (sys. error)
H.E.S.S. stereo (flux points)	45.5 (none)	35	33.6 (3%)
H.E.S.S. mono (flux points)	36.7 (none)	13	12.1 (4%)
Fermi-LAT (flux points)	41.7 (none)	26	27.7 (10%)
Synchrotron (flux points)	235.0 (5%)	194	152.7 (7%)
Fermi-LAT + H.E.S.S. (extension)	121.5 (none)	6	8.9 (see text)
Synchrotron (extension)	60.3 (n.a.)	13	13.0 (8″)

The χ^2 values are calculated for the respective data set and the variable B-field model. For each data set, we conservatively estimate the number of degrees of freedom (N_{dof}) as the number of data points minus one. The magnitude of the systematic uncertainties (specified in parentheses) are chosen such that a good fit quality is obtained, that is, $\chi^2 \sim N_{\mathrm{dof}}$, and thus do not represent estimates of the actual systematic uncertainty of each data set. The first section of the table summarises the flux measurements, where the systematic uncertainty is specified as a relative error on the flux level. The extension uncertainty, given in the second section of the table, is increased by a constant error for each data set (see main text for details). We note that we still add a systematic uncertainty of 5% to the synchrotron flux points for the 'w/o systematics' case, as the χ^2-value would otherwise increase to $> 10^6$, due to the small statistical uncertainties of some of the points. Similarly, the extension measurements in the synchrotron regime already contain systematic uncertainties, which are however not easily separable and thus not stated explicitly here (see Dirson and Horns 2023 for details).

an unsatisfactory model description or the presence of systematic uncertainties. For the H.E.S.S. stereo and mono flux points, an additional systematic flux uncertainty of 3% and 4%, respectively, leads to an acceptable fit quality. This flux uncertainty would correspond to an uncertainty on the energy scale of the instrument of 1.2% and 1.6%, respectively. For the Fermi-LAT data set, a systematic flux uncertainty of 10% is required, corresponding to a 5% uncertainty on the energy scale. We stress that these values are not generally valid estimates for the energy scale uncertainty of H.E.S.S. and Fermi-LAT, but only the level of systematic scaling required to achieve an acceptable goodness-of-fit in our analysis. The variations are, however, well within the typically adopted systematic uncertainties of the two instruments[38]. The χ^2 value of the synchrotron flux points depends sensitively on the assumed systematic error because of the relatively small statistical uncertainties on some of the points. We find that adding a 7% flux uncertainty leads to a χ^2 value well below N_{dof}, while 5% is not sufficient. Compatible best-fit parameters are obtained with either assumed systematic error.

Regarding the extension of the nebula, it is evident that without consideration of systematic uncertainties, the predicted extension in both the IC and synchrotron regime is strongly at odds with the measurements. For the Fermi-LAT and H.E.S.S. data sets, taking into account the previously estimated systematic uncertainties leads to a marginally acceptable fit quality. The assumed error bars of the synchroton data points, on the other hand, already contain systematic uncertainties (see Dirson and Horns, 2023). Nevertheless, an additional uncertainty of 8″, which is approximately twice as large as the uncertainty used in the fit (∼4″ on average), would be required to achieve $\chi^2 \approx N_{\mathrm{dof}}$. This illustrates again the previously discussed inability of the model to simultaneously describe the SED and the extension measurements. The simplifying assumptions of the model already discussed in the preceding Sect. 4.4.3, as for example radial symmetry and a simple power law describing the electron distribution size evolution with energy, may not be justified.

[38] See e.g. Aharonian et al. (2006) for H.E.S.S. and `https://fermi.gsfc.nasa.gov/ssc/data/analysis/LAT_caveats.html` for Fermi-LAT.

4.6 Conclusion

In this work, we present a joint Fermi-LAT and H.E.S.S. analysis of the Crab Nebula, carried out with the open-source analysis package Gammapy. Below, we first summarise our findings regarding the technical part of our work – related to the joint fit of the Fermi-LAT and H.E.S.S. data – before we discuss the implications of our analysis on emission models of the Crab Nebula.

First, we have demonstrated that applying the open-source analysis package Gammapy to Fermi-LAT and H.E.S.S. data, we are able to obtain results that are consistent with the traditionally used analysis chains. Specifically, for Fermi-LAT, we show that we can almost exactly reproduce results obtained with the Fermipy package after some minor adjustments in the data reduction procedure. In the context of this work, Gammapy has the advantage that it enables a combination of the Fermi-LAT data with that of H.E.S.S., and it offers the possibility to include customised physical models in the analysis. For H.E.S.S., on the other hand, Gammapy allows us to apply the three-dimensional likelihood analysis method, that is, to model the spectrum and morphology of the Crab Nebula simultaneously under full consideration of the Poisson event statistics. A key ingredient for this is a three-dimensional model for the residual hadronic background. We find consistent results with more traditional methods that estimate this residual background from the analysed observations themselves. Second, by combining the Fermi-LAT and H.E.S.S. data in a joint-likelihood analysis, we provide a fully consistent spectro-morphological analysis of the Crab Nebula over five decades in energy. We confirm previously found indications for an extension of the nebula in the IC regime that decreases with increasing energy – a result that agrees well with theoretical expectations. We discuss the possibility of taking into account possible systematic effects (e.g. different energy scales between instruments) in the form of nuisance parameters in the likelihood fit. Finally, to be able to fit physical emission models to our data that are consistent with other MWL observations, we demonstrate that it is possible to take into account MWL constraints through the addition of penalty terms to the fit statistic.

This has enabled us to consistently model the synchrotron and IC part of the emission from the Crab Nebula. Specifically, we have confronted three phenomenological models for the non-thermal emission of the Crab Nebula with our measurements: a constant B-field model based on Meyer et al. (2010), a variable B-field model based on Dirson and Horns (2023), and the K&C model by Kennel and Coroniti (1984a). We note that these models are open-source and publicly available[39]. All models predict the γ-ray emission not only as a function of energy, but also as a function of the distance from the centre of the nebula. Hence, by projecting the symmetric model on the sky, we were able to fit a three-dimensional model of the Crab Nebula emission directly to the measured event data from Fermi-LAT and H.E.S.S.. We conclude that, within the range of the estimated systematic uncertainties, none of the models are able to describe the full SED together with the extension of the nebula at different energies. We firmly rule out the constant B-field model, as it completely fails to describe the decreasing extension with energy and the spectrum at the same time. The K&C model describes the SED and the extension of the synchrotron nebula well, but under-predicts the size of the IC nebula. Furthermore, it requires a spectral hardening in the electron spectrum to fit the X-ray data, and the best-fit value of the magnetisation σ is at odds with the position of the shock and the expansion velocity of the nebula. Finally, the variable B-field model achieves the best agreement with the data. This indicates that the magnetic field strength in the nebula decreases with increasing distance from the pulsar. However, compared to the model prediction, the new H.E.S.S. measurements of the extension presented here are in tension with the extension

[39]See `https://github.com/me-manu/crabmeyerpy` for the implementation we have used.

measurements in the X-ray domain. As a consequence, the variable B-field model does not achieve the same fit quality as in Dirson and Horns (2023). In summary, even though we find strong evidence that the extension of the IC emission decreases with energy, it still appears too large compared to the distribution of the synchrotron photons, which are supposedly produced by the same electrons. This could suggest more complicated spatial profiles of the electron distribution and the magnetic field as predicted, for example, in non-ideal MHD calculations (e.g. Porth et al., 2014; Luo et al., 2020). Additionally, a non-spherical geometry (such as a toroidal or flattened profile) will also change the seed photon density, which could lead to a better agreement between the model predictions and data.

As a final note, we remark that the IC spectrum above $\sim$30 TeV is not well constrained by the data used in this work. Hence, differences between the models occur predominantly in this regime. In future, including data from instruments optimised for the highest energies, such as LHAASO, could help in placing further constraints on the models and in determining the shape of the magnetic field in more detail. Moreover, data from the upcoming Cherenkov Telescope Array (CTA; Acharya et al., 2018; Hofmann and Zanin, 2023) with its unprecedented angular resolution will allow us to measure the extension of the Crab Nebula in the IC regime with higher precision.

For everyone has sinned; we all fall short of God's glorious standard.

— Paul, Romans 3:23

5 Improvements to monoscopic analysis for imaging atmospheric Cherenkov telescopes: Application to H.E.S.S.

In the previous chapter, the Crab Nebula spectrum as measured by H.E.S.S. was reported using both monoscopic and stereoscopic event reconstruction methods. The monoscopic reconstruction reached lower energies due to the large light collection area of CT5, but its performance is inferior to that of the stereoscopic reconstruction. While this is naturally a result of missing a second viewing angle on the events, several ideas have been considered that might improve the performance of monoscopic analyses nonetheless and lower its energy threshold even further. The results have been published in Astronomy & Astrophysics (Unbehaun et al., 2025) and are reported here with minimal or no modifications.

5.1 Introduction

Since the success of the first generation of ground-based γ-ray telescopes (Weekes et al., 1989), significant advances have been made in both hardware and software development (Funk, 2015). The basic detection principle has remained the same: Cherenkov light, emitted by charged secondary particles in γ-ray induced air showers, is collected by Imaging Atmospheric Cherenkov Telescopes (IACTs). Modern arrays, such as VERITAS (Weekes et al., 2002), MAGIC (Aleksić et al., 2016), and H.E.S.S. (Aharonian et al., 2006), employ stereoscopic event reconstruction techniques, where one shower is observed by at least two telescopes. This stereoscopic approach improves the reconstruction accuracy of the properties of the primary particle and improves the rejection of background events arising from interactions of charged cosmic rays (Konopelko et al., 1999).

However, not all γ-ray events are captured by multiple telescopes, which makes monoscopic (or mono) event reconstruction still crucial. This is particularly relevant for the H.E.S.S. array, where the large central telescope, with its 28 m mirror diameter, operates in mono-trigger mode and primarily detects low-energy events ($\lesssim$ 100 GeV), often seen by this telescope alone. The importance and methodology for reconstructing these mono events are discussed in Murach et al. (2015). Their approach utilizes the traditional "Hillas parameters" (Hillas, 1985), which characterize the first four moments of the intensity distribution within the shower images, as input to machine-learning algorithms. Although other reconstruction techniques exist, such as template-based methods (Parsons and Hinton, 2014), background rejection for mono events in H.E.S.S. is currently performed exclusively using image parameters. Using intensity information directly in machine-learning models is an alternative (see, e.g., Holch et al., 2017; Parsons and Ohm, 2020; Lyard et al., 2020; Miener et al., 2022; Glombitza et al., 2023), but poses challenges due to the sensitivity of the models to discrepancies between simulations and recorded data (Shilon et al., 2019; Parsons et al., 2022). Improving the reconstruction and background rejection for low-energy γ rays can further lower the energy threshold and increase the sensitivity of our observations.

By including the pixel time information in the analysis of monoscopic data from the MAGIC telescope, Aliu et al. (2009) could already achieve notable improvements in point-source sensitivity. The construction and usage of additional image parameters in reconstruction algorithms, as well as the optimization of the event selection cut, is discussed in Voigt (2014). A recent study by Abe, K. et al. (2024) even included information from waveforms recorded by individual camera pixels in the reconstruction algorithms.

In this work, we explore the potential of incorporating additional image parameters that capture more detailed features of the amplitude and time distribution in the shower image. A systematic approach is used to assess the importance of each parameter for the reconstruction and background rejection algorithms, leading to an optimized subset of parameters tailored to each application. We also examine the systematic uncertainties arising from discrepancies between different observation conditions, both prior to and following the inclusion of these new image parameters. Moreover, we introduce a machine-learning algorithm trained to determine the direction of the shower development in the camera frame, enabling the calculation of the new image parameters based on a more accurate image orientation. Currently, the direction of the shower is determined solely using the Hillas-skewness (defined in Sect. 5.3.1), which is an unreliable parameter for both small and truncated images. We also implement a selection cut optimized for different event sizes (size here and in what follows stands for the total image intensity), which outperforms the standard constant selection cut used in Murach et al. (2015). This optimization is crucial because the performance of the classification algorithm improves significantly with event size, and a constant cut does not fully exploit the potential across all sizes (Voigt et al., 2014).

The new image parameters are introduced in Sect. 5.3, followed by the description of the machine-learning model architecture for event reconstruction and classification in Sect. 5.4, and the optimization of the size-dependent selection cut in Sect. 5.5. Finally, we assess the performance of the new reconstruction chain and compare it to the previous one in Sects. 5.6.1–5.6.3, with an application to real Crab Nebula data presented in Sect. 5.6.4.

5.2 Implementation

This study is based on γ-ray events simulated and observed using the central large telescope (CT5) of the H.E.S.S. array, equipped with the FlashCam camera (Eldik et al., 2016; Bi et al., 2021). Air showers are simulated using the `CORSIKA` package (Heck et al., 1998), and the telescope response is simulated using `sim_telarray` (Bernlöhr, 2008). Simulated events follow a power-law distribution $\sim E^{-\Gamma}$ with a spectral index of 1.8 to increase statistics at higher energies and are then re-weighted to a spectral index of 2.5. After extracting the pixel amplitudes and times (i.e., integrated photoelectrons (p.e.) and peak signal times), noise pixels are set to zero by a cleaning procedure. A tail-cut image cleaning is used to classify core pixels, which have an amplitude above 14 p.e and at least 2 neighbor pixels above 7 p.e. Core and neighbor pixels are kept, while the time information is not considered during this step. Algorithms that use time information for image cleaning have been developed for H.E.S.S. (Steinmaßl, 2023) but are not yet adopted in the standard analysis pipeline. For this reason, we adhere to the standard tail-cut method to maintain consistency and minimize introducing correlated changes into the analysis pipeline. Future studies will explore potential enhancements to the image cleaning technique and the resulting improvements in source detection sensitivity. Based on the remaining signal pixels, image parameters are computed, forming the basis for event reconstruction and classification. All these steps (after simulation) are implemented in the H.E.S.S. analysis program (HAP).

For this study, we apply preselection cuts, requiring a total image amplitude above 80 p.e. and a minimum of five pixels. This minimum image size is relatively close to the trigger threshold of the telescope at 69 p.e. (Bi et al., 2021), while maintaining a safe distance, to avoid systematic uncertainties due to mis-modeling of the camera response in this regime. The distance from the image center of gravity (CoG) to the center of the camera (so-called Hillas-local-distance, see Sect. 5.3.1) is required to be smaller than 0.8 m to reduce image truncation effects at the camera edges, which are between 1.0–1.2 m.

In the following subsections, we define the image parameters investigated in this study before presenting the reconstruction framework and architecture of the machine-learning models.

5.3 Definition of training variables

The variables described in this section characterize the spatial and temporal distribution of the pixel amplitudes and times, either for the whole image or parts of the image. To improve background rejection, they aim to be sensitive to differences between cosmic-ray-induced (hereafter hadronic) background showers and γ-ray-induced air showers. These differences are most prominently seen in the more irregular shower morphology for hadronic showers, caused by electromagnetic, muonic, and hadronic subshowers. In Appx. C, the distribution of each variable is shown for measured background data, together with proton and γ-ray simulations.

Even though one would not necessarily expect perfect agreement between background data and proton simulations due to various factors, such as the primary cosmic-ray composition or atmospheric and instrument conditions, a good agreement between these distributions indicates that the simulated atmosphere, telescope, and night sky background (NSB)light match reality. The consistency between the measured and simulated data for FlashCam in CT5 is discussed in detail by Leuschner et al. (2023). Since the background events are characterized by their isotropic arrival directions, we compare their distributions to those of diffuse γ-ray simulations[40]. These are available with a realistic NSB value, based on the average observed Galactic NSB, and a value that is ~ 1.65 times higher than this. A difference between these sets of simulations indicates that the given variable is sensitive to the details of the NSB and therefore introduces systematic uncertainties, as the NSB values vary between observations but are typically kept at a fixed value for most simulations. Large differences between the hadronic and γ-ray distributions imply strong separation power for this variable, although some variables are correlated, which reduces the gain in separation power when combining these variables.

The camera image reflects the development of the shower in the atmosphere and is typically parameterized as an ellipse. The longitudinal development is encoded along the major axis of the image, the head reflecting the top part of the shower where the first interaction takes place, while the tail represents the bottom part of the shower where many shower particles contribute to the emission. Since the charged shower particles travel at a slightly higher speed compared to the Cherenkov photons in the atmosphere, the arrival times do not necessarily follow the sequence head-center-tail. They rather depend on the impact distance, the distance between the shower's impact point on the ground and the telescope's position, for geometrical reasons.

For the computation of the variables, we consider the position of pixel i in the camera frame $(X_{\mathrm{CAM,i}}, Y_{\mathrm{CAM,i}})$, its amplitude A_i (integrated charge in the readout window), and time T_i (peak time of the charge time-evolution). The image coordinates (X_i, Y_i) then follow as a translation plus rotation

$$\begin{bmatrix} X_i \\ Y_i \end{bmatrix} = \begin{bmatrix} \cos(\alpha) & \sin(\alpha) \\ -\sin(\alpha) & \cos(\alpha) \end{bmatrix} \begin{bmatrix} X_{\mathrm{CAM,i}} - <X_{\mathrm{CAM}}> \\ Y_{\mathrm{CAM,i}} - <Y_{\mathrm{CAM}}> \end{bmatrix}, \tag{5.1}$$

where α is the angle that minimizes the root mean square (RMS) of the intensity distribution along the Y-direction and $(<X_{\mathrm{CAM}}>, <Y_{\mathrm{CAM}}>)$ is the CoG of the image in the camera frame. Consequently, the CoG lies at (0,0) in these coordinates, and the major axis of the ellipse is aligned with the X axis.

[40] Simulations with isotropic arrival directions, as opposed to point-source simulations with only one arrival direction.

5.3.1 Hillas parameter-based variables

The first set of variables was introduced by Hillas (1985) and characterizes the second, third, and fourth moments of the amplitude distribution. These variables are widely referred to as "Hillas parameters," and their calculation is described in Appendix A of Reynolds et al. (1993).

"Hillas-image-amplitude" is the total amplitude summed over all pixels $\sum_i A_i$. It is mainly a function of the γ-ray energy and impact distance on the ground. Additionally, the atmospheric transparency and telescope efficiency affect the total light yield of the showers. Therefore, the distribution of the Hillas-image-amplitude (or size, cf. Fig. C.1) is very similar for different primary particle showers, in particular if they follow similar energy spectra. It cannot and should not be used as a separating variable. However, since the gamma-hadron separation works better for images with a larger total amount of light in the camera, information about the size is very useful for separation and is implicitly available through correlations with other variables.

"Hillas-npix" is the number of pixels with $A_i > 0$ that pass the aforementioned image cleaning. Its distribution is shown in Fig. C.2. Hillas-npix is affected by the same shower properties as the Hillas-image-amplitude, and additionally by the shower morphology and the image cleaning.

"Hillas-local-distance" is the distance from the image CoG to the center of the camera, defined as $\sqrt{<X_{\mathrm{CAM}}>^2 + <Y_{\mathrm{CAM}}>^2}$. This parameter is solely determined by the position of the shower in the camera's field of view. Although it does not contain any physical information beyond the position, it is of interest to algorithms, as images recorded near the edges of the camera may require a different handling due to truncation effects.

"Hillas-width" is defined as the RMS along the Y-direction and can be computed as:

$$\text{Hillas-width} = \sqrt{\frac{\sum_i Y_i^2 \cdot A_i}{\sum_i A_i}}\,, \tag{5.2}$$

with the distribution shown in Fig. C.3. The characteristic dip located at $\sim 2\,\mathrm{cm}$, slightly below half of the camera pixel width (5 cm), occurs because images with only 5, 6, or 7 pixels have a sharp cutoff in their width distribution at this value. The vast majority of possible configurations for 5, 6, or 7 connected pixels in the hexagonal camera frame have their largest extent along one of the three symmetry axes, resulting in preferred directions of α. Therefore, most images with low pixel numbers have only two "rows" of pixels along the Y-direction, with a maximal RMS of half the pixel width. For images with more pixels, the distribution shifts toward larger widths and becomes more and more continuous.

"Hillas-length" is defined analogously as the RMS along the X-direction:

$$\text{Hillas-length} = \sqrt{\frac{\sum_i X_i^2 \cdot A_i}{\sum_i A_i}}\,, \tag{5.3}$$

with the distributions shown in Fig. C.4. The length and, especially, the width distributions show differences between hadrons and γ rays, with the latter being more abundant at smaller values, as expected for more compact and regular showers.

The third and fourth moments along the major axis can be computed as:

$$K_m = \frac{\sum_i X_i^m \cdot A_i}{\sum_i A_i} \cdot \frac{1}{\text{Hillas-length}^m}\,, \tag{5.4}$$

where K_m is the m'th moment.

"Hillas-skewness" is the third moment K_3 with the distribution shown in Fig. C.5. There are minor differences in the distributions, as the more irregular proton showers feature larger absolute values of skewness, indicating a broader distribution.

"Hillas-kurtosis" is the fourth moment K_4 with the distribution shown in Fig. C.6. The more irregular proton showers with their broader intensity distribution feature lower values of kurtosis.

"Hillas-logdensity" is a composite variable that includes the Hillas-image-amplitude and is defined as:

$$\text{Hillas-logdensity} = \log_{10}\left(\frac{\text{Hillas-image-amplitude}}{\text{Hillas-width} \cdot \text{Hillas-length}}\right). \tag{5.5}$$

The Hillas-image-amplitude does not enter the separation training directly, to avoid a strong dependence of the algorithm on the simulated spectrum, but is implicitly available through the composite variables. The distribution is shown in Fig. C.7, where γ-ray showers have a tail toward higher densities, while hadronic showers tend toward lower densities. This matches the Hillas-npix distributions, where the latter tend toward higher pixel numbers.

"Hillas-length-over-logsize" is also a composite variable and defined as:

$$\text{Hillas-length-over-logsize} = \frac{\text{Hillas-length}}{\log_{10}(\text{Hillas-image-amplitude})}. \tag{5.6}$$

The distribution of the Hillas-length-over-logsize is shown in Fig. C.8 and is very similar to that of the Hillas-length.

5.3.2 Sector-based variables

The following image parameters (also those introduced in Sects. 5.3.3 and 5.3.4) are part of a set of novel variables that have not yet been utilized in any previous analyses. These parameters are specifically designed to enhance both the reconstruction accuracy and background rejection in monoscopic IACT images.

The idea behind the sector-based variables is to increase the sensitivity to asymmetries in the image that arise from the asymmetric development of the shower in the atmosphere, such as the head-tail asymmetry, or potential asymmetries in the hadronic shower development. For this, we divide the image into three sectors along the major axis: the head, center, and tail sectors, and compute moments of the charge distribution in these sectors separately. When L = Hillas-length, all pixels with $X_i < -0.5 \cdot L$ belong to the first sector, pixels with $|X_i| < 0.5 \cdot L$ belong to the center sector, and pixels with $X_i > 0.5 \cdot L$ belong to the third sector (cf. Fig. 5.1). Due to the random image orientation in the camera, the assignment of sectors one and three to the head and tail sectors occurs later, after the correct image orientation is estimated (see Sect. 5.4.1).

For each of the sectors, we compute $<X>$ and $<Y>$, resulting in the variables "$\mathrm{x}_{\mathrm{head}}$," "$\mathrm{x}_{\mathrm{center}}$," and "$\mathrm{x}_{\mathrm{tail}}$," and "$\mathrm{y}_{\mathrm{head}}$," "$\mathrm{y}_{\mathrm{center}}$," and "$\mathrm{y}_{\mathrm{tail}}$," with the distributions shown in Figs. C.9–C.14.

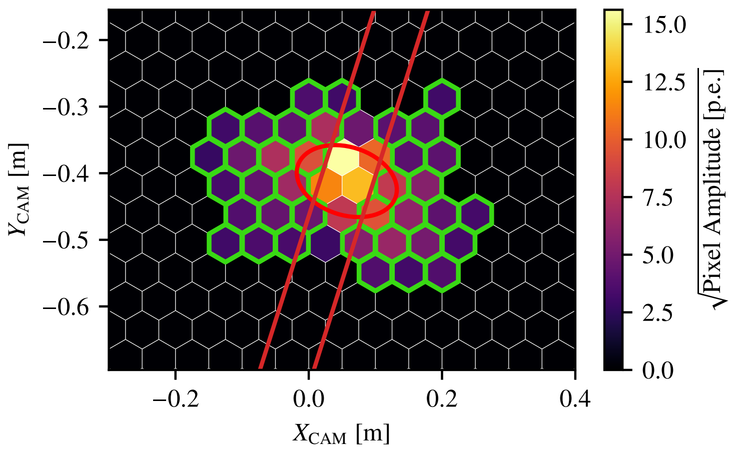

Figure 5.1: Simulated γ-ray event in the camera frame overlaid with a red ellipse illustrating the Hillas parametrization (width and length), and the lines separating the sectors. The pixels marked in green belong to either the head or the tail sector, while pixels that are not marked belong to the central sector.

Additionally, we compute the width according to Eq. 5.2 for each of the sectors, resulting in the variables "width$_{\mathrm{head}}$," "width$_{\mathrm{center}}$," and "width$_{\mathrm{tail}}$" (cf. Figs. C.15−C.17).

The peaks at zero for the distributions of the center sectors are caused by low-size events where the central sector has zero pixels. This corresponds to a division of the event into only two sectors. Variations of $<Y>$ from zero indicate a curvature of the image along the major axis, which is typical for high-impact distance muons where only part of the characteristic muon ring is visible. However, this feature may be better captured by the continuous "kink-major" variable described in Sect. 5.3.3. While width$_{\mathrm{center}}$ is strongly correlated with the Hillas-width, a comparison of the head and tail widths allows the characterization of a gradient in the width along the major axis. This is then correlated with the continuous variable "kink-minor" (cf. Sect. 5.3.3). The $<X>$ values for the head and tail sectors of the γ-ray showers are slightly closer to zero, which is connected to the larger kurtosis. Asymmetries between the head and tail values for one event are reflected in the skewness.

Finally, one can also compute the "charge-asymmetry" as:

$$\text{charge-asymmetry} = \frac{\sum_i A_{i,\mathrm{head}} - \sum_i A_{i,\mathrm{tail}}}{\sum_i A_i}\,, \tag{5.7}$$

which is also correlated with the Hillas-skewness and has a very similar distribution for background data and γ-ray simulations (cf. Fig. C.18).

5.3.3 Continuous variables

In the following, we aim to characterize additional features of the event images that the variables introduced up to here are not sensitive to. As the sector variables are not optimal, especially for low-size events, we no longer separate the pixels into three sectors but rather use all pixels to compute gradients and other correlations. The first set of variables is based on the gradient m between two pixel attributes x and y, which is computed via linear regression:

$$m = \frac{\sum_i (x_i - <x>) \cdot (y_i - <y>) \cdot w_i}{\sum_i w_i \cdot \mathrm{Var}(x)}\,, \tag{5.8}$$

where $<x>$, $<y>$ are the weighted averages of x and y, respectively, using the weights w. $\mathrm{Var}(x)$ is the weighted variance computed as follows:

$$\mathrm{Var}(x) = \frac{\sum_i (x_i - <x>)^2 \cdot w_i}{\sum_i w_i}\,, \tag{5.9}$$

again with $<x>$ being the weighted average of x. The y-value t at $x = 0$ is computed as:

$$t = <y> - m \cdot <x> \tag{5.10}$$

and the goodness-of-fit (GOF) or weighted squared deviation χ^2 from the linear curve:

$$\chi^2 = \frac{\sum_i (y_i - x_i \cdot m + t)^2 \cdot w_i}{\sum_i w_i}\,. \tag{5.11}$$

“Profile-gradient” The first example is the profile-gradient, where we compute the slope with which the logarithm of the pixel amplitudes A_i changes with distance to the CoG of the image (cf. Fig. 5.2). The distance to the CoG r is computed as:

$$r = \sqrt{\left(\frac{X}{\text{Hillas-length}}\right)^2 + \left(\frac{Y}{\text{Hillas-width}}\right)^2}\,. \tag{5.12}$$

The profile-gradient follows as slope m of Eq. 5.8 with $x = r$, $y = \ln(A\,[\text{p.e.}])$, and $w = A$. Using the same variables and the resulting m and t, one can also compute the spread around the profile-gradient as χ^2 from Eq. 5.11, resulting in the “profile-gradient-GOF.”

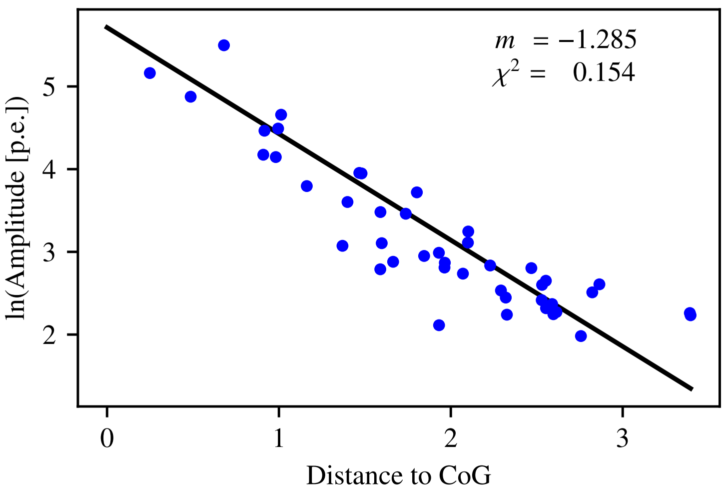

Figure 5.2: Profile-gradient for a simulated γ-ray event. The distance to the CoG is computed according to Eq. 5.12 and is therefore unitless.

Compared to Hillas-kurtosis, profile-gradient is sensitive not only to the charge distribution along the major axis but also along the minor axis. The distribution of profile-gradient in Fig. C.19 shows that γ-ray showers usually have larger negative gradients, typical for more compact showers. Very few, dominantly hadronic, showers have positive gradients, which are characteristic of muon rings where the intensity increases toward the edges. The distribution of the profile-gradient-GOF, shown in Fig. C.20, also indicates that proton showers are more irregular and therefore have a larger spread around the linear gradient. One can also compute the profile-gradient for pixels with $X_i > 0$, resulting in “profile-gradient$_{\text{head}}$,” and for pixels with $X_i < 0$, resulting in “profile-gradient$_{\text{tail}}$.” For asymmetric events, these values can be quite different.

"Kink-major" is the gradient m from Eq. 5.8, with $x = |X|$, $y = Y$, and $w = A$, and is sensitive to the curvature of the ellipse along the major axis. When muons are recorded at large impact distances, only part of the muon ring is visible in the camera, which might be confused with a γ-ray ellipse, except for its curvature. Fig. C.21 shows that γ-ray events tend to have values of kink-major closer to zero, while some hadronic events show larger absolute values for kink-major. The calculation of the "kink-major-GOF" as χ^2 of Eq. 5.11 is identical to the definition of the Hillas-width in the case of kink-major = 0. For values of kink-major $\neq 0$, the kink-major-GOF is smaller than the Hillas-width due to one more degree of freedom. To further reduce the correlation with Hillas-width and to make the distribution more similar for events of different sizes, we divide the kink-major-GOF additionally by Hillas-npix − 2, as m and t represent two additional degrees of freedom. With this computation, the distribution is smoothed and the characteristic dip present in the distribution of Hillas-width is eliminated.

"Kink-minor" is defined similarly as m from Eq. 5.8 with $x = Y^2$, $y = X$, and $w = A$, and represents a gradient in $<X>$ for increasing offsets to the major axis. This is tightly connected to a change in the ellipse's width along the major axis. We also tested the variable resulting from $y = |Y|$ but found that the separation between γ-ray and hadronic events is not as good, as the influence of low-intensity pixels far away from the major axis is reduced. From Fig. C.23, one can see that hadronic showers tend to have values closer to zero, while the γ-ray simulations show larger tendencies for more asymmetric images. The sign of the kink-minor is especially interesting, as shower images are expected to have a larger width in the tail of the shower facing the ground, so the sign of kink-minor is useful in the angular reconstruction of the events. The "kink-minor-GOF" follows as $\chi^2/(\text{Hillas-npix} - 2)$ and is proportional to the Hillas-length. Figure C.24 shows that the distributions for γ rays and background events are similar.

"Time-gradient-major" In the variables described so far, the time information in the pixels is not yet used. We compute the time-gradient-major as m from Eq. 5.8 with $x = X$, $y = T$, and $w = A$, and the "time-gradient-minor" with $x = Y$ and $y = T$, and $w = A$. The distributions for the two time gradients are shown in Figs. C.25 and C.26. While the time-gradient-minor is expected to be close to zero for all showers, the time-gradient-major is expected to be mainly a function of the impact distance for geometrical reasons. Therefore, the difference between the distributions of γ-ray and hadronic showers is somewhat surprising. As we will see in Sect. 5.3.5, however, these variables do not pass our selection procedure.

The difference between the time spreads "time-gradient-major-GOF" and "time-gradient-minor-GOF," shown in Figs. C.27 and C.28, is highly affected by different NSB rates. While this is expected for the tail-cut image cleaning, which is neglecting the pixel's time information, we cannot use these variables without introducing large systematic uncertainties.

"Roughness" The next set of variables is meant to be sensitive to the regularity or smoothness of the shower. One can compare a smoothed version of the image to the original by adding the differences for each pixel. This is done in the roughness variable, which is calculated as follows:

$$\text{roughness} = \sum_i \left(\frac{\sum_j (A_i - A_j)^2 \cdot w_{ij}}{\sum_j w_{ij}} \right) \frac{\text{Hillas-npix}}{\text{Hillas-image-amplitude}^2} \tag{5.13}$$

where w_{ij} represents weights of a Gaussian kernel with $\sigma = 1$ pixel width:

$$w_{ij} = \exp\left(-\frac{(X_i - X_j)^2 + (Y_i - Y_j)^2}{2\sigma^2}\right). \tag{5.14}$$

The roughness variable adds up differences in the pixel amplitude between neighboring pixels, while the "std-over-mean" variable adds differences to the mean from all shower pixels.

"Std-over-mean" converges to the roughness parameter in the limit of large kernel widths. It is computed as:

$$\text{std-over-mean} = \frac{\sqrt{\frac{\sum_i (A_i - <A>)^2}{\text{Hillas-npix}-1}}}{<A>}. \tag{5.15}$$

Therefore, the variables roughness and std-over-mean are correlated, but the strength of the correlation is different for γ rays (0.88) and background events (0.79). The distribution for both variables can be seen in Figs. C.29 and C.30. One can see that for both variables, the γ-ray simulations tend toward larger values due to their more compact shape, leading to larger differences in the amplitudes of neighboring pixels.

"Spatial-auto-correlation" An attempt to characterize differences from the expected event morphology resulted in the computation of the spatial-auto-correlation (Moran's I) of the residuals after subtracting the expected pixel amplitude based on the profile-gradient:

$$I = \frac{N \cdot (N-1)}{W} \frac{\sum_i \sum_j (R_i - <R>)(R_j - <R>) \cdot w_{ij}}{\sum_i (R_i - <R>)^2}, \tag{5.16}$$

with $N =$ Hillas-npix, w_{ij} the weights from Eq. 5.14, and $W = \sum_i \sum_j w_{ij}$. R_i is calculated from the previously determined profile-gradient m and the corresponding t (cf. Eq. 5.8 and 5.10):

$$R_i = \frac{A_i - \exp(r_i \cdot m + t)}{\sqrt{\exp(r_i \cdot m + t)}} \tag{5.17}$$

and

$$<R> = \frac{\sum_i R_i}{N}. \tag{5.18}$$

In the absence of any correlation, the expected value for I is -1, with more negative values indicating spatial anticorrelation and more positive values indicating spatial correlation. The distributions of the spatial-auto-correlation shown in Fig. C.31 are very similar between background and γ rays, with background events slightly more abundant at larger negative values.

5.3.4 Pixel Variables

To improve gamma-hadron separation, especially for low-size images, we also examine distributions focusing on the two brightest pixels. From their amplitude values $A1$ and $A2$, we compute "fraction-top-1" and "fraction-top-1+2" as

$$\text{fraction-top-1} = \frac{A1}{\text{Hillas-image-amplitude}} \tag{5.19}$$

and

$$\text{fraction-top-1+2} = \frac{A1 + A2}{\text{Hillas-image-amplitude}}, \tag{5.20}$$

respectively. If the machine-learning algorithm has access to both values, the ratio between the two brightest pixels is also accessible. The distributions in Figs. C.32 and C.33 show that γ-ray showers have a larger charge concentration in the brightest pixel(s).

The other three pixel parameters concern the position of the brightest two pixels with respect to the CoG and to each other:

$$\text{distance-top-1} = \frac{\sqrt{(X1 - {<}X{>})^2 + (Y1 - {<}Y{>})^2}}{\text{Hillas-length}}, \tag{5.21}$$

and

$$\text{distance-top-2} = \frac{\sqrt{(X2 - {<}X{>})^2 + (Y2 - {<}Y{>})^2}}{\text{Hillas-length}}, \tag{5.22}$$

and

$$\text{distance-top-1-2} = \frac{\sqrt{(X1 - X2)^2 + (Y1 - Y2)^2}}{\text{Hillas-length}}, \tag{5.23}$$

with $(X1, Y1)$ being the coordinates of the brightest pixel, $(X2, Y2)$ the coordinates of the second brightest pixel, and $({<}X{>}, {<}Y{>})$ the coordinates of the CoG.

The distributions in Figs. C.34-C.36 show that for γ-ray showers, it is more likely to find the brightest, but also the second brightest, pixel closer to the CoG, which is expected for more regular showers. For the distance between the two brightest pixels, there is a plateau in the distributions around one Hillas-length, which is more concentrated for γ-ray showers, while there is a larger spread for hadronic showers.

Finally, simply counting the number of pixels that exceed the thresholds of 10 p.e. and 30 p.e. results in the variables "$\text{npix}_{>10}$" and "$\text{npix}_{>30}$," respectively. Figures C.37 and C.38 show the distributions of these variables, where small γ-ray images tend to have brighter pixels, while for larger images, hadronic showers have a more homogeneous light distribution.

5.3.5 NSB sensitivity of the image parameters

By introducing additional variables, one not only increases sensitivity to physical differences between the shower types, but also to systematic differences between data and simulations. One possible source of systematic difference is the NSB level, which varies within the field of view (FoV) and between different observations, but is simulated at a constant averaged value. To obtain a more quantitative estimate of the NSB sensitivity per variable, we use point-source simulations for nominal and high NSB values. These simulations are more efficient than the diffuse simulations introduced earlier, which leads to a statistically more accurate estimate. As for the diffuse simulations, the high NSB value is 1.65 times larger compared to the nominal NSB value and exceeds the NSB values of the vast majority of observations.

For each variable, we employ an Anderson-Darling test for k-samples, which tests the null hypothesis that the two distributions are drawn from the same population. Figure 5.3 summarizes the results of these tests. The danger of an NSB-sensitive distribution is that the separation training will perform differently on observations taken under different NSB conditions, introducing systematic uncertainties in the reconstructed γ-ray rates. Additionally, the performance might also change across the FoV introducing background artifacts, like gradients.

Compared to all other variables, the time variables show the most significant NSB dependence. This is because the image cleaning completely ignores the pixel times and their clustering for shower pixels. Consequently, higher NSB rates lead to a higher rate of noise pixels with larger amplitudes that survive the image cleaning, but which are randomly distributed in time. These pixels can drastically change the time gradient, if the random

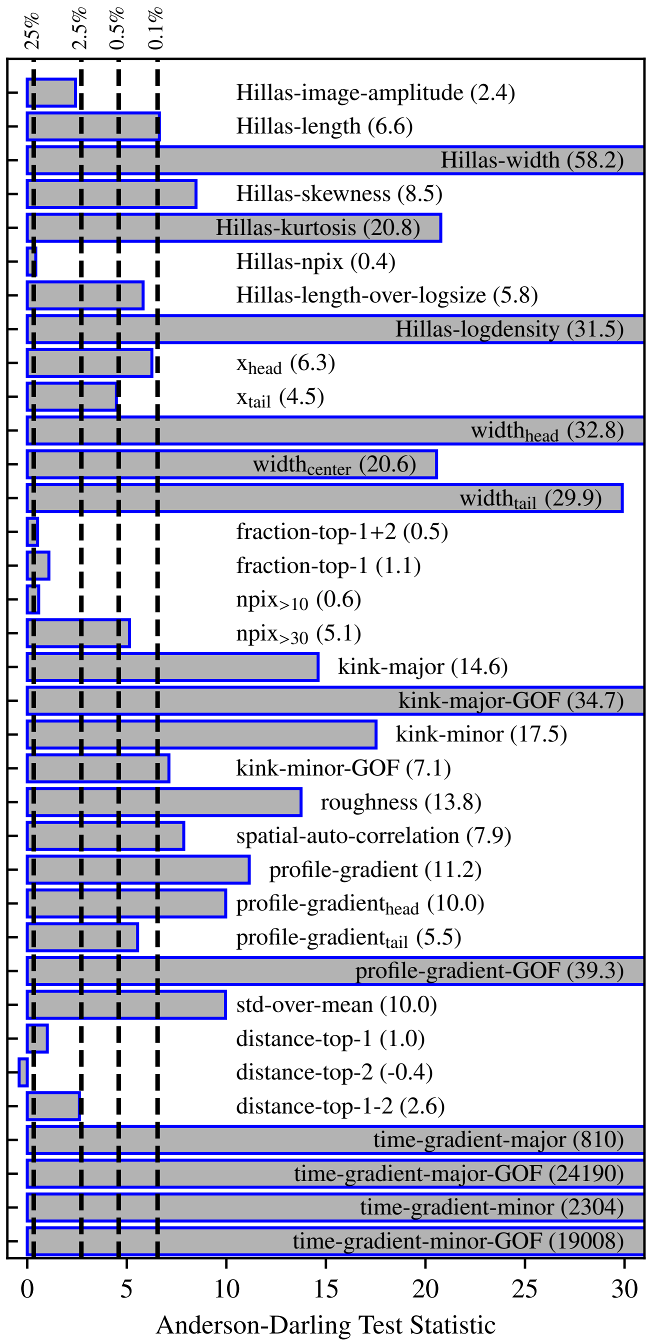

Figure 5.3: Anderson-Darling statistic for the distribution of nominal and high-NSB simulations. Larger values correspond to a more significant difference between the distributions. The vertical lines show four selected significance levels at 25%, 2.5%, 0.5%, and 0.1%. The numbers next to the variable names indicate the value of the Anderson-Darling statistic since some of the values extend beyond the plotted range.

pixel time is very different from the shower time. Therefore, we do not use time-based variables for the separation training.

A time-based image-cleaning technique might solve this issue and would allow time variables to be used in the separation training. The exact influence of the NSB rates on the effective area and thus the flux systematics will be evaluated in Sect. 5.6.2.

5.4 Architecture of training algorithms

The event reconstruction used in this work is based on the current H.E.S.S. monoscopic analysis procedure. The first step involves determining the so-called "flip" (F), which specifies whether the image center is to the left or right of the true source position in the camera frame. The source is expected to be located along the major axis of the

Hillas ellipse. However, for a monoscopic reconstruction, it is challenging to determine the direction along the axis.

Next, the distance between the CoG of the ellipse and the source location, called "disp" (δ), is reconstructed (Hofmann, 1999). The reconstructed source position in the camera reference frame can then be obtained using the following equations:

$$\begin{cases} X_{\mathrm{CAM}}^{\mathrm{rec}} = X_{\mathrm{CAM}}^{\mathrm{COG}} + F\cos(\alpha)\delta \\ Y_{\mathrm{CAM}}^{\mathrm{rec}} = Y_{\mathrm{CAM}}^{\mathrm{COG}} + F\sin(\alpha)\delta \end{cases}, \tag{5.24}$$

where $F = \pm 1$, and α is the angle of the major axis of the ellipse with respect to the camera frame.

In the standard H.E.S.S. analysis, the order in which flip and disp are determined is irrelevant. However, for this work, some of the new variables introduced depend on distinguishing the head and tail of the ellipse. Thus, the flip must be determined first and if it is positive, these variables change sign or are interchanged with their corresponding variables on the opposite side of the shower. The flipping behavior for each variable is detailed in Tab. D.1.

Moreover, the flip-dependent image parameters are also sensitive to the position of the source in the camera frame, while the simulations are always performed for a point source at $X_{\mathrm{CAM}} = +0.5°$. This would normally lead to an asymmetry in the flip distribution, since the region left to the source position is larger than that to the right. Therefore, we mirror half of the simulated events with respect to the Y_{CAM} axis ($X_{\mathrm{CAM}} \to -X_{\mathrm{CAM}}$), randomizing the distributions. With that, we ensure a performance independent of the camera sector.

The subsequent steps involve energy regression and the estimation of the event's gammaness, that is, a quantity reflecting the probability that the primary particle was a γ ray, compared to a hadronic particle. Also in these trainings, the flip determination and mirror operations described above are required beforehand due to the head- and tail-dependent variables being used. Aside from this, both reconstructions are independent of the other reconstruction steps. Here, we evaluate the performance of the separation as a function of the Hillas-image-amplitude, rather than the reconstructed energy typically used in stereoscopic analyses.

5.4.1 Flip determination algorithm

In Murach et al. (2015), the "flip" is determined by examining the sign of the Hillas-skewness. This asymmetry is a good first-order indicator of the orientation of the ellipse with respect to the source position. However, for truncated or small images with few pixels and a small Hillas-image-amplitude, the Hillas-skewness determination becomes less accurate, resulting in an increasing fraction of incorrectly flipped events.

In this work, we improve the flip determination by employing a boosted decision tree (BDT), a machine-learning algorithm known for its efficiency as a classifier and widely used in γ-ray astronomy for tasks such as gamma-hadron separation. We use the `XGBRegressor` from the XGBoost[41] Python package (Chen and Guestrin, 2016) with 100 trees, a maximum depth of 5, and a learning rate of 0.3.

The true flip for a simulated event, F_{true}, is defined as

$$F_{\mathrm{true}} = \begin{cases} 1, & \text{if } \mathrm{X}_{\mathrm{CAM}}^{\mathrm{COG}} < \mathrm{X}_{\mathrm{CAM}}^{\mathrm{true}} \\ -1, & \text{if } \mathrm{X}_{\mathrm{CAM}}^{\mathrm{COG}} > \mathrm{X}_{\mathrm{CAM}}^{\mathrm{true}} \end{cases}, \tag{5.25}$$

with $X_{\mathrm{CAM}}^{\mathrm{true}}$ being the true position of the source in the camera reference frame. The simulated point-source γ-ray events were divided into two sets, where we used 80% for

[41]Version 1.7.4

training and 20% for testing. The variables from Sect. 5.3 were given as input to the training, and the total fraction of wrongly flipped events after the BDT evaluation served as the score to be minimized. As BDTs return the relative variable importance for each input feature, we chose the following procedure for the selection of useful variables.

The selection process began by including all non-time-based variables, followed by an iterative process in which the least important variable was removed and the BDT was re-trained. This process continued until the false flip fraction over all energies increased by 2.5% with respect to the model trained with all variables. The final set of selected variables and their respective importance are shown in Figure 5.4.

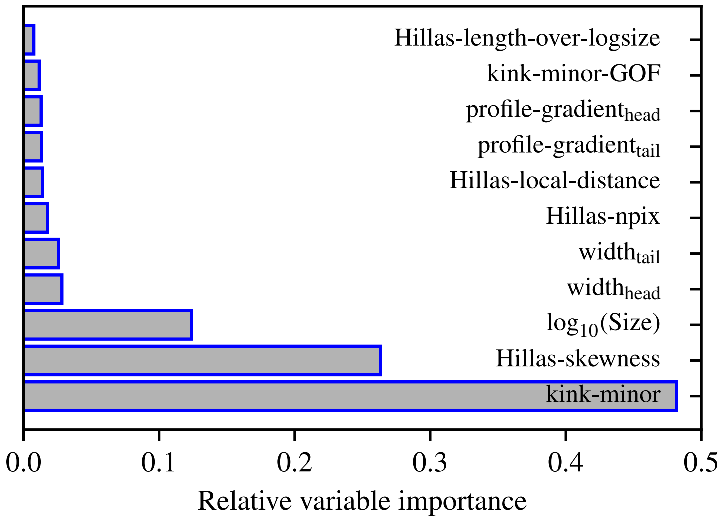

Figure 5.4: Relative variable importance for the flip training.

5.4.2 Energy and disp regression algorithm

Energy and "disp" regression are currently performed in H.E.S.S. using two independent shallow neural networks (NNs) based on the `tensorflow.keras` framework, with two hidden layers with 20 nodes each and a sigmoid activation. The mean squared error of the predicted variable (energy or disp) for all events was used as the variable loss to be minimized. The NNs were trained for up to 5000 epochs with a batch size of 1000. 90% of the data were used for training and 10% for validation, that is, estimation of the variable loss. For this work, the structure of the neural networks was kept, changing only the input variables. For the standard H.E.S.S. analyses, the variables used are: Hillas-image-amplitude, Hillas-length, Hillas-width, Hillas-skewness, Hillas-kurtosis, and Hillas-logdensity. Again, we explored the ideal subset of the variables from Sect. 5.3. As the variable importance is not available in NNs, the iterative procedure starts with all variables, conducting a training with N input variables. Subsequently, N individual trainings were performed, each omitting one of the N variables, and the final loss of each NN training with the $(N-1)$ variables was evaluated. The best-performing training indicated the least important variable and was used for the next iteration. This process was repeated until the performance (i.e., variable loss) dropped by 5% with respect to the model trained with all the variables. The same subset of variables was chosen for both energy and disp regression: Hillas-image-amplitude, Hillas-local-distance, Hillas-width, Hillas-length, Hillas-npix, Hillas-skewness, Hillas-kurtosis, Hillas-length-over-logsize, charge-asymmetry, time-gradient-major, and std-over-mean.

5.4.3 Particle identification algorithm

Due to the large number of hadronic background events, which exceed the number of γ-ray events by typically three orders of magnitude, an efficient classification algorithm is necessary. Its task is to assign a "gammaness" score to each event that is maximally different for hadronic and γ-ray events. The differences in the gammaness distribution allow the signal to be separated from background events by rejecting events below a certain value of the gammaness score. We refer to this value as selection or BDT cut. Similar to the flip training, we employ a BDT trained on simulated point-source γ rays and measured background data across all energy and size ranges, with 10% of the data reserved for validation to prevent over-fitting. After exploring various settings for the number of trees, tree depth, and learning rate, we identified an optimal configuration with 200 trees, a maximum depth of 6, and a learning rate of 0.3, yielding a stable and robust performance. We also investigated the impact of segregating the training data by size ranges, but this approach did not result in significant performance improvements. This indicates that the algorithm has enough information about the event sizes to treat different sizes appropriately.

For the separation training, the events are re-weighted from the simulated spectrum with an index of 1.8 to a more typical γ-ray spectrum with an index of 2.5. We do not expect any bias for sources with different spectral shapes or offsets from the telescope's pointing, as the instrument response functions (IRFs)[42] are binned in energy and offset; however, the performance might decrease slightly.

For the selection of useful variables, we again employ an iterative procedure that starts with all variables (except the time variables) and removes the least important variable after each training iteration. The performance of each training is evaluated based on the signal efficiency, requiring a background rejection fraction of 95% over all events. Additionally, the training is also evaluated on simulations with a high NSB value, and the difference in signal efficiency between the two simulations serves as an indicator of the training's sensitivity to NSB fluctuations. Figure 5.5 summarizes this procedure, where each bar, starting from the bottom, shows the result of the training after removing the respective variable. The result consists of two parts: the first is the relative improvement in signal efficiency compared to the reference training with the standard six Hillas variables ($\epsilon_{\mathrm{sig}}^{\mathrm{HillasOnly}} = 27.8\%$) for the nominal NSB value. Secondly, the signal efficiency is compared between nominal and high-NSB simulations for all trainings. The ideal training maximizes improvement in signal efficiency compared to the reference training while not increasing the difference between the two NSB simulation sets.

After removing the first four variables (charge-asymmetry, $\mathrm{y_{head}}$, $\mathrm{y_{center}}$, $\mathrm{y_{tail}}$), the signal efficiency slightly increases, indicating confusion in the BDT due to too many correlated or unimportant variables. Continuing to remove variables does not affect the performance but increases the NSB sensitivity of the trainings. Only after removing distance-top-1 do both the performance and the NSB sensitivity decrease, with the difference in signal efficiency between the two NSB simulation sets ending up at values smaller than 1.6% – the value for the reference training – for most of the trainings. The following variables survived the selection process beyond the iterations shown in Fig. 5.5 (in ascending order of their importance): std-over-mean, kink-major-GOF, Hillas-local-distance, Hillas-npix, $\mathrm{width_{head}}$, Hillas-logdensity, Hillas-width, and profile-gradient.

Mainly because of the sensitivity to different NSB rates, we decided to keep all variables except charge-asymmetry, $\mathrm{y_{head}}$, $\mathrm{y_{center}}$, $\mathrm{y_{tail}}$, although other selections could be justified as well. For the final training we remain with 31 input variables, with their relative variable importance given in Tab. D.1.

[42]Collection of functions describing the response of the telescope to a true source flux (effective area, energy dispersion, point spread function, and background model)

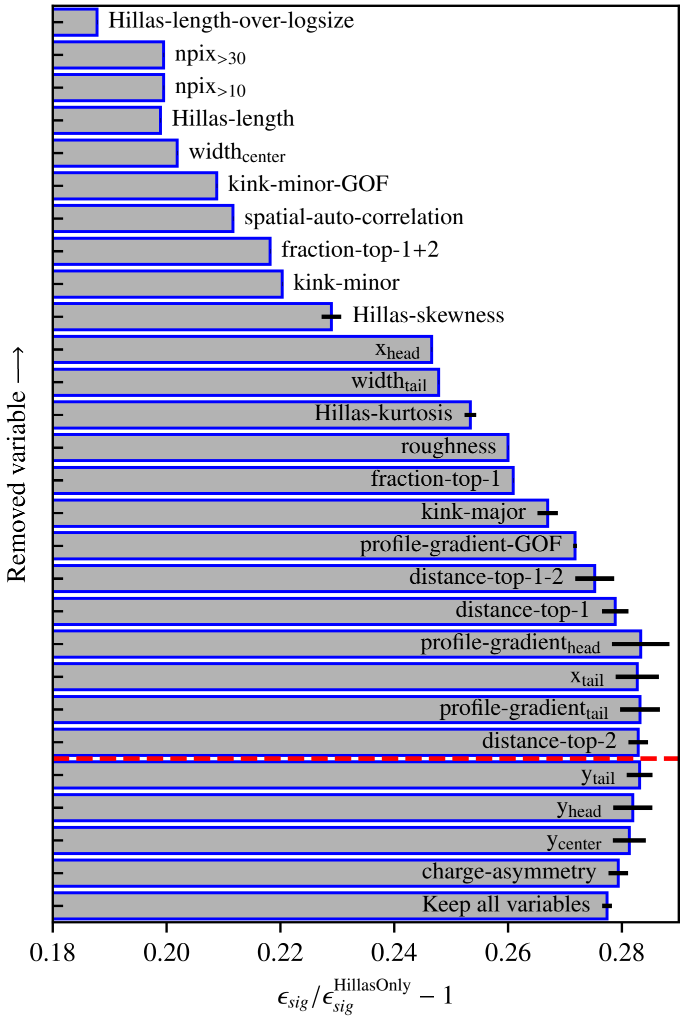

Figure 5.5: Relative change of the signal efficiency ϵ_{sig} during the iterative removal of the least important variable (from bottom to top). The signal efficiency for each training is compared to the signal efficiency of the reference training $\epsilon_{\mathrm{sig}}^{\mathrm{HillasOnly}}$ (the current training with the 6 Hillas variables) for a background rejection of 95%. The black error bars show the difference in the signal efficiency for simulations with nominal and high NSB values, which exceeds the difference present in the reference training. No error bar corresponds to a difference which is smaller than in the reference training. Variables below the dashed red line are not selected for the final training.

5.5 Size-dependent selection cut

To find the optimal BDT cut resulting in the best sensitivity, one can maximize the q-factor defined as $q = \epsilon_{\mathrm{sig}}/\sqrt{\epsilon_{\mathrm{bkg}}}$. This approach is effective because the observed significance σ for an on-off (i.e., aperture photometry) analysis is proportional to

$$\sigma \propto \frac{N_{\mathrm{sig}}}{\sqrt{N_{\mathrm{sig}} + N_{\mathrm{bkg}}}} = \frac{n_{\mathrm{sig}} \cdot \epsilon_{\mathrm{sig}}}{\sqrt{n_{\mathrm{sig}} \cdot \epsilon_{\mathrm{sig}} + n_{\mathrm{bkg}} \cdot \epsilon_{\mathrm{bkg}}}} \approx \frac{n_{\mathrm{sig}}}{\sqrt{n_{\mathrm{bkg}}}} \frac{\epsilon_{\mathrm{sig}}}{\sqrt{\epsilon_{\mathrm{bkg}}}}, \tag{5.26}$$

where N refers to counts after cuts and n refers to the number of events before cuts. The final approximation assumes $N_{\mathrm{sig}} \ll N_{\mathrm{bkg}}$, which is a good approximation in the low signal-to-noise case where optimization is most critical. The ratio of $n_{\mathrm{sig}}/\sqrt{n_{\mathrm{bkg}}}$ is fully determined by the source and background spectra together with the effective area, leaving the q-factor as the remaining quantity to optimize. Several tests carried out in the context of this study showed that the performance of the BDT within a certain size range is stable with respect to adding or removing events of different sizes[43]. However, the distribution of the BDT score changes, which can make the performance appear worse or better for the size range of interest if the BDT cut is optimized using events of all sizes. Therefore, we optimize the q-factor in different size bins by scanning through different BDT cuts (cf. Fig. 5.6). The optimal BDT cuts are then smoothed with a Gaussian kernel with width

[43]This holds as long as the algorithm has access to (implicit) information about the event size.

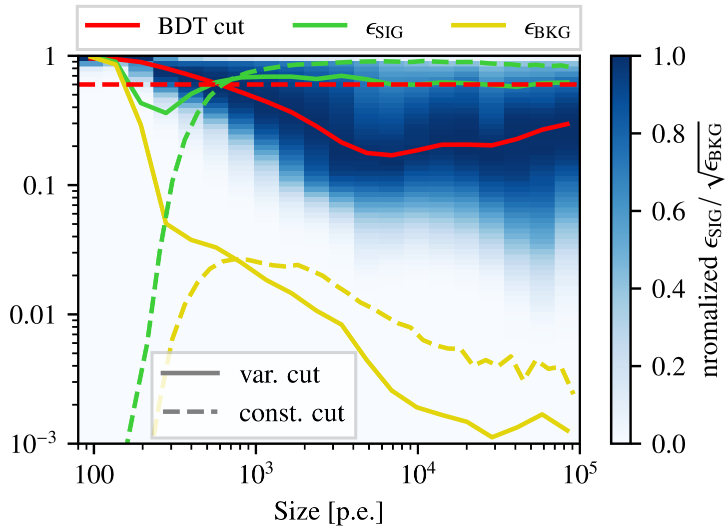

Figure 5.6: Scan of q-factors for different event sizes (x-axis) and BDT cuts (y-axis) using the 6 Hillas variables. For each size bin, the color map shows the q-factors (normalized to 1) for different BDT cuts. The resulting optimal BDT cut (red) is shown together with the signal (green) and background (yellow) efficiencies. The solid lines show the case for the size-dependent BDT cut while the dashed lines show the constant BDT cut.

equal to one bin, which results in the red line in Fig. 5.6. Events can now be selected based on the BDT cut interpolated at their respective size and their BDT score.

This approach allows for the retention of more low-size events, where due to poor separation, the best statistical significance is achieved by keeping nearly all events. While the sensitivity gain due to low-size events is limited by the high background contamination, it does lower the energy threshold and reduces the relative systematic uncertainty, which is highest for strict cuts in the distribution.

5.6 Performance evaluation

The performance evaluation is conducted for simulations at a zenith angle of 20° and an angular separation (offset) of 0.5° from the pointing direction of the telescopes. In the following, we compare the current standard analysis using the six Hillas variables and a constant BDT cut (labeled "Hillas variables (const. cut)") to an intermediate analysis with the Hillas variables but a size-dependent BDT cut (labeled "Hillas variables (var. cut)") and the new analysis with new variables and the size-dependent cut (labeled "New variables (var. cut)"). Details on how the size-dependent BDT cut is computed can be found in Sect. 5.5.

The performance presented in Murach et al. (2015) is based on different event (pre)selection cuts and the camera previously installed on CT5. In contrast to this study, they use a θ^2-cut on the angular mis-reconstruction, considerably lowering the effective area but improving the energy resolution. For these reasons, we do not directly compare to the results from Murach et al. (2015), but instead to the performance of current FlashCam analyses without θ^2-cut.

5.6.1 Event reconstruction

In this section, we evaluate the performance of the event reconstruction using the machine-learning models described in Sect. 5.4. First, the "flip" is determined, based on which the sign of variables like the Hillas-skewness is changed, and sector variables like x_{head} and

x_{tail} are interchanged according to Tab. D.1. The flipped variables then serve as input for the energy, direction, and particle type reconstruction.

False flip fractions The improvements in the flip determination are shown in Fig. 5.7, where the performance of the BDT model is compared with that of the flip determination based solely on the Hillas-skewness. At high energies, where an increasing fraction of the events is truncated at the camera edges, image skewness alone becomes an unreliable indicator. In contrast, the BDT model consistently demonstrates the expected behavior, with a decreasing false flip fraction as energy increases. For low-energy events with small images, determining the correct flip remains challenging. This is especially the case for highly symmetric events with their CoG close to the true source position. However, for these events, even an incorrect flip has only a minor effect on the reconstructed position and the associated parameters. As a result, the false flip fraction merely counts all events where the flip was incorrectly determined, while the angular resolution more accurately reflects the impact of the flip determination on the reconstruction.

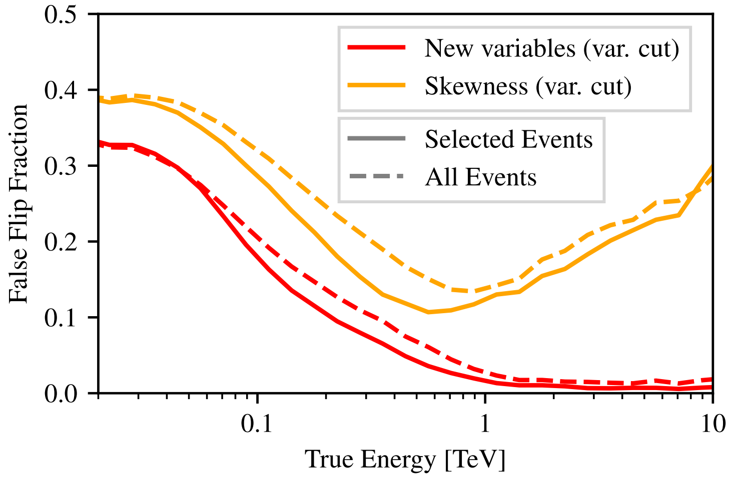

Figure 5.7: Fraction of wrongly flipped events as function of true energy. The dashed lines show the performance evaluated on all events after preselection, while the solid lines only include selected events passing the size-dependent gamma-hadron separation cut.

Angular resolution The angular resolution is defined as the 68% containment radius of the reconstructed position relative to the true one. It is important when disentangling sources close to each other and also affects the sensitivity of the instrument to isolated point-like sources, as the background increases with a larger integration area of the signal.

Based on the dashed lines in Fig. 5.8, the improvement achieved with the new variables is evident, lowering the angular resolution at 100 GeV by 57%. The dashed lines are always shown to represent the performance of the reconstruction independent of the BDT cut, while the solid lines represent the actual performance of the analysis, including only events passing the gamma-hadron separation. Since the constant BDT cut removes most low-size events, the good angular resolution of this analysis at low energies is a natural but mostly irrelevant consequence, due to the low event statistics in this range. The enhancement in angular resolution is partly attributable to the improved "disp" estimation and partly to the improved flip training, as incorrectly flipped events are often reconstructed far from the true position, particularly when the impact distance is large.

As the direction determination of the new analysis also makes use of very NSB dependent variables such as the time-gradient-major, the angular resolution is also evaluated on the high-NSB simulations. Here, we use simulations of γ-ray events with an increased NSB value (scaled by 1.65), which is higher than expected for the vast majority of observations (cf. Sect. 5.3.5). The difference in angular resolution is very small and is shown in the barely visible red-shaded region in Fig. 5.8.

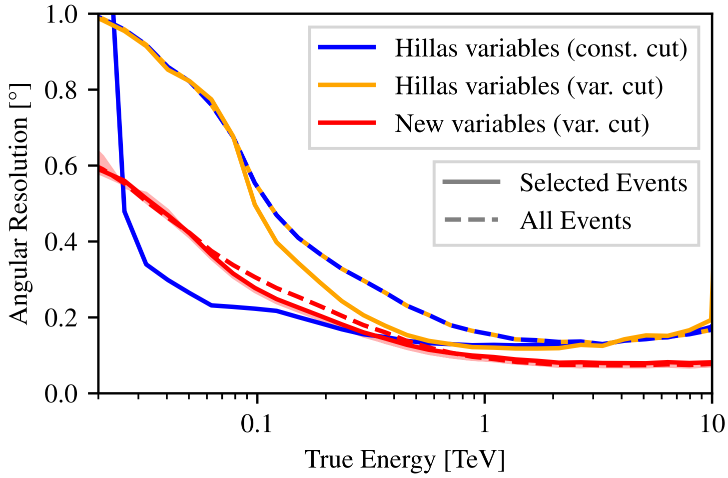

Figure 5.8: Angular resolution as a function of true energy. The blue curves show the performance for the current analysis, the orange ones for the intermediate analysis with the old training but the size-dependent BDT cut, and the red lines represent the new analysis. The red-shaded band shows the difference to high-NSB simulations.

Energy resolution The energy bias is defined as the mean of the energy migration $\mu = (E_{\text{reco}} - E_{\text{true}})/E_{\text{true}}$ and the energy resolution is the standard deviation of μ. For ideal reconstruction, the energy bias would be zero; however, if events with different true energies appear very similar to the algorithm, it assigns an average energy to minimize the loss. This leads to a positive bias for low-energy events and a negative bias for higher-energy events. The dip-like shape of the curves for a variable BDT cut in Fig. 5.9 can be understood when considering that events with low size are composed of events with low energies and small impact distance, as well as events with large energies and large impact distance. Compared to the other curves, the energy bias with the constant BDT cut appears shifted to the right,

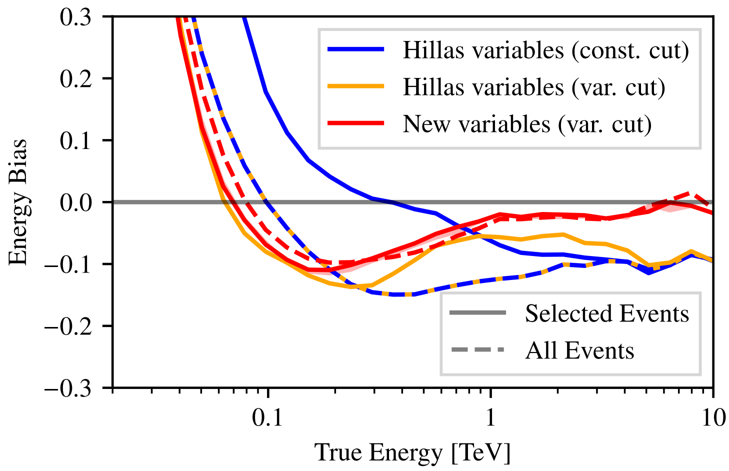

Figure 5.9: Energy bias as a function of true energy.

as only very few events with low sizes pass the BDT cut. The energy at which the bias exceeds a value of +10% is usually considered a safe choice for the energy threshold. Hence, we observe that the energy threshold can be lowered considerably using the size-dependent BDT cut. Comparing the dashed lines, for which no BDT cut is applied, one can see that the new variables help in moving the energy bias closer to zero.

The energy resolution, shown in Fig. 5.10, also shows significant improvement when evaluated on all events. Considering the BDT cuts, the improvement is most notable at higher energies $\gtrsim$200 GeV. The difference to high-NSB simulations is again illustrated based

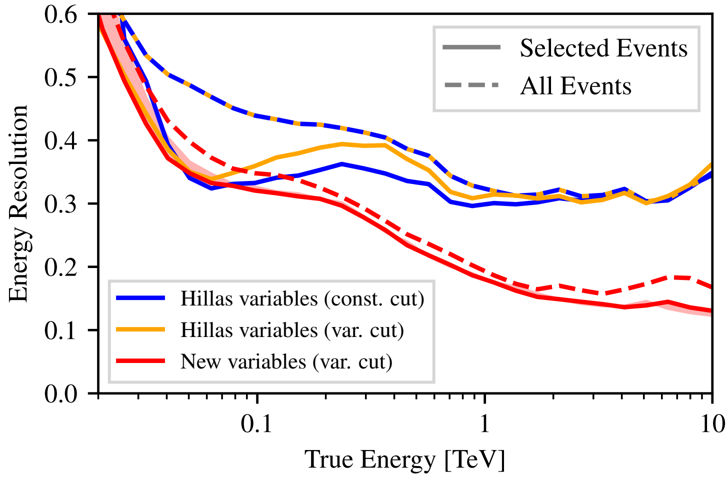

Figure 5.10: Energy resolution as a function of true energy. The red-shaded region shows the difference in energy resolution compared to the high-NSB simulations.

on the red-shaded regions. Although there is no significant difference in the energy bias, the energy resolution becomes clearly worse for low energies under high-NSB conditions. This is not unexpected, as during calibration, the pixel amplitudes are corrected on the basis of their average amplitude in the absence of a triggered event, leading to a minor effect of the NSB rates on the energy bias. However, the NSB fluctuations in the pixel amplitudes increase with the square root of the subtracted amplitude, causing also larger uncertainty in the energy reconstruction.

5.6.2 Background rejection

The difference in separation performance between the three configurations, measured in terms of the q-factor (see Sect. 5.5), is shown in Fig. 5.11. Here, the constant BDT cut is optimized for medium sizes around 600 p.e., resulting in similar q-factors for the two configurations that use the standard Hillas variables. At lower or higher sizes, the configurations employing the size-dependent cut achieve significantly higher q-factors. The benefit of the new variables is most pronounced for sizes around 200 p.e. (not considering the statistical fluctuations at larger sizes).

Finally, the effective areas shown in Fig. 5.12 also reflect the lower energy threshold for the configurations with a variable BDT cut, which is also often chosen as the energy at which the effective area drops below 10% of its maximum. This threshold is at 30 GeV for the configurations with a variable BDT cut and at 64 GeV for the configuration with the constant BDT cut.

In a real data analysis with the HAP framework, the corresponding IRFs are computed based on simulations at different zenith, azimuth, and offset angles, with atmospheric transparency also accounted for. One variable not considered is the rate of the night sky background light. In Fig. 5.13, the resulting effective area for the high-NSB simulations is

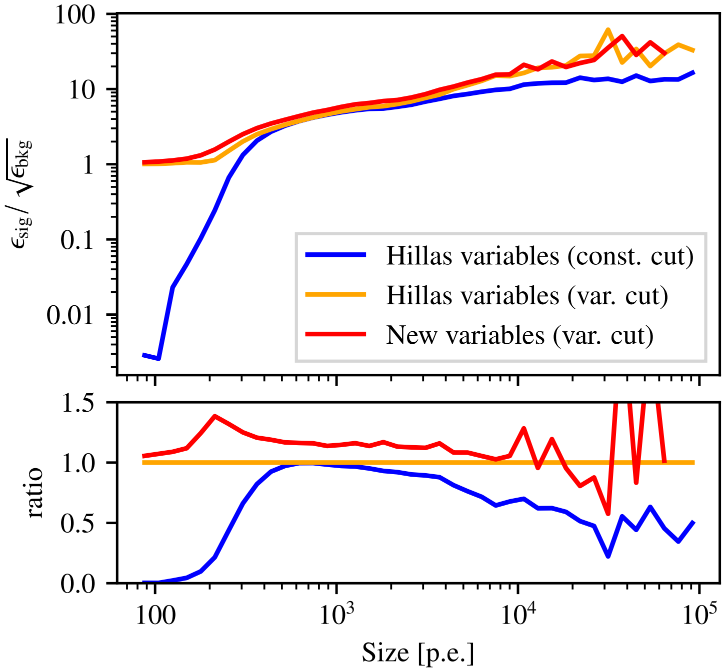

Figure 5.11: The absolute q-factors (upper panel) of the separation trainings as a function of event size, and their ratios (lower panel). The blue curves show the performance for the current analysis, the orange ones for the intermediate analysis with the old training but the size-dependent BDT cut, and the red lines represent the new analysis.

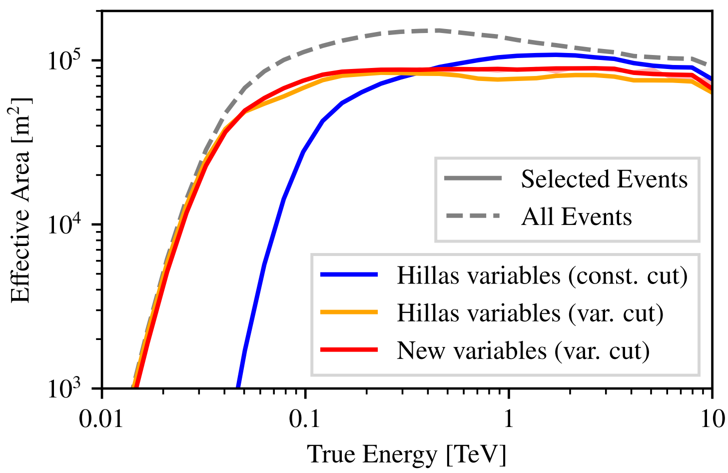

Figure 5.12: Effective areas for the three configurations as function of true energy.

compared to that from the default simulations. For observations taken under such high NSB rates, this difference would translate directly into a systematic error on the recovered flux. Since the number of events simulated for the high NSB value is considerably lower than for the default simulations, the ratio of the effective area is also affected by statistical fluctuations, especially toward the higher energies.

The shaded bands in Fig. 5.13 are constructed based on a systematic deviation of neighboring points from a value of 1 and therefore still include statistical fluctuations. Especially toward higher energies, the statistical fluctuations dominate and increase the difference between the two simulation sets. The width of the shaded bands can thus be interpreted as the maximum expected systematic uncertainty caused by different NSB

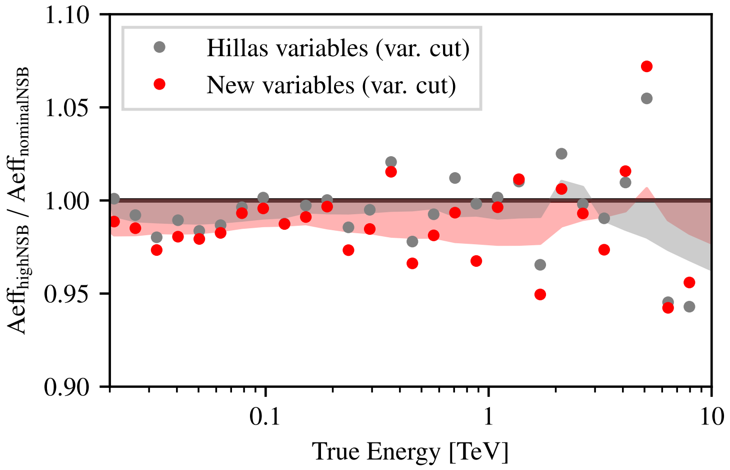

Figure 5.13: Ratio of the effective areas computed from simulations with nominal and high NSB values. The points show the ratio for each energy bin, while the shaded bands represent an estimate of the systematic uncertainty. For details see main text.

values. This systematic effect resulting from high NSB rates is expected to be opposite for observations taken under lower NSB rates, although less strong.

Quantitatively, the systematic uncertainty due to NSB differences is ∼2.5%, which is small compared to other systematic uncertainties, which are generally estimated to add up to ∼20% (see supplementary material of Aharonian et al., 2022a). However, it is still informative to compare this systematic uncertainty between the new and the old variables. This comparison is made for the two configurations with the size-dependent BDT cut, as these have similar effective areas, and demonstrates that the systematic uncertainty is slightly increased by approximately one percentage point. This suggests that the increased performance in gamma-hadron separation comes at the expense of a slight increase in susceptibility to data-simulation mismatches, as for example introduced by different NSB values.

5.6.3 Sensitivity

Using all the IRFs, we compute sensitivities for source detection in different energy bins. In each energy bin, the source flux ($\propto E^{-2.5}$) is scaled such that it leads to a 5σ detection for 50 h of observation time. Since the absolute values of this differential sensitivity depend on the size of the energy bins, they primarily serve as a means of comparison between different configurations.

Scanning through various preselection cuts for image size and pixel number showed that small events, with five or six pixels, generally decrease the sensitivity. These events exhibit low resolution during reconstruction and perform especially poorly in gamma-hadron separation. Including such events in the analysis significantly increases the background without a comparable enhancement in the signal. For this reason, the following analysis is based on slightly stricter preselection criteria, where events must contain seven or more pixels. While applying even more stringent cuts could further enhance performance at higher energies, this comes at the cost of diminished performance at lower energies, which is the primary focus of this study.

Figure 5.14 highlights the improvement in sensitivity, which roughly follows the improvement in q-factor already discussed in Fig. 5.11. The constant BDT cut is optimized for medium energies around 100 GeV, where due to the strict cut on low-size events, the sensitivity is slightly better compared to the new configurations. Improvements from

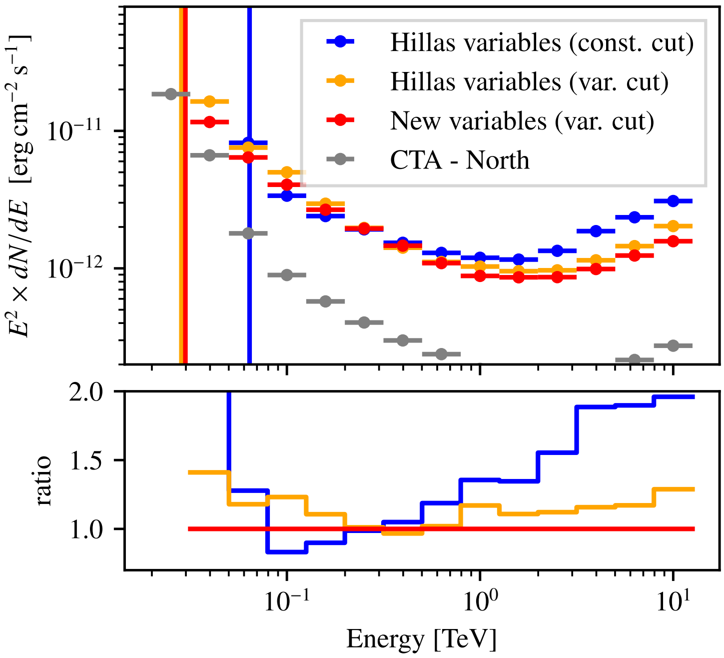

Figure 5.14: Comparison of the differential sensitivities (upper panel) and their ratios (lower panel). The vertical lines show the energy threshold at which the effective area drops below 10% of its maximum. The sensitivities are computed for 50 h of observation time and 5σ detection per energy bin. The points for CTA - North rely on prod5 v0.1 IRFs[44].

the variable cut are apparent at higher and lower energies. The new variables mainly increase the performance in the first few bins, where they mostly contribute to the increased background rejection and improved event reconstruction. At the threshold, an improvement of 41% could be achieved by adding the new variables.

5.6.4 Application to test dataset

In this section, we apply the new reconstruction to 65 observations ($\sim$30 h) of the Crab Nebula, taken under zenith angles between 44° and 55°. The dataset used is identical to that in Chapter 4 for the mono data, where the standard reconstruction technique was applied. For the current study, the background is estimated using reflected regions around the source position (Berge et al., 2007). A low-energy threshold of 100 GeV is chosen, which lies above the 10% effective area threshold and below the 10% energy bias threshold for this zenith range. At this energy threshold, the new analysis exhibits an energy bias of 41%, whereas the previous analysis demonstrated a bias of 128%. At the threshold energy of the previous analysis, 200 GeV, the new analysis shows a significantly reduced bias of 0.6%, compared to 27% for the old analysis.

Figure 5.15 provides a comparative overview of the spectra derived from the two analyses. The systematic uncertainty is estimated by grouping the observations into three different zenith and offset angle bins, respectively, and estimating the deviations beyond the statistical uncertainty. This kind of systematic can be regarded as lower limit of systematic uncertainties, particularly reliable at lower energies where statistical uncertainties are minimal. Overall, we find good agreement between the old and new analyses, with the latter extending to lower energies. As expected, systematic uncertainties increase at lower energies, primarily due to the inclusion of events near the instrument's trigger threshold.

[44] taken from: `https://www.ctao.org/for-scientists/performance/`

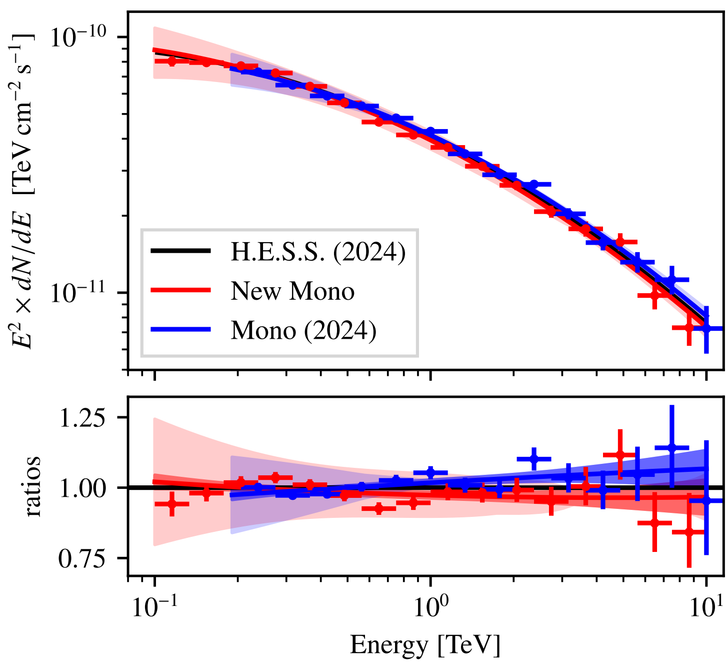

Figure 5.15: Spectral energy distribution of the Crab Nebula as measured by CT5. The blue data points correspond to the H.E.S.S. mono data from Aharonian et al. (2024), reflecting the performance of the standard reconstruction method. The black line represents the Crab spectrum obtained from the mono + stereo analysis (extrapolated to 100 GeV) also from Aharonian et al. (2024). The red data points indicate the results from the new reconstruction method. In the upper panel, the shaded error bands represent the combined statistical and systematic uncertainties. The lower panel illustrates the ratios relative to the black spectrum, with the darker shaded regions showing the statistical uncertainty in addition to the total uncertainty.

5.7 Conclusion

In this study, we introduced approximately 30 new image parameters and assessed their impact on the reconstruction and gamma-hadron separation of monoscopic IACT images. One of the primary challenges for monoscopic events is determining the correct image flip, that is, whether the arrival direction is to the left or right of the image's CoG. By employing a boosted decision tree for this task, we improved the accuracy of the flip determination by approximately eight percent points up to 1 TeV, with even larger improvements at higher energies. The fraction of wrongly flipped events could be reduced from 38% to 32% at threshold and from 29% to 17% at 100 GeV. The most important parameter for the BDT was the new kink-minor variable, which describes the change in image width along the major shower axis.

Unlike the traditional Hillas parameters, many of the new parameters lack symmetry with respect to the image center. Consequently, if the image is mirrored along the y-axis, the sign of certain variables may change, or variables associated with the head and tail regions may be swapped. Correctly determining the flip is therefore crucial not only for angular reconstruction but also for the accurate interpretation of these new variables. Throughout this study, we put great emphasis on removing any asymmetries between the distributions of γ-ray and background events by consistently mirroring half of the events. This approach ensures uniform performance regardless of the event's position within the camera frame, while fully leveraging the information provided by the image parameters. As a result, both the energy and angular resolutions showed considerable improvement. Additionally, the gamma-hadron separation saw a notable enhancement, with an average

20% increase in the q-factor for low to medium-size events.

When combined with the new size-dependent BDT cut, these reconstruction improvements allow for the inclusion of more low-energy events in the analysis, significantly lowering the energy threshold. For observations at a zenith angle of 20° and an offset of 0.5°, the 10% energy bias threshold was reduced from 120 GeV to 50 GeV, and the 10% effective area threshold from 64 GeV to 30 GeV. Although background rejection at low energies remains a challenge, the sensitivity curves presented in this work are promising. We also carefully evaluated the systematic uncertainties introduced by varying NSB rates and found only a minor increase in the systematic error on the effective area based on the new image parameters.

These three improvements to the analysis of monoscopic events were successfully applied to H.E.S.S. data, demonstrating their potential for integration into the analysis of other IACT arrays. Like the H.E.S.S. array, the upcoming Cherenkov Telescope Array Observatory (CTAO) will feature telescopes of various sizes, with only the largest telescopes detecting the faint light signals from low-energy γ rays. Consequently, the relevance of monoscopic event analysis will persist, even with the superior performance of stereoscopic events. In fact, mono- and stereoscopic events may be classified into distinct event types, allowing for a combined analysis of all events without sacrificing sensitivity.

Future studies could explore the analysis of IACT data split into different event-types and the potential of time-cleaning for the shower images observed with FlashCam. The latter might reduce the susceptibility of the time-related parameters to NSB fluctuations, enabling their inclusion in the background rejection algorithms, and further minimizing systematic uncertainties. Template-based reconstruction methods for monoscopic events offer additional potential for enhancing event reconstruction; however, their performance is highly dependent on the quality of the initial seeds. In this context, the improvements presented in this work are expected to provide substantial value.

God sent his Son into the world not to judge the world, but to save the world through him.

— Jesus, John 3:17

6 Asymmetries in the background of H.E.S.S. mono data

This chapter focuses on systematic uncertainties in the background estimation and their effects on the reconstructed source spectra. Generally, analyses of IACT data are affected by various sources of systematic uncertainties, primarily due to differences between simulations and real data. These include differences in the interaction models, atmospheric conditions, night sky background (NSB) rates, and broken pixels in the camera (Aharonian et al., 2006; Aharonian et al., 2022a). The relative importance of these factors varies between observations, but all result in inaccuracies in the instrument representation through the IRFs, thereby propagating into the final analysis. For instance, a 10% overestimation of the exposure leads directly to a 10% underestimation of the derived flux. Similarly, an unaccounted systematic energy reconstruction bias of 10% introduces a shift in the reconstructed spectrum, causing flux deviations of approximately 20% for an E^{-2} power-law spectrum. Misrepresentation of the IRFs in an energy-dependent manner can also distort spectral parameters, such as the spectral index or a cutoff or break in the energy spectrum. While the amplitude of these effects can be estimated for individual observations by dedicated simulations, it is more challenging to estimate the amount of systematic uncertainty in a set of observations. Some effects may average out, such as those stemming from varying atmospheric transparency, while others – like the impact of broken pixels – can combine non-linearly.

One widely used approach to estimate effective systematic uncertainties in datasets with multiple observations is the comparison between two independent reconstruction chains, a strategy commonly adopted by H.E.S.S. (Aharonian et al., 2006; Abramowski et al., 2013; Abdalla et al., 2017). However, this method has intrinsic limitations: shared sources of uncertainty (e.g., interaction models and atmospheric conditions) exist in both chains, which can lead to an underestimation. Conversely, overestimation of the systematic uncertainty in the main-analysis chain may occur if only the cross-check chain is affected, for example, due to stringent event selection criteria. Despite these challenges, most analyses estimate the systematic flux uncertainty around 20% (Aharonian et al., 2006; Abdalla et al., 2017; Aharonian et al., 2022a), consistent with a 10% uncertainty in the absolute energy scale of the instrument for a power-law spectrum with index -2.

While the uncertainties discussed so far affect the conversion from excess events to flux, systematic errors can also directly impact the number of excess events, N_{sig}, derived as:

$$N_{\mathrm{sig}} = N_{\mathrm{on}} - N_{\mathrm{bkg}} = N_{\mathrm{on}} - \frac{N_{\mathrm{off}}}{\alpha}, \tag{6.1}$$

where N_{on} denotes the number of events in the on-source region, and N_{bkg} represents the estimated background. In the reflected-region background method, N_{bkg} is inferred from counts in α off-regions (N_{off}), assuming azimuthal symmetry in the background distribution (cf. Sect. 1.6.2). Any deviation from this symmetry can result in a systematic bias in the background estimate, which affects N_{sig} and, consequently, the reconstructed flux. The relative uncertainty can be calculated from the relative difference δ between the true and estimated background rate and the signal-to-background ratio (SBR) ρ in the on-region:

$$\frac{\Delta N_{\mathrm{sig}}}{N_{\mathrm{sig}}} = \frac{\delta \cdot N_{\mathrm{bkg}}}{N_{\mathrm{sig}}} = \frac{\delta}{\rho}. \tag{6.2}$$

Typical SBRs for observations on the bright Crab Nebula, presented in Fig. 6.1, reveal that systematic background uncertainties have a far greater impact on monoscopic analyses than on stereoscopic ones. The development of the SBRs relative to the gray line, which represents the true SBR before event selection, shows that it is challenging to effectively suppress the background at low energies, which are only accessible by the mono analysis. For the Crab Nebula, a 10% uncertainty in background rates results in a 50% flux uncertainty at 0.1 TeV, whereas the corresponding uncertainty drops below 1% above 1 TeV. For less bright sources, e.g., 10% of the Crab flux, the reduced SBR increases the propagated systematic uncertainty by a factor of 10. Similarly, the systematics due to the background rates can easily dominate the ones propagated from other IRFs for extended sources with less surface brightness. As the signal must not be fully obscured by background systematics,

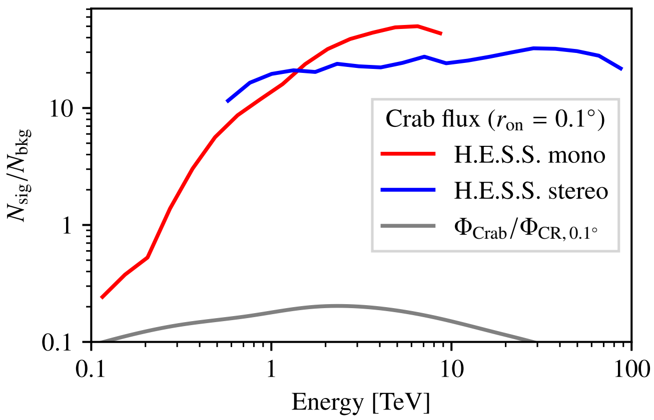

Figure 6.1: Signal-to-background ratios for typical H.E.S.S. observations on the Crab Nebula in an on-region with $r = 0.1°$. The gray line shows the true Crab flux in relation to the CR flux (Evoli, 2025), integrated in a 0.1° circle. Details on the observations and the assumed Crab spectrum are provided in Sects. 4.2.1 and 5.6.4.

a 10% uncertainty in the background estimation – such as observed in some energy bins using the 3D template method (Nakashima, 2023) – restricts analyses to regions where the SBR exceeds 10%. For point-like sources in stereo mode, this corresponds to flux levels of 0.3%–1% Crab flux, which is generally not restrictive beyond statistical limitations. However, toward the lower end of the mono analysis, sources need to have 10%–50% of the Crab flux. Similarly, if the source is extended, e.g. a disc with $r = 1°$, the background in that region is increased by a factor 100 compared to the 0.1° on-region for point-like sources. As a result, flux levels of 30%–100% Crab are required even for stereo analyses to maintain a viable signal, rendering mono analyses impractical for such cases unless background systematics can be reduced to a few percent.

In the following, systematic uncertainties in the reflected regions background estimation technique are investigated and improvements are presented, exemplary for the monoscopic reconstruction.

6.1 Plane background correction

The reflected regions background estimation method relies on the fundamental assumption that background rates in the camera depend solely on the radial offset from the camera center, and not on the azimuthal angle φ in the camera plane. This offset dependence is expected and originates from radial variations in camera acceptance and differences in image parameter distributions, which impact the performance of the gamma-hadron separation algorithms (Mohrmann et al., 2019). Consequently, systematic uncertainties in the reflected regions method stem from azimuthal asymmetries in the background rates at fixed offsets. These asymmetries may arise due to multiple factors, such as gradients in the field of view (FoV) induced by zenith angle dependence, deflections of charged shower particles in the geomagnetic field, or instrumental effects including broken pixels and imperfect flat-fielding[45]. Combined with a different performance of the background rejection algorithms, clear azimuthal asymmetries arise in the background rates, as can be seen in Fig. 12 of Mohrmann et al., 2019. The most prominent feature in these maps is a gradient aligned along the zenith direction.

A first-order correction to this asymmetry can be applied by determining a gradient in the off-region counts as illustrated in Fig. 6.2. The gradient is determined via linear

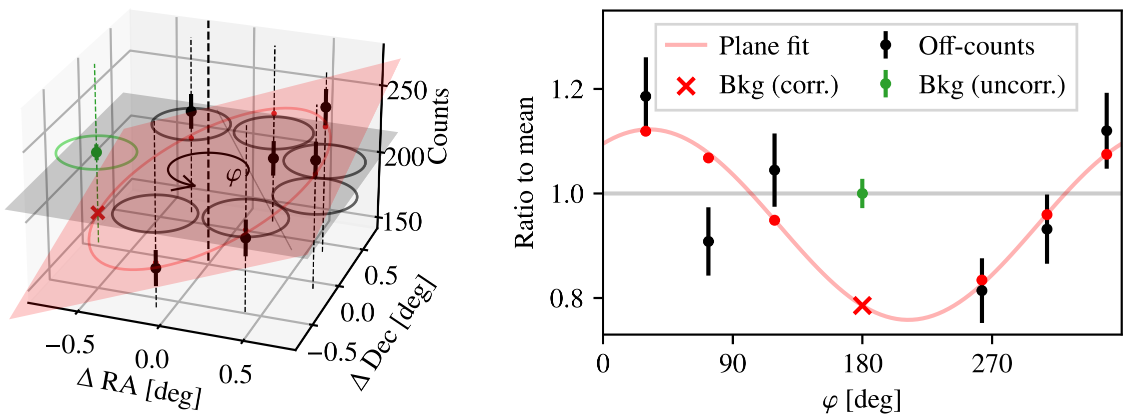

Figure 6.2: Example of the gradient correction for one observation on the Crab Nebula in the mono configuration. *Left:* The circles represent the on-region (green) and off-regions (black) on the gray plane at the average off-counts. The dashed lines indicate the centers of the regions, with error bars showing the off-counts per region with Poisson error. For the on-region, the green error bar represents the background estimated from counts in the off-regions, while the red 'x' marker denotes the corrected background value. *Right:* Projection along the azimuth angle in the camera plane φ. The individual counts are shown relative to the average counts in the off-regions.

regression in two dimensions, where $\Delta\text{RA} \equiv X = [x_1, x_2, ...x_n]^T$ and $\Delta\text{Dec} \equiv Y = [y_1, y_2, ...y_n]^T$ are vectors containing the center coordinates of the off-regions relative to the pointing position. The off-counts N_i from each region are contained in the vector $Z = [N_1, N_2, ...N_n]^T$, with the equation of the plane given by:

$$Z' = aX + bY + c, \tag{6.3}$$

where the gradients a, b along the RA, Dec direction and the constant offset c are summarized in the coefficient vector $C = [a, b, c]^T$. The normal equation for linear regression minimizes the squared deviation of predicted off-counts Z' and observed ones Z and reads

$$\left(A^T A\right) C = A^T Z, \tag{6.4}$$

with $A = [X, Y, 1]$ the feature matrix. This is solved for the coefficient vector, yielding the red plane in the left panel of Fig. 6.2.

[45]Correction factors are applied per pixel such that uniform camera illumination results in equal pixel amplitudes across the camera.

This procedure is applied independently for each energy bin, provided the average number of events per off-region exceeds three. The direction and magnitude of the gradient vary across energy bins, and statistical fluctuations in high-energy bins, with only a few background events, may lead to negative corrected background values. However, since high-energy bins generally feature larger SBRs, the impact of residual systematic uncertainties on the excess rates is reduced. The right panel of Fig. 6.2 illustrates an extreme example in the energy range 0.1–0.3 TeV, where the background correction reaches approximately 20%. Without this correction, the excess count estimation would yield a significantly negative value, even for a bright source like the Crab Nebula. The correction factor, given by the ratio between background after and before the correction, is also applied to the exposure of the energy bin, under the assumption that the same asymmetry affecting background rates also influences the signal rate. This is justified, as only gamma-like background events pass the event selection, and hence the asymmetry is expected to be similar in actual γ-ray events.

In a mirrored scenario, where the pointing position is symmetrically opposite to the source, the same background asymmetry would lead to an underestimation of the background and an overestimation of the signal if no correction were applied. This configuration facilitates partial cancellation of systematic uncertainties across symmetric runs, even in the absence of explicit correction. However, the degree of residual systematics depends not only on the symmetry of the pointing positions but also on the stability of the background asymmetry, which may vary between observations due to changing observational conditions (e.g., atmospheric transparency or zenith angle). Imperfect symmetry, particularly at the low-energy threshold, impedes full cancellation – precisely where low systematics are most critical.

The correction presented here is thus particularly beneficial in improving the accuracy of excess estimates on a run-by-run basis and for datasets with asymmetric pointing patterns, such as those from survey observations or transient follow-ups. In contrast, for targeted observations, H.E.S.S. typically employs symmetric pointing strategies to naturally mitigate such systematics. However, the limitation of this first-order correction method lies in the assumption that background asymmetries can be well approximated by a planar gradient, which is not always valid across all datasets.

6.2 Profile background correction

When background asymmetries cannot be adequately described by a linear gradient, corrections can still be applied by leveraging prior knowledge of the asymmetry's spatial structure. This approach is utilized in the 3D background template method (Mohrmann et al., 2019), where background events are stacked in camera coordinates across numerous observations to construct a high-statistics model. A similar strategy is adopted here, albeit with a key modification: the offset dependence of the background rates is not modeled, and the dataset used to derive the background profile is the same as the one to which the correction is applied. This prevents a mixture of different observational conditions and asymmetry patterns. While this approach does not offer the statistical precision of the full 3D background model, it avoids potential inconsistencies arising from heterogeneous datasets. Furthermore, limited statistics primarily affect high-energy bins, where the impact of background asymmetries on the excess rate is comparatively minor. Unlike the 3D model, this method is restricted to events at a fixed offset, as all on- and off-regions in the reflected region technique lie at the same radial distance from the camera center. Therefore, modeling the offset dependence is unnecessary.

Figure 6.3 shows the profile of background rates in camera sectors for datasets taken on the Crab Nebula and PKS 2155−304. All events passing the event selection cuts with reconstructed energies between 0.1–1 TeV are assigned to one of 16 sectors based on their reconstructed position in the camera. An offset cut is applied at 1.5°, as events with larger offsets to the camera center are not relevant for the reflected regions in this dataset, where the maximum pointing offset from the target is 1.0°. The region around the source is not excluded in this example, as background events vastly outnumber signal events in this energy range – even for the bright Crab Nebula – due to the large size of the sectors. Moreover, for the datasets examined, the distribution of source positions in the camera is approximately uniform, such that any minor contamination with signal counts averages out. In scenarios with higher SBRs or unevenly distributed source positions, one can exclude the events around the source and carefully correct for the reduced solid angle in the affected sectors. To normalize for observational variations, the number of events in each sector is divided by the mean event count per sector for that observation. This highlights relative differences across sectors, independent of absolute background rates.

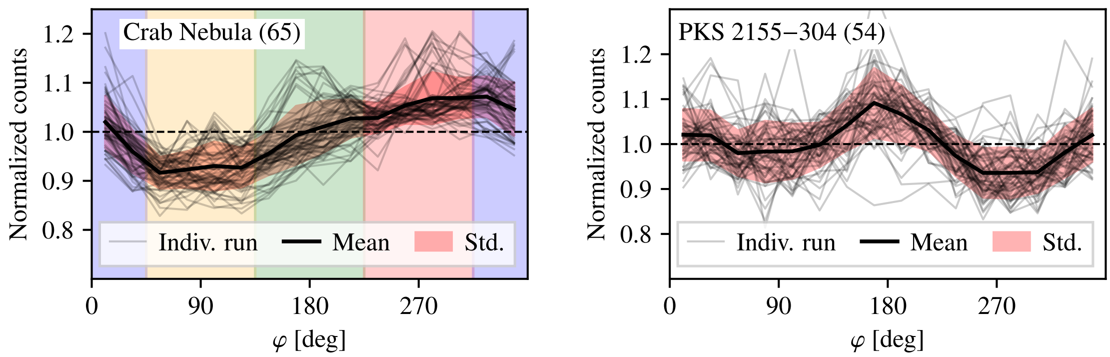

Figure 6.3: Azimuthal background rate profiles for 65 observations on the Crab Nebula (*Left*) and 54 observations on PKS 2155−304 (*Right*). The number of background events in each of the 16 sectors is divided by the average. The gray lines represent the profiles for individual observations, while the black line with the red shaded region indicates the mean and standard deviation for each sector. The azimuth angle φ corresponds to the angle in the camera plane, and the colored regions refer to Fig. 6.5: Left (blue), Top (towards zenith, orange), Right (green), Bottom (red).

The resulting profiles show clear differences between the two datasets. The Crab Nebula data exhibit a smooth gradient, consistent with zenith-aligned asymmetry and well captured by a linear model. In contrast, the PKS 2155−304 dataset shows a more complex structure: lower background rates in the upper and lower camera regions, with elevated rates in the lateral sectors – particularly on the right-hand side. Such a configuration cannot be effectively modeled using a linear gradient, as opposing variations cancel each other out in a planar fit.

A third example is shown in Fig. 6.4 for a dataset of 105 observations of Centaurus A. Here, the profile shows a dip around $\varphi = 270°$, corresponding to the high-zenith region in the camera – similar in location to the PKS 2155−304 dataset, but opposite in behavior to the Crab Nebula data. Aside from this dip, the background profile for Centaurus A appears relatively flat, differing significantly from both previous cases. One factor potentially contributing to these differences is the zenith angle distribution of the pointings, as summarized in Table 6.1. Other possible sources of variation include differences in magnetic field orientation relative to the pointing direction at the H.E.S.S. site, which may influence charged particle propagation in air showers. However, the role of magnetic fields in shaping these asymmetries requires further investigation. Additional contributing factors may include varying NSB levels across the FoV, seasonal atmospheric changes, and thermal gradients within the camera system. Further studies are required to quantify the contribution of these effects to the observed asymmetry patterns.

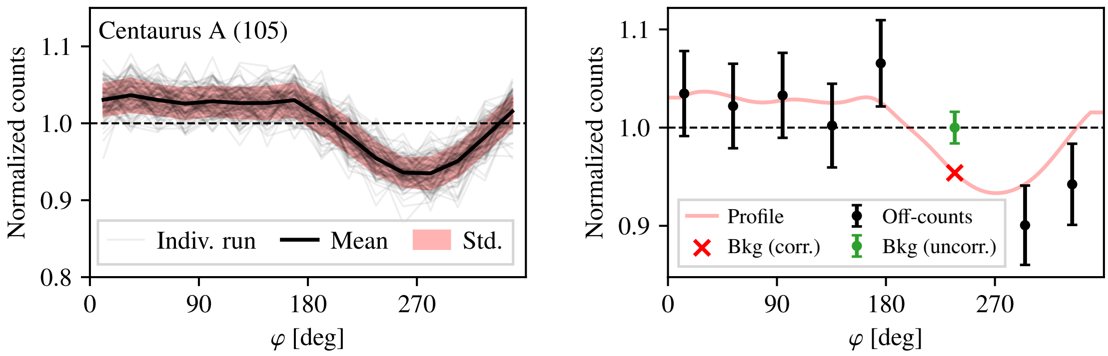

Figure 6.4: *Left:* Background rate profile for 105 observations on Centaurus A (cf. Fig. 6.3 for more details). *Right:* Illustration of the profile correction. The transparent red line represents the mean from the left panel, shown alongside the counts in individual off-regions divided by the average off-counts. The green error bar indicates the uncorrected background value (at 1 by definition), and the red 'x' marker shows the corrected value.

Table 6.1: Minimum, maximum, and average zenith angles (Φ) for the datasets from Figs. 6.3 and 6.4.

Source	Φ_{min} [°]	Φ_{max} [°]	Φ_{mean} [°]
Centaurus A	19.9	31.5	22.1
PKS 2155−304	24.3	44.6	31.4
Crab Nebula	45.3	55.2	46.9

The profile correction procedure is illustrated in the right panel of Fig. 6.4. In contrast to the plane correction, the profile can be more complex and is not constrained to a linear xy-dependence. While the plane correction can be determined in any coordinate frame – such as the sky frame where the on- and off-regions are defined – the asymmetry profile of this method is given in camera coordinates, requiring a transformation from sky coordinates into camera coordinates. The correction factor is interpolated from the profile at the on-region's location within the camera. Therefore, the equatorial coordinates of the on-region are transformed into the local altitude-azimuth frame at the midpoint of the observation at the H.E.S.S. site, which aligns with the camera frame. Similar to the plane background correction, the correction factor is applied to both the background estimate and the exposure, under the assumption that background and signal rates are affected similarly by the asymmetry. In this analysis, a single correction profile is used across all energy bins, as the limited number of observations does not yield statistically distinct profiles across energies.

6.3 Application to data

In the following, we apply and compare three background estimation methods – standard reflected regions, plane-correction, and profile-correction – using the Crab Nebula dataset. The observations and monoscopic reconstruction are the ones used in Sect. 5.6.4, with a reduced on-region of 0.13° (compared to 0.2°), resulting in higher SBRs. Since the source positions in the camera are nearly uniformly distributed along φ for this dataset, significant differences between the corrected and uncorrected background estimation methods are not expected. To better visualize the impact of the correction procedures for less uniform datasets, the dataset is divided into four subsets according to the quadrant of the camera in which the source is located. The results are presented in Fig. 6.5, showing the plane-correction on the left and the profile-correction on the right. The substantial differences of

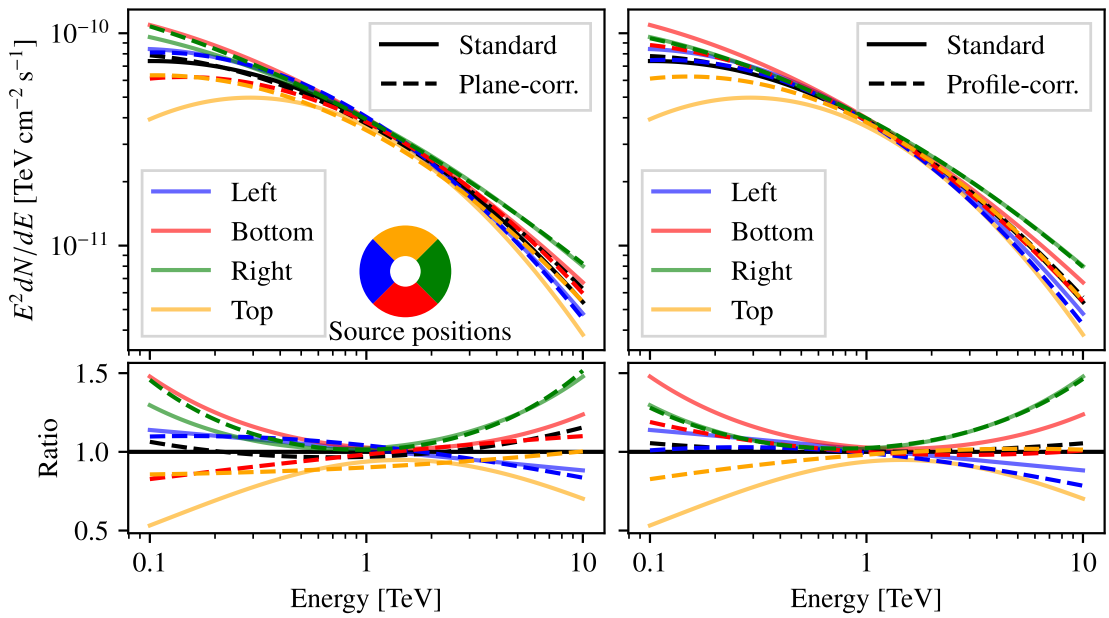

Figure 6.5: Crab spectra for runs divided based on the camera quadrant containing the source position. The solid lines show the standard spectrum without correction, while the spectra with the plane correction (*Left*) and profile correction (*Right*) are depicted as dashed lines. The lower panel shows the ratio to the combined spectrum without correction. All spectra are extracted from on-regions with $r = 0.13°$.

≈50% at low energies result from the background asymmetries with an amplitude of ≈ 10% (cf. Fig. 6.3) combined with the low SBR of ≈ 20% in this energy range (cf. Fig. 6.1, considering the slightly enlarged on-region with $r = 0.13°$ compared to $r = 0.1°$). The similarly pronounced differences at high energies are a consequence of the differences at low energies, the model constraints imposed by the log-parabola functional form, and the low statistics at high energies. The parameters of each model are strongly constrained by the low to medium energies, such that the trend of disagreement (at low energies) to agreement (at medium energies) naturally propagates as disagreement to the higher energies. However, in contrast to the deviations at low energies, the deviations at high energies are not statistically significant.

Comparing the two correction methods reveals that the plane-correction effectively mitigates the discrepancy between ‘Top’ and ‘Bottom’ source positions, a contrast to the profile-based approach, which only partially resolves this difference. However, the plane method introduces a larger deviation for the ‘Right’ sector, not observed under the profile correction. Due to the azimuthal symmetry of the pointing strategy in the dataset, these opposing effects largely cancel out in the total flux estimate, leading to only minor differences between the corrected and uncorrected full-dataset results.

One can conclude that both correction methods demonstrate effectiveness in reducing sector-to-sector variations in the estimated excess rates. The plane-correction is computed per observation and per energy bin, making it adaptable to variations in asymmetry between observations and energy bins. Moreover, it does not require a large dataset or additional archival observations, unlike the 3D background model. However, this method is sensitive to statistical fluctuations due to the limited number of events per off-region, particularly at high energies or for fine energy binning. In such bins, the statistical uncertainty often dominates, rendering precise correction less critical.

Besides the statistical fluctuations, the level of remaining systematic uncertainty depends on the extent to which the true asymmetry deviates from a linear gradient. This method performs well for the Crab dataset, but it is less effective for sources like PKS 2155−304 or Centaurus A (cf. Figs. 6.3 and 6.4), where asymmetries are non-linear.

In contrast, the profile correction is derived from aggregated data over multiple observations and energy bins. This improves statistical stability and allows the method to correct for more complex asymmetry shapes. However, systematic differences in background profiles between individual observations and energy bins are not fully captured. This limitation is analogous to the challenge faced in the 3D background template method, where the average profile may not represent the true asymmetry for all runs. This is illustrated by the red-shaded bands in Figs. 6.3 and 6.4, which indicate the standard deviation of sector-wise background rates. While this estimate still includes statistical fluctuations and ignores energy-dependent effects, it offers a rough estimate of remaining systematics per observation after the profile correction. To ensure robustness, one must verify that the number of events per sector is sufficient to suppress statistical fluctuations and check for possible energy-dependent variations in the profile. If significant, such variations can be accounted for through the construction and application of an energy-dependent profile.

Yet God, in his grace, freely makes us right in his sight. He did this through Christ Jesus when he freed us from the penalty for our sins.

— Paul, Romans 3:24

7 Fermi-LAT and H.E.S.S. analysis of Centaurus A

The unique nature of Centaurus A (NGC 5128) has been recognized as early as 1847 (Israel, 1998). At a distance of approximately 3.8 Mpc (Harris et al., 2010), it is the closest known radio-loud AGN to the Solar System, and its location is consistent with the positive excess in the UHECR anisotropy (cf. Chapter 1), considering deflection from magnetic fields (Oliveira and Souza, 2022). This proximity and location, combined with its energetic properties, make Centaurus A a prominent candidate for the origin of UHECRs (Cavallo, 1978; Biermann and De Souza, 2012; Oliveira et al., 2025).

Centaurus A is detected across the full electromagnetic spectrum – from radio to TeV energies (see Fig. 7.1) – with notable contributions from its jets, which are believed to be powered by a central supermassive black hole of mass $\sim 5\times10^7 M_\odot$ (Neumayer, 2010). Radio observations provide the best angular resolution, revealing a complex structure that

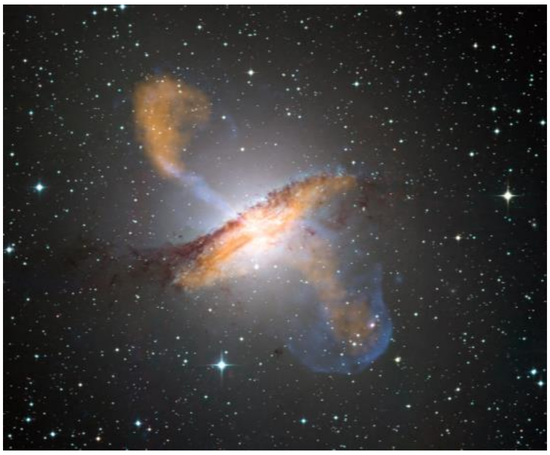

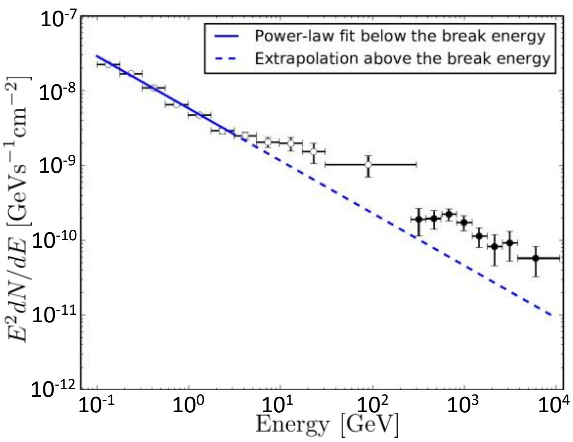

Figure 7.1: *Left:* Color composite image of Centaurus A, revealing the inner lobes and jets emanating from the active galaxy's central black hole (cutout from: `https://www.eso.org/public/images/eso0903a/`). The spatial extent is roughly 0.3° in angular size or 20 kpc in real space. The 870-micron data, from LABOCA on APEX, are shown in orange. X-ray data from the Chandra X-ray Observatory are shown in blue. Visible light data from the Wide Field Imager on the MPG/ESO 2.2 m telescope show the stars and the galaxy's characteristic dust lane close to "true color". (Credit: ESO/WFI (Optical); MPIfR/ESO/APEX/A.Weiss et al. (Submillimeter); NASA/CXC/CfA/R.Kraft et al. (X-ray))
Right: SED of the core, possibly including emission from the inner jets, as measured with Fermi-LAT (open circles) and H.E.S.S. (filled circles) from 100 MeV to 10 TeV (H.E.S.S. Collaboration et al., 2018).

extends from parsec-scale nuclear jets to giant outer lobes reaching ~250 kpc. Starting from the core, the nuclear jets extending out to 1 pc are followed by central jets (1.35 kpc), the inner lobes (5 kpc), the northern middle lobe (30 kpc) to which no southern counter part exists, and finally low surface-brightness giant outer lobes extending up to 250 kpc

(Israel, 1998). X-ray observations reveal compact, bright "knots" within the lobes, with spectra that steepen away from the jet axis (Worrall et al., 2008). This might be the result of transverse motion relative to the jet flow, which causes the emission regions to migrate outwards, while the emitting particles lose energy.

At γ-ray energies, resolving extended structures becomes challenging due to limited angular resolution and increased background contamination. Nonetheless, studies of the point-like core emission using Fermi-LAT and H.E.S.S. have uncovered unexpected spectral features (H.E.S.S. Collaboration et al., 2018). Notably, the Fermi-LAT spectrum exhibits a hardening above $\sim$3 GeV, with H.E.S.S. flux points lying above the extrapolated Fermi-LAT power law. However, the transition between the two datasets remains poorly constrained.

The broadband emission from the large-scale jets is typically attributed to synchrotron and inverse Compton processes involving relativistic electrons and positrons. This interpretation is supported by morphological similarities between the radio and the X-ray band and is now also substantiated by spectral similarities in the X-ray and VHE γ-ray flux (Abdalla et al., 2020a). Prior to the 2009 H.E.S.S. detection (Aharonian et al., 2009b), the core's SED was modeled using a simple, one-zone homogeneous SSC scenario. However, improved high-energy measurements reveal deviations that such a model cannot accommodate. A second emission component has been proposed that could originate from several regions and mechanisms discussed in H.E.S.S. Collaboration et al. (2018) and references therein. Abdalla et al. (2020a) favor the scenario of a harder component from the inner jets mixing into the core spectrum, where the two cannot be resolved spatially with the current VHE instruments. In this scenario, the emission is fully leptonic without the necessity of highly relativistic hadronic particles adding to the γ-ray emission (Tanada et al., 2019). Nevertheless, alternative models with an additional hadronic component have also successfully explained the high-energy excess (Fraija, 2014). The required proton luminosities between $2.0 \times 10^{43}\,\mathrm{erg\,s^{-1}}$ and $2.2 \times 10^{44}\,\mathrm{erg\,s^{-1}}$ (Fraija, 2014) are not sufficient to account for the flux of UHECRs at earth (Petropoulou, M. et al., 2014). An additional acceleration, e.g. in the lobes, would be required to make this proton distribution a significant contributor.

This work aims to close the observational gap between the Fermi-LAT and H.E.S.S. energy ranges and to better constrain the γ-ray emission above the spectral break at $\sim$3 GeV. To this end, the Fermi-LAT analysis is extended to 1 TeV using an enlarged dataset, with the results discussed in Section 7.1, alongside a systematic study of background and lobe templates on the core emission. Section 7.2 presents an attempt to reduce the energy threshold of H.E.S.S. observations using data from the large CT5 telescope, incorporating reconstruction and analysis improvements from Chapters 5 and 6. Finally, Section 7.3 describes the joint analysis combining Fermi-LAT and H.E.S.S. data at the event level to test various spectral model hypotheses, before concluding in Section 7.4.

7.1 Fermipy analysis

The following analysis includes almost 15 years of Fermi-LAT data taken between August 2008 and July 2023. The region of interest (RoI) spans $16° \times 16°$ with a pixel size of $0.05°$ and covers the energy range from 100 MeV to 1 TeV with 8 bins per decade. To avoid contamination from the bright γ-ray limb of the Earth, only events with zenith angles[46] smaller than $90°$ are included. Additionally, all events need to pass the `P8R3 Source V3` selection cuts (Atwood et al., 2013). The analysis itself is carried out using Fermipy[47] (version 1.2.0) and the Fermitools[48] (version 2.2.0) (Wood et al., 2017).

[46] The angle relative to the satellite–Earth axis; $180°$ corresponds to events originating from the Earth's center.

[47] `https://fermipy.readthedocs.io/`

[48] `https://fermi.gsfc.nasa.gov/ssc/data/analysis/software/`

Energy dispersion corrections are applied to all sources except the isotropic diffuse template, which is already provided in reconstructed energy.

7.1.1 The core model

The analysis employs the two standard background templates: one for the isotropic diffuse emission and one for the Galactic diffuse emission[49]. Additional resolved sources within a $24° \times 24°$ region are taken from the fourth Fermi-LAT source catalog (4FGL; Abdollahi et al., 2020), with their catalog parameters serving as initial conditions for model optimization. The first optimization step (`gta.optimize()`) performs a joint fit of the two background templates together with the core and lobe models of Centaurus A, followed by individual optimizations for sources with significance $>5\sigma$. Based on this optimization, all sources with significances below 2σ (TS<4) are removed. To reduce the number of free parameters in the following fit, all parameters of sources with TS<50 are frozen, and sources in the TS range 50–500 have a free normalization only. The resulting residual map is reasonably flat, and the optimized RoI model serves as the input for the GAMMAPY analysis.

The resulting SED for the core emission is shown in Fig. 7.2 and compared to the flux points from H.E.S.S. Collaboration et al. (2018). A single power law (cf. Eq. 4.2) fit to the

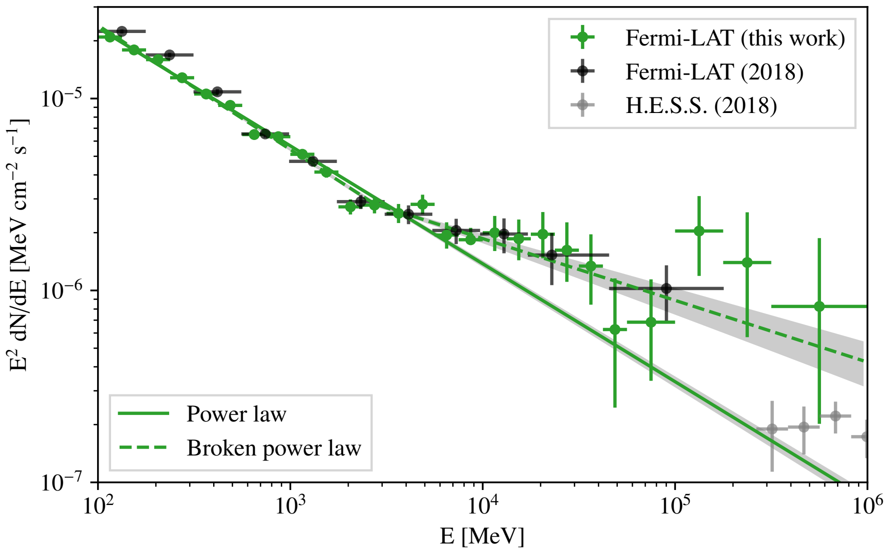

Figure 7.2: SED of the core model from this analysis (green) and from H.E.S.S. Collaboration et al. (2018) (black and gray). The solid line represents the best-fitting power-law model, and the dashed line represents the broken power-law model, each with 1σ statistical error bands. The errors on the flux points also indicate the 1σ statistical uncertainties.

entire energy range yields $N_0 = (8.1 \pm 0.7) \times 10^{-14}\,\mathrm{TeV^{-1}s^{-1}cm^{-2}}$ (with $E_0 = 1\,\mathrm{TeV}$) and a spectral index $\Gamma = 2.61 \pm 0.01$ with reasonable agreement to the catalog value of 2.57 ± 0.02. However, it is also evident from this analysis that the flux points above $\sim$10 GeV are not well described by the simple power-law model. To better describe this behavior, a broken power-law model is employed:

$$\frac{dN}{dE} = N_0 \times \begin{cases} \left(\dfrac{E}{E_{\mathrm{break}}}\right)^{-\Gamma_1}, & \text{if } E < E_{\mathrm{break}} \\ \left(\dfrac{E}{E_{\mathrm{break}}}\right)^{-\Gamma_2}, & \text{if } E \geq E_{\mathrm{break}} \end{cases} \tag{7.1}$$

[49]The files are `gll_iem_v07.fits` and `iso_P8R3_SOURCE_V3_v1.txt` from `https://fermi.gsfc.nasa.gov/ssc/data/access/lat/BackgroundModels.html`

This model is favored over the simple power law with a significance of 5.3σ ($\chi^2 = 31.4$ with 2 D.o.F.), thus crossing the 5σ threshold for a scientific discovery and improving upon the 4σ result in H.E.S.S. Collaboration et al. (2018). The best-fit parameters, presented in Table 7.1, are in good agreement with the previous study. The only notable difference is in the spectral index below the break energy, which is slightly harder in this new analysis.

Table 7.1: Comparison of broken power law parameters (cf. Eq. 7.1) from this analysis and H.E.S.S. Collaboration et al. (2018).

Parameter	This analysis	H.E.S.S. Collaboration et al. (2018)
N_0 [$10^{-13}\,\mathrm{MeV^{-1}s^{-1}cm^{-2}}$]	3.77±0.18	3.64±0.15
index 1	2.65±0.01	2.70±0.02
index 2	2.32±0.05	2.31±0.07
E_{break} [GeV]	$2.7^{+0.8}_{-0.6}$	$2.8^{+1.0}_{-0.6}$

Extending the energy range up to 1 TeV with significant ($>2\sigma$) flux points is possible due to the larger dataset and the merging of energy bins. However, the three flux points above 100 GeV rely on 5, 2, and 1 events only, in a region with $r = 0.3°$ around the core of Centaurus A.

7.1.2 The lobe models

The extended emission from the lobes cannot be described by a simple parametric model, such as a disk or Gaussian, necessitating the use of a spatial template. There are several approaches to constructing such a template. One method involves deriving a template from theoretical models, wherein certain parameters can be fitted to the data. However, as discussed previously, the morphology of the lobes is highly complex, exhibiting an asymmetric shape and multiple hotspots. This complexity requires an equally sophisticated model that accounts not only for jet properties but also for variations in particle distributions and environmental conditions. Moreover, this approach demands detailed knowledge of the underlying physical processes or necessitates assumptions that can significantly affect the final outcome. It appears unrealistic to constrain such a model using Fermi-LAT data alone, and incorporating data from other telescopes would demand an even more complex model, which lies beyond the scope of this work.

An alternative, previously attempted method for constructing a template involves using the residual flux that remains when the lobes' emission is not accounted for (Magill, 2018). The primary advantage of this method, compared to the theoretical approach, is that it avoids assumptions or simplifications concerning the physical processes about which conclusions are eventually to be drawn. On the other hand, it requires assumptions regarding the background – specifically, the Galactic foreground emission and other sources within the FoV. This is not straightforward, first due to the proximity to the Galactic plane (Galactic latitude $\sim 19°$), which is a bright source of diffuse γ-ray emission, and second because the region overlaps with the extent of the eROSITA bubbles[50] and the large radio lobe Loop I[51]. Figure 7.3 shows the location of the RoI in Galactic coordinates overlaid on the X-ray emission measured by eROSITA (Zheng, Xueying et al., 2024), along with a zoom into the analysis region[52]. While emission from large-scale structures is generally expected to be homogeneous on the scale of a few degrees and would thus be accounted for by the isotropic background template, one cannot rule out that residual inhomogeneities affect

[50] Regions of bright diffuse X-ray emission, the counterparts to the Fermi bubbles

[51] A supershell near the Galactic center, presumably formed by supernovae and stellar winds

[52] Data taken from `https://erosita.mpe.mpg.de/dr1/AllSkySurveyData_dr1/HalfSkyMaps_dr1/`

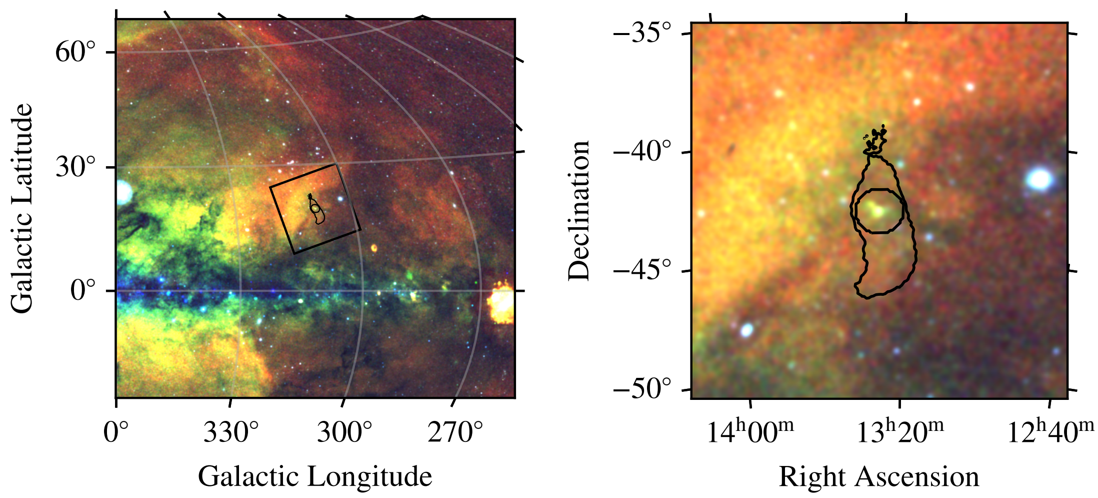

Figure 7.3: eROSITA half-sky-maps around the position of Centaurus A, with the energy bands 0.2–0.6 keV encoded in red, 0.6–1.0 keV in green, and 1.0–2.3 keV in blue. The contours illustrate the *WMAP* lobe template from Fig. 7.5a. *Left:* Large-scale view in Galactic coordinates, with the analysis region indicated as black rectangle. *Right:* The 16° × 16° RoI in equatorial coordinates.

the shape of the residuals. Attributing the residuals either to extragalactic origin from Centaurus A or to Galactic emitters like the Galactic plane or the bubbles is challenging but of fundamental importance. Mis-modeling the Galactic emission could have substantial consequences for the derived template.

Patches in the Galactic diffuse template A combination of the two methods mentioned above is employed to construct the template of the Galactic diffuse background emission. The primary component is derived based on templates of the observed gas distribution and diffuse CRs, which produce γ rays in hadronic interactions. The CR density is fitted to the observed residuals in Fermi-LAT data, accounting for known point sources (for details see Ackermann et al., 2012c)[53]. In regions with remaining diffuse γ-ray excess, so-called “patches” are added to the template, accounting for the residuals after subtracting the adjusted CR model (Acero et al., 2016; The Fermi-LAT collaboration, 2019). These patches lack direct physical motivation and are purely empirical. However, this does not imply that the residual flux is of extragalactic origin, since other mechanisms for γ-ray production – such as leptonic processes – may play a role and are less dependent on gas density. For this reason, it is generally assumed that most of the emission in the patches is of Galactic origin.

Figure 7.4 shows the patch component around Centaurus A in the second row, peaking at the position of the Centaurus A lobes and contributing ∼50% of the total flux in the template (third row) within the energy range 0.1–100 GeV. At higher energies (0.1–1.0 TeV), the patch component is clearly correlated with the lobe template and accounts for the majority of the flux in that region. Given that the patch component is derived from residuals after modeling the emission around Centaurus A using this particular lobe template, it is likely that the patches in this region are not (only) capturing Galactic foreground emission but are instead compensating for the shortcomings of the lobe template. Disentangling the multiple sources and background components in the vicinity of Centaurus A and constructing a reliable background template is challenging due to the poor angular resolution below 1 GeV

[53]Additional modifications for version `gll_iem_v07.fits` are described in: `https://fermi.gsfc.nasa.gov/ssc/data/analysis/software/aux/4fgl/Galactic_Diffuse_Emission_Model_for_the_4FGL_Catalog_Analysis.pdf`

(with a >1.8° 90% containment radius) and the reduced statistics at higher energies.

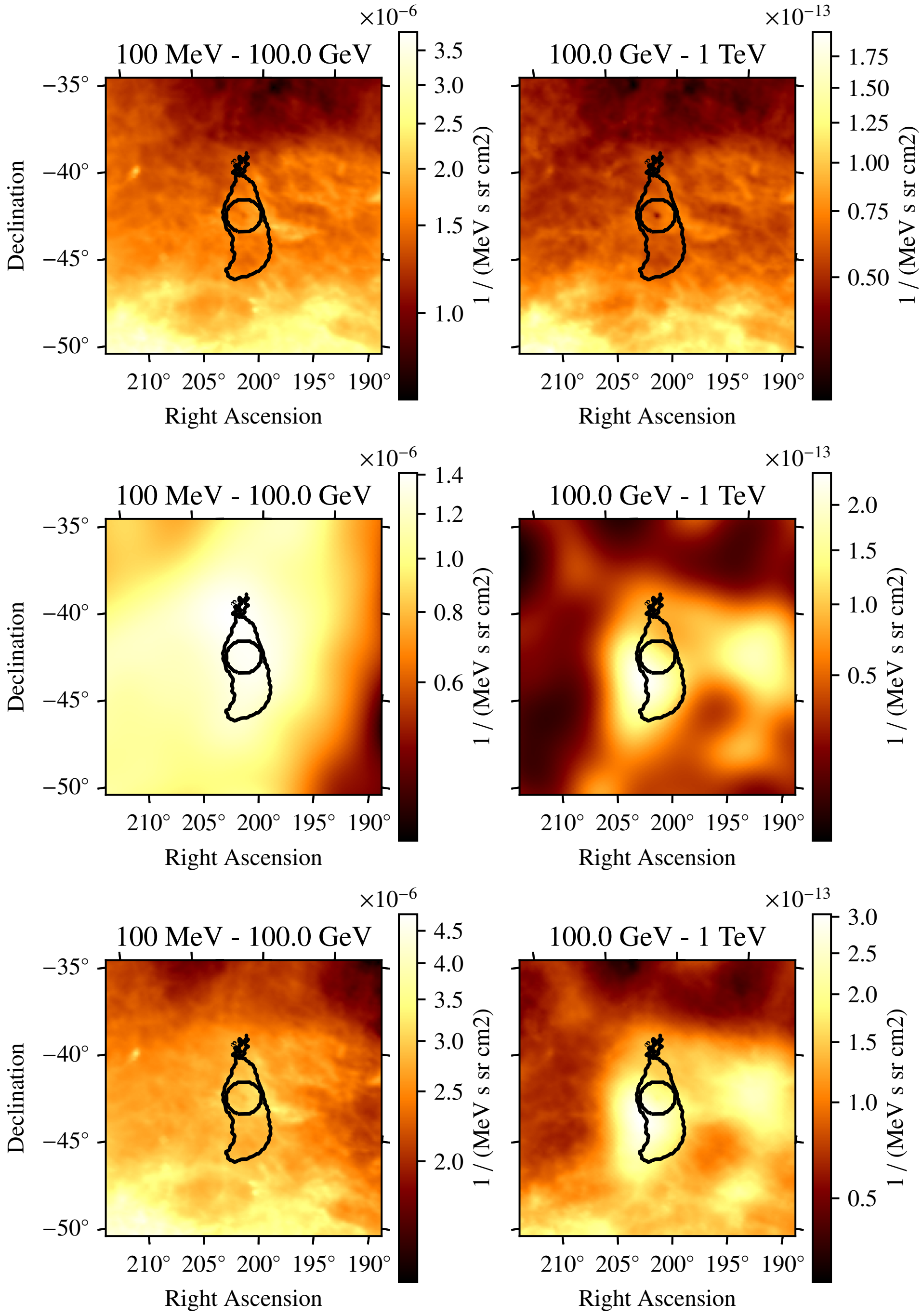

Figure 7.4: Galactic diffuse emission template in the RoI overlaid with the lobe contours. The left column shows the flux in the energy range 0.1–100 GeV, while the right column shows the flux between 0.1–1.0 TeV. The first row displays only the "physical" component without the "patches". The second row shows the "patch" component separately. The third row presents the sum, which is the official `gll_iem_v07.fit` template.

This introduces systematic uncertainties when it comes to the lobe template. When constructing a template from residuals, an additional step of deconvolution is required to infer the true morphology of the lobes and compare it to data from instruments with superior angular resolution. While residuals are a useful tool for evaluating and fitting templates, they are too ambiguous to serve as the sole basis for template construction, as different assumptions – regarding patches, point sources, and deconvolution – can lead to significantly different morphologies.

Construction from radio data The third approach, that is used for the catalog template, assumes that the same particles emitting synchrotron radiation in the radio band are also responsible for the γ-ray flux. This method utilizes MWL data and the connections between different emission mechanisms associated with a single particle population. One major advantage of this approach is the high angular resolution of radio telescopes, which allows for a detailed mapping of the particle distribution — under the assumption that these particles also drive the γ-ray emission. However, a key caveat is that the energy radiated via synchrotron emission is proportional to the square of the magnetic field strength, B^2 (Eq. 8.2 in Longair, 2011), whereas the energy emitted via proton-proton interactions or IC scattering depends on the density of seed particles, rather than the B-field. Consequently, the brightness distribution in the radio band may significantly differ from that in γ rays, particularly if the magnetic field exhibits strong spatial variation.

The Fermi-LAT source catalogs use a publicly available template based on *WAMP*[54] data in the K-band (22 GHz), which is intended to characterize Galactic emission in contrast to the CMB. Pixels within 1° around the core are dominated by the core emission and are set to zero, along with all pixels identified as background[55]. The resulting template is displayed in Fig. 7.5a, where a conspicuous central void is clearly visible. With increased exposure and improved event reconstruction, the limitations of the *WMAP* template become evident (Magill, 2018).

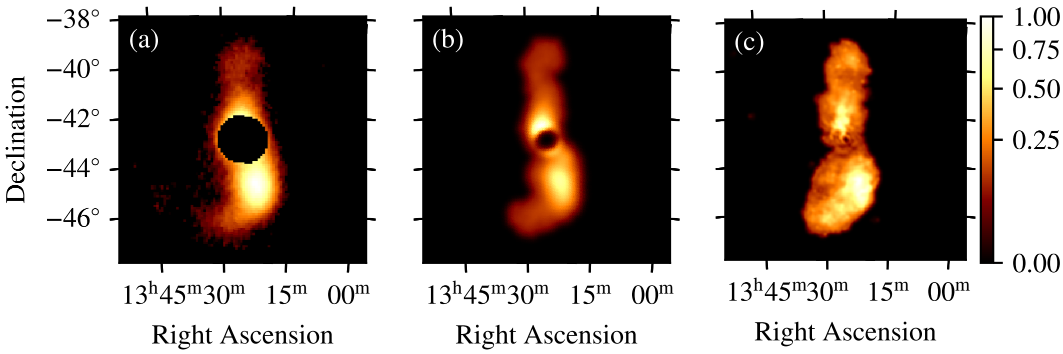

Figure 7.5: Templates for lobe emission derived from different datasets: (a) *WMAP* data, (b) *PLANCK* data, and (c) MWA data. Template (a) is the default, taken from the catalog, while (b) and (c) are alternative templates generated in this work. All templates are scaled to 1 and displayed using a square root scaling of the color map. For more details, refer to the main text.

The *PLANCK*[56] satellite offers better angular resolution and covers slightly different frequency bands (30, 44, 70, and 100 GHz). An association and modeling of the Fermi-LAT and *PLANCK* data was previously conducted by Sun, Xiao-na et al. (2016), indicating that an improved lobe emission template using *PLANCK* data is a promising avenue. As with the *WMAP* template, the starting point is a CMB-subtracted image of the astrophysical foreground, obtained from the archive[57]. For this purpose, the 30 GHz frequency band is selected, as it reveals the most extended lobe emission. The production of the lobe template is analogous to the procedure for the *WMAP* template, where the

[54] `https://wmap.gsfc.nasa.gov/`

[55] `https://fermi.gsfc.nasa.gov/ssc/data/analysis/scitools/extended/extended.html`

[56] `http://www.esa.int/Planck`

[57] `https://irsa.ipac.caltech.edu/data/Planck/release_3/all-sky-maps/matrix_foreground.html`

background and emission from the bright central point-source are removed. A $10^\circ \times 10^\circ$ region centered on Centaurus A (in equatorial coordinates) is smoothed with a Gaussian kernel corresponding to the approximate angular resolution of 0.11°. The smoothed background distribution is estimated from adjacent regions outside the lobes and exhibits a cutoff at an intensity of approximately $2.5 \times 10^{-4}\,\mathrm{K_{CMB}}$, corresponding to roughly 1.5% of its maximum. Contamination from the bright central source was found to extend out to 0.5°, allowing for a central exclusion zone that is half the size of that used in the *WMAP* template. All raw image pixels within 0.5° of the center or with a smoothed intensity below $2.5 \times 10^{-4}\,\mathrm{K_{CMB}}$ are set to zero. The final template is produced by re-smoothing the cleaned raw image using the same 0.11° kernel (cf. Fig. 7.5b).

An alternative template can be constructed from data taken by the Murchison-Widefield-Array (MWA)[58] during the GLEAM survey (Wayth et al., 2015; Hurley-Walker et al., 2017) at 118 MHz. After performing background subtraction – based on a smoothed intensity distribution with a 0.08° kernel and a threshold of 0.3 Jy/beam – numerous point-like sources remain, both inside and outside the lobes. These are identified by comparing the raw and smoothed images, where differences are especially prominent at locations containing point sources. Regions with $r = 0.08^\circ$ around each identified source are inpainted using surrounding pixel values that are free of source contamination. This also effectively removes most of the bright central source's intensity. However, fitting the resulting template revealed that cutting a hole with $r = 0.1^\circ$ is strongly preferred compared to the infilling of the central pixels[59]. The final step involves smoothing the raw, cleaned, filled, and masked image with a 0.05° kernel – slightly larger than the native angular resolution – to adequately smooth out the filled pixels. This process yields a template with a barely visible central hole (cf. Fig. 7.5c) and other spatial structures that lie well below the angular resolution of Fermi-LAT.

Evaluation of the different templates To assess the agreement of each template with the data, the previously mentioned "patches" of the Galactic diffuse emission template are removed due to the concerns about their validity in the region around Centaurus A. Since these patches are derived from residuals after subtracting the *WMAP* template, a systematic bias in favor of this template is expected when including the patches in the comparison. The modified Galactic emission template without the patches is shown in the top row of Fig. 7.4 and used for the following analyses. The *Cash* statistics value (cf. Eq. 1.17) is computed within the GAMMAPY framework, where the following parameters are jointly optimized:

- $N_0, E_{\mathrm{break}}, \Gamma_1, \Gamma_2$ of the core model's broken power law,
- N_0, α, β of the lobe model's log-parabola,
- the normalization of the isotropic background model,
- the normalization and spectral tilt of the Galactic diffuse background,
- and one normalization of the 4FGL sources, which are combined into a single template.

Relative to the *WMAP* template, the *PLANCK* template yields an improvement of $TS = 54.3$, while the MWA template is preferred by $TS = 72.2$ (reduced to 43.1 if the central hole is infilled instead of excluded).

Given the dependency of the synchrotron-based radio template on the magnetic field strength, it is possible to investigate spatial variations in the B-field. Since the synchrotron

[58]`https://www.mwatelescope.org/`. Data around Centaurus A was provided by Miroslav Filipovic.
[59]The value of 0.1° is not optimized but oriented on the angular resolution of MWA.

intensity I_{sync} scales with B^2, whereas the IC emission does not (ignoring synchrotron seed photon contributions), a declining B-field toward the lobe outskirts would result in radio templates underestimating the corresponding γ-ray flux there. To investigate this, each pixel of the MWA template is scaled based on its radius r from the Centaurus A core position following a r^α profile. In addition to the original template with $\alpha = 0$, three more values of the exponent $\alpha \in [0.3, 0.6, 0.9]$ are tested to probe the likelihood profile.

Figure 7.6 shows the resulting profile likelihood scan, where the parabola fitted to the values identifies the minimum at $\alpha = 0.38 \pm 0.07$, with the error based on the curvature of the parabola. Due to the complexity of the fit and the good description by the parabola,

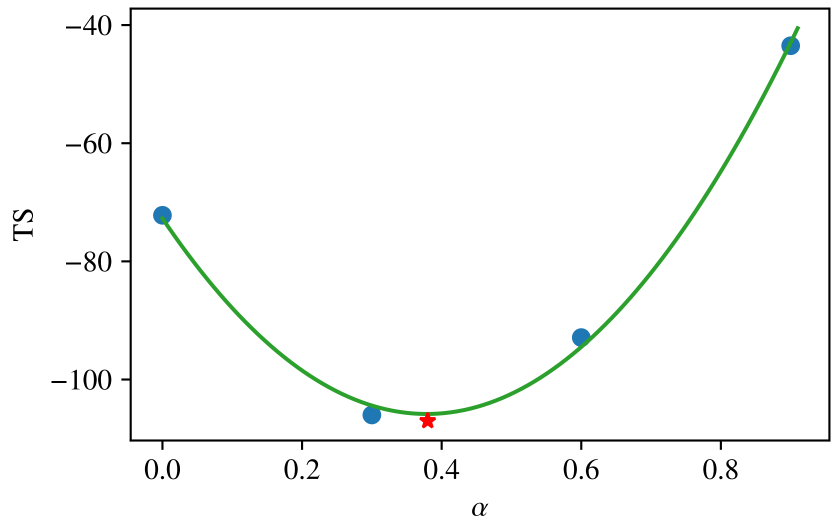

Figure 7.6: Profile likelihood scan of the α-value for the radially re-weighted templates ($\propto r^\alpha$). The TS is computed with respect to the *Cash* value of the *WMAP* template, i.e., $TS = \mathcal{C}_{\mathrm{WMAP}} - \mathcal{C}_{\mathrm{MWA},\alpha}$. The green line represents the parabola fitted to the blue points, while the red star shows the value at the minimum of the parabola.

only one more template is generated with the optimal $\alpha = 0.38$ and fitted to the data. This radially re-weighting MWA template is preferred over the original *WMAP* template by $TS = 107$, and by $TS = 34.8$ over the unweighted MWA template. This result indicates that the B-field responsible for the radio emission is indeed decreasing with further distance from the galaxy. As $I_{\mathrm{sync}} \propto B^2 \propto r^{-(0.38\pm0.07)}$, the B-field itself decreases with $B \propto r^{-0.19}$. This slope is considerably smaller compared to the $B \propto r^{-0.47}$ dependence found for the Crab Nebula system (cf. Sect. 4.4.3), where not only the scale but also the physical processes involved are different. However, as detailed in the next paragraph, the flux associated with the lobes is subject to an increased level of systematic uncertainty due to the uncertainties in the description of the background morphology. Therefore, further interpretation of this result is not attempted here.

Effects on the core spectrum In the following, the attention will return to the core spectrum, where the different options of lobe and background templates are treated as systematic uncertainties. The analysis is carried out in Gammapy, following the procedure outlined in Sect. 4.3.1, yielding results consistent with the Fermipy analysis. The main difference is the exclusion of the first two energy bins from the Gammapy analysis[60], a small disadvantage compared to the flexible Gammapy model interface.

[60]The effective area of Fermi-LAT is rapidly changing for $E \lesssim 0.2\,\mathrm{GeV}$, leading to larger systematic uncertainties (see also Abdo et al., 2010)

To estimate the influence of the different templates on the core and lobe flux, three analyses are compared in Fig. 7.7. The baseline configuration (solid lines) uses the standard *WMAP* lobe template and includes the patch component in the diffuse model. It therefore follows the analyses carried out for the Fermi-LAT catalogs and publications on Centaurus A (H.E.S.S. Collaboration et al., 2018; Abdollahi et al., 2020), with a broken power-law spectral model for the core component and a log-parabola spectral model for the lobes. For this and the following analyses, the free parameters are identical to the ones mentioned in the previous paragraph (one combined normalization for all 4FGL sources in the model RoI; the normalization and spectral tilt for the Galactic diffuse model; the normalization of the isotropic background; and the spectral parameters for the lobe and core models).

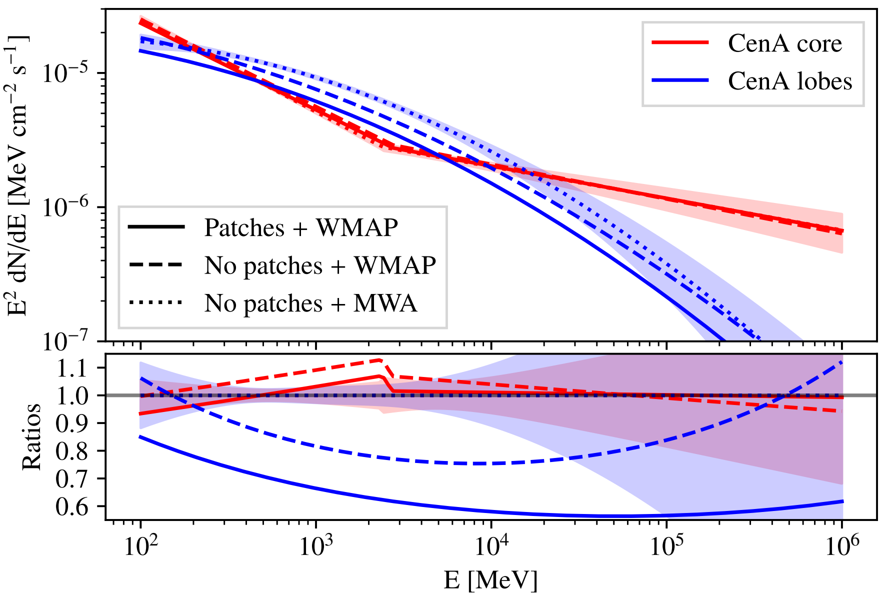

Figure 7.7: SEDs of the core and lobe models for different spatial templates of the Galactic diffuse emission (with and without the patches) and for the lobe emission (the *WMAP* template and the weighted MWA template).

Removing the patch component but keeping the *WMAP* template (dashed lines) leads to a $\sim$23% increase in the lobe flux, particularly at higher energies. The core flux increases by less than 10%, likely due to its compact morphology and large surface luminosity compared to the diffuse emission.

In a final step, the lobe template is replaced with the radially re-weighted MWA version (dotted lines). The impact is a $\sim$20% increase in lobe flux near 10 GeV, with negligible change at lower and higher energies. Correspondingly, the core flux decreases by approximately 10% around its spectral break energy.

In summary, while variations in the lobe template significantly affect the inferred extended flux – up to 50% – the core spectrum remains relatively stable, with changes limited to 10% and mostly within statistical uncertainties. In the following combination with H.E.S.S. data, the Fermi-LAT dataset will employ the re-weighted MWA template alongside the patchless Galactic diffuse template.

7.2 H.E.S.S. analysis

Centaurus A was extensively observed by H.E.S.S. between April 2004 and July 2010 in the H.E.S.S. I configuration, prior to the construction of CT5. The resulting dataset, comprising 189 h of observation time, has been utilized in previous publications such as H.E.S.S. Collaboration et al. (2018) and Abdalla et al. (2020a). Between March and July

2020, an additional 48.7 h of data were collected, now incorporating the large CT5 telescope. With the aim of lowering the energy threshold and bridging the gap to the Fermi-LAT energy range, this new dataset is analyzed using the monoscopic configuration presented in Chapter 5.

Currently, no 3D background template exists for this configuration, making the reflected regions method the most suitable approach for background estimation. Due to the circular asymmetries in the background rates (cf. Fig. 6.4), the profile correction described in Sect. 6.2 is applied. An optimization of the on-region size for the energy range below 1 TeV resulted in $r_{\text{on}} = 0.13°$. By default, a loose energy threshold is selected per observation, at the energy at which the effective area drops below 10% of its maximum. Data from the H.E.S.S.-I era is also reanalyzed using the ImPACT stereo configuration (Parsons and Hinton, 2014), with an on-region size of $r_{\text{on}} = 0.1°$. The only relevant source component in the H.E.S.S. energy range is the core emission of Centaurus A, which can be modeled by a simple power law. While the on-region also encloses parts of the lobe template used in the Fermi-LAT analysis, it is evident from Fig. 7.7 that the spatially integrated flux from the extended lobes is subdominant above 100 GeV, allowing the lobe contribution to be safely neglected in the H.E.S.S. analysis.

Furthermore, at the distance of Centaurus A, attenuation of the spectrum due to EBL absorption is only expected above ~30 TeV (Dominguez et al., 2011). This effect does not affect the energy range analyzed in this work and is therefore neglected.

The resulting core spectrum of Centaurus A is shown in Fig. 7.8, together with the Fermi-LAT spectrum and the flux points from H.E.S.S. Collaboration et al. (2018). In

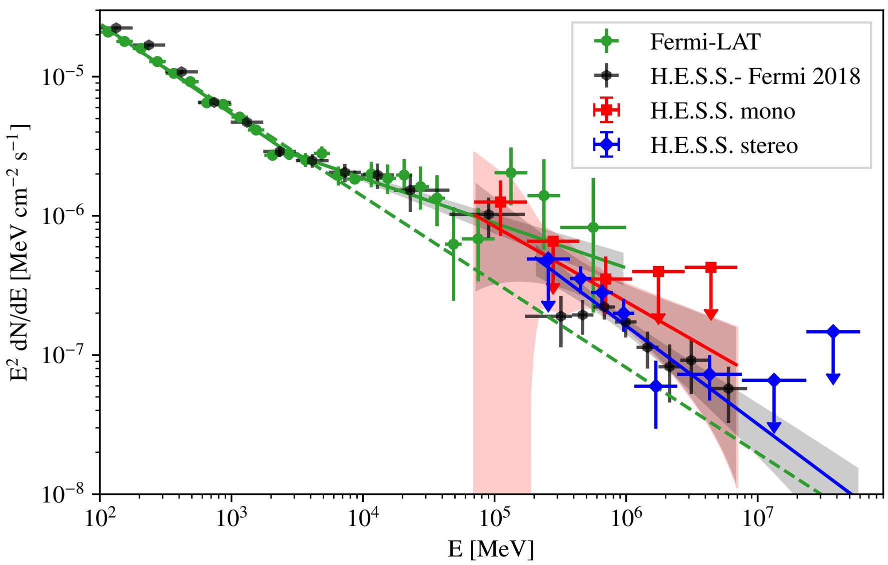

Figure 7.8: SED of the core model from this analysis (green, red, blue) and from H.E.S.S. Collaboration et al. (2018) (black). The solid lines represent the best-fitting models for the individual datasets, each with 1σ statistical error bands, except for H.E.S.S. mono where the outer contours show the systematic uncertainty from a 2% background scaling added to the statistical uncertainty. Flux points below 2σ significance (TS< 4) are shown as 2σ upper limits.

the relatively small monoscopic dataset, Centaurus A is detected at a significance level of 3σ, yielding only two flux points above 2σ significance. The spectrum is consistent with both the Fermi-LAT spectrum and the H.E.S.S. stereo spectra, although the uncertainties are large. The error bars on the flux points and the model envelopes represent 1σ statistical uncertainties, except for the mono spectrum, where the outer model envelopes reflect combined statistical and systematic uncertainties derived by scaling the background estimate by ±2%. This 2% background uncertainty is estimated from the standard deviation of the asymmetry shown in Fig. 7.8. Below 200 GeV, the total uncertainty is heavily dominated by the systematic uncertainty on the background estimate due to the low SBR in this range.

Figure 7.9 illustrates the SBRs from monoscopic analyses of Centaurus A, PKS 2155−304, and the Crab Nebula. The spectral models of PKS 2155−304 and Centaurus A predict 17% and 1.4% of the Crab flux at 100 GeV true energy, respectively. The apparent shift between the curves of Centaurus A and PKS 2155−304 relative to that of the Crab Nebula results from the larger zenith angles in the Crab observations, necessitating higher true event energies to achieve equivalent γ/h-separation performance. In contrast to Fig. 6.1, the on-region used here is slightly larger, and the shaded regions indicate the regimes where the signal is fully covered by the respective background systematic. For Centaurus A, the regime of 2% background systematics is reached just below 200 GeV, establishing this energy as the effective low-energy threshold for this analysis.

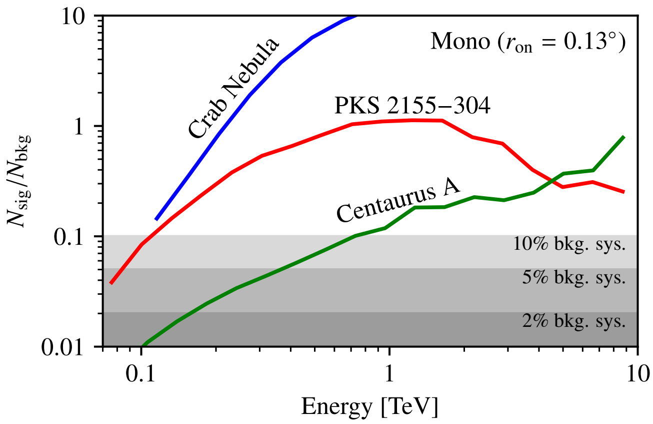

Figure 7.9: Signal-to-background ratios for H.E.S.S. mono observations on the Crab Nebula, PKS 2155−304, and Centaurus A in an on-region with $r = 0.13°$. The crossing points of the lines with the shaded regions indicate the energy thresholds for the respective level of systematic uncertainty in the background estimation.

To probe the spectrum of a source like Centaurus A to even lower energies, higher performance in background rejection is required, without introducing additional asymmetry in the background. Alternatively, systematic uncertainties in the background model could be reduced through the development of a 3D template model or other advanced techniques. Nevertheless, achieving an accuracy better than 2% remains an ambitious goal.

7.3 Combined analysis

After generating the Fermi-LAT dataset in Sect. 7.1 and creating the H.E.S.S. datasets (mono and stereo) in Sect. 7.2, the data can now be combined at the event level. For the H.E.S.S. mono dataset, energy bins below 200 GeV are excluded from the combined analysis due to the background systematic threshold. The analysis is similar to the one detailed in Chapter 4, with the key difference being that the two H.E.S.S. datasets are 1D spectral datasets, in contrast to the 3D datasets used for the Crab Nebula. However, this does not constrain the analysis since only spectral information is of interest, and not the morphology of the source. For the Fermi-LAT data, a 3D dataset is necessary due to the crowded RoI, where source disentanglement is only possible when considering the spatial information.

As discussed in the beginning of this Chapter, the deviation from a simple power law above 3 GeV can be modeled using either a hadronic component from the core, or an additional leptonic component from the inner lobes. The largest potential to distinguish between these models lies in the morphology measured by H.E.S.S., which is not accessible in this analysis and would require advanced, complex modeling beyond the scope of this work. Therefore, this analysis evaluates different parametric models and their ability to describe the data. The spectral component of the core model is described by one of the following models:

- a simple power law (PL) (cf. Eq. 4.2),
- a broken power law (bPL) (cf. Eq. 7.1),
- a exponential-cutoff broken power law (ECbPL)

$$\frac{dN}{dE} = N_0 \times \exp\left(-\frac{E}{E_{\mathrm{cut}}}\right) \times \begin{cases} \left(\frac{E}{E_{\mathrm{break}}}\right)^{-\Gamma_1}, & \text{if } E < E_{\mathrm{break}} \\ \left(\frac{E}{E_{\mathrm{break}}}\right)^{-\Gamma_2}, & \text{if } E \geq E_{\mathrm{break}} \end{cases}, \tag{7.2}$$

- the sum of a power law and a logarithmic-parabola (PL+LP) (cf. Eq. 4.1 for the LP).

The other free parameters in the combined fit affect only the Fermi-LAT dataset. As before, the spectral parameters of the lobe model are free (amplitude, index, and curvature of the log-parabola), in addition to one global normalization for all other 4FGL sources in the RoI, the normalization of the isotropic background component, and a norm and spectral tilt for the Galactic diffuse emission template.

The resulting best-fit models are shown in Fig. 7.10, together with the flux points from the individual instruments. Their parameters are summarized in Tab. 7.2. Note that the models are fitted to the event-level data rather than to the flux points. While this distinction is negligible for most of the Fermi-LAT energy range, it allows proper treatment of asymmetric uncertainties and upper limits in the H.E.S.S. datasets. The TS values for different model combinations are listed in Tab. 7.3. Based on the difference in TS and the number of free parameters, one can compute the Gaussian significance

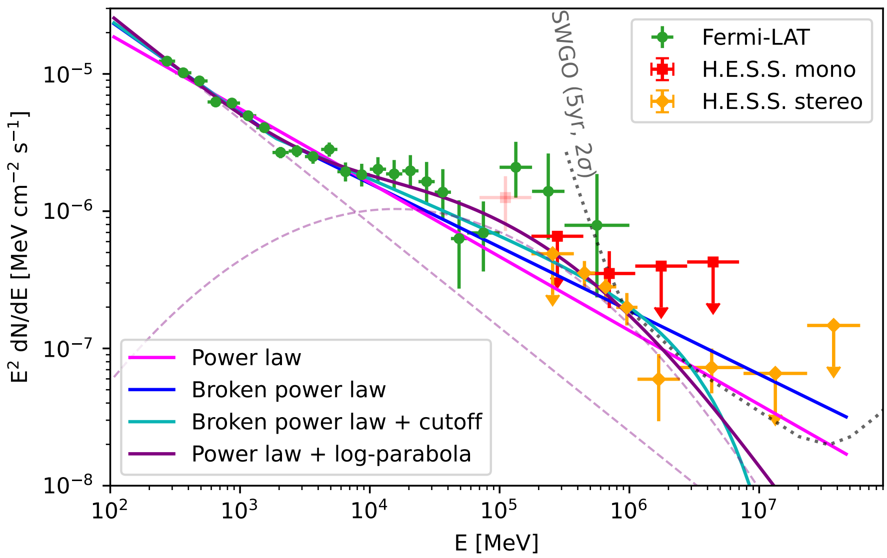

Figure 7.10: SED of the core emission, along with the fitted models and the SWGO differential sensitivity (Conceição, 2023, scaled to 5 yrs and 2σ per energy bin). Energy bins from the transparent red flux point do not contribute to this analysis due to large systematic uncertainties.

Table 7.2: Parameters for the various core models.

Model	N_0 [MeV^{-1} s^{-1} cm^{-2}]	Γ_1/α	Γ_2/β	E_{cut}[TeV]	E_{break} [GeV]
PL	$(1.35\pm0.13)\times10^{-19}$	2.538 ± 0.014	–	–	–
bPL	$(1.01\pm0.17)\times10^{-12}$	2.666 ± 0.030	2.463 ± 0.016	–	1.86 ± 0.13
EcbPL	$(9.98\pm0.16)\times10^{-13}$	2.677 ± 0.013	2.406 ± 0.029	3.5 ± 1.9	1.851 ± 0.011
PL+	$(2.48\pm0.13)\times10^{-20}$	2.758 ± 0.007	–	–	–
LP	$(9.5\pm6.1)\times10^{-23}$	3.46 ± 0.17	0.113 ± 0.010	–	–

The reference energy E_0 for the power laws is 1 TeV and for the log-parabola 10 TeV.

using the χ^2-distribution with degrees of freedom equal to the difference in the number of parameters. If the number of parameters is the same, one degree of freedom is assumed. The best-fitting model is the combination of power law and log-parabola, where the power law dominates before the energy break. Around the break, the log-parabola component becomes significant and dominates the spectrum above ∼10 GeV. This combination is clearly preferred over a simple power law with a TS of 37.3 (5.5σ), considering that the models are nested with three additional parameters.

An alternative description for the second component is the broken power law, which is favored over the simple power law with a TS of 27.3 (4.9σ), slightly less than what was found using the Fermi-LAT data alone. This reduction can be attributed to a softer post-break slope to match the stereo data, thus reducing the contrast with the simple power law. Comparing the broken power law to the PL+LP model is not straightforward, as these models are not nested. However, the observed TS difference of 10 suggests that the curvature in the second component is favored at approximately 3σ.

Table 7.3: Comparison of the core models in terms of relative fit statistics (TS), with corresponding significance shown in parentheses.

Model	PL (2)	bPL (4)	ECbPL (5)	PL+LP (5)
PL (2)	0	27.3 (4.9σ)	34.1 (5.2σ)	37.3 (5.5σ)
bPL (4)	–	0	6.8 (2.6σ)	10.0 (3.2σ)
ECbPL (5)	–	–	0	3.2 (1.8σ)

The model indicated by the column is always preferred over the model in the row. The numbers following the model names indicate the number of free parameters for each core model.

This curvature is also introduced by the exponential cutoff in the ECbPL model, which is preferred over the bPL model with a TS of 6.8 (2.6σ), adding one parameter (the cutoff energy). If the ECbPL model approximates the true source spectrum, this preference could be interpreted as evidence of a spectral cutoff in the core emission. However, although a hard continuation of the spectrum as implied by the Fermi-LAT data is unlikely, the log-parabola still provides a slightly better fit than the exponential cutoff. Therefore, one cannot definitively claim a spectral cutoff in the core component, but rather a softening of the index at higher energies.

The comparison between models does not account for systematic uncertainties, such as those related to the effective area or background estimates of the individual instruments. While it is, in principle, possible to include such effects, doing so would require a more sophisticated analysis framework involving a modified likelihood function and the introduction of nuisance parameters that accurately model these uncertainties, as outlined in Streil (2025). In this study, a simpler approach is adopted: energy bins dominated by systematic uncertainties are excluded, and it is assumed that statistical uncertainties dominate in the remaining energy range, rendering systematics subdominant. In addition to instrument-specific systematic effects, a potential relative energy shift between datasets from different instruments should be considered in a combined analysis — particularly if not all instruments are cross-calibrated. However, estimating both the direction and magnitude of such energy shifts is challenging and strongly depends on the assumed spectral shape (cf. Sect. 4.5). When the true spectral shape is unknown, allowing too much freedom in energy shift modeling can lead to biased results, just as restricting it too much or neglecting it entirely can. Therefore, caution is warranted when interpreting results based on low TS values presented here, as their significance may diminish once systematic uncertainties are fully accounted for.

Figure 7.10 also includes the sensitivity of the Southern Wide-Field Gamma-Ray Observatory (SWGO) (Conceição, 2023), scaled by ⅖ to convert from 5σ to 2σ and divided by $\sqrt{5}$ to adjust from one to five years of observation. It indicates the flux level required to achieve the first 2σ flux point detections after five years. This time is approximately required to confirm the softening of the second component, in contrast to the harder models that connect the Fermi-LAT and H.E.S.S. points linearly. Other currently operating water Cherenkov detectors, such as HAWC or LHAASO, are located in the Northern Hemisphere and are therefore unable to observe the southern sky location of Centaurus A.

7.4 Conclusion

Despite the improvements to the reconstruction of monoscopic H.E.S.S. events, it was not possible to lower the energy threshold below that of the stereoscopic events. This limitation arises from the low SBR resulting from the current background rejection technique, in combination with systematic uncertainties in the background estimation. These two factors restrict the range in which a significant signal can be measured to energies above 200 GeV, regardless of the observation time. Nevertheless, potential future improvements in the background rejection or a more accurate background modeling could potentially lower this threshold.

The new results presented in this section primarily originate from the enhanced Fermi-LAT analysis, benefiting from increased statistics, the revised lobe model, and the combination of Fermi-LAT and H.E.S.S. data at the event level. Based solely on the Fermi-LAT data, a spectral break in the core emission near 3 GeV was identified with a significance exceeding 5σ. This feature was confirmed to be robust across multiple analyses using different background and lobe templates.

The newly constructed lobe model is based on MWA data, which offers superior angular resolution and eliminates the large, unphysical central hole present in previous templates. Compared to other radio templates, it provides a better match to the observed data once the patches are removed from the Galactic diffuse model. A radial reweighting of the template accounts for spatial variations in magnetic field strength, with the best-fit profile indicating a declining magnetic field with increasing distance from the core — a behavior reminiscent of that seen in the Crab Nebula, although less pronounced.

In the combined analysis, multiple parametric models for the core emission were tested against the data of the two instruments. Unlike most approaches that rely on high-level data products such as flux points, the event-level combination accurately incorporates upper limits from the monoscopic analysis and asymmetric uncertainties in low-statistics energy bins. Deviation of the simple power law remain significant above the 5σ level, although not for the broken power-law model. Instead, a cutoff or a composite model combining a power law with a log-parabola is required.

This suggests that the spectral hardening above 3 GeV softens again within the H.E.S.S. energy range. However, a definitive spectral cutoff for the core emission of Centaurus A cannot yet be established.

Due to its southern location, Centaurus A is inaccessible to northern hemisphere γ-ray observatories such as HAWC and LHAASO. Future facilities like SWGO and the southern site of CTAO can help to constrain the high-energy component of the core spectrum. In particular, CTAO will offer enhanced spatial resolution, potentially enabling a clearer distinction between different emission scenarios and particle acceleration sites. These advancements could provide critical insight into whether Centaurus A is a source of UHE cosmic rays.

'Call to me and I will answer you and tell you great and unsearchable things you do not know.'

— God, Jeremiah 33:3

8 Summary and Discussion

Investigating high-energy phenomena in our universe comprises three main components: data acquisition, event reconstruction, and analysis, including statistical comparison to physical or phenomenological models. While it is generally true that more data leads to increased sensitivity, the amount of available data is limited by instrumental and financial constraints. Therefore, improved event reconstruction and intelligent data combination present an alternative – and often more cost-effective – path to new insights, as demonstrated by this work.

8.1 Improvements to the analyses

For the following discussion, the improvements introduced in this work are categorized into two distinct parts. First, the improvements to the low-level analysis, which refers to the event reconstruction, and second, the improvements to the high-level data analysis.

8.1.1 Low-level analysis

The low-level improvements are applied to and evaluated on monoscopic events from the H.E.S.S. array, which arguably offer the largest potential for improvements. In contrast to stereoscopic events, where observations from multiple angles allow geometric reconstruction via the intersection of major axes, monoscopic event reconstruction is inherently more challenging. Due to the unique design of H.E.S.S., with a single large telescope surrounded by four smaller ones, most low-energy ($\lesssim$100 GeV) events are observed only by the large telescope. Furthermore, due to the steeply falling power-law spectra, most γ-ray events lie at the lower end of the energy spectrum. Thus, optimal reconstruction and analysis of these events are crucial for fully exploiting the potential of the instrument.

Additional image parameters To extract more information from the recorded data, this work introduces and evaluates 32 novel image parameters that capture intensity and timing features as input to the reconstruction algorithms. Each parameter is computed analytically, allowing efficient processing of the $\mathcal{O}(10^7)$ events observed per hour. These parameters are either sensitive to differences between leptonic and hadronic showers, thereby boosting γ/h-separation, or provide geometric insight that improves the reconstruction accuracy. Several parameters demonstrate substantial value in complementing traditional Hillas parameters, particularly for direction reconstruction and background rejection. They contribute significantly to the improved monoscopic sensitivity achieved in this work and can find application in stereoscopic analyses as well.

Beyond performance improvements, this work proposes systematic strategies to address two key challenges when supplying additional inputs to machine-learning algorithms: parameter redundancy and mismatch between data and simulations. Redundancy is mitigated by using iterative training and performance evaluations, removing the least important feature each time until the performance degrades significantly. Mismatches between real and simulated data pose a more critical challenge, as poorly simulated features can introduce systematic uncertainties in the derived IRFs when provided to the algorithms. To assess this, the distributions of each parameter are compared across real background events, simulated proton showers, and γ-ray showers simulated with two distinct NSB levels. This makes it possible to evaluate how well a feature discriminates between signal and background, and how susceptible it is to simulation inaccuracies or NSB variations.

By comparing distributions of real background and simulated protons, confidence in the simulation accuracy of certain features is established. However, discrepancies in this comparison may also stem from differences in the CR composition at TeV energies, as well as inaccuracies in the hadronic interaction model. Ideally, comparisons would be made directly between real and simulated γ-ray images, but the lack of a clean γ-ray sample – due to the dominant hadronic background – complicates this. Such samples can only be approximated using event selection cuts and bright sources like the Crab Nebula, though these cuts distort the original γ-ray distributions and may affect real and simulated data differently. Nevertheless, good agreement between real and simulated background data strengthens confidence in the shared components of the simulation pipeline, including photon propagation and camera signal modeling. Most parameters based on pixel amplitudes show good agreement, while those involving pixel timing reveal notable discrepancies. This suggests that timing information is simulated with less accuracy, potentially introducing systematic uncertainties if used for γ/h-separation.

However, these discrepancies may only propagate fully to the time gradients because pixel times are not considered in the standard image cleaning process. A time-cleaning algorithm that excludes pixels with large temporal deviations from the shower mean could improve agreement and enable effective use of time variables in CT5 analyses for the first time. The potential of such approaches is explored in (Ćelić et al., 2025), a study to which this work also contributed. Together, both efforts pioneer the use of FlashCam's timing information and explore possible solutions to the associated challenges.

As more detailed image information is exploited, sensitivity to subtle data-simulation mismatches increases. Thus, improvements in reconstruction performance must be carefully balanced against the accuracy of simulations. This trade-off is evident in the interplay between statistical and systematic uncertainties: gains in one at the cost of the other may not yield an overall improvement. Imperfect simulations can therefore limit the full potential of advanced machine-learning techniques. As some modern methods operate directly on raw pixel data and extract even more detailed features, the need for precise and reliable simulations becomes even more critical. The precision of simulations, in turn, depends on stable instrumentation and accurate calibration — emphasizing the tight coupling between data acquisition, reconstruction, and analysis, where the final result is limited by the least accurate component. When using neural networks, it is often unclear which features drive decisions, making it difficult to hide poorly modeled inputs. This highlights a key advantage of image parameters over raw pixel data: they offer transparency and explicit control over what the algorithm learns. Even as simulation quality improves, simpler and more robust methods should continue to serve as benchmarks and cross-checks for more complex approaches.

Therefore, final validation of the complete reconstruction chain is achieved by applying it to Crab Nebula data and comparing the results to those obtained with the previous pipeline. Due to its high brightness and correspondingly low statistical uncertainties, the Crab serves as an ideal testbed for identifying and evaluating potential systematic limitations.

Flip-BDT This machine-learning algorithm enhances the determination of the correct image orientation in the camera, improving upon the earlier method based solely on the Hillas-skewness. It leverages the newly introduced image parameters and, in turn, is essential for their effective use in subsequent reconstruction algorithms due to their definition. Many of these parameters are constructed relative to the head-tail direction of the shower, which is initially random in the camera frame and must be accurately reconstructed. The flip-BDT primarily contributes to the improved angular resolution, but also indirectly to the other reconstruction and classification algorithms by enabling the proper interpretation of the new image parameters.

In air showers, the velocities of the secondary particles slightly exceed the propagation speed of the emitted Cherenkov photons. As a result, for shower impact points close to the telescope, light from the lower parts of the shower reaches the camera before light from the upper parts. At larger impact distances, however, the longer path length of light from the lower shower inverts this effect. This is a geometric effect, influenced by the increased Cherenkov angle in the denser lower atmosphere. The combined time for particle propagation through the shower and subsequent photon travel to the telescope therefore exceeds the travel time for photons emitted higher up, which follow a more direct path. Consequently, the time gradient along the major image axis carries valuable information about the shower orientation and impact distance. In future work, this parameter could further enhance the precision of the flip determination, provided simulation accuracy and robustness to NSB conditions are improved.

Variable selection cut The third improvement introduced in this work is the amplitude-dependent event selection cut, which allows fainter, lower-energy events to pass the cuts, thereby substantially lowering the analysis energy threshold. Similar to the novel image parameters, this variable cut is not limited to monoscopic analyses only, but can be applied in other configurations and instruments as well. Its main advantage lies in the optimized γ/h-separation performance across all image amplitudes, coupled with a smooth and more constant signal efficiency profile, directly propagating to the effective area.

Although image amplitude, rather than event energy, determines separation performance, the final analysis is performed in energy bins, where this optimization truly matters. In hindsight, defining and optimizing the variable selection cut as a function of reconstructed energy might have been a more natural approach, but due to the correlation between energy and image amplitude, major differences are not expected. While the variable cut clearly improves over a constant cut without obvious drawbacks, there are analysis methods proposed that avoid the cut entirely and incorporate the information about the gammaness of the events directly in a Bayesian framework (D'Amico et al., 2021). Although not yet widely adopted, such techniques may represent a promising direction for future methodological advances.

When it comes to the lowest energy events, the flip-BDT improved the angular resolution by 40% in combination with the new variables, which also improved the γ/h-separation by 20% in the q-factor. The variable selection cut reduced the energy threshold by 50%, and together, these three improvements resulted in a 41% increase in sensitivity. Alternative event reconstruction techniques, such as ImPACT, have already demonstrated superior performance compared to the standard approach based on image parameters. However, there are currently no established alternatives for γ/h-separation in H.E.S.S.. Consequently, the observed improvements in the q-factor and the reduction in the energy threshold represent highly relevant advancements within the overall reconstruction pipeline.

Further note that improvements observed in simulations do not necessarily translate directly to real data. These performance figures do not account for systematic uncertainties, such as those affecting the background rate due to asymmetries across different camera sectors — estimated at 2–10%. At the lowest energies, where the SBR is low due to poor γ/h-separation, such uncertainties can dominate. Consequently, an effective lowering of the energy threshold is only possible for bright point-like sources similar to the Crab Nebula. For fainter sources like Centaurus A, a reduced threshold could not be achieved, although the improved sensitivity above the threshold remains beneficial. This highlights once more that gains in a single component of the analysis chain can only reach their full potential when no other part imposes limiting constraints.

8.1.2 High-level analyses

Background corrections One of the first steps in the high-level analysis is the estimation of the background, performed after the event reconstruction and selection, which is required for the signal estimation that is subsequently compared to models. As demonstrated in this work, its accurate determination is especially important for faint and extended sources. Background estimation is challenging because the background rates vary between different observations, but also between different camera sectors of one observations. Current methods rely either on the same camera sector in archival observations or on different sectors within the same observation. In the absence of a 3D background model, which relies on the former method, the monoscopic analyses utilize the latter technique, making them susceptible to observed asymmetries in background rates.

This work introduces two correction schemes for the reflected regions method. One is based on a linear gradient in the off-region counts, while the other leverages a larger set of observations to estimate the asymmetry profile. The gradient correction is only applicable when asymmetries follow a linear trend, whereas the profile correction requires a sufficiently large set of observations. Both methods, when applied to appropriate datasets, effectively reduce discrepancies between observations with differing source positions in the camera. However, a notable improvement for larger datasets is only expected when the source positions are not symmetrically distributed in the camera, or when varying observational conditions prevent the cancellation of effects from opposing camera regions. Therefore, symmetrically distributing the pointing positions around the source remains a key strategy for reducing background systematics.

Understanding the origin of these asymmetries and reducing them to subdominant levels will require further investigation into dependencies on zenith angle, geomagnetic effects, and asymmetries in the camera response. Achieving background estimation accuracies better than 2% in IACTs remains an ambitious target.

Unbinned analyses Another analysis step prior to data analysis is the binning of the events into an analysis geometry. This process inherently leads to information loss, as all events within a bin are associated with the bin center and not their actual location within its bin. On the other hand, this loss is only relevant when the reconstruction uncertainty is smaller than the bin size, i.e., when the information is resolvable. The resolution of current-generation IACTs in angular space and energy is not good enough to require bin sizes that challenge modern computational systems.

Unbinned likelihood formulations are widely used in neutrino astronomy, where the relatively low event counts make this approach both feasible and advantageous. One might also expect the unbinned analysis to be more sensitive compared to binned methods. To properly evaluate this expectation, one must differentiate between analyses of a single "event type" and analyses that use many event types. In single-type analyses, all events are treated with identical reconstruction uncertainties, regardless of actual reconstruction quality, leading to averaged IRFs and a sensitivity loss compared to joint analyses of different event types. For example, Fermi-LAT analyses can utilize up to four event types, assigning a type based on either the direction- or energy-reconstruction quality. Currently, Gammapy supports only one set of IRFs per dataset with the option of analyzing multiple datasets jointly. However, the optimal sensitivity is reached when each event is analyzed with its own IRFs, necessitating one dataset per event, which quickly becomes infeasible for more than $\mathcal{O}(100)$ events. Therefore, per-event analyses are naturally suited to an unbinned framework. They have the potential to outperform binned or unbinned analyses, if these average events with vastly different reconstruction quality. However, implementing per-event analyses in Gammapy would require a new data format for the IRFs and many more novelties, such that the unbinned analysis also utilizes one set of IRFs, as a first step. Under these conditions, a performance gain over binned analyses is not expected for neutrino telescopes, due to their lower resolution, which allows for sufficiently fine binning.

Nevertheless, unbinned analysis can outperform binned approaches computationally in low-statistics regimes. The computation time reduces when the number of events for which the likelihood is computed in the unbinned analysis becomes smaller than the number of bins for which the likelihood is computed in the binned approach. This difference can become particularly large as the dimensionality of the analysis increases. While 1D spectral analyses typically involve $\mathcal{O}(10)$ bins, 3D analyses often require $\mathcal{O}(10^5)$ bins due to the two extra spatial dimensions. In analyses with an additional time dimension, the number of bins increases even further. IACTs exhibit excellent time resolution on the order of nanoseconds, making time binning dependent on source variability alone. The shortest timescales of variability are observed in pulsars in the order of a few milliseconds. If the period of the pulsar is known and each event has an assigned phase, a phase dimension can be added to the analysis, increasing bin counts to $\mathcal{O}(10^6)$. However, the timing model of the pulsar cannot be optimized, as each model update would require a rebinning of the data. The unbinned analysis offers the only viable solution to optimize the timing models of pulsars in the Gammapy framework.

Joint-likelihood analyses between different instruments Joint analyses are a well-established concept. In fact, the most basic example is the standard method of

γ-ray data analysis, where the likelihoods of individual energy bins are multiplied. The alternative, a stacked analysis, implies in this context that the data is combined into a single energy bin, for which one likelihood value is computed. In general, joint analyses maximize sensitivity but increase computational cost.

Performing multi-messenger analyses across different instruments is well motivated, as each instrument provides sensitivity to a different part of the emission model. For instance, γ-ray instruments are sensitive to the IC or PD emission, while X-ray, optical, and radio instruments constrain the synchrotron component. Neutrino observations are able to distinguish between hadronic and leptonic emission scenarios. Therefore, a comprehensive source model is best constrained using all available multi-wavelength and multi-messenger data.

When combining such heterogeneous data, joint analysis is the only viable method, due to differing energy ranges and instrument characteristics. In the past, this combination was performed on high-level data products, such as flux points, by multiplying the likelihood (χ^2) values computed based on the agreement of the model with the individual points. Two potential issues with this approach are discussed below. First, the flux points inherently depend on the assumed spectral model due to the finite energy resolution and the bin width of the flux point. Similarly, they also depend on the spatial model used for calculations, whether it is modeled as a point source, a Gaussian, or disc model. However, a consistent analysis can also be achieved by simply utilizing the same source model for the flux points extraction. Second, asymmetric uncertainties and upper limits require a special treatment in the likelihood, rather than the simple χ^2 computation. Since the Poisson distribution only approximates Gaussians at larger counts and is notably asymmetric at small counts, asymmetric uncertainties and upper limits are common for high-energy bins or neutrino observations. Information about event counts and uncertainty asymmetries is often lost in high-level data products, which can bias results or reduce sensitivity. However, applying appropriate Poisson statistics for flux points or upper limits should yield results equivalent to those derived from the event-level combination.

While the novel approach of combining data at the event level is not strictly required once these issues are addressed, it remains a promising approach, as demonstrated by several applications in this thesis. Furthermore, performing all analyses within a unified, user-friendly framework such as Gammapy enhances usability and reproducibility.

8.2 Applications of the improvements

The combination of data from different instruments is applied across three projects discussed hereafter.

CTAO-KM3NeT analysis In the combined γ-neutrino analysis, operating on simulations only, the sensitivity of the method was estimated in terms of its ability to distinguish emission scenarios for Galactic γ-ray sources. The analysis revealed that this task is highly challenging — even for the brightest sources, considering moderate exposure times. However, including data from additional instruments in future studies may further constrain the emission models. The joint analysis yielded consistent results with the individual instrument analyses, thereby validating the overall approach. It also showed that while the joint likelihood fit is not the only viable implementation strategy, it offers the most consistent and arguably the most convenient framework.

Although the analysis was not repeated using the unbinned method for the neutrino datasets, this alternative could have improved computational performance slightly, though not sensitivity. This conclusion was supported by testing different bin sizes, which showed performance saturation at the selected binning level. If more sophisticated neutrino analyses with higher sensitivity become available in the future and cannot be implemented in Gammapy, data combination can instead be performed using likelihood values computed by the respective analysis chains. This strategy is realized in the 3ML project (Vianello et al., 2015)[61].

Fermi-LAT - H.E.S.S. analysis of the Crab Nebula This analysis of the Crab Nebula was originally intended as proof of concept that joint-instrument analyses within Gammapy yield results consistent with those from dedicated individual analyses on real data. Aligning the individual analyses in Gammapy with the established chains of the respective instruments was the main challenge. This required special treatment of the Fermi-LAT data due to the presence of multiple sources with spatially overlapping contributions.

For the first time, the expanded Fermi-LAT and H.E.S.S. datasets enabled a self-consistent measurement of the Crab Nebula's energy-dependent morphology across five orders of magnitude in energy. Multi-wavelength data from radio to X-ray energies were incorporated into the analysis as spectral and extension measurements through a modified likelihood.[62] The combined dataset allowed to test and constrain different phenomenological SSC models and revealed a notable tension between the X-ray and H.E.S.S. extension measurements. Assuming that the systematic uncertainties are not significantly underestimated in this analysis, these results suggest that more complex models are required, probably abandoning assumptions such as spherical symmetry. This introduces a major computational challenge, considering that the numerical computation of the models needs to balance precision and speed. Even with the symmetric models used in this study, the combined fit (with 18 free parameters) required $\mathcal{O}$(days) to complete, and the resulting likelihood surface was insufficiently smooth to reliably estimate parameter uncertainties. Significant effort was invested in ensuring the fit's convergence to the global likelihood minimum by experimenting with different optimizers and fixing individual parameters in iterative procedures. Nonetheless, the statistical uncertainties reported by various fitting algorithms were unreasonably small. Furthermore, properly propagating systematic uncertainties in the IRFs to individual model parameters would require more sophisticated methods, such as incorporating additional nuisance parameters (Streil, 2025). The inability to report uncertainties on best-fit parameters is highly unusual and restricts further interpretation of key quantities. However, it does not affect the exclusions of certain models, which are disfavored with large TS differences, significantly beyond any plausible uncertainties in the likelihood values. For the parameter α, describing the radial decline of the B-field, a non-zero value is favored by $\approx 20\sigma$, suggesting a relative uncertainty of $\approx 1/20 = 5\%$.

The extensive dataset available for the Crab Nebula has already yielded valuable insights into the non-thermal emission processes at play in young pulsar wind nebulae. Looking ahead, future studies can build upon this foundation by incorporating more

[61] `https://threeml.readthedocs.io/en/stable/`

[62] This method is functionally equivalent to including a `FluxPointsDataset`, though the latter was avoided due to the substantial model evaluation time (∼2 seconds per dataset per iteration). Instead, the model prediction was cached for one dataset and compared to the flux points during its likelihood computation, minimizing redundant evaluations.

realistic and complex emission models and fitting them to the data in a consistent manner. With continued improvements in computational tools and statistical techniques, it will become increasingly feasible to derive meaningful confidence intervals and better quantify uncertainties, ultimately deepening our understanding of the underlying physics.

Fermi-LAT - H.E.S.S. analysis of Centaurus A Centaurus A is the only extragalactic source investigated in this work — excluding PKS 2155−304, which served only calibration purposes. Although Centaurus A is comparatively faint, emitting only about 1% of the Crab Nebula's flux, its southern location allows for observations at low zenith angles with H.E.S.S.. The combined analysis of Fermi-LAT and H.E.S.S. data followed the approach developed for the Crab Nebula, which served as a methodological blueprint.

As the final project of the thesis, this analysis combines nearly all previously discussed improvements, with the exception of the unbinned method, which did not offer a performance advantage in this case. However, improvements to the H.E.S.S. monoscopic analysis were partially offset by potential background systematics, even after applying the profile correction. Therefore, novel key insights, such as the radial magnetic field dependence within the lobes, arose primarily from the Fermi-LAT analysis, providing also the tightest constraints on the core spectrum. A detailed systematics study demonstrated the robustness of the core spectrum with respect to different background templates, while the lobe emission was found to be more sensitive to such variations. In the combined analysis, the VHE lever arm provided by the H.E.S.S. data supports spectral models slightly more complex than the broken power law preferred by the Fermi-LAT data alone. A modest preference was found for spectral curvature in the second component, which – if confirmed by future measurements – could favor leptonic models, as these naturally exhibit this feature.

However, unlike the Crab Nebula, where the precise measurements complicate the development of a single model that can describe all available data, Centaurus A is currently limited by larger spectral uncertainties. Additional data are required to exclude several viable scenarios for Centaurus A. The most promising future measurements involve either improved morphological constraints in the VHE regime or the development of the spectrum beyond 10 TeV. Future experiments such as CTAO and SWGO, located in the Southern Hemisphere, will significantly contribute towards the endeavor of understanding the particle acceleration in the Centaurus A region.

Improving pulsar analyses Due to their rapid temporal variation and the associated fourth analysis dimension, pulsar analyses profit most from using unbinned analysis strategies. They additionally benefit from the lower energy thresholds achieved by the monoscopic improvements, given their typically soft spectra. However, since background rejection becomes increasingly difficult at low energies, the reduced threshold primarily benefits bright sources. In the case of pulsed emission, background suppression can be further enhanced by selecting events along the temporal dimension based on the pulsar phase, providing an energy-independent method to reject background. As a result, all improvements discussed in this work are directly applicable to pulsar analyses. This was demonstrated with two examples, where timing models can be fit simultaneously to spectral or event spatial parameters. Due to the limited amount of data, the analysis of the Crab Pulsar yielded only an upper limit, whereas the estimation of the glitch epoch for PSR J1906+0722 showed slightly reduced uncertainties compared to the reference analysis — demonstrating the sensitivity of the method.

The implementation of this analysis within the Gammapy framework during the course of this thesis also allows for joint analyses across multiple instruments. Although such a combined analysis was not demonstrated here, the results presented in previous sections suggest that integration is straightforward. This functionality will enable a wide range of previously inaccessible analysis scenarios for future users of the public Gammapy package.

Remaining challenges primarily concern the stability and convergence of the fitting algorithms. They are often faced with multiple parameters of vastly different scale, including those with periodic behavior, such as the reference time, that wraps around at each period. As Gammapy supports multiple fitting backends with various optimization strategies, users can experiment to identify the most suitable option. Additional backends tailored for timing model optimization may be implemented in the future and could serve the community as new tool to understand the nature of CR acceleration at pulsars.

But test everything that is said. Hold on to what is good.

— Paul, 1. Thessalonians 5:21

9 Conclusion and Outlook

Despite decades of research since the discovery of an isotropic CR flux extending to extreme energies, the question of where and how these particles are accelerated remains unresolved. Galactic sources must be capable of accelerating protons and heavier nuclei up to approximately 3 PeV, while extragalactic sources likely reach energies beyond 100 EeV. In recent years, a vast amount of multi-wavelength observations has been accumulated, covering a wide variety of astrophysical objects. Notably, the detection of ∼PeV γ rays from sources such as the Crab Nebula confirms their potential to accelerate particles to the required energies. However, conclusively establishing a hadronic origin remains difficult, as both leptonic and hadronic emission models can often reproduce observed γ-ray spectra if given sufficient freedom in the assumed particle distributions and environmental parameters. Without additional information – such as neutrino detections or constraints on magnetic field strengths and ambient matter densities – this degeneracy persists.

In this context, the present thesis contributes through a combination of improved event reconstruction methods and high-level analysis techniques designed to enhance the sensitivity and enable the joint analysis of multi-messenger datasets. At the reconstruction level, several new image parameters were introduced alongside an amplitude-dependent event selection cut and an algorithm to determine the correct image orientation in the camera, all of which improved the sensitivity of monoscopic CT5 analyses. As CT5 remains the largest IACT to date, with unique sensitivity to faint, low-energy showers, particular emphasis was placed on reducing the energy threshold — cutting it by approximately half. Combined with the improved background rejection, these advances enable access to energies previously unreachable with H.E.S.S., particularly relevant for sources with soft spectra. Although originally developed for monoscopic analyses, the newly introduced image parameters and amplitude-dependent selection cut are also applicable to stereoscopic configurations. At the analysis level, multiple tools and methods were implemented within the Gammapy framework, including background asymmetry corrections, an unbinned likelihood framework, and event-level joint-likelihood analyses. They address challenges such as analyzing sources with strong temporal variability – like pulsars – and enable a consistent treatment of multi-instrument data by fully accounting for Poisson event statistics and reducing systematic uncertainties. Several astrophysical case studies demonstrate the impact of these methods, all of which benefit from Gammapy's flexible architecture. This framework also allowed for the integration of custom models, including various SSC implementations tested against multi-wavelength data from the Crab Nebula.

The joint-likelihood analysis of Fermi-LAT and H.E.S.S. data of the Crab Nebula revealed an energy-dependent morphology in the IC regime, with extensions decreasing with energy — as expected from electron cooling, and analogous to the much more precisely measured synchrotron extensions. However, assuming the same underlying electron distribution, the IC extensions above ∼0.3 TeV appear too large compared to the synchrotron data. This analysis also provided constraints on the magnetic field structure within the nebula, favoring a model in which the magnetic field strength declines with radial distance. A similar trend was inferred for the extended lobes of the radio galaxy Centaurus A, based on a comparison of the radio template and Fermi-LAT fluxes. For the core component of Centaurus A, a joint analysis of Fermi-LAT and H.E.S.S. data enabled tests of various spectral shapes under consideration of systematic uncertainties arising from different background templates. A spectral hardening above 3 GeV was confirmed, and indications of curvature at higher energies were observed — features which, if confirmed, may favor a leptonic origin of the emission. Nevertheless, neutrino (non-)detections remain a more robust probe for distinguishing hadronic contributions. In this context, the combination of γ-ray and neutrino data to constrain emission scenarios of several Galactic sources showed promising results in a simulation study based on CTAO and KM3NeT datasets. While this work does not directly test specific particle acceleration models, it has successfully demonstrated that novel methods can yield new insights into the nature and distribution of primary particles at their sources.

Looking ahead, ongoing developments in event reconstruction and classification using machine-learning and associated techniques promise to further improve sensitivity. However, to fully exploit these methods and reduce systematic uncertainties, improvements in the accuracy of IACT image simulations will be essential. Proper quantification and propagation of systematics will remain a central challenge in this new era of high-statistics analyses, where statistical uncertainties are increasingly diminished. Multi-messenger analyses leveraging high-precision data will become increasingly important as a new generation of observatories comes online. On the γ-ray side, arrays such as CTAO (with its northern and southern arrays), ASTRI (Scuderi et al., 2022), LACT (Zhang et al., 2024), as well as SWGO will advance hardware capabilities, sensitivity, and sky coverage. Similarly on the neutrino side, KM3NeT, P-ONE (Agostini et al., 2020), and the extensions planned for IceCube-Gen2 (Aartsen et al., 2021), as well as RNO-G (Aguilar et al., 2021) will collect complementary information about the neutrino sky. These new datasets will challenge existing models and foster the development of more sophisticated ones, enabling deeper insights into the physical processes occurring in extreme environments.

Acronyms

A_{eff} effective area. 22, 24, 25

a.s.l. above sea level. 19, 23

ADC analogue to digital converter. 20

AGN active galactic nuclei. 4, 12, 13, 14, 52, 136

AIC Akaike information criterion. 81, 92, 93, 94

ARCA Astroparticle Research with Cosmics in the Abyss. 35

ASTRI Astronomia a Specchi a Tecnologia Replicante Italiana. 162

BDT boosted decision tree. 39, 115, 116, 117, 118, 119, 120, 121, 122, 123, 124, 126, 127, 154, 155

bPL broken power law. 148, 149

CMB cosmic microwave background. 5, 11, 14, 85, 97, 99, 142

CMS center of mass system. 2

CoG center of gravity. 21, 105, 106, 107, 110, 113, 115, 120, 126

CPU central processing unit. 62, 63

CR cosmic ray. 1, 2, 3, 4, 5, 7, 11, 12, 14, 16, 17, 34, 38, 48, 49, 129, 140, 151, 153, 160, 161

CTA Cherenkov Telescope Array. 35, 36, 37, 38, 39, 40, 41, 43, 44, 47, 48, 49, 50, 51, 73, 103, 125

CTAO Cherenkov Telescope Array Observatory. 23, 24, 25, 26, 27, 31, 35, 52, 58, 61, 127, 151, 159, 162

D.o.F. degrees of freedom. 139

DOM digital optical module. 35

EBL extragalactic background light. 5, 6, 146

ECbPL exponential-cutoff broken power law. 148, 149

EDisp energy dispersion. 22, 24, 26, 27, 54, 55, 56, 60, 66

EDM estimated distance to minimum. 60

Fermi-LAT Fermi Large Area Telescope. 9, 13, 15, 16, 24, 33, 63, 64, 66, 70, 71, 73, 77, 78, 79, 80, 81, 82, 83, 84, 86, 90, 91, 96, 99, 100, 101, 102, 136, 137, 138, 139, 140, 142, 143, 144, 145, 146, 147, 148, 149, 150, 156, 158, 159, 161, 162, 189

FoV field of view. 16, 27, 33, 52, 53, 113, 130, 132, 139

GBM Gamma-ray Burst Monitor. 15

GOF goodness-of-fit. 110

H.E.S.S. High Energy Stereoscopic System. 7, 23, 33, 63, 64, 71, 73, 74, 75, 76, 77, 80, 81, 82, 83, 84, 86, 90, 91, 96, 99, 100, 101, 102, 104, 105, 114, 115, 116, 126, 127, 128, 129, 131, 132, 133, 136, 137, 145, 146, 147, 148, 150, 151, 152, 155, 158, 159, 161, 162, 169, 179, 180

HAP H.E.S.S. analysis program. 105, 122, 169

HAWC High-Altitude Water Cherenkov Observatory. 19, 24, 36, 51, 150, 151

HE high-energy. 6, 71, 72

HEGRA High Energy Gamma Ray Astronomy. 23

IACT Imaging Atmospheric Cherenkov Telescope. 20, 21, 23, 24, 25, 33, 35, 36, 38, 39, 63, 64, 70, 73, 104, 108, 126, 127, 128, 156, 161, 162

IC Inverse Compton. 5, 8, 9, 11, 12, 14, 34, 36, 41, 42, 43, 44, 46, 47, 48, 50, 51, 71, 72, 73, 77, 78, 79, 80, 81, 83, 84, 85, 86, 90, 91, 92, 93, 95, 96, 97, 98, 99, 100, 101, 102, 103, 142, 144, 157, 161, 167

ImPACT Image Pixel-wise fit for Atmospheric Cherenkov Telescopes. 22, 73, 146, 155

IR infrared. 5, 11, 95

IRF instrument response function. 22, 23, 24, 31, 35, 37, 38, 39, 40, 43, 44, 51, 57, 58, 60, 61, 64, 66, 69, 70, 74, 75, 77, 79, 80, 90, 92, 128, 129, 153, 156, 158

ISM interstellar medium. 2, 7, 11

LACT Large Array of imaging atmospheric Cherenkov Telescope. 162

LAT Large Area Telescope. 15

LHAASO Large High Altitude Air Shower Observatory. 36, 72, 81, 96, 103, 150, 151

LHC Large Hadron Collider. 1, 2

LoS line of sight. 13, 14, 86, 87

LP logarithmic parabola. 148, 149

MAGIC Major Atmospheric Gamma Imaging Cherenkov. 9, 23, 63, 64, 65, 104

MC Monte Carlo. 22, 25

MHD magneto-hydrodynamic. 84, 89, 90, 96, 98, 99, 103

MWA Murchison-Widefield-Array. 142, 143, 144, 145, 150

MWL multi-wavelength. 72, 73, 84, 102, 142

NN neural network. 116

NSB night sky background. 21, 106, 111, 113, 114, 117, 118, 120, 121, 122, 123, 124, 127, 128, 132, 153, 154

ORCA Oscillation Research with Cosmics in the Abyss. 35

P-ONE The pacific ocean neutrino experiment. 162

PD pion decay. 8, 34, 41, 42, 43, 44, 45, 46, 47, 48, 157, 167

PDF probability density function. 26, 27, 46, 47, 53

PL power law. 1, 3, 7, 148, 149

PMT photo multiplier tube. 20

PSF point spread function. 22, 24, 25, 26, 31, 32, 37, 39, 40, 41, 54, 55, 56, 58, 59, 60, 66, 74, 75, 76, 79, 80, 82, 91, 99

PWN pulsar wind nebula. 9, 10, 11

RMS root mean square. 21, 106, 107

RNO-G Radio Neutrino Observatory in Greenland. 162

RoI region of interest. 53, 56, 57, 61, 63, 66, 75, 77, 78, 80, 82, 90, 137, 138, 139, 140, 141, 145, 147, 148

SBR signal-to-background ratio. 20, 67, 129, 131, 132, 133, 134, 147, 150, 155

SED spectral energy distribution. 1, 5, 6, 8, 9, 10, 11, 13, 14, 65, 71, 72, 87, 91, 94, 95, 96, 98, 99, 101, 102, 136, 137, 138, 145, 146, 148

SiPM silicon photomultiplier. 20

SNR supernova remnant. 4, 7, 8, 10, 11

SSC self-synchrotron Compton. 84, 90, 96, 97, 137, 158, 161

SWGO Southern Wide-Field Gamma-Ray Observatory. 148, 150, 151, 159, 162

TOA time of arrival. 63, 64, 66

TS test statistic. 29, 45, 46, 47, 48, 50, 61, 65, 66, 68, 77, 78, 80, 82, 138, 143, 144, 146, 148, 149, 150

UHE ultra-high-energy. 14, 151

UHECR ultra-high-energy cosmic ray. 136, 137

VERITAS Very Energetic Radiation Imaging Telescope Array System. 23, 63, 104

VHE very-high-energy. 6, 11, 12, 13, 16, 34, 35, 36, 71, 72, 94, 137, 159

Appendix

A Likelihood scan results for all sources

Likelihood scan results for Vela X and RX J1713.7−3946 are shown in Fig. A.1, while those for Westerlund 1 and eHWC J1907+063 are shown in Fig. A.2.

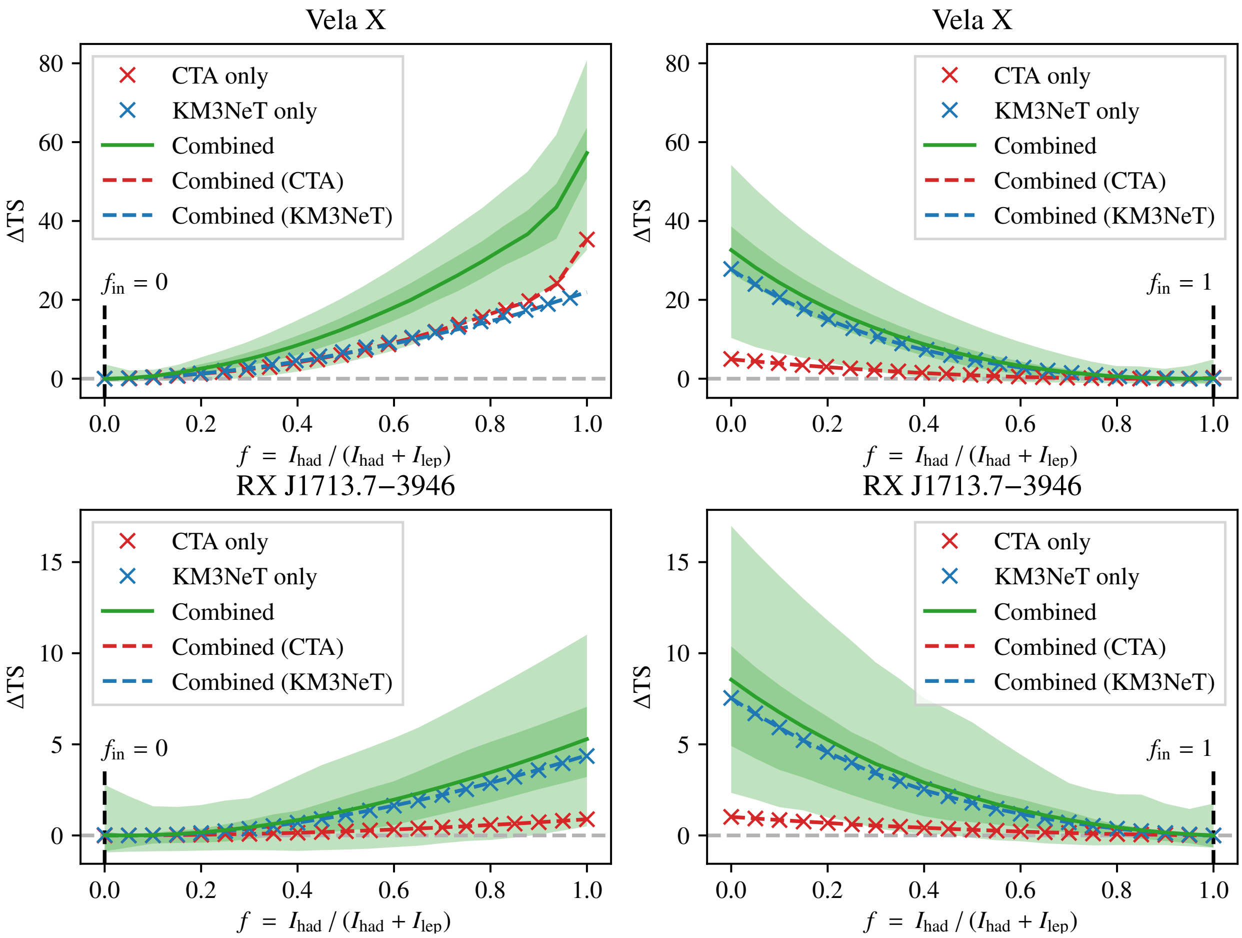

Figure A.1: Profile likelihood scan results for the sources Vela X and RX J1713.7−3946. The plots on the left hand side display the results for a purely leptonic (IC) input model ($f_{\mathrm{in}} = 0$), whereas the plots on the right hand side show those for a purely hadronic (PD) input model ($f_{\mathrm{in}} = 1$). For more details, please refer to the caption of Fig. 2.12.

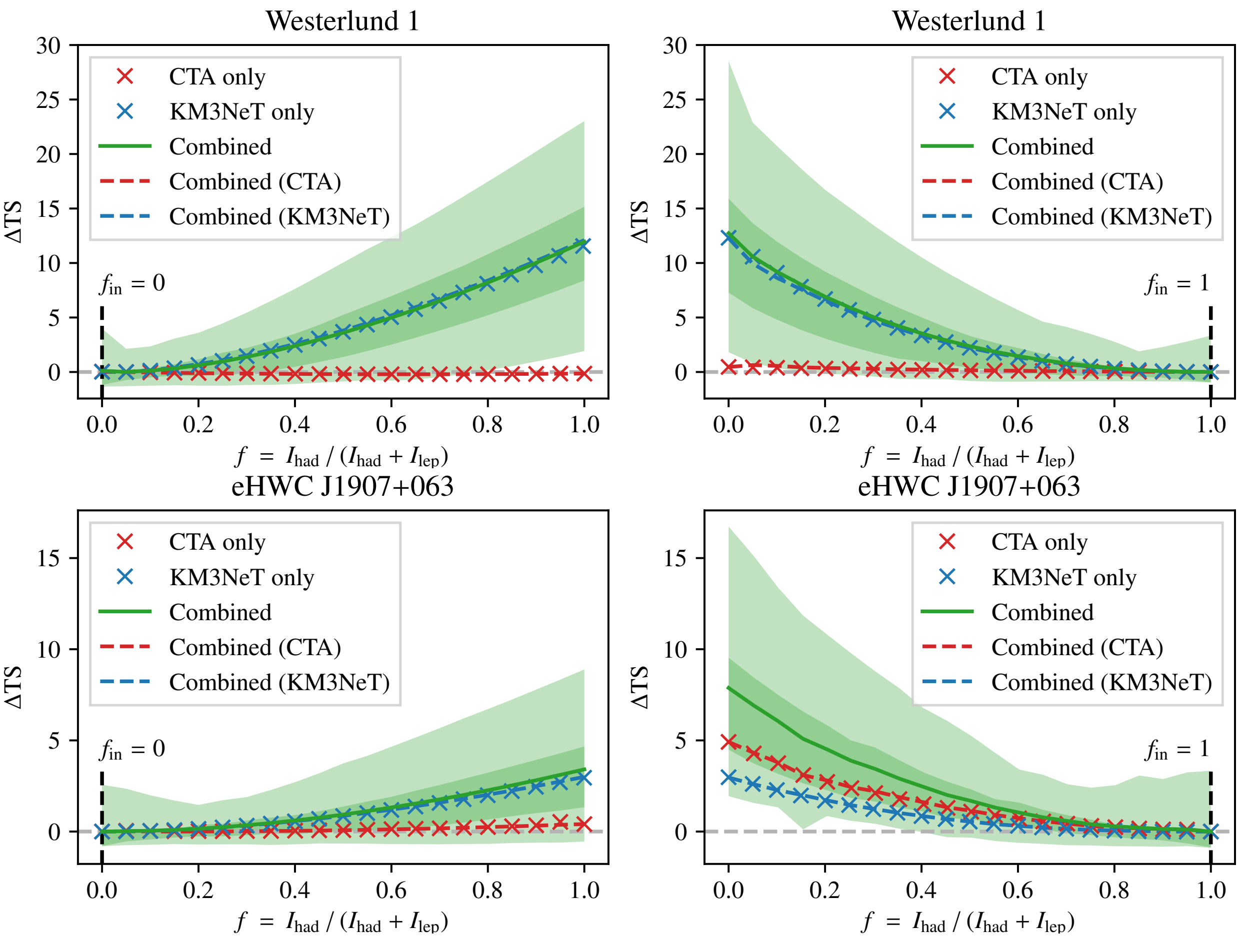

Figure A.2: Same as in Fig. A.1, but for the sources Westerlund 1 and eHWC J1907+063.

B Comparison with the reflected regions background method

In this section we compare the H.E.S.S. flux points derived with the three-dimensional (3D) likelihood analysis as described in this paper to those derived with a more traditional one-dimensional (1D) analysis, in which only the energy dimension is considered. The main difference between the two methods lies in the estimation of the residual hadronic background. While the 3D analysis requires a background model, the background for the 1D analysis is estimated using 'Off' regions in the field of view ('reflected regions method', see Fomin et al., 1994; Berge et al., 2007). The 1D analysis has been carried out using the H.E.S.S.-internal 'HAP' pipeline. Because the Crab Nebula is slightly extended we choose a comparatively large 'On' region of 0.1° radius. For technical reasons, we also split the H.E.S.S. stereo data set into two subsets for this test, corresponding to the different phases of the instrument. The comparison of the derived spectra is shown in Fig. B.1. At low energies, the Gammapy points tend to be higher than those obtained with HAP. We attribute this partly to the fact that the 1D analysis corrects for leakage of γ rays outside of the On region under the assumption of a point-like source, whereas the Crab Nebula appears increasingly extended towards lower energies.

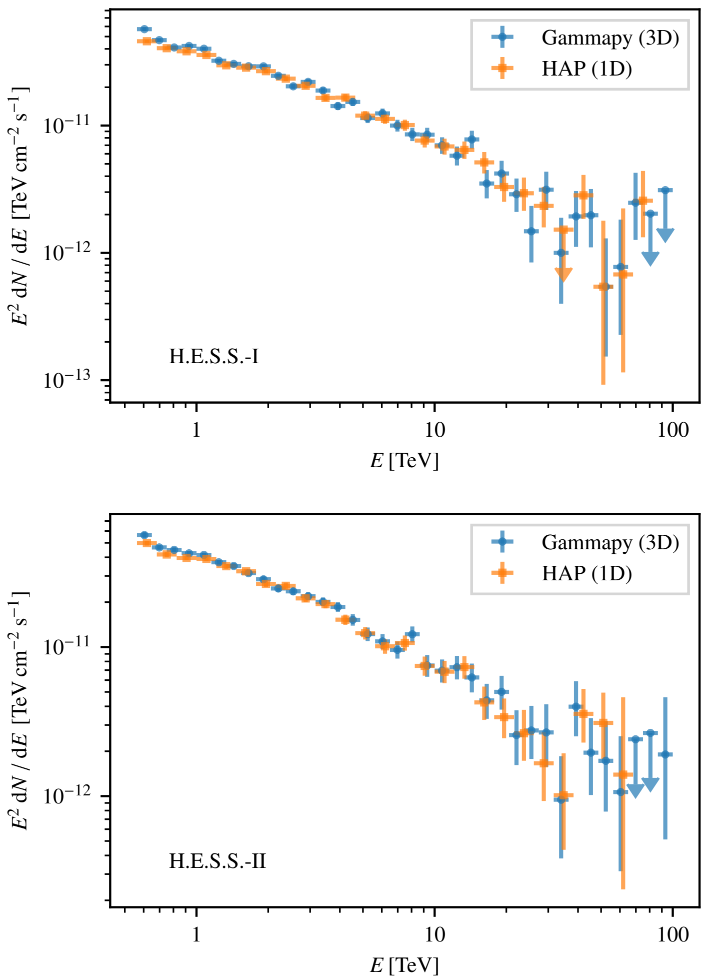

Figure B.1: Comparison of the Crab Nebula γ-ray flux measured with H.E.S.S. using different analysis techniques. The blue points with circle markers show the result as derived in the three-dimensional likelihood analysis with Gammapy described in this work. The orange points with square markers have been computed with the H.E.S.S. analysis program (HAP), using a traditional one-dimensional analysis based on the 'reflected background' method. (a) Data from H.E.S.S. Phase-I (2004–2009, cf. Table 4.1). (b) Data from H.E.S.S. Phase-II (2013–2015).

C Variable distribution plots

For each of the variables, we show the distribution of $\sim 7 \times 10^6$ background events taken from observations where known γ-ray sources are excluded. We compare this distribution to the distribution of $\sim 8 \times 10^4$ simulated protons. Additionally, we show the distributions of $\sim 4 \times 10^5$ diffuse γ rays simulated with the realistic NSB value and a NSB value which is ~ 1.65 times higher. All simulations are done for 20 deg zenith angle and the simulated spectrum $\sim E^{-1.8}$ is re-weighted to $E^{-2.5}$. The distributions are normalized to 1 such that the difference in event numbers is not visible, which means the y-axis of the plots shows the normalized number of entries in that bin. The correct image orientation is determined based on the *Flip*-BDT described in Sect. 2.2.1 of the main paper, leading to asymmetries between the head and tail sectors.

C.1 Hillas parameter-based variables

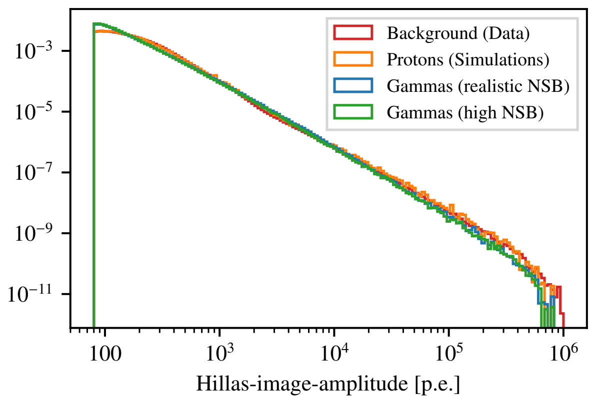

Figure C.1: Distribution of the Hillas-image-amplitude. Protons and gammas are simulated, while background events are measured data.

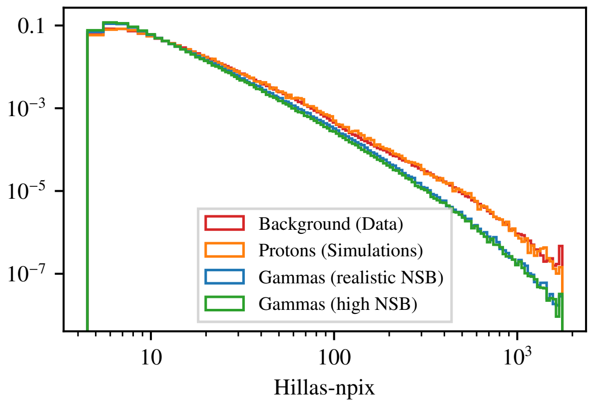

Figure C.2: Distribution of the Hillas-npix.

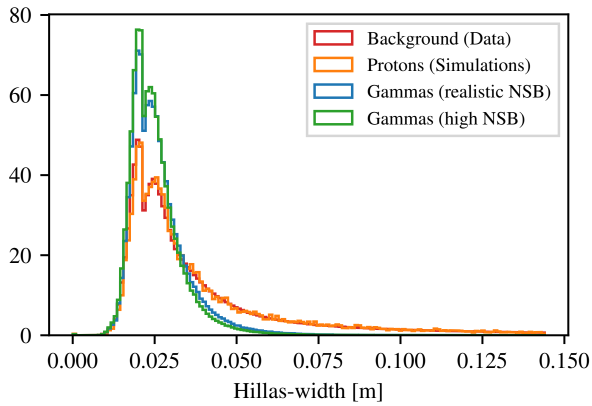

Figure C.3: Distribution of the Hillas-width.

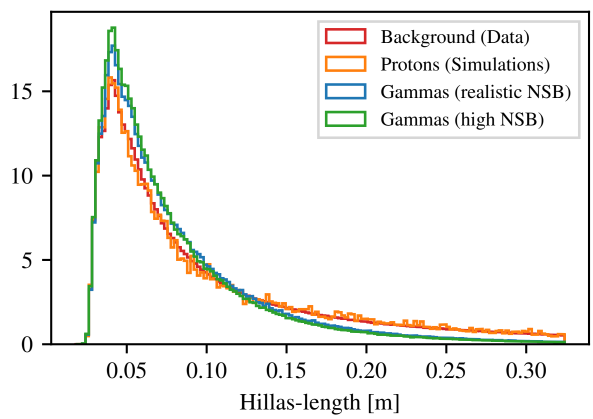

Figure C.4: Distribution of the Hillas-length.

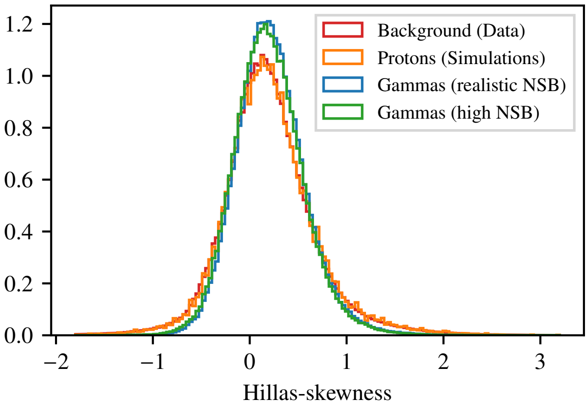

Figure C.5: Distribution of the Hillas-skewness.

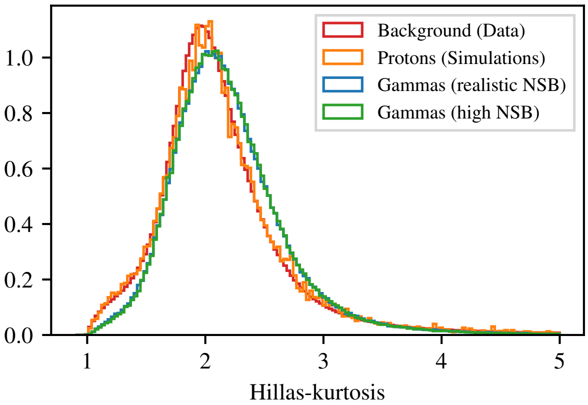

Figure C.6: Distribution of the Hillas-kurtosis.

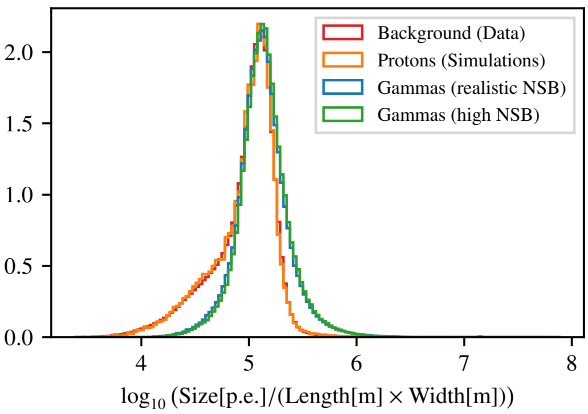

Figure C.7: Distribution of the Hillas-logdensity.

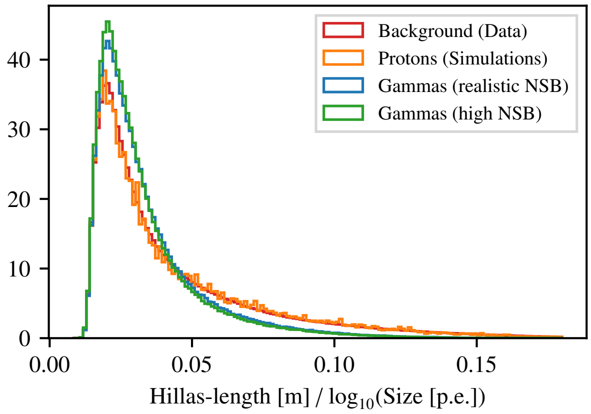

Figure C.8: Distribution of the Hillas-length-over-logsize.

C.2 Sector-based variables

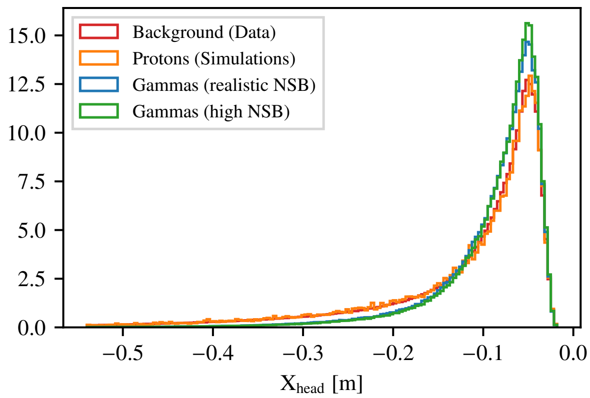

Figure C.9: Distribution of the x_{tail}.

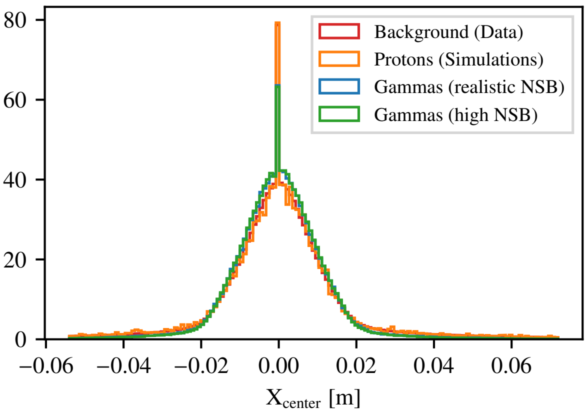

Figure C.10: Distribution of the x_{center}.

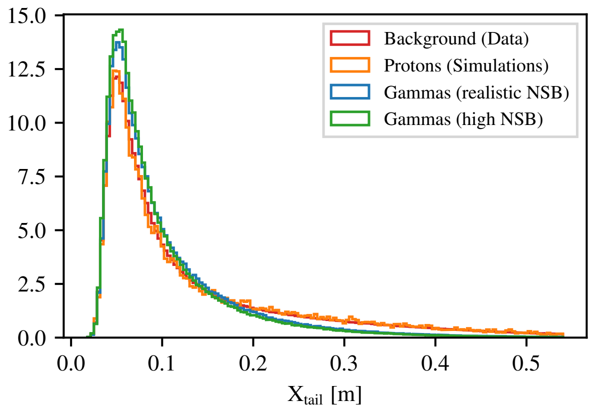

Figure C.11: Distribution of the x_{head}.

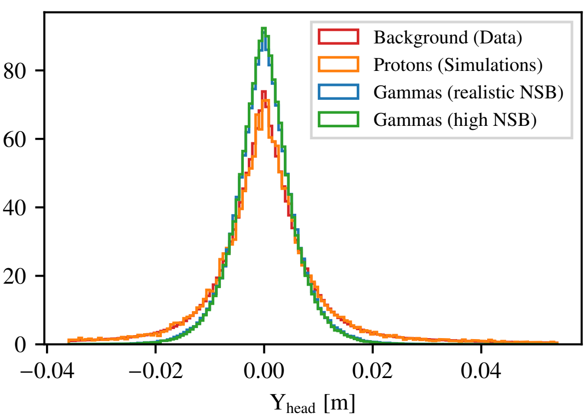

Figure C.12: Distribution of the y_{head}.

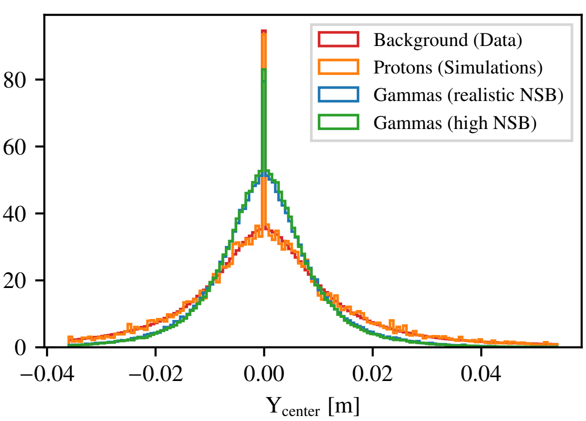

Figure C.13: Distribution of the y_{center}.

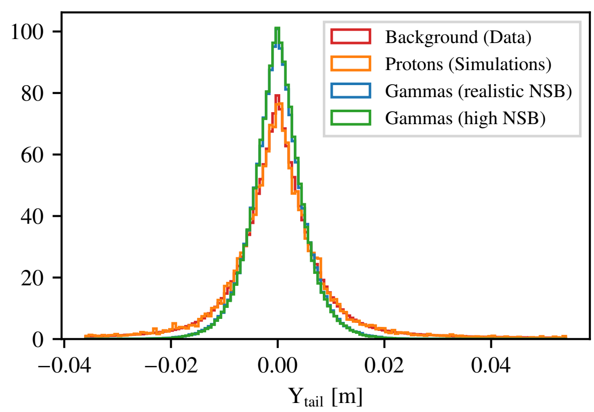

Figure C.14: Distribution of the y_{tail}.

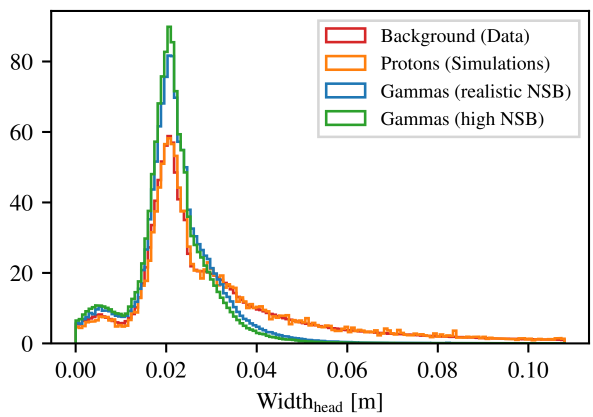

Figure C.15: Distribution of the $\mathrm{width}_{\mathrm{head}}$.

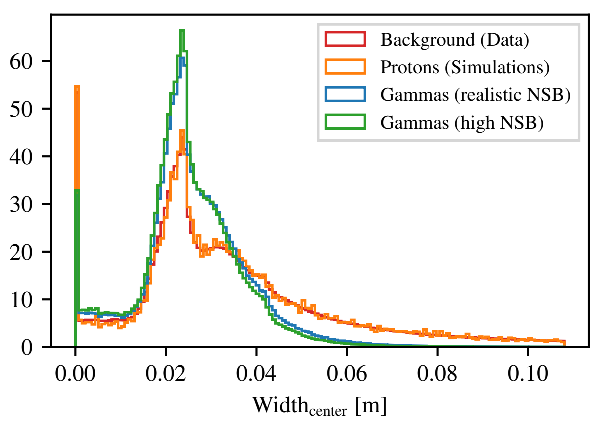

Figure C.16: Distribution of the $\mathrm{width}_{\mathrm{center}}$.

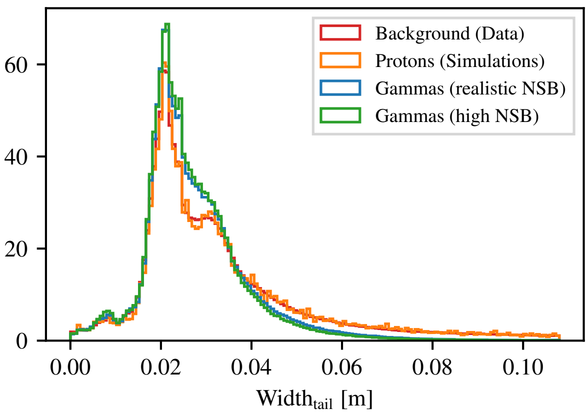

Figure C.17: Distribution of the width$_{\text{tail}}$.

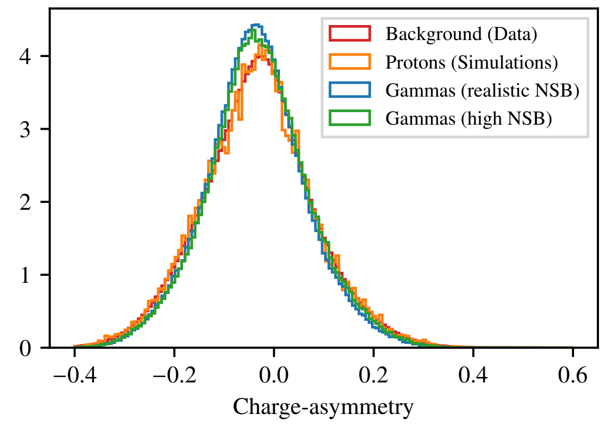

Figure C.18: Distribution of the charge-asymmetry.

C.3 Continuous variables

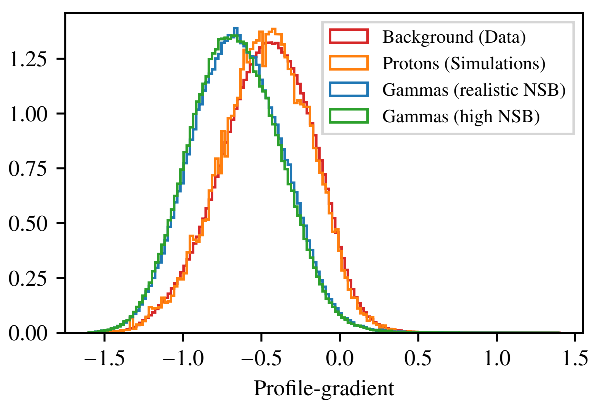

Figure C.19: Distribution of the profile-gradient.

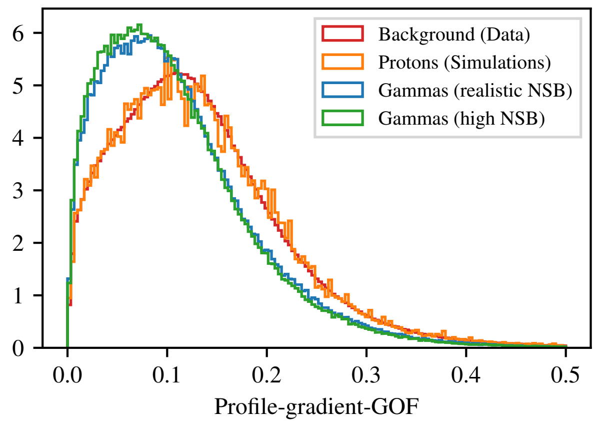

Figure C.20: Distribution of the profile-gradient-GOF.

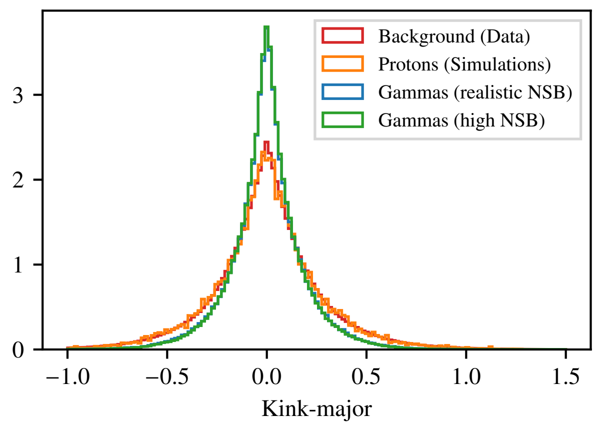

Figure C.21: Distribution of the kink-major.

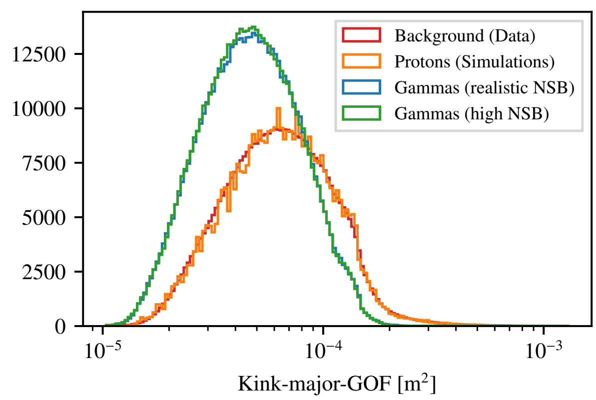

Figure C.22: Distribution of the kink-major-GOF.

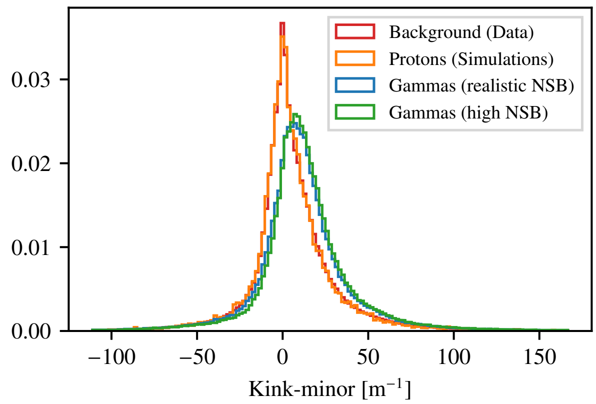

Figure C.23: Distribution of the kink-minor.

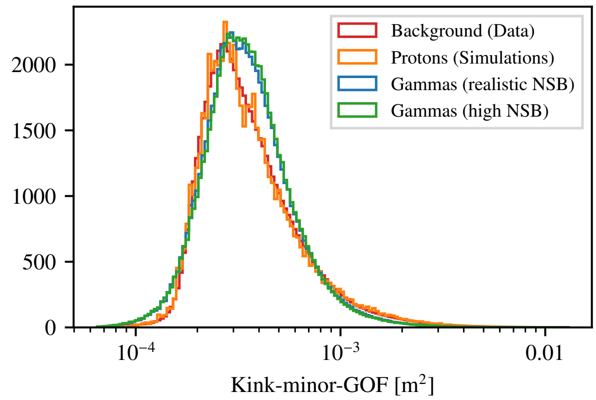

Figure C.24: Distribution of the kink-minor-GOF.

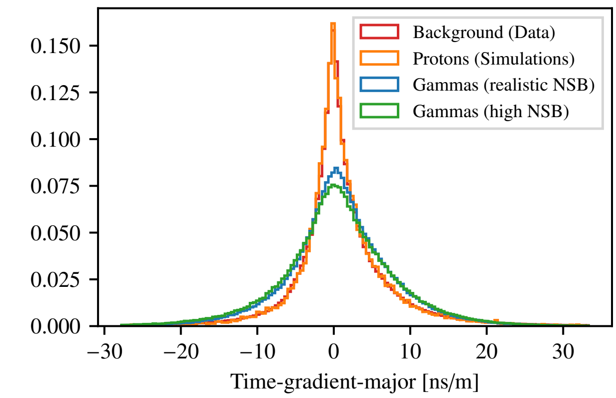

Figure C.25: Distribution of the time-gradient-major.

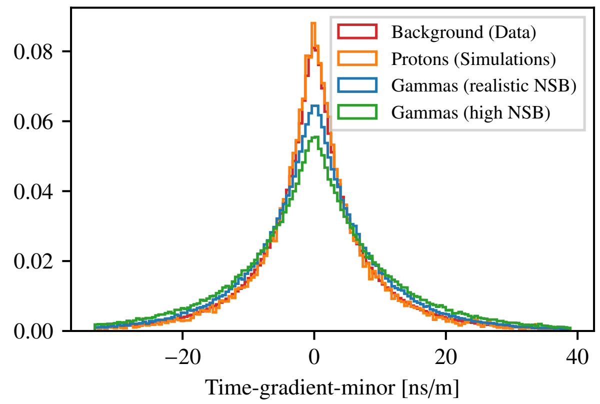

Figure C.26: Distribution of the time-gradient-minor.

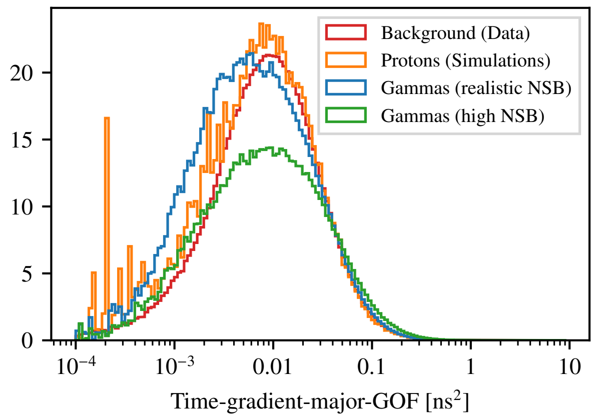

Figure C.27: Distribution of the time-gradient-major-GOF.

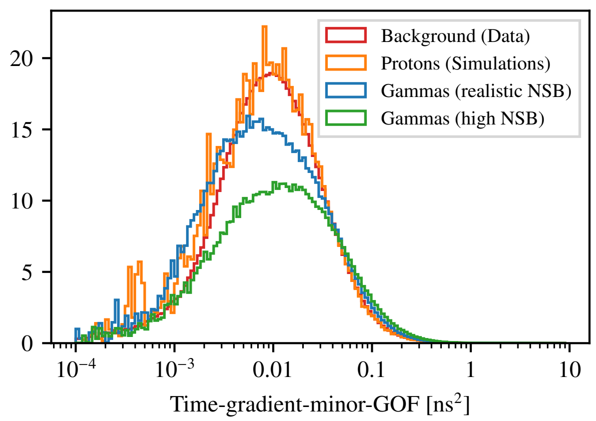

Figure C.28: Distribution of the time-gradient-minor-GOF.

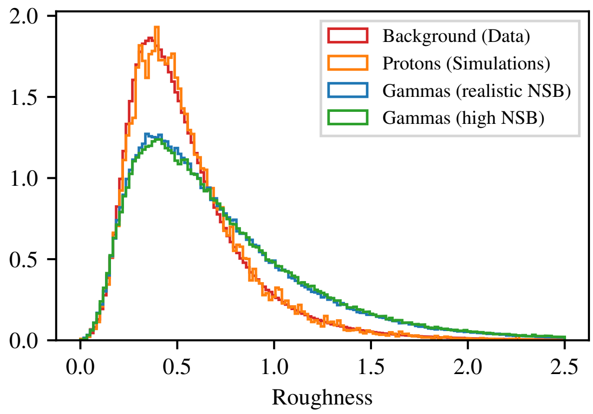

Figure C.29: Distribution of the roughness.

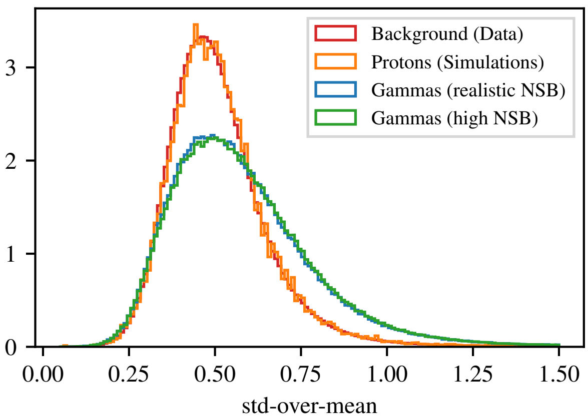

Figure C.30: Distribution of the std-over-mean.

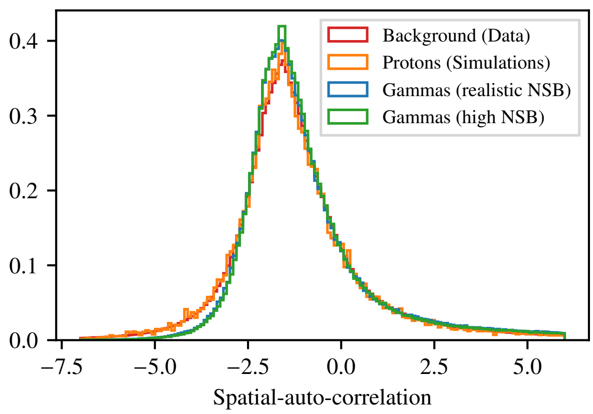

Figure C.31: Distribution of the spatial-auto-correlation.

C.4 Pixel Variables

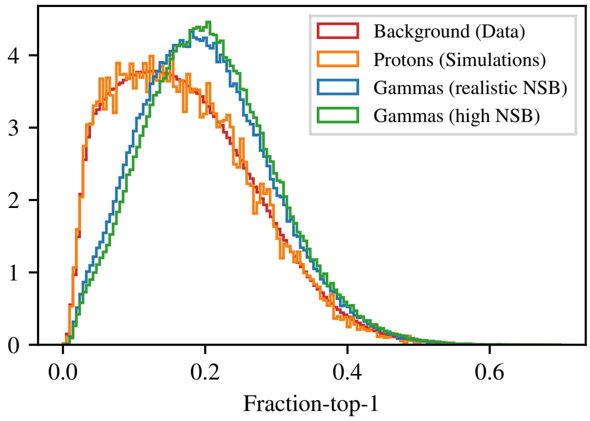

Figure C.32: Distribution of the fraction-top-1.

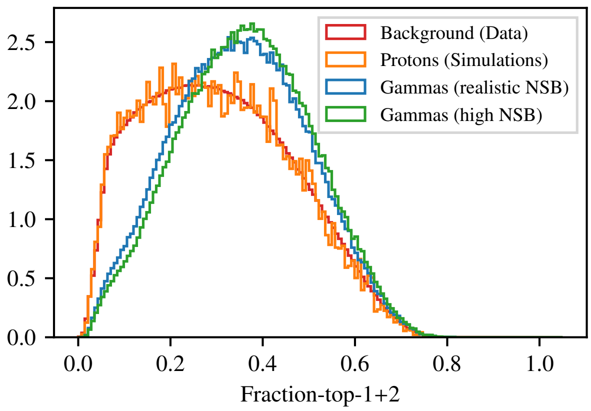

Figure C.33: Distribution of the fraction-top-1+2.

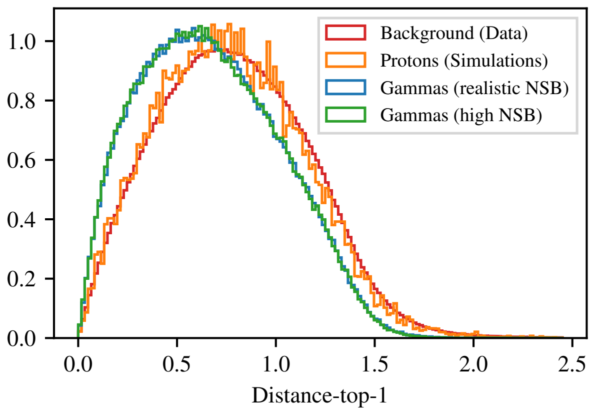

Figure C.34: Distribution of the distance-top-1.

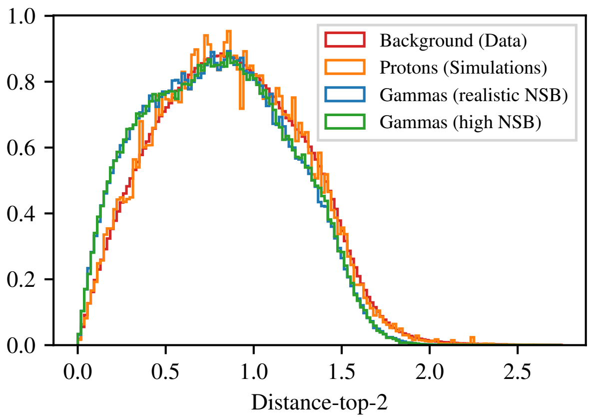

Figure C.35: Distribution of the distance-top-2.

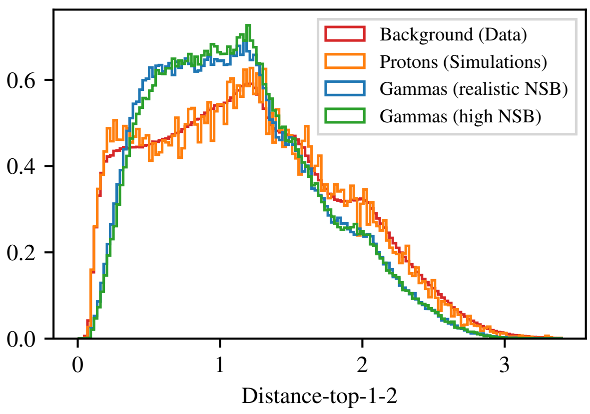

Figure C.36: Distribution of the distance-top-1-2.

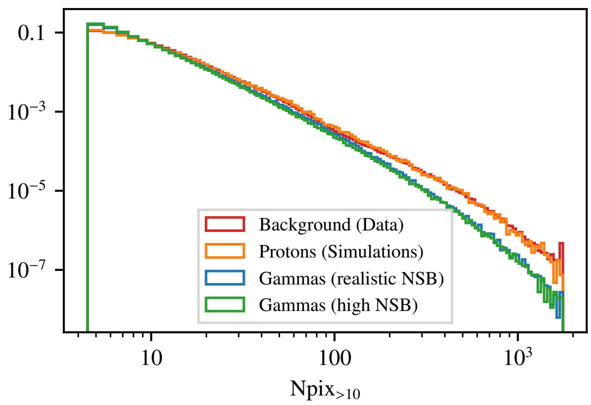

Figure C.37: Distribution of the $\mathrm{npix}_{>10}$.

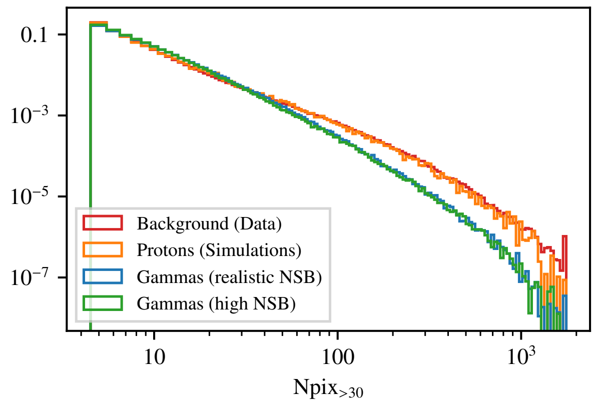

Figure C.38: Distribution of the $\mathrm{npix}_{>30}$.

D Variables summary

In the following we list all variables investigated in this work, segmented in Hillas, sector, continuous, and pixel variables.

Table D.1: Summary table of the variables

Variable	Mirror	Flip	Reco	γ/h-Sep.	A-stat.
Hillas-image-amplitude		x	Yes	x	2.422
Hillas-local-distance		0.014	Yes	0.033	x
Hillas-npix		0.018	Yes	0.058	0.427
Hillas-length		x	Yes	0.045	6.637
Hillas-width		x	Yes	0.241	58.172
Hillas-skewness	$\times(-1)$	0.263	Yes	0.013	8.476
Hillas-kurtosis		x	Yes	0.008	20.770
Hillas-length-over-logsize		0.008	Yes	0.021	5.819
Hillas-logdensity		x	No	0.066	31.479
$\mathrm{x}_{\mathrm{head}}$	$-\mathrm{x}_{\mathrm{tail}}$	x	No	0.011	6.259
$\mathrm{x}_{\mathrm{center}}$		x	No	x	x
$\mathrm{x}_{\mathrm{tail}}$	$-\mathrm{x}_{\mathrm{head}}$	x	No	0.004	4.478
$\mathrm{y}_{\mathrm{head}}$	$\mathrm{y}_{\mathrm{tail}}$	x	No	x	x
$\mathrm{y}_{\mathrm{center}}$		x	No	x	x
$\mathrm{y}_{\mathrm{tail}}$	$\mathrm{y}_{\mathrm{head}}$	x	No	x	x
$\mathrm{width}_{\mathrm{head}}$	$\mathrm{width}_{\mathrm{tail}}$	0.028	No	0.046	32.785
$\mathrm{width}_{\mathrm{center}}$		x	No	0.015	20.559
$\mathrm{width}_{\mathrm{tail}}$	$\mathrm{width}_{\mathrm{head}}$	0.026	No	0.008	29.886
charge-asymmetry	$\times(-1)$	x	Yes	x	x
kink-major		x	No	0.007	14.610
kink-major-GOF		x	No	0.026	34.703
kink-minor	$\times(-1)$	0.482	No	0.011	17.520
kink-minor-GOF		0.012	No	0.016	7.115
roughness		x	No	0.006	13.753
spatial-auto-correlation		x	No	0.012	7.860
profile-gradient		x	No	0.186	11.150
$\text{profile-gradient}_{\mathrm{head}}$	$\text{profile-gradient}_{\mathrm{tail}}$	0.013	No	0.005	9.967
$\text{profile-gradient}_{\mathrm{tail}}$	$\text{profile-gradient}_{\mathrm{head}}$	0.013	No	0.004	5.542
profile-gradient-GOF		x	No	0.007	39.337
std-over-mean		x	Yes	0.057	9.958
time-gradient-major	$\times(-1)$	x	Yes	x	809.564
time-gradient-major-GOF		x	No	x	24190.345
time-gradient-minor		x	No	x	2303.658
time-gradient-minor-GOF		x	No	x	19008.329
fraction-top-1+2		x	No	0.011	0.519
fraction-top-1		x	No	0.009	1.086
$\mathrm{npix}_{>10}$		x	No	0.018	0.574
$\mathrm{npix}_{>30}$		x	No	0.042	5.133
distance-top-1		x	No	0.006	1.007
distance-top-2		x	No	0.003	-0.408
distance-top-1-2		x	No	0.006	2.619

The “Mirror” column shows how the variables behave when being flipped, i.e., no change, change of sign, or change of variable (with sign change). Numbers in the columns for the flip and gamma-hadron separation training indicate the relative variable importance, whereas “x” denotes that the variable is not used for the respective training. For the direction and energy reconstruction, the choice of variables is identical, and no importance is estimated from the neural networks. The last column “A-stat.” gives the Anderson-Darling test statistics from Sect. 5.3.5.

Bibliography

Aartsen, M. G., R. Abbasi, M. Ackermann, et al. (2014). „Search for a diffuse flux of astrophysical muon neutrinos with the IceCube 59-string configuration". In: *PRD* 89, p. 062007. DOI: 10.1103/PhysRevD.89.062007.

Aartsen, M. G., M. Ackermann, J. Adams, et al. (2018). „Multimessenger observations of a flaring blazar coincident with high-energy neutrino IceCube-170922A". In: *Science* 361, eaat1378. DOI: 10.1126/science.aat1378.

Aartsen, Mark G, R Abbasi, M Ackermann, J Adams, et al. (2021). „IceCube-Gen2: the window to the extreme Universe". In: *Journal of Physics G: Nuclear and Particle Physics* 48.6, p. 060501.

Abbasi, R., M. Ackermann, J. Adams, et al. (2022a). „Evidence for neutrino emission from the nearby active galaxy NGC 1068". In: *Science* 378, pp. 538–543. DOI: 10.1126/science.abg3395.

— (2022b). „Improved Characterization of the Astrophysical Muon–neutrino Flux with 9.5 Years of IceCube Data". In: *ApJ* 928, p. 50. DOI: 10.3847/1538-4357/ac4d29.

Abbott, B. P., R. Abbott, T. D. Abbott, et al. (2017). „Multi-messenger Observations of a Binary Neutron Star Merger". In: *ApJ* 848, p. L12. DOI: 10.3847/2041-8213/aa91c9.

Abdalla, H., A. Abramowski, F. Aharonian, F. Ait Benkhali, et al. (2016). „H.E.S.S. Limits on Linelike Dark Matter Signatures in the 100 GeV to 2 TeV Energy Range Close to the Galactic Center". In: *Phys. Rev. Lett.* 117 (15), p. 151302. DOI: 10.1103/PhysRevLett.117.151302.

Abdalla, H., A. Abramowski, F. Aharonian, et al. (2017). „Gamma-ray blazar spectra with H.E.S.S. II mono analysis: The case of PKS 2155–304 and PG 1553+113". In: *A&A* 600, A89. DOI: 10.1051/0004-6361/201629427.

— (2018a). „H.E.S.S. observations of RX J1713.7−3946 with improved angular and spectral resolution: Evidence for gamma-ray emission extending beyond the X-ray emitting shell". In: *A&A* 612, A6. DOI: 10.1051/0004-6361/201629790.

Abdalla, H., R. Adam, F. Aharonian, F. Ait Benkhali, et al. (2020a). „Resolving acceleration to very high energies along the jet of Centaurus A". In: *Nature* 582.7812, pp. 356–359. ISSN: 1476-4687. DOI: 10.1038/s41586-020-2354-1.

Abdalla, H., F. Aharonian, F. Ait Benkhali, et al. (2018b). „First ground-based measurement of sub-20 GeV to 100 GeV γ-Rays from the Vela pulsar with H.E.S.S. II". In: *A&A* 620, A66. DOI: 10.1051/0004-6361/201732153.

— (2020b). „Resolving the Crab pulsar wind nebula at teraelectronvolt energies". In: *Nat. Astron.* 4, pp. 167–173. DOI: 10.1038/s41550-019-0910-0.

Abdo, A. A., M. Ackermann, M. Ajello, et al. (2011). „Gamma-Ray Flares from the Crab Nebula". In: *Science* 331, p. 739. DOI: 10.1126/science.1199705.

Abdo, AA, Markus Ackermann, Marco Ajello, WB Atwood, et al. (2010). „Fermi large area telescope view of the core of the radio galaxy Centaurus A". In: *The Astrophysical Journal* 719.2, p. 1433.

Abdo, AA, Marco Ajello, A Allafort, Luca Baldini, et al. (2013). „The second Fermi Large Area Telescope catalog of gamma-ray pulsars". In: *The Astrophysical Journal Supplement Series* 208.2, p. 17.

Abdollahi, S., F. Acero, M. Ackermann, et al. (2020). „Fermi Large Area Telescope Fourth Source Catalog". In: *ApJS* 247, p. 33. DOI: 10.3847/1538-4365/ab6bcb.

Abe, H., K. Abe, S. Abe, et al. (2023). „Observations of the Crab Nebula and Pulsar with the Large-sized Telescope Prototype of the Cherenkov Telescope Array". In: *ApJ* 956, p. 80. DOI: 10.3847/1538-4357/ace89d.

Abe, K., Abe, S., Abhishek, A., Acero, F., et al. (2024). „A new method of reconstructing images of gamma-ray telescopes applied to the LST-1 of CTAO". In: *A&A* 691, A328. DOI: 10.1051/0004-6361/202450889.

Abeysekara, A. U., A. Albert, R. Alfaro, et al. (2017). „Observation of the Crab Nebula with the HAWC Gamma-Ray Observatory". In: *ApJ* 843, p. 39. DOI: 10.3847/1538-4357/aa7555.

— (2019). „Measurement of the Crab Nebula Spectrum Past 100 TeV with HAWC". In: *ApJ* 881, p. 134. DOI: 10.3847/1538-4357/ab2f7d.

— (2020). „Multiple Galactic Sources with Emission Above 56 TeV Detected by HAWC". In: *PRL* 124, p. 021102. DOI: 10.1103/PhysRevLett.124.021102.

Abeysekara, Anushka Udara, Andrea Albert, R Alfaro, C Alvarez, et al. (2023). „The high-altitude water cherenkov (HAWC) observatory in méxico: The primary detector". In: *Nuclear Instruments and Methods in Physics Research Section A: Accelerators, Spectrometers, Detectors and Associated Equipment* 1052, p. 168253.

Abramowski, A., F. Acero, F. Aharonian, et al. (2010). „VHE γ-ray emission of PKS 2155–304: spectral and temporal variability". In: *A&A* 520, A83. DOI: 10.1051/0004-6361/201014484.

Abramowski, A., F. Acero, F. Aharonian, et al. (2012a). „Discovery of extended VHE γ-ray emission from the vicinity of the young massive stellar cluster Westerlund 1“. In: *A&A* 537, A114. DOI: 10.1051/0004-6361/201117928.

— (2012b). „Probing the extent of the non-thermal emission from the Vela X region at TeV energies with H.E.S.S. “ In: *A&A* 548, A38. DOI: 10.1051/0004-6361/201219919.

Abramowski, A, Fabio Acero, F Aharonian, AG Akhperjanian, et al. (2013). „Measurement of the extragalactic background light imprint on the spectra of the brightest blazars observed with HESS“. In: *Astronomy & Astrophysics* 550, A4.

Abu-Zayyad, T., R. Aida, M. Allen, R. Anderson, et al. (2012). „The surface detector array of the Telescope Array experiment“. In: *Nuclear Instruments and Methods in Physics Research Section A: Accelerators, Spectrometers, Detectors and Associated Equipment* 689, pp. 87–97. ISSN: 0168-9002. DOI: https://doi.org/10.1016/j.nima.2012.05.079.

Acciari, V. A., S. Ansoldi, L. A. Antonelli, et al. (2020). „MAGIC very large zenith angle observations of the Crab Nebula up to 100 TeV“. In: *A&A* 635, A158. DOI: 10.1051/0004-6361/201936899.

Acero, F., M. Ackermann, M. Ajello, A. Albert, et al. (Apr. 2016). „Development of the Model of Galactic Interstellar Emission for Standard Point-Source Analysis of Fermi Large Area Telescope Data“. In: *The Astrophysical Journal Supplement Series* 223.2, p. 26. ISSN: 1538-4365. DOI: 10.3847/0067-0049/223/2/26.

Acharya, B. A., I. Agudo, I. Al Samarai, et al. (2018). *Science with the Cherenkov Telescope Array*. World Scientific Publishing. DOI: 10.1142/10986.

Ackermann, M., M. Ajello, A. Allafort, et al. (2012a). „In-flight measurement of the absolute energy scale of the Fermi Large Area Telescope“. In: *Astropart. Phys.* 35, pp. 346–353. DOI: 10.1016/j.astropartphys.2011.10.007.

Ackermann, M., M. Ajello, L. Baldini, et al. (2018). „The Search for Spatial Extension in High-latitude Sources Detected by the Fermi Large Area Telescope“. In: *ApJS* 237, p. 32. DOI: 10.3847/1538-4365/aacdf7.

Ackermann, Markus, Marco Ajello, Andrea Albert, A Allafort, et al. (2012b). „The Fermi large area telescope on orbit: event classification, instrument response functions, and calibration“. In: *The Astrophysical Journal Supplement Series* 203.1, p. 4.

Ackermann, Markus, Marco Ajello, WB Atwood, Luca Baldini, et al. (2012c). „Fermi-LAT observations of the diffuse γ-ray emission: implications for cosmic rays and the interstellar medium“. In: *The Astrophysical Journal* 750.1, p. 3.

Adrián-Martínez, S., M. Ageron, F. Aharonian, et al. (2014). „Deep sea tests of a prototype of the KM3NeT digital optical module“. In: *Eur. Phys. J. C* 74, p. 3056. DOI: 10.1140/epjc/s10052-014-3056-3.

— (2016a). „Letter of intent for KM3NeT 2.0“. In: *J. Phys. G Nucl. Part.* 43, p. 084001.

— (2016b). „The prototype detection unit of the KM3NeT detector“. In: *Eur. Phys. J. C* 76, p. 54. DOI: 10.1140/epjc/s10052-015-3868-9.

Agostini, Matteo, Michael Böhmer, Jeff Bosma, Kenneth Clark, et al. (2020). „The pacific ocean neutrino experiment“. In: *Nature Astronomy* 4.10, pp. 913–915.

Aguilar, Juan A, P Allison, JJ Beatty, Hans Bernhoff, et al. (2021). „Design and sensitivity of the Radio Neutrino Observatory in Greenland (RNO-G)“. In: *Journal of Instrumentation* 16.03, P03025.

Aharonian, F., F. Ait Benkhali, E. O. Angüner, et al. (2022a). „Time-resolved hadronic particle acceleration in the recurrent nova RS Ophiuchi“. In: *Science* 376.6588, pp. 77–80. DOI: 10.1126/science.abn0567.

Aharonian, F., A. Akhperjanian, M. Beilicke, et al. (2004). „The Crab Nebula and Pulsar between 500 GeV and 80 TeV: Observations with the HEGRA Stereoscopic Air Cerenkov Telescopes“. In: *ApJ* 614, p. 897. DOI: 10.1086/423931.

Aharonian, F., A. G. Akhperjanian, G. Anton, et al. (2009a). „Detection of very high energy radiation from HESS J1908+063 confirms the Milagro unidentified source MGRO J1908+06“. In: *A&A* 499, pp. 723–728. DOI: 10.1051/0004-6361/200811357.

Aharonian, F., A. G. Akhperjanian, A. R. Bazer-Bachi, et al. (2006). „Observations of the Crab nebula with HESS“. In: *A&A* 457, pp. 899–915. DOI: 10.1051/0004-6361:20065351.

Aharonian, F, AG Akhperjanian, G Anton, U Barres De Almeida, et al. (2009b). „Discovery of very high energy γ-ray emission from Centaurus A with HESS“. In: *The astrophysical journal* 695.1, p. L40.

Aharonian, F., Q. An, Axigeku, et al. (2021). „Observation of the Crab Nebula with LHAASO-KM2A – a performance study“. In: *Chinese Phys. C* 45, p. 025002. DOI: 10.1088/1674-1137/abd01b.

Aharonian, F., H. Ashkar, M. Backes, et al. (2022b). „A deep spectromorphological study of the γ-ray emission surrounding the young massive stellar cluster Westerlund 1“. In: *A&A* 666, A124. DOI: 10.1051/0004-6361/202244323.

Aharonian, F, F Ait Benkhali, J Aschersleben, H Ashkar, et al. (2024). „Spectrum and extension of the inverse-Compton emission of the Crab Nebula from a combined Fermi-LAT and HESS analysis“. In: *Astronomy & Astrophysics* 686, A308. DOI: 10.1051/0004-6361/202348651.

Aharonian, F, J Buckley, T Kifune, and G Sinnis (2008). „High energy astrophysics with ground-based gamma ray detectors“. In: *Reports on Progress in Physics* 71.9, p. 096901. DOI: 10.1088/0034-4885/71/9/096901.

Aharonian, F., R. Yang, and E. de Oña Wilhelmi (2019). „Massive stars as major factories of Galactic cosmic rays“. In: *Nat. Astron.* 3, pp. 561–567. DOI: 10.1038/s41550-019-0724-0.

Aharonian, F. A., A. G. Akhperjanian, J. A. Barrio, et al. (2000). „Optimizing the angular resolution of the HEGRA telescope system to study the emission region of VHE gamma rays in the Crab Nebula“. In: *A&A* 361, pp. 1073–1078.

Aharonian, F. A., S. R. Kelner, and A. Yu. Prosekin (2010). „Angular, spectral, and time distributions of highest energy protons and associated secondary gamma rays and neutrinos propagating through extragalactic magnetic and radiation fields“. In: *PRD* 82, p. 043002. DOI: 10.1103/PhysRevD.82.043002.

Aharonian, Felix A (2004). *Very high energy cosmic gamma radiation: a crucial window on the extreme Universe*. World Scientific.

Ahlers, Markus and Francis Halzen (2017). „IceCube: Neutrinos and multimessenger astronomy“. In: *Prog. Theor. Exp. Phys.* 2017, 12A105. DOI: 10.1093/ptep/ptx021.

— (2018). „Opening a new window onto the universe with IceCube“. In: *Prog. Part. Nucl. Phys.* 102, pp. 73–88. DOI: 10.1016/j.ppnp.2018.05.001.

Aiello, S., S. E. Akrame, F. Ameli, et al. (2019). „Sensitivity of the KM3NeT/ARCA neutrino telescope to point-like neutrino sources“. In: *Astropart. Phys.* 111, pp. 100–110. DOI: 10.1016/j.astropartphys.2019.04.002.

Aiello, S., A. Albert, M. Alshamsi, et al. (2022a). „The KM3NeT multi-PMT optical module“. In: *J. Instrum.* 17, P07038. DOI: 10.1088/1748-0221/17/07/P07038.

Aiello, S., A. Albert, S. Alves Garre, et al. (2020). „gSeaGen: The KM3NeT GENIE-based code for neutrino telescopes“. In: *Comput. Phys. Commun.* 256, p. 107477. DOI: 10.1016/j.cpc.2020.107477.

— (2022b). „Determining the neutrino mass ordering and oscillation parameters with KM3NeT/ORCA“. In: *Eur. Phys. J. C* 82, p. 26. DOI: 10.1140/epjc/s10052-021-09893-0.

Ajello, M., W. B. Atwood, L. Baldini, et al. (2022). „A gamma-ray pulsar timing array constrains the nanohertz gravitational wave background“. In: *Science* 376, p. 521. DOI: 10.1126/science.abm32.

Akaike, H. (1974). „A new look at the statistical model identification“. In: *IEEE Trans. Automat. Contr.* 19, pp. 716–723. DOI: 10.1109/TAC.1974.1100705.

Albert, A., R. Alfaro, J. C. Arteaga-Velázquez, et al. (2022). „Validation of standardized data formats and tools for ground-level particle-based gamma-ray observatories“. In: *A&A* 667, A36. DOI: 10.1051/0004-6361/202243527.

Albert, A., M. André, M. Anghinolfi, et al. (2021). „Monte Carlo simulations for the ANTARES underwater neutrino telescope“. In: *JCAP* 01, p. 064. DOI: 10.1088/1475-7516/2021/01/064.

Albert, J., E. Aliu, H. Anderhub, et al. (2008). „VHE γ-Ray Observation of the Crab Nebula and its Pulsar with the MAGIC Telescope“. In: *ApJ* 674, p. 1037. DOI: 10.1086/525270.

Aleksić, J., S. Ansoldi, L. A. Antonelli, et al. (2015). „Measurement of the Crab Nebula spectrum over three decades in energy with the MAGIC telescopes“. In: *JHEAp* 5–6, pp. 30–38. DOI: 10.1016/j.jheap.2015.01.002.

Aleksić, Jelena, EA Alvarez, LA t Antonelli, P Antoranz, et al. (2011). „Observations of the Crab Pulsar between 25 and 100 GeV with the MAGIC I Telescope“. In: *The Astrophysical Journal* 742.1, p. 43.

Aleksić, J., S. Ansoldi, L.A. Antonelli, P. Antoranz, et al. (2016). „The major upgrade of the MAGIC telescopes, Part I: The hardware improvements and the commissioning of the system“. In: *Astroparticle Physics* 72, pp. 61–75. ISSN: 0927-6505. DOI: https://doi.org/10.1016/j.astropartphys.2015.04.004.

Alfvén, Hannes (1942). „Existence of electromagnetic-hydrodynamic waves“. In: *Nature* 150.3805, pp. 405–406.

Aliu, E., H. Anderhub, L. A. Antonelli, P. Antoranz, M. Backes, et al. (Jan. 2009). „Improving the performance of the single-dish Cherenkov telescope MAGIC through the use of signal timing“. In: *Astropart. Phys.* 30.6, pp. 293–305. DOI: 10.1016/j.astropartphys.2008.10.003.

Aliu, Ester, H Anderhub, LA t Antonelli, P Antoranz, et al. (2008). „Observation of pulsed γ-Rays above 25 GeV from the Crab Pulsar with MAGIC“. In: *Science* 322.5905, pp. 1221–1224.

Alonso, M. Fernández, A. D. Supanitsky, and A. C. Rovero (2018). „Probing the IGMF with the Next Generation of Cherenkov Telescopes“. In: *The Astrophysical Journal* 869.1, p. 43. DOI: 10.3847/1538-4357/aae976.

Amato, E. and B. Olmi (2021a). „The Crab Pulsar and Nebula as Seen in Gamma-Rays“. In: *Universe* 7, p. 448. DOI: 10.3390/universe7110448.

Amato, Elena and Sabrina Casanova (2021). „On particle acceleration and transport in plasmas in the Galaxy: theory and observations“. In: *Journal of Plasma Physics* 87.1, p. 845870101.

Amato, Elena and Barbara Olmi (2021b). „The Crab Pulsar and Nebula as seen in gamma-rays“. In: *Universe* 7.11, p. 448.

Ambrogi, L., S. Celli, and F. Aharonian (2018). „On the potential of Cherenkov Telescope Arrays and KM3 Neutrino Telescopes for the detection of extended sources“. In: *Astropart. Phys.* 100, pp. 69–79. DOI: 10.1016/j.astropartphys.2018.03.001.

Amenomori, M., Y. W. Bao, X. J. Bi, et al. (2019). „First Detection of Photons with Energy beyond 100 TeV from an Astrophysical Source“. In: *PRL* 123, p. 051101. DOI: 10.1103/PhysRevLett.123.051101.

Andreopoulos, C., A. Bell, D. Bhattacharya, F. Cavanna, et al. (2010). „The GENIE neutrino Monte Carlo generator“. In: *Nucl. Instrum. Methods Phys. Res. A* 614, pp. 87–104. DOI: 10.1016/j.nima.2009.12.009.

Ansoldi, S., L. A. Antonelli, P. Antoranz, et al. (2016). „Teraelectronvolt pulsed emission from the Crab Pulsar detected by MAGIC“. In: *A&A* 585, A133. DOI: 10.1051/0004-6361/201526853.

Antonucci, Robert (1993). „Unified models for active galactic nuclei and quasars“. In: *In: Annual review of astronomy and astrophysics. Vol. 31 (A94-12726 02-90), p. 473-521.* 31, pp. 473–521.

Arons, J. (1998). „On the coupling of rotation powered pulsars to plerionic nebulae.“ In: *Mem. Soc. Ast. Ital.* 69, pp. 989–1007.

Astropy Collaboration (2013). „Astropy: A community Python package for astronomy“. In: *A&A* 558, A33. DOI: 10.1051/0004-6361/201322068.

— (2018). „The Astropy Project: Building an Open-science Project and Status of the v2.0 Core Package“. In: *AJ* 156, p. 123. DOI: 10.3847/1538-3881/aabc4f.

— (2022). „The Astropy Project: Sustaining and Growing a Community-oriented Open-source Project and the Latest Major Release (v5.0) of the Core Package“. In: *ApJ* 935, p. 167. DOI: 10.3847/1538-4357/ac7c74.

Atoyan, A. M. (1999). „Radio spectrum of the Crab nebula as an evidence for fast initial spin of its pulsar“. In: *A&A* 346, pp. L49–L52.

Atoyan, A. M. and F. A. Aharonian (1996). „On the mechanisms of gamma radiation in the Crab Nebula“. In: *MNRAS* 278, pp. 525–541. DOI: 10.1093/mnras/278.2.525.

Atwood, W., A. Albert, L. Baldini, et al. (2013). „Pass 8: Toward the Full Realization of the Fermi-LAT Scientific Potential“. In: *arXiv e-prints*.

Atwood, W. B., A. A. Abdo, M. Ackermann, et al. (2009). „The Large Area Telescope on the Fermi Gamma-Ray Space Telescope Mission“. In: *ApJ* 697, pp. 1071–1102. DOI: 10.1088/0004-637X/697/2/1071.

Ballet, J., P. Bruel, T. H. Burnett, B. Lott, and The Fermi-LAT collaboration (2024). *Fermi Large Area Telescope Fourth Source Catalog Data Release 4 (4FGL-DR4)*. URL: https://arxiv.org/abs/2307.12546.

Banik, Prabir (2024). „Studying the role of supernova remnants as cosmic ray PeVatron with LHAASO observations“. In: *Journal of High Energy Astrophysics* 43, pp. 61–65. ISSN: 2214-4048. DOI: https://doi.org/10.1016/j.jheap.2024.06.008.

Becherini, Y., A. Margiotta, M. Sioli, and M. Spurio (2006). „A parameterisation of single and multiple muons in the deep water or ice“. In: *Astropart. Phys.* 25, pp. 1–13. DOI: 10.1016/j.astropartphys.2005.10.005.

Bednarek, W. (2003). „Neutrinos from the pulsar wind nebulae“. In: *A&A* 407, pp. 1–6. DOI: 10.1051/0004-6361:20030929.

Bell, AR (1978). „The acceleration of cosmic rays in shock fronts–I“. In: *Monthly Notices of the Royal Astronomical Society* 182.2, pp. 147–156.

Bell, AR and SG Lucek (2001). „Cosmic ray acceleration to very high energy through the non-linear amplification by cosmic rays of the seed magnetic field“. In: *Monthly Notices of the Royal Astronomical Society* 321.3, pp. 433–438.

Berge, D., S. Funk, and J. Hinton (2007). „Background modelling in very-high-energy γ-ray astronomy“. In: *A&A* 466, pp. 1219–1229. DOI: 10.1051/0004-6361:20066674.

Berger, James O. (1980). *Statistical Decision Theory: Foundations, Concepts, and Methods*. New York: Springer. DOI: 10.1007/978-1-4757-1727-3.

Bernlöhr, K. (2008). „Simulation of imaging atmospheric Cherenkov telescopes with CORSIKA and sim-telarray“. In: *Astropart. Phys.* 30, pp. 149–158. DOI: 10.1016/j.astropartphys.2008.07.009.

Bi, Baiyang, Miquel Barcelo, Christian W. Bauer, et al. (2021). „Performance of the new FlashCam-based camera in the 28m telescope of H.E.S.S.“ In: *Proc. 37th Int. Cosmic Ray Conf. — PoS(ICRC2021)*. Vol. 395, p. 743. DOI: 10.22323/1.395.0743.

Biermann, Peter L and Vitor De Souza (2012). „Centaurus A: The extragalactic source of cosmic rays with energies above the knee“. In: *The Astrophysical Journal* 746.1, p. 72.

Biteau, Jonathan and Manuel Meyer (2022). „Gamma-Ray Cosmology and Tests of Fundamental Physics“. In: *Galaxies* 10.2. ISSN: 2075-4434. DOI: 10.3390/galaxies10020039.

Blumenthal, George R. and Robert J. Gould (1970). „Bremsstrahlung, Synchrotron Radiation, and Compton Scattering of High-Energy Electrons Traversing Dilute Gases“. In: *Rev. Mod. Phys.* 42, pp. 237–271. DOI: 10.1103/RevModPhys.42.237.

Bogovalov, SV and DV Khangoulyan (2002). „The Crab Nebula: interpretation of chandra observations“. In: *Astronomy Letters* 28, pp. 373–385.

Bose, D, VR Chitnis, P Majumdar, and A Shukla (2022). „Galactic and extragalactic sources of very high energy gamma rays“. In: *The European Physical Journal Special Topics* 231.1, pp. 27–66.

Braun, Isabel (2007). „Improving the Pointing Precision of the H.E.S.S. Experiment“. PhD thesis. Ruprecht-Karls-Universität Heidelberg. DOI: 10.11588/heidok.00007354. URL: https://archiv.ub.uni-heidelberg.de/volltextserver/7354/.

Bucciantini, N., R. Bandiera, B. Olmi, and L. Del Zanna (2017). „Modeling the effect of small-scale magnetic turbulence on the X-ray properties of Pulsar Wind Nebulae“. In: *MNRAS* 470, pp. 4066–4074. DOI: 10.1093/mnras/stx993.

Buehler, R. and R. Blandford (2014). „The surprising Crab pulsar and its nebula: a review“. In: *Rep. Prog. Phys.* 77, p. 066901. DOI: 10.1088/0034-4885/77/6/066901.

Buehler, R., J. D. Scargle, R. D. Blandford, L. Baldini, et al. (2012). „Gamma-Ray Activity in the Crab Nebula: The Exceptional Flare of 2011 April“. In: *ApJ* 749, p. 26. DOI: 10.1088/0004-637X/749/1/26.

Bykov, Andrei M, Alexandre Marcowith, Elena Amato, Maria E Kalyashova, et al. (2020). „High-energy particles and radiation in star-forming regions“. In: *Space Science Reviews* 216, pp. 1–37.

Cao, Z., F. Aharonian, Q. An, et al. (2021a). „Peta–electron volt gamma-ray emission from the Crab Nebula“. In: *Science* 373, pp. 425–430. DOI: 10.1126/science.abg5137.

Cao, Z., F. A. Aharonian, Q. An, et al. (2021b). „Ultrahigh-energy photons up to 1.4 petaelectronvolts from 12 γ-ray Galactic sources“. In: *Nature* 594, pp. 33–36. DOI: 10.1038/s41586-021-03498-z.

Cardillo, Martina, Elena Amato, and Pasquale Blasi (2015). „On the cosmic ray spectrum from type II supernovae expanding in their red giant presupernova wind“. In: *Astroparticle Physics* 69, pp. 1–10.

Carminati, G., M. Bazzotti, A. Margiotta, and M. Spurio (2008). „Atmospheric MUons from PArametric formulas: a fast GEnerator for neutrino telescopes (MUPAGE)“. In: *Comput. Phys. Commun.* 179, pp. 915–923. DOI: 10.1016/j.cpc.2008.07.014.

Cash, W. (1979). „Parameter estimation in astronomy through application of the likelihood ratio“. In: *ApJ* 228, pp. 939–947. DOI: 10.1086/156922.

Cavallo, G (1978). „On the sources of ultra-high energy cosmic rays“. In: *Astronomy and Astrophysics, vol. 65, no. 3, May 1978, p. 415-419.* 65, pp. 415–419.

Ćelić, Jelena, Rodrigo Guedes Lang, Simon Steinmassl, Jim Hinton, and Stefan Funk (2025). „A novel approach of optimizing the image cleaning performance of Imaging Atmospheric Cherenkov Telescopes: Application to a time-based cleaning for HESS“. In: *arXiv preprint arXiv:2503.22361.*

Celli, S., A. Palladino, and F. Vissani (2017). „Neutrinos and γ-rays from the Galactic Center Region after H.E.S.S. multi-TeV measurements“. In: *Eur. Phys. J. C* 77, p. 66. DOI: 10.1140/epjc/s10052-017-4635-x.

Chen, Tianqi and Carlos Guestrin (2016). „Xgboost: A scalable tree boosting system“. In: *Proceedings of the 22nd ACM SIGKDD International Conference on Knowledge Discovery and Data Mining*, pp. 785–794. DOI: 10.1145/2939672.293978.

Cherenkov Telescope Array Observatory and Cherenkov Telescope Array Consortium (Sept. 2021). *CTAO Instrument Response Functions - prod5 version v0.1.* Version v0.1. DOI: 10.5281/zenodo.5499840. URL: https://doi.org/10.5281/zenodo.5499840.

Chianese, Marco, Damiano F.G. Fiorillo, Rasmi Hajjar, Gennaro Miele, and Ninetta Saviano (2021). „Constraints on heavy decaying dark matter with current gamma-ray measurements“. In: *Journal of Cosmology and Astroparticle Physics* 2021.11, p. 035. DOI: 10.1088/1475-7516/2021/11/035.

Clark, C. J., H. J. Pletsch, J. Wu, L. Guillemot, et al. (2015). „PSR J1906+0722: AN ELUSIVE GAMMA-RAY PULSAR". In: *The Astrophysical Journal Letters* 809.1, p. L2. DOI: 10.1088/2041-8205/809/1/L2.

Clark, J. S., I. Negueruela, P.A. Crowther, and S. P. Goodwin (2005). „On the massive stellar population of the super star cluster Westerlund 1". In: *A&A* 434, pp. 949–969. DOI: 10.1051/0004-6361:20042413.

Conceição, Ruben (2023). *The Southern Wide-field Gamma-ray Observatory.* URL: https://arxiv.org/abs/2309.04577.

Cowan, Glen, Kyle Cranmer, Eilam Gross, and Ofer Vitells (2011). „Asymptotic formulae for likelihood-based tests of new physics". In: *Eur. Phys. J. C* 71, p. 1554.

Cristofari, P., V. Niro, and S. Gabici (2021). „Gamma-rays and neutrinos from RX J1713–3946 in a lepto–hadronic scenario". In: *MNRAS* 508, pp. 2204–2209. DOI: 10.1093/mnras/stab2380.

CTAO & CTAC (2021). *CTAO Instrument Response Functions - prod5 version v0.1.* Version v0.1. DOI: 10.5281/zenodo.5499840.

Daum, A., G. Hermann, M. Heß, W. Hofmann, et al. (1997). „First results on the performance of the HEGRA IACT array". In: *Astroparticle Physics* 8.1, pp. 1–11. ISSN: 0927-6505. DOI: https://doi.org/10.1016/S0927-6505(97)00031-5.

de Jager, O. C. and A. K. Harding (1992). „The Expected High-Energy to Ultra–High-Energy Gamma-Ray Spectrum of the Crab Nebula". In: *ApJ* 396, p. 161. DOI: 10.1086/171706.

Deil, C., A. Donath, R. Terrier, et al. (2020). „gammapy/gammapy: v0.17". In: *Zenodo.* DOI: 10.5281/zenodo.4701492.

Deil, C., R. Zanin, J. Lefaucheur, et al. (2017). „Gammapy - A prototype for the CTA science tools". In: *Proc. 35th Int. Cosmic Ray Conf.* ICRC2017, 766, p. 766.

Deil, Christoph, Axel Donath, Régis Terrier, et al. (2020). *gammapy/gammapy: v.0.18.2.* Zenodo. Version v0.18.2. DOI: 10.5281/zenodo.4701500.

Deil, Christoph, Matthew Wood, Tarek Hassan, et al. (2022). *Data formats for gamma-ray astronomy - version 0.3.* DOI: 10.5281/zenodo.7304668.

Dermer, Charles D and Govind Menon (2009). *High energy radiation from black holes: gamma rays, cosmic rays, and neutrinos.* Princeton University Press.

Dirson, L. and D. Horns (2023). „Phenomenological modelling of the Crab Nebula's broadband energy spectrum and its apparent extension". In: *A&A* 671, A67. DOI: 10.1051/0004-6361/202243578.

Dominguez, Alberto, Joel R Primack, DJ Rosario, F Prada, et al. (2011). „Extragalactic background light inferred from AEGIS galaxy-SED-type fractions". In: *Monthly Notices of the Royal Astronomical Society* 410.4, pp. 2556–2578.

Donath, Axel, Régis Terrier, Quentin Remy, Atreyee Sinha, et al. (2023). „Gammapy: A Python package for gamma-ray astronomy". In: *A&A* 678, A157. DOI: 10.1051/0004-6361/202346488.

D'Amico, Giacomo, Tomislav Terzić, Jelena Strišković, Michele Doro, et al. (2021). „Signal estimation in on/off measurements including event-by-event variables". In: *Physical Review D* 103.12, p. 123001.

Eldik, Christopher van, Markus Holler, David Berge, Dmitry Zaborov, et al. (2016). „Observations of the Crab Nebula with H.E.S.S. phase II ". In: *PoS* ICRC2015, p. 847. DOI: 10.22323/1.236.0847.

Enberg, R., M. H. Reno, and I. Sarcevic (2008). „Prompt neutrino fluxes from atmospheric charm". In: *PRD* 78, p. 043005. DOI: 10.1103/PhysRevD.78.043005.

Evans, Lyndon (2011). „The large hadron collider". In: *Annual review of nuclear and particle science* 61.1, pp. 435–466.

Evoli, Carmelo (Jan. 2025). *The Cosmic-Ray Energy Spectrum.* DOI: 10.5281/zenodo.14635074. URL: https://doi.org/10.5281/zenodo.14635074.

Fermi, Enrico (1949). „On the origin of the cosmic radiation". In: *Physical review* 75.8, p. 1169.

Fomin, V. P., A. A. Stepanian, R. C. Lamb, D. A. Lewis, et al. (1994). „New methods of atmospheric Cherenkov imaging for gamma-ray astronomy. I. The false source method". In: *Astropart. Phys.* 2, pp. 137–150. DOI: 10.1016/0927-6505(94)90036-1.

Fraija, Nissim (2014). „Gamma-ray fluxes from the core emission of Centaurus A: A puzzle solved". In: *Monthly Notices of the Royal Astronomical Society* 441.2, pp. 1209–1216.

Fruck, Christian (2015). „The Galactic Center resolved with MAGIC and a new technique for Atmospheric Calibration". PhD thesis. Technische Universität München.

Fukui, Y., H. Sano, Y. Yamane, T. Hayakawa, et al. (2021). „Pursuing the Origin of the Gamma Rays in RX J1713.7−3946 Quantifying the Hadronic and Leptonic Components". In: *ApJ* 915, p. 84. DOI: 10.3847/1538-4357/abff4a.

Funk, Stefan (2015). „Ground- and Space-Based Gamma-Ray Astronomy“. In: *Annual Review of Nuclear and Particle Science* 65.1, 245–277. DOI: 10.1146/annurev-nucl-102014-022036.

Gaisser, T. K. (2012). „Spectrum of cosmic-ray nucleons, kaon production, and the atmospheric muon charge ratio“. In: *Astropart. Phys.* 35, pp. 801–806. DOI: 10.1016/j.astropartphys.2012.02.010.

Giacinti, G, AMW Mitchell, R López-Coto, V Joshi, et al. (2020). „Halo fraction in TeV-bright pulsar wind nebulae“. In: *Astronomy & Astrophysics* 636, A113.

Giustini, Margherita and Daniel Proga (2019). „A global view of the inner accretion and ejection flow around super massive black holes-Radiation-driven accretion disk winds in a physical context“. In: *Astronomy & Astrophysics* 630, A94.

Glombitza, J., V. Joshi, B. Bruno, and S. Funk (2023). „Application of graph networks to background rejection in Imaging Air Cherenkov Telescopes“. In: *JCAP* 11.11, p. 008. DOI: 10.1088/1475-7516/2023/11/008.

Gonzalez-Garcia, M. C., F. Halzen, and V. Niro (2014). „Reevaluation of the prospect of observing neutrinos from Galactic sources in the light of recent results in gamma ray and neutrino astronomy“. In: *Astropart. Phys.* 57–58, pp. 39–48. DOI: 10.1016/j.astropartphys.2014.04.001.

Gossan, S. E., E. D. Hall, and S. M. Nissanke (2022). „Optimizing the Third Generation of Gravitational-wave Observatories for Galactic Astrophysics“. In: *ApJ* 926, p. 231. DOI: 10.3847/1538-4357/ac4164.

Hahn, J., R. de los Reyes, K. Bernlöhr, P. Krüger, et al. (2014). „Impact of aerosols and adverse atmospheric conditions on the data quality for spectral analysis of the H.E.S.S. telescopes“. In: *Astropart. Phys.* 54, pp. 25–32. DOI: 10.1016/j.astropartphys.2013.10.003.

Halzen, F. (2013). „Pionic photons and neutrinos from cosmic ray accelerators“. In: *Astropart. Phys.* 43, pp. 155–162. DOI: 10.1016/j.astropartphys.2011.10.003.

Halzen, F., A. Kheirandish, and V. Niro (2017). „Prospects for detecting galactic sources of cosmic neutrinos with IceCube: An update“. In: *Astropart. Phys.* 86, pp. 46–56. DOI: 10.1016/j.astropartphys.2016.11.004.

Härer, Lucia K, Brian Reville, Jim Hinton, Lars Mohrmann, and Thibault Vieu (2023). „Understanding the TeV γ-ray emission surrounding the young massive star cluster Westerlund 1“. In: *Astronomy & Astrophysics* 671, A4.

Harris, C. R., K. J. Millman, S. J. van der Walt, et al. (2020). „Array programming with NumPy“. In: *Nature* 585, pp. 357–362. DOI: 10.1038/s41586-020-2649-2.

Harris, Gretchen L. H., Marina Rejkuba, and William E. Harris (2010). „The Distance to NGC 5128 (Centaurus A)“. In: *Publications of the Astronomical Society of Australia* 27.4, 457–462. DOI: 10.1071/AS09061.

Haubner, Konstantin, Manami Sasaki, Alison Mitchell, Gabriele Ponti, et al. (2025). „eROSITA X-ray Analysis of the PeVatron Candidate Westerlund 1“. In: *arXiv preprint arXiv:2501.12990*.

Heck, Dieter, Johannes Knapp, JN Capdevielle, G Schatz, T Thouw, et al. (1998). *CORSIKA: A Monte Carlo code to simulate extensive air showers*. Tech. rep. FZKA 6019. Forschungszentrum Karlsruhe.

Hess, Victor F. (1912). „Über Beobachtungen der durchdringenden Strahlung bei sieben Freiballonfahrten“. In: *Phys. Z.* 13, pp. 1084–1091.

H.E.S.S. Collaboration, Abdalla, H., Abramowski, A., Aharonian, F., et al. (2018). „The γ-ray spectrum of the core of Centaurus A as observed with H.E.S.S. and Fermi-LAT“. In: *A&A* 619, A71. DOI: 10.1051/0004-6361/201832640.

HESS Collaboration, F Aharonian, F Ait Benkhali, J Aschersleben, et al. (2023). „Discovery of a Radiation Component from the Vela Pulsar Reaching 20 Teraelectronvolts“. In: *arXiv preprint arXiv:2310.06181*.

Hester, J. J. (2008). „The Crab Nebula: An Astrophysical Chimera“. In: *ARA&A* 46, pp. 127–155. DOI: 10.1146/annurev.astro.45.051806.110608.

Hillas, A. M., C. W. Akerlof, S. D. Biller, J. H. Buckley, et al. (1998). „The Spectrum of Teravolt Gamma Rays from the Crab Nebula“. In: *ApJ* 503, pp. 744–759. DOI: 10.1086/306005.

Hillas, A Michael (1985). „Cerenkov light images of EAS produced by primary gamma“. In: *19th Intern. Cosmic Ray Conf-Vol. 3.* OG-9.5-3.

Hillas, Anthony M (1984). „The origin of ultra-high-energy cosmic rays“. In: *Annual review of astronomy and astrophysics. Volume 22. Palo Alto, CA, Annual Reviews, Inc., 1984, p. 425-444.* 22, pp. 425–444.

Hobbs, G. B., R. T. Edwards, and R. N. Manchester (June 2006). „TEMPO2, a new pulsar-timing package - I. An overview“. In: *MNRAS* 369.2, pp. 655–672. DOI: 10.1111/j.1365-2966.2006.10302.x.

Hofmann, W (Nov. 1999). „Comparison of techniques to reconstruct VHE gamma-ray showers from multiple stereoscopic Cherenkov images“. In: *Astropart. Phys.* 12.3, 135–143. ISSN: 0927-6505. DOI: 10.1016/s0927-6505(99)00084-5.

Hofmann, Werner and Roberta Zanin (2023). „The Cherenkov Telescope Array“. In: *arXiv e-prints.*

Holch, Tim Lukas, Idan Shilon, Matthias Büchele, Tobias Fischer, et al. (2017). „Probing Convolutional Neural Networks for Event Reconstruction in Gamma-Ray Astronomy with Cherenkov Telescopes“. In: *PoS* ICRC2017, p. 795. DOI: 10.22323/1.301.0795.

Honda, M., T. Kajita, K. Kasahara, S. Midorikawa, and T. Sanuki (2007). „Calculation of atmospheric neutrino flux using the interaction model calibrated with atmospheric muon data“. In: *PRD* 75, p. 043006. DOI: 10.1103/PhysRevD.75.043006.

Horns, D., F. Aharonian, A. Santangelo, A. I. D. Hoffmann, and C. Masterson (2006). „Nucleonic gamma-ray production in Vela X“. In: *A&A* 451, pp. L51–L54. DOI: 10.1051/0004-6361:20065116.

Huang, Zhi-Qiu, Brian Reville, John G Kirk, and Gwenael Giacinti (2023). „Prospects for ultra-high-energy particle acceleration at relativistic shocks“. In: *Monthly Notices of the Royal Astronomical Society* 522.4, pp. 4955–4962.

Hunter, J. D. (2007). „Matplotlib: A 2D graphics environment“. In: *Comput. Sci. Eng.* 9, pp. 90–95. DOI: 10.1109/MCSE.2007.55.

Hurley-Walker, Natasha, Joseph R Callingham, Paul J Hancock, Thomas MO Franzen, et al. (2017). „GaLactic and Extragalactic All-sky Murchison Widefield Array (GLEAM) survey–I. A low-frequency extragalactic catalogue“. In: *Monthly Notices of the Royal Astronomical Society* 464.1, pp. 1146–1167.

Israel, F.P. (1998). „Centaurus A – NGC 5128“. In: *The Astronomy and Astrophysics Review* 8, pp. 237–278. DOI: 10.1007/s001590050011.

Jourdain, E. and J. P. Roques (2020). „2003-2019 Monitoring of the Crab Emission through INTEGRAL SPI, or Vice Versa“. In: *ApJ* 899, p. 131. DOI: 10.3847/1538-4357/aba8a4.

Kafexhiu, E., F. Aharonian, A. M. Taylor, and G. S. Vila (2014). „Parametrization of gamma-ray production cross sections for pp interactions in a broad proton energy range from the kinematic threshold to PeV energies“. In: *PRD* 90, p. 123014. DOI: 10.1103/PhysRevD.90.123014.

Kappes, A., J. Hinton, C. Stegmann, and F. Aharonian (2007). „Potential Neutrino Signals from Galactic γ-Ray Sources“. In: *ApJ* 656, pp. 870–878. DOI: 10.1086/508936.

Kelner, S. R., F. A. Aharonian, and V. V. Bugayov (2006). „Energy spectra of gamma rays, electrons, and neutrinos produced at proton-proton interactions in the very high energy regime“. In: *PRD* 74, p. 034018.

Kennel, C. F. and F. V. Coroniti (1984a). „Confinement of the Crab pulsar’s wind by its supernova remnant.“ In: *ApJ* 283, pp. 694–709. DOI: 10.1086/162356.

— (1984b). „Magnetohydrodynamic model of Crab nebula radiation.“ In: *ApJ* 283, pp. 710–730. DOI: 10.1086/162357.

Kildea, J, RW Atkins, HM Badran, G Blaylock, et al. (2007). „The Whipple Observatory 10 m gamma-ray telescope, 1997–2006“. In: *Astroparticle Physics* 28.2, pp. 182–195.

Kirk, John G, Brian Reville, and Zhi-Qiu Huang (2023). „Particle acceleration at ultrarelativistic, perpendicular shock fronts“. In: *Monthly Notices of the Royal Astronomical Society* 519.1, pp. 1022–1029.

Kistler, M. D. and J. F. Beacom (2006). „Guaranteed and prospective Galactic TeV neutrino sources“. In: *PRD* 74, p. 063007. DOI: 10.1103/PhysRevD.74.063007.

Konopelko, A, M Hemberger, F Aharonian, A Daum, et al. (1999). „Performance of the stereoscopic system of the HEGRA imaging air Čerenkov telescopes: Monte Carlo simulations and observations“. In: *Astroparticle Physics* 10.4, pp. 275–289.

Kotera, Kumiko, Elena Amato, and Pasquale Blasi (2015). „The fate of ultrahigh energy nuclei in the immediate environment of young fast-rotating pulsars“. In: *Journal of Cosmology and Astroparticle Physics* 2015.08, p. 026. DOI: 10.1088/1475-7516/2015/08/026.

Lam, Siu Kwan, Antoine Pitrou, and Stanley Seibert (2015). „Numba: A llvm-based python jit compiler“. In: *Proceedings of the Second Workshop on the LLVM Compiler Infrastructure in HPC*, pp. 1–6.

Lang, Rodrigo Guedes, Humberto Martínez-Huerta, and Vitor de Souza (2019). „Improved limits on Lorentz invariance violation from astrophysical gamma-ray sources“. In: *Phys. Rev. D* 99 (4), p. 043015. DOI: 10.1103/PhysRevD.99.043015.

Leuschner, Fabian, Johannes Schäfer, Simon Steinmassl, Tim Lukas Holch, et al. (2023). „Validation of Monte Carlo Simulations for an analysis chain in H.E.S.S.“ In: *PoS* Gamma2022, p. 231. DOI: 10.22323/1.417.0231.

Liu, Ruo-Yu and Xiang-Yu Wang (2021). „Pev emission of the Crab Nebula: constraints on the proton content in pulsar wind and implications“. In: *The Astrophysical Journal* 922.2, p. 221.

Longair, Malcolm S. (2011). *High Energy Astrophysics. 3rd ed. Cambridge.* New York: Cambridge University Press. ISBN: 978-0-521-75618-1.

Luo, Jing, Scott Ransom, Paul Demorest, Paul S. Ray, et al. (2021). „PINT: A Modern Software Package for Pulsar Timing“. In: *The Astrophysical Journal* 911.1, p. 45. DOI: 10.3847/1538-4357/abe62f.

Luo, Yonggang, Maxim Lyutikov, Tea Temim, and Luca Comisso (2020). „Turbulent Model of Crab Nebula Radiation“. In: *ApJ* 896, p. 147. DOI: 10.3847/1538-4357/ab93c0.

Lyard, E, R Walter, V Sliusar, N Produit, and for the CTA Consortium (2020). „Probing Neural Networks for the Gamma/Hadron Separation of the Cherenkov Telescope Array“. In: *Journal of Physics: Conference Series* 1525.1, p. 012084. DOI: 10.1088/1742-6596/1525/1/012084.

Lyutikov, Maxim, Tea Temim, Sergey Komissarov, Patrick Slane, et al. (2019). „Interpreting Crab Nebula's synchrotron spectrum: two acceleration mechanisms“. In: *MNRAS* 489, pp. 2403–2416. DOI: 10.1093/mnras/stz2023.

Magill, Jeffrey David (2018). „Probing the Nature of Radiative Processes within Radio Galaxies using the Fermi Gamma-Ray Large Area Telescope“. PhD thesis. University of Maryland. DOI: https://doi.org/10.13016/duge-cifu. URL: http://hdl.handle.net/1903/21652.

Malyshev, Denys and Lars Mohrmann (2023). „Analysis Methods for Gamma-ray Astronomy“. In: *Handbook of X-ray and Gamma-ray Astrophysics*, 137, p. 137. DOI: 10.1007/978-981-16-4544-0_177-1.

Mascaretti, Carlo, Pasquale Blasi, and Carmelo Evoli (2020). „Atmospheric neutrinos and the knee of the cosmic ray spectrum“. In: *Astropart. Phys.* 114, pp. 22–29. DOI: 10.1016/j.astropartphys.2019.06.002.

Mattox, J. R., D. L. Bertsch, J. Chiang, et al. (1996). „The Likelihood Analysis of EGRET Data“. In: *ApJ* 461, p. 396. DOI: 10.1086/177068.

Mayall, NU and JH Oort (1942). „Further data bearing on the identification of the Crab Nebula with the supernova of 1054 AD Part II. The astronomical aspects“. In: *Publications of the Astronomical Society of the Pacific* 54.318, pp. 95–104.

Meagher, K. (2015). „Six years of VERITAS observations of the Crab Nebula“. In: *Proc. 34th Int. Cosmic Ray Conf.* 236 792. DOI: 10.22323/1.236.0792. URL: https://pos.sissa.it/236/792.

Mészáros, P., D. B. Fox, C. Hanna, and K. Murase (2019). „Multi-messenger astrophysics“. In: *Nat. Rev. Phys.* 1, pp. 585–599. DOI: 10.1038/s42254-019-0101-z.

Meyer, M., D. Horns, and H.-S. Zechlin (2010). „The Crab Nebula as a standard candle in very high-energy astrophysics“. In: *A&A* 523, A2. DOI: 10.1051/0004-6361/201014108.

Meyer, Manuel, Jeffrey D. Scargle, and Roger D. Blandford (2019). „Characterizing the Gamma-Ray Variability of the Brightest Flat Spectrum Radio Quasars Observed with the Fermi LAT“. In: *ApJ* 877, p. 39. DOI: 10.3847/1538-4357/ab1651.

Miener, Tjark, D. Nieto, R. López-Coto, J. L. Contreras, et al. (2022). „The performance of the MAGIC telescopes using deep convolutional neural networks with CTLearn“. In: *PoS* Gamma2022, p. 220. DOI: 10.22323/1.417.0220.

Mitchell, A. M. W. (2016). „Optical Efficiency Calibration for Inhomogeneous IACT Arrays and a Detailed Study of the Highly Extended Pulsar Wind Nebula HESS J1825−137“. PhD thesis. Ruperto-Carola-University Heidelberg. DOI: 10.11588/heidok.00021768.

Mitchell, AMW and J Gelfand (2022). „Pulsar Wind Nebulae“. In: *Handbook of X-ray and Gamma-ray Astrophysics.* Springer, pp. 1–52.

Mohrmann, L., A. Specovius, D. Tiziani, S. Funk, et al. (2019). „Validation of open-source science tools and background model construction in γ-ray astronomy“. In: *A&A* 632, A72. DOI: 10.1051/0004-6361/201936452.

Morlino, G., P. Blasi, E. Peretti, and P. Cristofari (July 2021). „Particle acceleration in winds of star clusters“. In: *MNRAS* 504.4, pp. 6096–6105. DOI: 10.1093/mnras/stab690.

Muller, R., A. Heijboer, A. Garcia Soto, et al. (2021). „Sensitivity estimates for diffuse, point-like and extended neutrino sources with KM3NeT/ARCA“. In: *Proc. 37th Int. Cosmic Ray Conf.* ICRC2021, 1077, p. 1077. DOI: 10.22323/1.395.1077.

Murach, Thomas, Michael Gajdus, and Robert Daniel Parsons (2015). „A Neural Network-based Reconstruction Algorithm for monoscopically detected Air Showers observed with the H.E.S.S. Experiment“. In: *Proc. 34th Int. Cosmic Ray Conf. — PoS(ICRC2015).* Vol. 236, p. 1022. DOI: 10.22323/1.236.1022.

Nakashima, Danielle Kaori (2023). „Systematic Errors of a 3D Template Background Model for IACTs and its Application to the Galactic Center“. PhD thesis. Friedrich-Alexander-Universität Erlangen-Nürnberg. URL: https://open.fau.de/handle/openfau/23856.

Naurois, M. de and L. Rolland (2009). „A high performance likelihood reconstruction of γ-rays for imaging atmospheric Cherenkov telescopes“. In: *Astropart. Phys.* 32, pp. 231–252. DOI: 10.1016/j.astropartphys.2009.09.001.

Netzer, Hagai (2015). „Revisiting the unified model of active galactic nuclei“. In: *Annual Review of Astronomy and Astrophysics* 53.1, pp. 365–408.

Neumayer, Nadine (2010). „The Supermassive Black Hole at the Heart of Centaurus A: Revealed by the Kinematics of Gas and Stars“. In: *Publications of the Astronomical Society of Australia* 27.4, 449–456. DOI: 10.1071/AS09080.

Nie, L., Y. Liu, Z. Jiang, and X. Geng (2022a). „Ultra-high-energy Gamma-Ray Radiation from the Crab Pulsar Wind Nebula“. In: *ApJ* 924, p. 42. DOI: 10.3847/1538-4357/ac348d.

Nie, Lin, Yang Liu, Zejun Jiang, and Xiongfei Geng (2022b). „Ultra-high-energy Gamma-ray radiation from the crab pulsar wind nebula“. In: *The Astrophysical Journal* 924.2, p. 42.

Nigro, C., C. Deil, R. Zanin, T. Hassan, et al. (2019). „Towards open and reproducible multi-instrument analysis in gamma-ray astronomy“. In: *A&A* 625, A10. DOI: 10.1051/0004-6361/201834938.

Ohm, S., C. van Eldik, and K. Egberts (2009). „γ/hadron separation in very-high-energy γ-ray astronomy using a multivariate analysis method“. In: *Astropart. Phys.* 31, pp. 383–391. DOI: 10.1016/j.astropartphys.2009.04.001.

Oliveira, Cainã de, Rodrigo Guedes Lang, and Pedro Batista (2025). „On Gamma Rays as Predictors of Ultra-high-energy Cosmic-Ray Flux in Active Galactic Nuclei“. In: *The Astrophysical Journal* 981.2, p. 123.

Oliveira, Cainã de and Vitor de Souza (2022). „Magnetically induced anisotropies in the arrival directions of ultra-high-energy cosmic rays from nearby radio galaxies“. In: *The Astrophysical Journal* 925.1, p. 42.

Parsons, R. D., A. M. W. Mitchell, and S. Ohm (2022). „Investigations of the systematic uncertainties in convolutional neural network based analysis of atmospheric Cherenkov telescope data“. In: *arXiv e-prints*.

Parsons, R.D. and J.A. Hinton (2014). „A Monte Carlo template based analysis for air-Cherenkov arrays“. In: *Astropart. Phys.* 56, pp. 26–34. DOI: 10.1016/j.astropartphys.2014.03.002.

Parsons, Robert Daniel and S Ohm (2020). „Background rejection in atmospheric Cherenkov telescopes using recurrent convolutional neural networks“. In: *The European Physical Journal C* 80, pp. 1–11.

Peng, Q.-Y., B.-W. Bao, F.-W. Lu, and L. Zhang (2022a). „Multiband Emission up to PeV Energy from the Crab Nebula in a Spatially Dependent Lepto-hadronic Model“. In: *ApJ* 926, p. 7. DOI: 10.3847/1538-4357/ac4161.

Peng, Qi-Yong, Bi-Wen Bao, Fang-Wu Lu, and Li Zhang (2022b). „Multiband Emission up to PeV Energy from the Crab Nebula in a Spatially Dependent Lepto-hadronic Model“. In: *The Astrophysical Journal* 926.1, p. 7.

Petropoulou, M., Lefa, E., Dimitrakoudis, S., and Mastichiadis, A. (2014). „One-zone synchrotron self-Compton model for the core emission of Centaurus A revisited“. In: *A&A* 562, A12. DOI: 10.1051/0004-6361/201322833.

Pierre Auger Collaboration (2015). „The Pierre Auger Cosmic Ray Observatory“. In: *Nuclear Instruments and Methods in Physics Research Section A: Accelerators, Spectrometers, Detectors and Associated Equipment* 798, pp. 172–213. ISSN: 0168-9002. DOI: https://doi.org/10.1016/j.nima.2015.06.058.

Pierre Auger Collaboration, A. Aab, P. Abreu, M. Aglietta, et al. (June 2017). „Multi-resolution anisotropy studies of ultrahigh-energy cosmic rays detected at the Pierre Auger Observatory“. English. In: *Journal of Cosmology and Astroparticle Physics* 2017.6. ISSN: 1475-7516. DOI: 10.1088/1475-7516/2017/06/026.

Pletsch, Holger J. and Colin J. Clark (2014). „OPTIMIZED BLIND GAMMA-RAY PULSAR SEARCHES AT FIXED COMPUTING BUDGET“. In: *The Astrophysical Journal* 795.1, p. 75. DOI: 10.1088/0004-637X/795/1/75.

Porth, Oliver, Serguei S. Komissarov, and Rony Keppens (2014). „Three-dimensional magnetohydrodynamic simulations of the Crab nebula“. In: *MNRAS* 438, pp. 278–306. DOI: 10.1093/mnras/stt2176.

Pühlhofer, G., O. Bolz, N. Götting, et al. (2003). „The technical performance of the HEGRA system of imaging air Cherenkov telescopes“. In: *Astropart. Phys.* 20, pp. 267–291. DOI: 10.1016/j.astropartphys.2003.06.001.

Pühlhofer, Gerd, Konrad Bernlöhr, Baiyang Bi, et al. (2021). „Science verification of the new FlashCam-based camera in the 28m telescope of H.E.S.S.“ In: *Proc. 37th Int. Cosmic Ray Conf. — PoS(ICRC2021).* Vol. 395, p. 764. DOI: 10.22323/1.395.0764.

Rees, M. J. and J. E. Gunn (1974). „The Origin of the Magnetic Field and Relativistic Particles in the Crab Nebula“. In: *MNRAS* 167, pp. 1–12. DOI: 10.1093/mnras/167.1.1.

Reynolds, P. T., C. W. Akerlof, M. F. Cawley, et al. (1993). „Survey of candidate gamma-ray sources at TeV energies using a high-resolution Cerenkov imaging system: 1988–1991“. In: *ApJ* 404, pp. 206–218. DOI: 10.1086/172269.

Reynolds, Stephen P (2008). „Supernova remnants at high energy“. In: *Annu. Rev. Astron. Astrophys.* 46.1, pp. 89–126.

Rozwadowska, Karolina, Francesco Vissani, and Enrico Cappellaro (2021). „On the rate of core collapse supernovae in the milky way“. In: *New Astronomy* 83, p. 101498.

Schlickeiser, Reinhard (1996). „Gamma-rays from Active Galactic Nuclei: Emission processes and particle acceleration“. In: *Space Science Reviews* 75, pp. 299–315.

Scuderi, Salvatore, Andrea Giuliani, Giovanni Pareschi, G Tosti, et al. (2022). „The astri mini-array of cherenkov telescopes at the observatorio del teide“. In: *Journal of High Energy Astrophysics* 35, pp. 52–68.

Shilon, I., M. Kraus, M. Büchele, K. Egberts, et al. (2019). „Application of deep learning methods to analysis of imaging atmospheric Cherenkov telescopes data“. In: *Astropart. Phys.* 105, pp. 44–53. DOI: 10.1016/j.astropartphys.2018.10.003.

Singh, KK, KK Yadav, and PJ Meintjes (2021). „Probing the evolution of the EBL photon density out to z 1 via γ-ray propagation measurements with Fermi“. In: *Astrophysics and Space Science* 366.6, p. 51.

Sinitsyna, Vera G and Vera Y Sinitsyna (2024). „Particle acceleration test with Cas A multiwavelength emission“. In: *Astronomische Nachrichten* 345.2-3, e240006.

Steinmaßl, Simon Felix (2023). „Probing particle acceleration in stellar binary systems using gamma-ray observations“. PhD thesis. Ruperto-Carola-University Heidelberg. DOI: 10.11588/heidok.00033375.

Streil, Katrin (2025). „A Comprehensive Study of the Galactic Centre with H.E.S.S.: Systematic Uncertainties, Diffuse Emission and WIMP Annihilation“. PhD thesis. Friedrich-Alexander-Universität Erlangen-Nürnberg.

Sudoh, Takahiro and John F. Beacom (2023). „Identifying extended PeVatron sources via neutrino shower detection“. In: *PRD* 108, p. 043016. DOI: 10.1103/PhysRevD.108.043016.

Sun, Xiao-na, Yang, Rui-zhi, Mckinley, Benjamin, and Aharonian, Felix (2016). „Giant lobes of Centaurus A as seen in radio and γ-ray images obtained with the Fermi-LAT and Planck satellites“. In: *A&A* 595, A29. DOI: 10.1051/0004-6361/201629069.

Tanada, Kazuhisa, Jun Kataoka, and Yoshiyuki Inoue (2019). „Inverse Compton scattering of starlight in the kiloparsec-scale jet in Centaurus A: the origin of excess TeV γ-ray emission“. In: *The Astrophysical Journal* 878.2, p. 139.

Tanaka, Shuta J., Kenji Toma, and Nozomu Tominaga (2018). „Confinement of the Crab Nebula with tangled magnetic field by its supernova remnant“. In: *MNRAS* 478, pp. 4622–4633. DOI: 10.1093/mnras/sty1356.

Tang, X. and R. A. Chevalier (2012). „Particle Transport in Young Pulsar Wind Nebulae“. In: *ApJ* 752, p. 83. DOI: 10.1088/0004-637X/752/2/83.

The Fermi-LAT collaboration (2019). *Galactic Interstellar Emission Model for the 4FGL Catalog Analysis.* URL: https://fermi.gsfc.nasa.gov/ssc/data/analysis/software/aux/4fgl/Galactic_Diffuse_Emission_Model_for_the_4FGL_Catalog_Analysis.pdf.

Tibaldo, L., R. Zanin, G. Faggioli, J. Ballet, et al. (2018). „Disentangling multiple high-energy emission components in the Vela X pulsar wind nebula with the Fermi Large Area Telescope“. In: *A&A* 617, A78. DOI: 10.1051/0004-6361/201833356.

Tjus, Julia Becker and Lukas Merten (2020). „Closing in on the origin of Galactic cosmic rays using multimessenger information“. In: *Physics Reports* 872, pp. 1–98.

Tokuno, H, R U Abbasi, T Abu-Zayyad, R Azuma, et al. (2008). „The Telescope Array experiment: status and prospects“. In: *Journal of Physics: Conference Series* 120.6, p. 062027. DOI: 10.1088/1742-6596/120/6/062027.

Torres, D. F., A. Cillis, J. Martín, and E. de Oña Wilhelmi (2014). „Time-dependent modeling of TeV-detected, young pulsar wind nebulae“. In: *J. High Energy Astrophys.* 1, pp. 31–62. DOI: 10.1016/j.jheap.2014.02.001.

Torres, Diego F (2017). *Modelling pulsar wind nebulae.* Vol. 446. Springer.

Ulrich, Ralf, Ralph Engel, and Michael Unger (2011). „Hadronic multiparticle production at ultrahigh energies and extensive air showers“. In: *Phys. Rev. D* 83 (5), p. 054026. DOI: 10.1103/PhysRevD.83.054026.

Unbehaun, T, L Mohrmann, S Funk, S Aiello, et al. (2024). „Prospects for combined analyses of hadronic emission from γ-ray sources in the Milky Way with CTA and KM3NeT“. In: *The European Physical Journal C* 84.2, p. 112. DOI: 10.1140/epjc/s10052-023-12279-z.

Unbehaun, Tim (2020). „Joint-instrument analyses with Gammapy“. Master's thesis. Friedrich-Alexander-Universität Erlangen-Nürnberg. URL: https://ecap.nat.fau.de/wp-content/uploads/2021/01/2020_Unbehaun_Master.pdf.

Unbehaun, Tim, Rodrigo Guedes Lang, Anita Deka Baruah, Prajath Bedur Ramesh, et al. (2025). „Improvements to monoscopic analysis for imaging atmospheric Cherenkov telescopes: Application to HESS“. In: *Astronomy & Astrophysics* 694, A162.

Unbehaun, Tim, Lars Mohrmann, Mikhail Smirnov, Jutta Schnabel, and Tamás Gál (2023). *Prospects for combined galactic source searches with CTA and KM3NeT*. Version 1.0.0. DOI: 10.5281/zenodo.8298464. URL: https://doi.org/10.5281/zenodo.8298464.

Vacanti, G., M. F. Cawley, E. Colombo, D. J. Fegan, et al. (1991). „Gamma-ray observations of the Crab Nebula at TeV energies". In: *ApJ* 377, pp. 467–479. DOI: 10.1086/170376.

van Rensburg, C., P. P. Krüger, and C. Venter (2018). „Spatially dependent modelling of pulsar wind nebula G0.9+0.1". In: *MNRAS* 477, pp. 3853–3868. DOI: 10.1093/mnras/sty826.

VERITAS collaboration, E Aliu, T Arlen, T Aune, et al. (2011). „Detection of pulsed gamma rays above 100 GeV from the Crab pulsar". In: *Science* 334.6052, pp. 69–72.

Vianello, Giacomo, Robert J Lauer, Patrick Younk, Luigi Tibaldo, et al. (2015). „The multi-mission maximum likelihood framework (3ML)". In: *arXiv preprint arXiv:1507.08343*.

Villante, F. L. and F. Vissani (2008). „How precisely can neutrino emission from supernova remnants be constrained by gamma ray observations?" In: *PRD* 78, p. 103007. DOI: 10.1103/PhysRevD.78.103007.

Vink, Jacco (2020). *Physics and evolution of supernova remnants*. Springer. URL: https://doi.org/10.1007/978-3-030-55231-2.

Virtanen, P., R. Gommers, T. E. Oliphant, et al. (2020). „SciPy 1.0: Fundamental Algorithms for Scientific Computing in Python". In: *Nature Methods* 17, pp. 261–272. DOI: 10.1038/s41592-019-0686-2.

Vissani, F. (2006). „Neutrinos from galactic sources of cosmic rays with known γ-ray spectra". In: *Astropart. Phys.* 26, pp. 310–313. DOI: 10.1016/j.astropartphys.2006.07.005.

Voigt, Tobias (2014). „Threshold optimization and variable construction for classification in the MAGIC and FACT experiments". PhD thesis. Technische Universität Dortmund. DOI: 10.17877/DE290R-14114.

Voigt, Tobias, Roland Fried, Michael Backes, and Wolfgang Rhode (2014). „Threshold optimization for classification in imbalanced data in a problem of gamma-ray astronomy". In: *Advances in Data Analysis and Classification* 8, pp. 195–216.

Wayth, RB, E Lenc, ME Bell, JR Callingham, et al. (2015). „GLEAM: The galactic and extragalactic all-sky MWA survey". In: *Publications of the Astronomical Society of Australia* 32, e025.

Weekes, T. C., M. F. Cawley, D. J. Fegan, K. G. Gibbs, et al. (1989). „Observation of TeV gamma rays from the Crab nebula using the atmospheric Cerenkov imaging technique". In: *ApJ* 342, pp. 379–395. DOI: 10.1086/167599.

Weekes, TC, H Badran, SD Biller, I Bond, et al. (2002). „VERITAS: the very energetic radiation imaging telescope array system". In: *Astropart. Phys.* 17.2, pp. 221–243.

Weisskopf, Martin C., Ronald F. Elsner, Jeffery J. Kolodziejczak, Stephen L. O'Dell, and Allyn F. Tennant (2012). „Unraveling the Geometry of the Crab Nebula's "Inner Ring"". In: *ApJ* 746, p. 41. DOI: 10.1088/0004-637X/746/1/41.

Weisskopf, Martin C., J. Jeff Hester, Allyn F. Tennant, Ronald F. Elsner, et al. (2000). „Discovery of Spatial and Spectral Structure in the X-Ray Emission from the Crab Nebula". In: *ApJ* 536, p. L81. DOI: 10.1086/312733.

Wentzel, Donat G (1974). „Cosmic-ray propagation in the Galaxy-Collective effects". In: *In: Annual review of astronomy and astrophysics. Volume 12.(A75-13476 03-90) Palo Alto, Calif., Annual Reviews, Inc., 1974, p. 71-96.* 12, pp. 71–96.

Wilks, S. S. (1938). „The Large-Sample Distribution of the Likelihood Ratio for Testing Composite Hypotheses". In: *Ann. Math. Stat.* 9, pp. 60–62. DOI: 10.1214/aoms/1177732360.

Wilson-Hodge, Colleen A., Michael L. Cherry, Gary L. Case, Wayne H. Baumgartner, et al. (2011). „When a Standard Candle Flickers". In: *ApJ* 727, p. L40. DOI: 10.1088/2041-8205/727/2/L40.

Wood, M., R. Caputo, E. Charles, M. Di Mauro, et al. (2017). „Fermipy: An open-source Python package for analysis of Fermi-LAT Data". In: *arXiv e-prints*.

Workman, R. L. et al. (2022). „Review of Particle Physics". In: *Prog. Theor. Exp. Phys.* 2022, p. 083C01. DOI: 10.1093/ptep/ptac097.

Worrall, D. M., M. Birkinshaw, R. P. Kraft, G. R. Sivakoff, et al. (2008). „Where Centaurus A Gets Its X-Ray Knottiness". In: *The Astrophysical Journal* 673.2, p. L135. DOI: 10.1086/528681.

Yeung, P. K. H. and D. Horns (2019). „The Energy-dependent γ-Ray Morphology of the Crab Nebula Observed with the Fermi Large Area Telescope". In: *ApJ* 875, p. 123. DOI: 10.3847/1538-4357/ab107a.

— (2021). „Erratum: "The Energy-dependent γ-Ray Morphology of the Crab Nebula Observed with the Fermi Large Area Telescope" (2019, ApJ, 875, 123)". In: *ApJ* 909, p. 221. DOI: 10.3847/1538-4357/abea1b.

Zabalza, V. (2015). „Naima: a Python package for inference of particle distribution properties from nonthermal spectra". In: *Proc. 34th Int. Cosmic Ray Conf.* ICRC2015, 922, p. 922.

Zhang, L. and X. C. Yang (2009). „TeV Gamma-Ray Emission from Vela X: Leptonic or Hadronic?" In: *ApJ* 699, p. L153. DOI: 10.1088/0004-637X/699/2/L153.

Zhang, Zhipeng, Ruizhi Yang, Shoushan Zhang, Zhen Xie, et al. (2024). „Layout optimization and Performance of Large Array of imaging atmospheric Cherenkov Telescope (LACT)". In: *Chinese Physics C*.

Zheng, Xueying, Ponti, Gabriele, Freyberg, Michael, Sanders, Jeremy, et al. (2024). „Broadband maps of eROSITA and their comparison with the ROSAT survey". In: *A&A* 681, A77. DOI: 10.1051/0004-6361/202346576.

Zhou, Shiqi, Erbil Gügercinoğlu, Jianping Yuan, Mingyu Ge, and Cong Yu (2022). „Pulsar glitches: A review". In: *Universe* 8.12, p. 641.

Acknowledgments

First of all, I want to thank Jesus for his voluntary sacrifice — an overpayment for all my debts. Thank you for never being far and for saving me even when I didn't understand it. You changed my life with the truth you speak and the hope you give. I would also like to thank everyone else who supported me during my studies, provided feedback on chapters of this thesis, or simply engaged in stimulating discussions. Special thanks go to:

- Prof. Dr. Stefan Funk, for the opportunity to be part of his research group and the many fruitful discussions. I really appreciate your warm and open nature, the patience you showed when I was new to the group, and your pragmatic approach to complex problems. Thank you for always taking the time to actively think about my problems despite your numerous responsibilities and for sharing your experience as a senior researcher.

- Lars Mohrmann, for his insights and advice during our many discussions. It is my pleasure to have you as a co-author on all my publications, and I appreciate the effort you put into turning each of these projects into a success.

- Manuel Meyer, for the close cooperation on the Crab Nebula project, especially the Fermipy analysis and modeling part. Thank you for sharing your expertise with me.

- Rodrigo Guedes Lang, for his close supervision on the monoscopic reconstruction project and his realistic assessment of possible solutions to many problems. Thank you for your appreciative nature, patience, and for sharing the frustration during the HAP debug sessions.

- My office members: Gerrit, for branding and representing the "shadow office" to the outside; Martin, for his good advice to add some humor to the acknowledgments; and Franzi, for perfectly monitoring and regulating the office temperature. I really enjoyed coming to the office.

- All the colleagues at ECAP, for the productive working environment, in addition to the extended table tennis sessions and coffee breaks. Besonders auch dir, Gabriele Eckner, für deine super Unterstützung in allen bürokratischen Angelegenheiten.

- Giacomo D'Amico and Julia Djuvsland, for their contribution to the unbinned analysis in Gammapy, all the fruitful discussions, and the fun we had during the time in Heidelberg.

- The Multi-Messenger School and colleagues therein, for connecting young researchers and enabling the very enjoyable trip to Israel.

- Martin, Christel, Nick und Lisa, meinen Eltern und Geschwistern, für die ständige Unterstützung. Besonders während des Lockdowns und den Tagen im Homeoffice war ich froh, eine so tolle und fürsorgliche Familie zu haben.

This research has made use of the CTA instrument response functions provided by the CTA Consortium and Observatory, see `https://www.ctao-observatory.org/science/cta-performance/` (version prod5 v0.1; Cherenkov Telescope Array Observatory and Cherenkov Telescope Array Consortium, 2021) for more details. This research made use of the Astropy (`http://www.astropy.org`; Astropy Collaboration, 2013; Astropy Collaboration, 2018), NUMPY (Harris et al., 2020), SCIPY (Virtanen et al., 2020), and MATPLOTLIB (`http://www.matplotlib.org`; Hunter, 2007) software packages. I gratefully acknowledge the computing resources and support provided by the Erlangen National High Performance Computing Center (NHR@FAU). The unbinned analysis project was supported by KONWIHR (`https://www.konwihr.de/`).